Silver nanoparticles and thin films for strained-silicon surface enhanced Raman spectroscopy and capacitively-coupled radiofrequency heating

By

Stuart James Corr

BEng (hons), MEng

Thesis Submitted for the degree of

Doctor of Philosophy

Research Supervisor

Prof. Patrick J. McNally

Dublin City University

School of Electronic Engineering

January 2011

I hereby certify that this material, which I now submit for assessment on the programme of study leading to the award of Doctor of Philosophy is entirely my own work, that I have exercised reasonable care to ensure that the work is original, and does not to the best of my knowledge breach any law of copyright, and has not been taken from the work of others save and to the extent that such work has been cited and acknowledged within the text of my work.

Signed:

Candidate ID No.: 56210318 Date: 25th January 2011

Acknowledgements

Although the original intention of this project was to spend two years working on a research Master's thesis whilst saving the capital for a year immersed in space studies at the International Space University in Strasbourg, France I have to acknowledge the fact that without the overwhelming help, support and dedication from my supervisors Dr. Lisa O'Reilly and Prof. Patrick McNally, this work would never have evolved into a PhD thesis. Their endless guidance and enthusiasm for my ideas combined with support for establishing an international collaboration at Rice University meant that I could fulfil the original project requirements as well as develop and extend our nanotechnology research into new areas to help contribute to NPL's main objectives.

I am indebted to the Irish FÁS Science Challenge 2006 – 2007 which placed me at the heart and soul of a thriving international nanotechnology industry and kicked off my career as a young, nanotech researcher. Dr. Pauline Ward and John Cahill were paramount in the smooth running and establishment of this programme and were kind enough to let me be a part of it. To this end I have to give an overwhelming debt of gratitude and kindness to Prof. Lon. J. Wilson who was completely sound in having a young engineer 'tinkle' with all kinds of chemistry experiments within his bioinorganic and biomaterials research lab. Kindness goes out to the entire Wilson research group for their time and hospitality as well as our collaborators at M.D. Anderson Cancer Centre (Dr. Curley's surgical oncology group) for allowing me use of the precious John Kanzius RF machine. A warm thank you also goes out to all of the NPL group, especially Dr. Aidan Cowley whose anecdotes and Gedanken experiments continuously gave me an intellectual booster. Thank you. A warm thank you also goes out Billy Roarty, Ger Considine, Robert Clare, Liam Meaney, Conor Maguire, Paul Wogan, Breeda McManus, Dr. Noel Murphy, and Dr. Stephen Daniels.

Finally, my family. Mick, Les and Liam. I am nothing without the love and support you have given me. "*...For magic doors there is this, you do not see them even as you're walking through....*"

Abstract

Silver nanoparticles and thin films for strained silicon surface enhanced Raman spectroscopy and capacitively-coupled radiofrequency heating.

Stuart James Corr

The unique properties of silver nanoparticles (Ag NP) have been exploited within the fields of photonics and biotechnology over the last decade due to their wide range of novel uses and applications. The surface plasmon polariton response of Ag NPs and thin films dispersed onto nm-thin layers of strained silicon (ε-Si) grown on $Si_{1-x}Ge_x$ virtual substrates can be utilised to provide surface enhanced Raman spectroscopy (SERS) of the ε-Si layer compared to the bulk $Si_{1-x}Ge_x$ virtual substrate – overcoming the need to use low resolution, expensive ultra-violet Raman excitation sources. For biological applications it is thought (based on recent work on Au NPs) that Ag NPs can also be applied as effective thermal agents for cancer hyperthermia due to their ability to heat under the influence of a high-power, radiofrequency (RF) electric field operating at 13.56 MHz – potentially allowing for *single-cellular* cancer treatment, eliminating the current trends of invasive and life-threatening cancer treatments such as radiation, proton, gene and immunotherapy, and generic surgical resections.

In the first instance, thin films of Ag NPs were deposited onto a variety of ε-Si samples (9 nm [Ge 30 %], 17.5 nm [Ge 20 %], and 42 nm [Ge 20 %]) via high pressure, direct thermal evaporation of Ag nanopowder (source-to-substrate distance of 21 cm). Alternatively, Ag NPs synthesised via a chemical reduction technique (polyol process) using poly(vinylpyrrolidone) as the capping agent, as well as citrate stabalised NPs, were also dispersed onto identical samples. Both techniques were analysed for their SERS viability via micro-Raman spectroscopy (488 nm Ar^+ excitation source). Where SERS evidence is shown, enhancement factors and strain values are calculated. Evidence is also given to shown that small ε-Si peak shifts may be due to point-to-point ε-Si strain fluctuations. Where appropriate, the plasmonic origin of the SERS effects are highlighted using SEM and UV-VIS data.

For the cell hyperthermia studies the heating efficacies of commercially available Ag and Au NPs, synthesied via citrate reduction techniques, were also investigated by means of a capacitively-coupled RF heating system with a thermal imaging camera. Although there was rapid heat production from the as-purchased Ag NP/buffer solutions, NPs dispersed in ultra-pure high pressure liquid chromatography water were indeed shown to exhibit heat production, albeit on a lesser scale. The fact that buffer heating rates are greater than NP heating rates contradicts recent work as these researchers did not take these heating attributes into account. Theoretical analysis using a metallic volumetric heating equation as a function of NP size and solution volume, combined with a modified metallic conductivity due to a reduction in the electron mean free path, allowed for close similarities between experimental and theoretical values to be drawn. These results have ultimately shown the potential for Ag NPs as single cellular cancer hyperthermic treatment agents – a technique *unrivalled* by any current existing technology.

Table of Contents

Declaration....................i

Acknowledgements....................ii

Abstract....................iii

Table of Contents....................iv

List of Figures....................vi

List of Tables....................xi

Glossary....................xii

CHAPTER 1: *Introduction*

1.1 Silver nanoparticles & applications....................1

1.2 Strained silicon....................5

1.3 Surface enhanced Raman spectroscopy....................9

1.4 Optical excitation of surface plasmon polaritons....................13

1.5 Nanotechnology for cancer therapeutics....................18

1.6 Project objectives & overview....................20

1.7 References....................22

CHAPTER 2: *Silver Nanoparticle Synthesis Techniques*

2.1 Introduction....................27

2.2 Direct thermal evaporation....................28

2.3 Evaporation rate and nucleation kinetics....................33

2.4 Chemical synthesis (polyol process)....................37

2.5 Solution based nanoparticle growth kinetics....................40

2.6 Chemical synthesis setup and components....................43

2.7 Conclusion....................47

2.8 References....................49

CHAPTER 3: ***Characterisation Techniques***

3.1 Introduction....52

3.2 Micro-Raman spectroscopy (μ-Raman)....53

3.3 Scanning electron microscopy (SEM)....58

3.4 Transmission electron microscopy (TEM)....61

3.5 Ultra-Violet visible spectroscopy (UV-VIS)....64

3.6 Inductively-coupled plasma optical emission spectroscopy (ICP-OES)....67

3.7 Conclusions....70

3.8 References....70

CHAPTER 4: ***Sticky SERS (Evaporation)***

4.1 Introduction & Aims....72

4.2 Sample preparation....74

4.3 Strained-silicon SERS optimisation results....75

4.4 SERS enhancement factor calculations....87

4.5 Plasmonic considerations....89

4.6 Conclusions....95

4.7 References....97

CHAPTER 5: ***SOL-SERS (Chemical)***

5.1 Introduction & Aims....99

5.2 Sample preparation....101

5.3 SEM & UV-VIS results....103

5.4 Micro-Raman SERS results....117

5.5 SERS enhancement factor calculations....129

5.6 Conclusion....130

5.7 References....131

CHAPTER 6: *Capacitively-coupled radiofrequency heating*

6.1 Introduction..132

6.2 J. Kanzius RF heating apparatus..133

6.3 Sample preparation and characterisation...136

6.4 RF heating results...140

6.5 Theoretical analysis..147

6.6 Conclusions..165

6.7 References..166

CHAPTER 7: *Conclusions & further work*

7.1 Conclusions & future work..170

APPENDIX

A: Chapter 6 supplementary data...175

B: Possible mechanism behind hydrogen-oxygen dissociation from aqueous NaCl solution..184

List of Figures

Chapter 1:

Fig. 1.1a Schematic of a typical NMOS strained-silicon transistor, and strain induced within relaxed silicon when grown on top of a SiGe substrate……………..7

Fig. 1.1b Raman spectrum for 9 nm, 17.5 nm, and 42 nm thick ε-Si layers grown on $Si_{0.7}Ge_{0.3}$, $Si_{0.8}Ge_{0.2}$, and $Si_{0.8}Ge_{0.2}$ virtual substrates respectively...7

Fig. 1.2 Schematic of electromagnetic wave entering a slab of two semi-infinite media with dielectric functions ε_1 and ε_2 separated by a planar interface at z = 0 travelling along the x-axis (left to right of page)..14

Chapter 2:

Fig. 2.1 Edwards Auto 306 system diagram..30

Fig. 2.2 Schematic of evaporation chamber with modified stage holder……………………….31

Fig. 2.3 Chamber pressure versus time for five identical evaporations; A, B, C, D, and E, using a constant current (30 A), source material weight (120 mg), and evaporation starting pressure ($1x10^{-4}$ mbar)…………………………………………………….32

Fig. 2.4 Film thickness uniformity (d/d_o) for a point source as a function of substrate Geometry (l/h)..35

Fig. 2.5 Three modes of thin-film growth…………………………………………….....................36

Fig. 2.6 Generic experimental chemical schematic for polyol process……………………….....39

Fig. 2.7 Possible Ag NP morphologies……………………………………….……………….....42

Fig. 2.8 Experimental setup…………………………………………..………………………46

Chapter 3:

Fig, 3.1 Energy diagram for Rayleigh, Stokes, and Anti-Stokes scattering................................53

Fig. 3.2 Energy level diagram for first-order Stokes scattering..54

Fig. 3.3 System schematic of Hitachi S-4700 SEM beam column...56

Fig. 3.4 Bremsstrahlung energy diagram for impact of electrons with specimen under SEM...57

Fig. 3.5 Schematic electron ray path for TEM equipped for additional x-ray and electron loss spectroscopy...59

Fig. 3.6 UV-VIS spectra for Ag NPs 40 nm and 60 nm in diameter (suspended in water)...62

Fig. 3.7 ICP-OES system schematic..65

Chapter 4:

Fig, 4.1 Raman spectrum for 9 nm, 17.5 nm, and 42 nm ε-Si samples.......................................76

Fig. 4.2 17.5 nm strained-silicon SERS enhancement at 4 random locations.............................77

Fig. 4.3 SERS SiGe and ε-Si peak shifts as a function of focal height.......................................80

Fig. 4.4 9 nm ε-Si SERS enhancement at 6 random locations..85

Fig. 4.5 42 nm ε-Si SERS enhancement at 5 random locations..85

Fig. 4.6 Raman spectra of 9 nm thick ε-Si using un-polarised light (9 nm), and p-polarised light...91

Fig. 4.7 Raman spectra of 9 nm thick ε-Si using un-polarised light (9 nm), and s-polarised light...91

Fig. 4.8 SEM micrographs of Ag nanoparticle growth on 9 nm thick ε-Si via direct thermal evaporation..93

Fig. 4.9 UV-VIS data for Ag NPs on glass slide (co-evaporated simultaneously with 17.5 nm thick ε-Si sample)...94

Fig. 4.10 µ-Raman spectroscopy data for 9 nm ε-Si sample for multiple scans, on the same spot, across a 60 minute time interval..94

Chapter 5:

Fig. 5.1 Ted Pella industrial samples 1 to 4 (photo)...102

Fig. 5.2 Polyol samples 5 to 8 (photo)...102

Fig. 5.3 SEM (JEOL) micrograph of sample 1 (Ted Pella, 20 nm)..104

Fig. 5.4 SEM (JEOL) micrograph of sample 2 (Ted Pella, 40 nm)..105

Fig. 5.5 SEM (JEOL) micrograph of sample 3 (Ted Pella , 60 nm)..106

Fig. 5.6 SEM (JEOL) micrograph of sample 4 (Ted Pella, 80 nm)...107

Fig. 5.7 SEM (S-550) micrograph of sample 5 (polyol)...107

Fig. 5.8 SEM (S-550) micrograph of sample 5 (polyol)..108

Fig. 5.9 SEM (S-550) micrograph of sample 6 (polyol)..109

Fig. 5.10 SEM (Zeiss) micrograph of sample 6 (polyol)...110

Fig. 5.11 SEM (S-550) micrograph of sample 7 (polyol)..111

Fig. 5.12 SEM (S-550) micrograph of sample 8 (polyol)..111

Fig. 5.13 UV-VIS absorption spectra for samples 1 to 4 (Ted Pella silver NPs of diameter 26 ± 4 nm, 49.6 ± 9 nm, 76 ± 11 nm , and 115 ± 20 nm, respectively)......................112

Fig. 5.14 UV-VIS spectrum for samples 5 to 9 (polyol synthesised silver NPs of diameter 33 ± 11 nm, 78 ± 19 nm, 80 ± 18 nm, and 147 ± 38 nm respectively).......................113

Fig. 5.15 Histogram of particle sizes for samples 1 to 4...114

Fig. 5.16 Histogram of particle sizes for samples 5 to 8...114

Fig. 5.17 Raman spectra for 9 nm, 17.5 nm, and 42 nm thick ε-Si samples............................118

Fig. 5.18 Micro-Raman optical image of Ag NP coverage on 17.5 nm ε-Si (black-white image, 20 µm scale). Superimposed on top are areas of 17.5 nm SERS enhancements shown by varying red intensities…………………………………………………………........118

Fig. 5.19 ε-Si SERS enhancements using sample 1 NPs of average size 26 ± 4 nm……........119

Fig. 5.20 ε-Si SERS enhancements using sample 2 NPs of average size 49 ± 9 nm................119

Fig. 5.21 ε-Si SERS enhancements using sample 3 NPs of average size 76 ±11 nm……........120

Fig. 5.22 ε -Si SERS enhancements using sample 4 NPs of average size 115 ±20 nm…..........121

Fig. 5.23 ε -Si SERS enhancements using sample 5 polyol stabalised Ag NPs of average size 33 ± 11 nm..122

Fig. 5.24 ε -Si SERS enhancements using sample 6 polyol stabalised Ag NPs of average size 78 ± 19 nm..122

Fig. 5.25 ε -Si SERS enhancements using sample 7 polyol stabalised Ag NPs of average size 80 ± 18 nm………………………………………………………………….........123

Fig. 5.26 ε -Si SERS enhancements using sample 8 polyol stabalised Ag NPs of average size 147 ± 38 nm………………………………………………………………...124

Fig. 5.27 ε -Si SERS enhancements using sample 7 polyol stabalised Ag NPs of average size 80 ± 18 nm on 9 nm thick ε-Si...125

Fig. 5.28 ε -Si SERS enhancements using sample sample 7 polyol stabalised Ag NPs of average size 80 ± 18 nm on 42 nm thick ε-Si...126

Chapter 6:

Fig. 6.1 Prototype of the RF J. Kanzius heating system...134

Fig. 6.2 UV-VIS spectra of Ag and Au NPs...138

Fig. 6.3 Heating rate of HPLC water in a variety of glass and plastic containers....................140

Fig. 6.4 Heating rates of Ag and Au buffers versus as-purchased solutions (i.e. NPs suspended in buffers) for a concentration of 5 mg/l.. 141

Fig. 6.5 Hydrogen-oxygen dissociation effect..143

Fig. 6.6 Heating rates of Ag and Au NPs of various diameters (20, 40, 60, and 80 nm) and concentrations (0.5, 5, and 50 mg/l)...144

Fig. 6.7 Heating rate versus Ag NP diameter for 0.5, 5, and 50 mg/l concentrations. Also shown are the *average* heating rates as a function of concentration.................................145

Fig. 6.8 Average heating rate versus concentration curves for Ag and Au NPs.......................146

Fig. 6.9 Heating rate per NP versus NP diameter for Ag experimental studies of 0.5, 5.0, and 50 mg/l concentrations...154

Fig. 6.10 Heating rate per NP versus NP diameter for Au experimental studies of 0.5, 5.0, and 50 mg/l concentrations..154

Fig. 6.11 TEM image of 20 nm Ag NPs dispersed in as-purchased buffer solutions...............156

Fig. 6.12 TEM image of 20 nm Ag NPs dispersed in HPLC after centrifugation procedure....156

Fig. 6.13 Illustration of the surface interaction of water molecules on an Ag NP under equilibrium conditions (no external electric field)...159

Fig. 6.14 Illustration of Ag NP/water interactions in electric field..161

Fig. 6.15 Heating rate per 20 nm Ag NP suspended in a variety of HPLC water volumes…...163

Fig. 6.16 Heat production versus volume (for a 20 nm Ag NP) using equation 6.21…………164

Fig 6.17: TEM image of 20 nm Ag NPs fused together after RF exposure………………..…165

Appendix A:

Fig. A.1 Ag NPs of dimensions 20.1 ± 2 suspended in HPLC water…………………………175

Fig. A.2 Ag NPs of dimensions 41.2 ± 4 suspended in HPLC water…………………………176

Fig. A.3 Ag NPs of dimensions 62.5 ± 6.1 suspended in HPLC water……………………….176

Fig. A.4 Ag NPs of dimensions 80.1 ± 8.6 suspended in HPLC water……………………….177

Fig. A.5 Au NPs of dimensions 17.3 ± 1.9 suspended in HPLC water……………………….178

Fig. A.6 Au NPs of dimensions 39.4 ± 4.3 suspended in HPLC water……………………….179

Fig A.7 Au NPs of dimensions 61.1 ± 6.8 suspended in HPLC water………………………..179

Fig. A.8 Au NPs of dimensions 83.4 ± 7.4 suspended in HPLC water……………………….180

Fig. A.9 UV-VIS spectrum of 40 nm Ag NPs suspended in HPLC water for concentrations 0.5, 5, and 50 mg/l..181

Fig. A.10 UV-VIS spectrum of 40 nm Au NPs suspended in HPLC water for concentrations 0.5, 5, and 50 mg/l..181

Appendix B:

Fig. B.1 Electrolysis chemical reaction pathway...185

Fig. B.2 Heating rates for 0.5, 5, and 50 mg/l NaCl solutions..188

Fig. B.3 pH of NaCl solutions before and after exposure to RF field.......................................188

Fig. B.4 Proposed chemical reaction pathway for H_2 dissociation from water..........................189

Fig. B.5 Starch iodide paper after RF exposure..190

Fig. B.6 Possible evidence of Cl_2 by-products...191

List of Tables:

Chapter 4:

Table 4.1 SiGe and e-Si peak positions (non-SERS and SERS) for 9 nm, 17. 5nm and 42 nm e-Si samples..86

Table 4.2 Values for enhancement factor calculations...89

Chapter 5:

Table 5.1 Summary of ε-Si SERS peaks and strain values for samples 1 to 8 applied to 17.5 nm thick ε-Si samples as well as sample 7 applied to 9 nm and 42 nm thick ε-Si samples..127

Table 5.2 Calculated SERS enhancement values for sample 7 deposited onto 9 nm, 17.5 nm, and 42 nm ε-Si samples...129

Chapter 6:

Table 6.1 Characterisation data for Ag and Au NPs...137

Table 6.2 Calculated mean free path (m.f.p.) and conductivity (σ) for Ag and Au NPs used in experiment..148

Appendix A:

Table. A.1 Theoretical evaluation data for Ag NPs at a 0.5 mg/l concentration.......................182

Table. A.2 Theoretical evaluation data for Ag NPs at a 5 mg/l concentration..........................183

Table A.3 Theoretical evaluation data for Ag NPs at a 50 mg/l concentration.........................183

Table. A.4 Theoretical evaluation data for Au NPs at a 0.5 mg/l concentration.......................183

Table. A.5 Theoretical evaluation data for Au NPs at a 5 mg/l concentration..........................183

Table. A.6 Theoretical evaluation data for Au NPs at a 50 mg/l concentration........................183

Glossary

AFM – atomic force microscopy

Ag – silver

Au – gold

DTE - direct thermal evaporation

EG – ethylene glycol

GA – glycoaldehyde

HR-XRD – high resolution XRD

IC – integrated circuit

ICP-MS – inductively coupled plasma mass spectroscopy

NPs - nanoparticle(s)

PVP – Polyvinylpyrrolidone

RF - radiofrequency

SEM – scanning electron microscopy

SERS – surface enhanced Raman spectroscopy

SiGe – silicon-germanium

SPP – surface plasmon polariton

TEM – transmission electron spectroscopy

TERS – tip enhanced Raman spectroscopy

μ-Raman – micro Raman spectroscopy

UV-VIS – Ultra-violet visible spectroscopy

UV – Ultra violet

XRD – X-ray Diffraction

ε-Si – strained-silicon

Chapter 1

Introduction

1.1 Silver nanoparticles & applications

Silver nanoparticles (Ag NPs) in the size regime of 1 nm to 100 nm have been extensively studied in the fields of photonics and biotechnology over the last decade due to their wide range of novel uses and applications. Considering that their optical response can be tuned across the visible range via control of their size and morphology they have been used in applications such as chemical and biological sensors [1-7], probes for surface enhanced Raman spectroscopy [8-11], and metameterials [12,13]. They have also shown considerable potential in the biotechnology market due to their inherent antimicrobial and antifungal properties and have already found use in applications such as the inhibition of the HIV-I virus [14], anti-angiogenesis properties [15], and topical wound treatment [16].

The optical, plasmonic response of Ag NPs can be exploited to allow for single molecular characterisation via Raman spectroscopy [17, 18] due to localized electric field enhancements from resonant surface plasmon polaritons (SPPs)*. These SPPs have a resonance condition which if tuned to the incident optical wavelength allows for the amplification of light in the near-field. It is this near-field amplification which

- *A SPP is a quasiparticle resulting from the quantization of plasma oscillations which are collective oscillations of the free electron gas density – described in section 1.3-1.4* provides selective characterisation of single molecular analytes in close proximity (~5 nm) to the Ag NPs. Also, new optical sensor technologies can use plasmon resonance effects - a function of the Ag NPs internal and external dielectric functions – where changes in the local refractive index, and thus visible absorption spectra, can occur for attachment of specific analytes to functionalised Ag NPs which can then be ‘optically read’ using specific optical instruments such as UV-VIS [1-7].

With regards to bio-applications, historical references have speculated that silver has been used for centuries. In the times of the Greeks and Romans it was observed that slime would not proliferate on silver lined jugs and there are even stories that early American pioneers would put a silver dollar in milk jugs to extend its freshness. This is due to silver ions being bioactive, readily killing bacteria *in vitro* at sufficient concentrations as well as killing bacteria on infected external wounds on living tissue and has led physicians to use wound dressings containing silver-sulfadiazine and Ag NPs to treat external infections [19-21].

Silver colloidal solutions, marketed as alternative medicine and dietary supplements, can also be purchased on the health-food market to help treat various remedies and ailments. Before the 1940’s silver was even sparsely used internally for diseases such as tropical sprue and gonorrhoea [22, 23] although its use diminished rapidly due to the establishment of large pharmaceutical companies and their antibiotic products – a fact which seems to be a contentious issue between current pro-silver activists and governmental regulatory organisations such as the American Food and Drug Administration [24].

Throughout this work, the SPP response of silver thin films and Ag NPs is utilised to provide selective Raman enhancement of nm thin strained-silicon (ε-Si) layers on top of silicon-germanium ($Si_{1-x}Ge_x$) substrates – materials which are being extensively used throughout the semiconductor industry for next-generation, faster, integrated circuits (IC). The techniques used herein to employ this ε-Si Raman enhancement are such that they allow for a truly portable probe deployment, enabling rapid, on-site IC characterisation to take place without the need for extensive hardware configurations, as well as overcoming the need to use lower resolution, expensive ultra-violet (UV) Raman excitation laser sources which until now were the only way of probing such nm thin ε-Si layers. The results from these experiments have led to a poster presentation at the 4th Annual Surface Plasmon Photonics 4 conference, Amsterdam, 2009, as well as a manuscript submission to *J. Raman Spectroscopy* entitled "*Poly(vinylpyrrolidone) stabilized silver nanoparticles for strained-silicon surface enhanced Raman spectroscopy*" which has been accepted for publication. Having successfully achieved these goals the use of Ag NPs was then extended into the field of bio-nanotechnology which aided in forming new international collaborations and technology transfer initiatives.

Silver NPs were hence investigated for their use as potential cancer therapeutic agents via cellular hyperthermia from capacitively-coupled radiofrequency (RF) heating. This work was part of an international collaboration with a highly respected nanotechnology institute: the Richard E. Smalley Institute for Nanoscale Science and Technology at Rice University, Houston, Texas, as well as the M.D. Anderson Cancer Center, Houston, Texas, USA. This work is ultimately centred on the utilization of nanotechnology for minimally invasive, *single cancer cell treatment*, eliminating the current trends of potentially life-threatening cancer treatments such as radiation, proton, gene and immunotherapy, and invasive surgical resections.

Radiofrequency ablation techniques have been used to successfully treat small cerebral tumours over the past 40 years and has proved to be a safe and reproducible technique for well-defined regions of coagulation necrosis*. A power generator supplies RF power to an active electrode tip which is directly inserted into the tumour. Local resistive tissue heating is produced as ions in close proximity follow RF electric field oscillations. Heating is instantaneous and induces cellular death via irreversible protein denaturation. However, there are still severe disadvantages [25-27] to these techniques such as large needle size (1.6 to 2.5 mm) and restrictive penetration depth due to organ proximities; extensive tissue charring in close proximity to the active electrodes; non-uniform tumour heating profiles which actively kill healthy cells; use restricted by tumour size – tumours larger than 3-5 cm may need multiple overlapping sequential ablations whilst tumours smaller than the needle electrode diameter may be untreatable.

With these factors in mind it is thought that if Ag (or Au) NPs could internalise within cancer cells via antibody targeting moieties* and be subjected to an external, high-power RF field, cellular necrosis could take place at a *single cellular level* due to the NPs supplying energy via RF resistive heating. This may allow for controlled, cancer treatment protocols at the earliest stage possible – reducing the development of terminal metastatic cancer.

Using a high-power, capacitively-coupled RF apparatus located within the S. Curley surgical oncology lab at M.D. Anderson we tested the heating efficacies of Ag and Au NPs, across a variety of diameters, suspended in as-purchased buffer solutions and ultra pure high pressure liquid chromatography (HPLC) water. It was shown that Ag NPs do in fact heat up in the RF field and can thus be used as thermal heat agents for

**Coagulation necrosis describes cell death due to a lack of oxygen or restriction of blood vessels.*

** Functionalised Au NPs have already been shown to be non-toxic and internalise within cells. They are also FDA approved [28]. The FDA has also approved the use of metallic silver (not colloidal).*

hyperthermic cancer treatments. To this author's knowledge this is the first time this has been documented. A theoretical framework was also developed to account for the internal heating mechanism of both Ag and Au NPs which would ultimately allow for maximum optimisation of both NP and system design. This work led to a poster presentation at the first annual symposium of the University of Southern California's Physical Sciences in Oncology Center, as well as a manuscript submission to ACS Nano entitled "*Silver nanoparticles as thermal agents in a capacitively-coupled radiofrequency field*" which is also currently under review.

1.2 Strained Silicon

The evolution of the semiconductor and computer industries since the invention of the transistor in the late 1940's has closely adhered to the standards and prerequisites set by Moore's law in that the number of transistors on an integrated circuit would approximately double every 24 months via miniaturization. With current transistor gate dimensions reducing into the nano regime (35 nm gate length with 1.2 nm gate oxide thickness [29]) severe limitations are placed upon further transistor miniaturisation due to problems such as excessive dielectric SiO_2 gate leakage currents via direct electron tunnelling [30], increasing device-to-device variation [31], increased source-drain parasitic access resistance, and reduced channel carrier concentration [32].

Significant developments and improvements regarding these issues have been achieved through the use of ε-Si structures. Strained silicon layers epitaxially grown on lattice mismatched $Si_{1-x}Ge_x$ virtual substrates are becoming extremely important for high-frequency microelectronics applications. Used in the channel region of transistors these ε-Si structures have been demonstrated to produce an improvement in the charge carrier transport properties above that of bulk silicon [33]. As the underlying $Si_{1-x}Ge_x$ epilayers

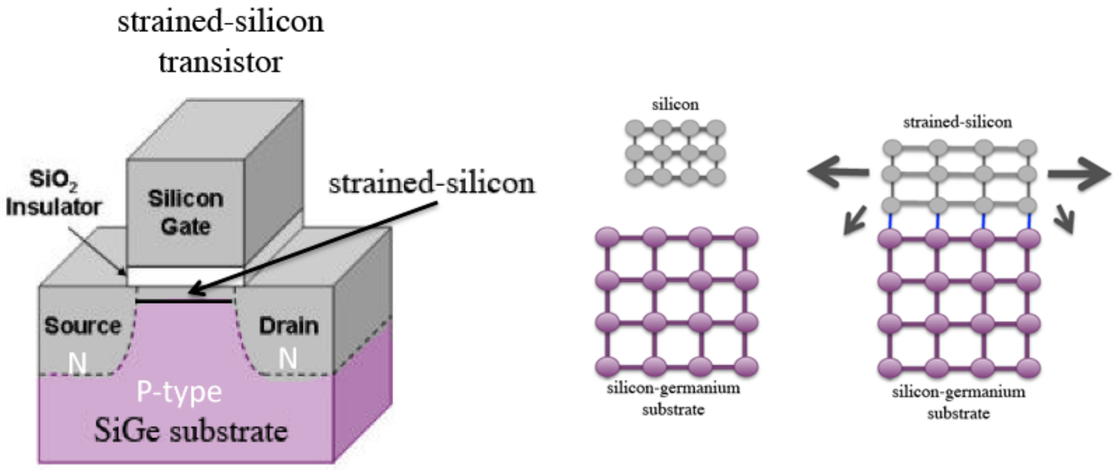

Figure 1.1a: Left: schematic of a typical NMOS strained-silicon transistor. Right: relaxed silicon layer grown on SiGe substrate becomes stretched and 'strained' to match the underlying SiGe lattice constant.

have a larger lattice constant than that of bulk Si, the epitaxy of thin pseudomorphic Si layers creates biaxial tensile strain in the epitaxial layer. Biaxial tensile strain of the order of ~1% in silicon increases the electron and hole mobilities due to the effective mass reduction and the band structure modification induced by strain [34-36]. A schematic of a typical NMOS ε-Si transistor is depicted in figure 1.1a.

As ε-Si surfaces can suffer from nanoscale fluctuations of strain distribution it is imperative to be able to characterise these distributions on the nanoscale. Micro-Raman spectroscopy is a non-destructive tool which can be used for ε-Si characterisation. Micro-Raman studies investigating ε-Si characterization using a variety of laser sources and techniques have shown promising results [37 - 40]. It has been shown that only expensive ultra-violet (325 nm) laser sources with a low penetration depth (~9 nm) are capable of non-destructive strain investigation [37, 40]. Longer laser probe wavelengths such as 514.5 nm propagate deep into the bulk substrate (~770 nm [41]) with the $Si_{1-x}Ge_x$ peak dominating the inherently weak ε-Si signal. Hence, ε-Si analysis at these wavelengths has to be done in combination with etching and software deconvolution

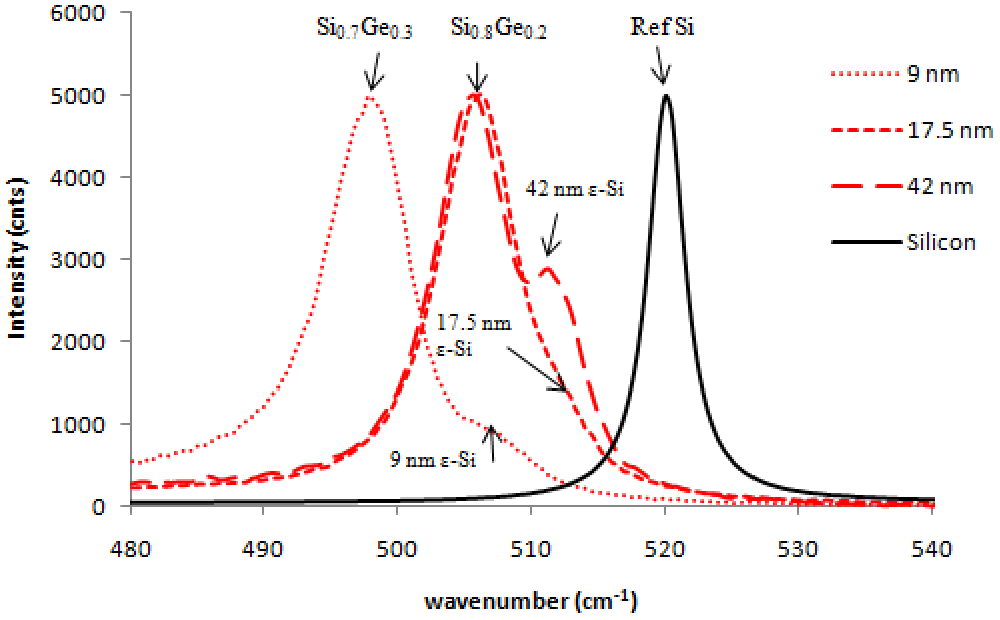

Figure 1.1b: Left: using a 488 nm excitation source a Raman spectra was taken for our 9, 17.5, and 42 nm thick ε-Si layers grown on $Si_{0.7}Ge_{0.3}$, $Si_{0.8}Ge_{0.2}$, and $Si_{0.8}Ge_{0.2}$ virtual substrates, respectively. Data represents a total of 300 scans (20 accumulations for each point, 5 points per sample, three experimental runs). A reference non-strained silicon peak is also shown (black). Both the $Si_{1-x}Ge_x$ and ε-Si peak positions are red-shifted from the standard non-strained reference Si peak for an increase in Ge concentration. A definitive ε-Si peak can only been seen for 42 nm ε-Si.

techniques [39] to separate this weak ε-Si signal. The ability to accurately map ε-Si layers using a non-destructive technique at wavelengths longer than 325 nm is imperative for higher resolution strain mapping and characterization.

Notwithstanding these limitations, Raman spectroscopy can still be used profitably to measure material strain, which allows for theoretical calculations to determine the electrical operating behaviour of the ε-Si layers. Compared to other strain analysis techniques such as x-ray diffraction [42], cross-sectional transmission electron microscopy (XTEM) [43], and convergent beam electron diffraction (CBED) [44] which are either destructive in nature or do not provide the spatial resolution for µm strain analysis, Raman spectroscopy is a far more effective technique.

Experimental analysis of ε-Si and $Si_{1-x}Ge_x$ structures has shown that the concentration of germanium (Ge) in the underlying $Si_{1-x}Ge_x$ virtual substrate layer determines the Raman shift of both the $Si_{1-x}Ge_x$ and ε-Si layers, whereby an increase in Ge concentration results in a red-shifted $Si_{1-x}Ge_x$ and ε-Si Raman peak [45] for the common 520.07 cm^{-1} longitudinal phonon mode (LO). As can be seen from initial Raman analysis of our strained and unstrained silicon samples (figure 1.1b) for standard, non-strained Si only one optical mode is visible at 520.07 cm^{-1} (this is the generic Si-Si vibrational mode). For $Si_{1-x}Ge_x$ structures where the Ge concentration varies from 20 % to 30 % the $Si_{1-x}Ge_x$ peak is red-shifted from approximately 506.55 cm^{-1} to 498.25 cm^{-1} respectively, with corresponding ε-Si peak shifts from 512.52 cm^{-1} to 507.64 cm^{-1}, respectively. This red-shifting corresponds to biaxial tensile strain (blue-shifts of the Si-Si peak would indicate compressive strain [45]).

Also, as can clearly be seen, for ε-Si thicknesses smaller than 42 nm Raman characterisation becomes problematic as no significant peak can easily be identified. This in turn limits theoretical calculations when assessing strain distributions throughout the sample as it is imperative to be able to find an exact value for these ε-Si peak positions.

Theoretical analysis states that for ε-Si the magnitude and sense of strain ($\epsilon_{||}^{\mathrm{StSi}}$) is related to the Raman frequency shift ($\Delta\omega_{\mathrm{Si-Si}}^{\mathrm{St-Si}}$) by the strain shift coefficient of ε-Si ($b_{\mathrm{Si-Si}}^{\mathrm{StSi}}$) according to equation 1.1 [46] where the Raman frequency shift is the difference between the phonon frequency of ε-Si ($\omega_{\mathrm{Si-Si}}^{\mathrm{St-Si}}$) and bulk silicon ($\omega_{0\,\mathrm{Si-Si}}^{\mathrm{bulk\ Si}}$).

$$\Delta\omega_{\mathrm{Si-Si}}^{\mathrm{St-Si}} = \left(\omega_{\mathrm{Si-Si}}^{\mathrm{St-Si}} - \omega_{0\,\mathrm{Si-Si}}^{\mathrm{bulk\ Si}}\right) = b_{\mathrm{Si-Si}}^{\mathrm{StSi}} \cdot \epsilon_{||}^{\mathrm{StSi}} \qquad (1.1)$$

The strain shift coefficient ($b_{\mathrm{Si-Si}}^{\mathrm{StSi}}$) is critical in determining accurate strain values and is either theoretically derived or directly measured via high-resolution X-ray diffraction (HR-XRD) and Raman measurements [45, 46]. However, unless a precise, accurate Raman measurement of the Si-Si vibration modes in the ε-Si layer can be made in the first place (i.e. accurately determining $\omega_{\mathrm{Si-Si}}^{\mathrm{St-Si}}$), these calculations become useless. This is especially prevalent for ε-Si thicknesses smaller than the 42 nm described herein, where determination of the exact location of the ε-Si peak is difficult due to domination by the $\mathrm{Si_{1-x}Ge_x}$ peak. Excellent progress has recently been made, however, via the use of surface enhanced Raman spectroscopy (SERS) to overcome these limitations.

1.3 Surface enhanced Raman spectroscopy

Surface enhanced Raman spectroscopy (SERS) is a Raman spectroscopic technique which refers to the observation that for specific analytes absorbed onto specially prepared metallic NPs an increase in Raman signal is observed [47] (usually of the order 10^5 to 10^6 although enhancements up to 10^{14} have also been recorded [48]). Since the accidental discovery of SERS by Fleischmann *et al*. in 1974 [49] and the subsequent insightful observations of Jeanmaire, Van Duyne, Albrecht and Creighton [50, 51] SERS has been the focus of much research and investigation over the past three decades due to its effectiveness and importance as a spectroscopic tool especially for single molecular recognition schemes needed in industries such as forensics, pharmaceutical, and biotechnology.

Compared to standard Raman spectroscopy SERS allows for sensitive and accurate surface measurements. If, for example, several analytes present upon the surface of a substrate were to be analysed the incident photons from a Raman laser source would tend to propagate deep into the bulk substrate, whose Raman signal would simply overwhelm the relatively weak signal from the analytes. However, due to the enhancement nature of SERS the Raman signal from the surface analytes will be greatly enhanced and appear more pronounced in the Raman data. This is the main reason why SERS is an excellent tool for examining extremely thin (9 nm to 42 nm herein) ε-Si surface layers as the ε-Si Raman spectra becomes more pronounced relative to the bulk $Si_{1-x}Ge_x$ signal.

SERS is most prominent when using surface roughened (10 to 100 nm features) coinage metals such as copper, gold, and silver although results have also been obtained for alkali materials [52]. Methods of SERS-active particle production include: electrode surfaces roughened by oxidation reduction cycles [53]; island film deposition at elevated temperatures [54]; aggregated colloids [55], and nanowire fabrication [56]. It is believed by most that SERS is primarily the result of the electromagnetic enhancement associated with the excitation of intense and sharp localized surface plasmons. This is essentially the electromagnetic theory of SERS. However, there are other, non-electromagnetic theories circulating which try to account for peculiarities for which electromagnetic theories cannot account. As the bulk of recent work in relation to SERS applications for ε-Si detection primarily involve electromagnetic studies, these alternative theories have been omitted from this report but an excellent review can be sought in the literature [47].

In general small, metallic spheres with dimensions smaller than the wavelength of illuminating light will sustain oscillating surface plasmon multipoles of various orders which are induced by the time varying electric field light vector. Also known as SPPs they can either propagate along the interface between a metallic structure and a dielectric or vacuum (along the surface of a grating for example) or can be localized to the surface of a spherical NP. If these metallic spheres are subjected to light of wavelength close to the dipolar plasmon resonance then the metal particle will radiate light characteristic of dipolar radiation [57]. Hence, close to the surface of the NP the incident light will be enhanced in some spatial configurations but decreased in others. Surface plasmon resonance increases both the field of the incident light as well as the scattered Raman field from adsorbed analytes as can be seen from the following brief theoretical summary.

If the field enhancement averaged over the surface of a NP is g, then the average magnitude of the field radiated by this metal NP (E_s) is given by equation 1.2, where E_o is the magnitude of the incident field [57]:

$$E_s = gE_o \quad (1.2)$$

The field induced at the surface of the metallic sphere can be given by equation 1.3 where $\varepsilon_1(\omega)$ is the complex, frequency dependent dielectric function of the metal and ε_2 is the relative permittivity of the ambient phase [52]. The resonance condition of the field induced at the surface of the sphere will be set when Re $(\varepsilon_1) = -2\varepsilon_2$.

$$E_{INDUCED} = \left\{\frac{[\varepsilon_1(\omega) - \varepsilon_2]}{[\varepsilon_1(\omega) + 2\varepsilon_2]}\right\} E_{LASER} \quad (1.3)$$

An analyte absorbed onto the surface of a metallic NP will be excited by this field and scatter light at the Raman-shifted wavelength enhanced by a scaling factor. It can be shown that the amplitude of the SERS-scattered field is proportional to average field enhancement (g), the average Raman-shifted field enhancement (g'), and the incident field (E_o). This is shown in equation 1.4, where α_R is the appropriate combination of components from the Raman tensor [57].

$$E_{SERS} = \alpha_R g g' E_o \qquad (1.4)$$

This SERS enhancement effect (*G*) is often defined as the ratio of the Raman-scattered intensity in the presence of the metal NP to its value in the absence of a metal NP as given by equation 1.5, where α_{RO} is the Raman polarizability of the isolated molecule [50].

$$G = \left|\frac{\alpha_R}{\alpha_{RO}}\right| . |gg'|^{\mathbf{2}} \qquad (1.5)$$

This is very similar to the equation given by Lee *et al.* [58] (equation 1.6) which utilises λ and λ' for the incident and Stokes-shifted wavelengths, respectively, as well as E_o and E for the incident and enhanced SERS field, respectively.

$$G_{SERS} = \left|\frac{E(\lambda)}{E_o(\lambda)}\right|^2 . \left|\frac{E(\lambda')}{E_o(\lambda')}\right|^2 \qquad (1.6)$$

It must be noted however that most SERS observations cannot be understood in terms of simple, isolated NPs. It is the complex, near-field interactions among nanostructures (so-called EM hot-spots) as well as the polarization of the incident light from which the largest SERS enhancements originate due to the increased concentration of both incident and Raman-scattered optical fields. Although this idea arises primarily through theory, recent experiments by Lee *et al.* [58] have successfully validated decades of theoretical debate into the physical and geometrical parameters upon the sensitivity of SERS effects and indicate that SERS has an overwhelmingly *plasmonic* origin.

The extent of the research to date regarding SERS for enhanced ε-Si detection has mostly been based around a procedure known as tip-enhanced Raman spectroscopy

(TERS) which combines both atomic force microscopy (AFM) images and Raman data. TERS involves a sharpened metallic tip (such as a thin layer of silver evaporated onto an AFM cantilever) brought into close proximity of the analyte being investigated which is then illuminated with light. As the cantilever performs AFM contouring operations the light reflected from the surface is fed into a Raman detector, which allows for simultaneous AFM and Raman data to be combined producing nano-accurate ε-Si strain mapping. This tip-enhanced effect can go beyond the diffraction limit of light (down to 250 nm resolutions have been reported [59]) and can even be used for single molecular detection schemes [60]. However, due to technical limitations and 'ease-of-use' issues other researchers are investigating alternative, simpler techniques for enhanced ε-Si detection via SERS.

Hayazawa *et al.* [61] have recently successfully demonstrated that a significantly enhanced ε-Si Raman signal could be produced by the direct thermal evaporation of a thin (10 nm) silver island film straight onto a ε-Si surface. By probing this SERS modified structure with a 488 nm Raman laser source they were able to produce a SERS enhanced ε-Si Raman signal, which was greatly amplified and almost equal to the Raman signal from the underlying $Si_{1-x}Ge_x$ layer. Hence, it was this technique which was the starting point for investigating a portable probe technique for enhanced ε-Si detection via SERS and is discussed in more detail in chapter 2.

1.4 Optical excitation of surface plasmon polaritons

Although a brief summary of the underlying fundamental mechanism of SERS was given in section 1.3, it is worth highlighting several more issues surrounding optical excitation of SPPs as these will be dealt with in more detail in further chapters –

especially when giving evidence for the plasmonic origin of ε-Si Raman enhancements as opposed to generic signal attenuations due to thin silver films.

Surface plasmon polaritons are charge density waves which propagate along the interface between a dielectric and metal composite. Although there are a range of interfaces such as dielectric-dielectric and dielectric-semiconductor which can generate interesting surface excitations, we will deal primarily with dielectric-metal interfaces (strong reflector) where a trapped surface mode may exist at the interface which has electromagnetic fields decaying into both media but are tied to the oscillating surface charge density thereby allowing propagation along the interface.

The surface-plasmon condition can be modelled classically by considering two semi-infinite non-magnetic media with frequency-dependent dielectric functions (ε_1 and ε_2) separated by a planar interface at z = 0, shown in figure 1.2. In the absence of external sources Maxwell's equations (expressed in cgs) are [62]:

$$\nabla \times H_i = \epsilon_i \frac{1}{c}\frac{\partial}{\partial t} E_i \qquad (1.7)$$

$$\nabla \times E_i = -\frac{1}{c}\frac{\partial}{\partial t} H_i \qquad (1.8)$$

$$\nabla . (\epsilon_i E_i) = 0 \qquad (1.9)$$

$$\nabla . H_i = 0 \qquad (1.10)$$

where the index *i* describes the media: *i* = 1 at z > 0, and *i* = 2 at z < 0. If waves are to propagate along the interface there must be a component of the electromagnetic field which is normal to the surface to account for time-dependent polarization charge at the surface. If the *electric field* is parallel to the surface the wave is s-polarised (TE). If the *magnetic field* if parallel to the surface the wave is p-polarised (TM). Hence, surface

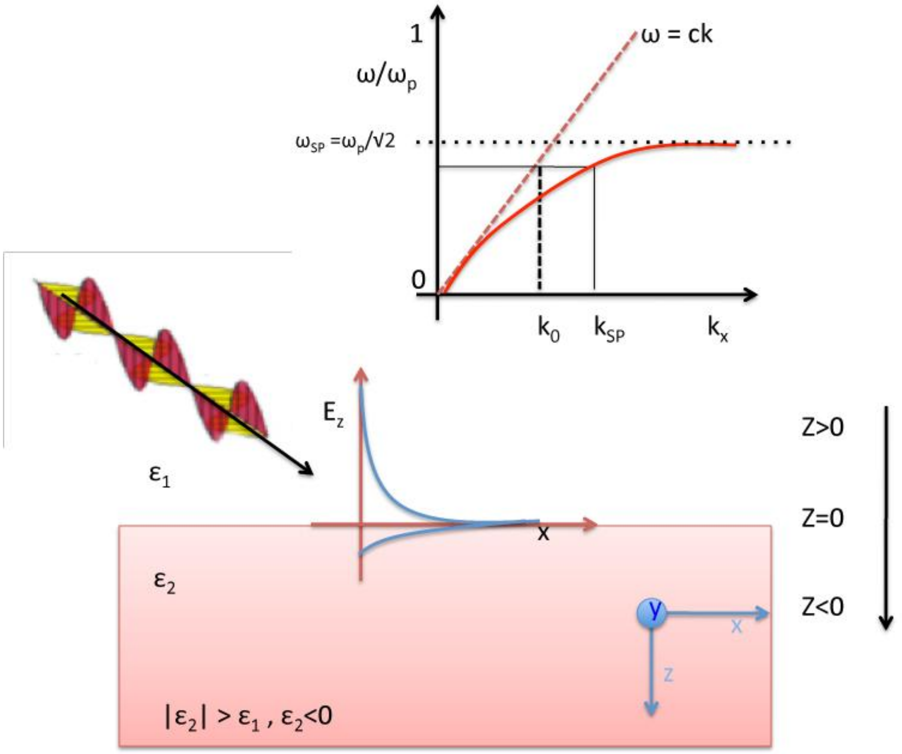

Figure 1.2: Schematic of electromagnetic wave entering a slab of two semi-infinite media with dielectric functions ε_1 and ε_2 separated by a planar interface at z = 0 travelling along the x-axis (left to right of page). Electromagnetic wave has magnetic components parallel to planar surface (p-polarised) along the y-axis (out of page) with the electric field perpendicular to the surface (z-axis, top to bottom of page). Intensity of electric field (E_z) decays exponentially into both media as surface plasmons propagate along x-direction. Also shown is energy dispersion curve (top right) for free light photon curve (ω = ck) and surface plasmon ($\omega_s = \omega_p/\sqrt{2}$).

plasmon modes will only be excited and propagate along the wave direction for a p-polarised wave (as the electric field is normal to the surface) and will be attenuated in the positive (z > 0) and negative (z < 0) directions (figure 1.2). A propagating electromagnetic wave can be described for both electric and magnetic components with propagation along the x-direction via the following equations [53]:

$$E_i = \left(E_{i_x}, 0, E_{i_z}\right) e^{-k_i|z|} e^{-i(q_i x - wt)} \qquad (1.11)$$

$$H_i = \left(0, E_{i_y}, 0\right) e^{-k_i|z|} e^{-i(q_i x - wt)} \qquad (1.12)$$

where q_i represents the magnitude of the wave vector parallel to the surface and k_i is the wave number in media 1 or 2 (i.e. k_1 or k_2). Substituting equations 1.11 and 1.12 into equations 1.7 – 1.10 we find:

$$i\, k_1 H_{1_y} = +\frac{\omega}{c} \epsilon_1 E_{1_x} \qquad (1.13)$$

$$i\, k_2 H_{2_y} = -\frac{\omega}{c} \epsilon_2 E_{2_x} \qquad (1.14)$$

$$k_i = \sqrt{q_i^2 - \epsilon_i \frac{\omega^2}{c^2}} \qquad (1.15)$$

Applying the boundary conditions at z = 0, where the components of the electric and magnetic field parallel to the surface are continuous, i.e. $H_{1_y} = H_{2_y}$ and $E_{1_y} = E_{2_y}$, leads to a simple relationship between the media permittivities and wave vectors:

$$\frac{\epsilon_1}{k_1} + \frac{\epsilon_2}{k_2} = 0 \qquad (1.16)$$

This is known as the surface plasmon condition [53]. Also, the continuity of the 2D wave vector q_i (equation 1.15) must satisfy the boundary conditions, i.e. $q_1 = q_2 = q$. Therefore the surface-plasmon condition (equation 1.16) can now be expressed by the plasmon dispersion formula:

$$q(\omega) = k_x = \frac{\omega}{c} \sqrt{\frac{\epsilon_1 \epsilon_2}{\epsilon_1 + \epsilon_2}} \qquad (1.17)$$

where $\frac{\omega}{c}$ is equal to the wave vector k. For a semi-infinite vacuum-metal interface, equation 1.17 can also be represented to take into account the complex permittivity of the metal (ϵ_2) where large scattering and absorption coefficients cause an imaginary component ($\widetilde{\epsilon_2} = \epsilon_2 + i\epsilon_2$). This is represented by equation 1.18:

$$q\,(\omega) = \frac{\omega}{c}\sqrt{\frac{\epsilon_1(\epsilon_2 + i\epsilon_2)}{\epsilon_1 + (\epsilon_2 + i\epsilon_2)}} \qquad (1.18)$$

Alternatively, by using Drude's case for a semi-infinite metal in a vacuum [63] and taking the following permittivity relations:

$$\epsilon_1 = 1 \qquad (1.19)$$

$$\epsilon_2 = 1 - \frac{\omega_p^2}{\omega(\omega + i\eta)} \qquad (1.20)$$

where ω_p is the solid metal bulk plasma frequency, ŋ is a positive infinitesimal, and ϵ_1 is the relative permittivity of a vacuum, equation 1.17 can now be re-written in terms of the energy dispersion relation for both light in a solid and SPP, via equations 1.21 and 1.22, respectively:

$$q\,(\omega) = \frac{\omega}{c}\sqrt{\frac{\omega^2 - \omega_p^2}{2\omega^2 - \omega_p^2}} \qquad (1.21)$$

$$\omega^2(q) = \frac{\omega_p^2}{2} + c^2q^2 - \sqrt{\frac{\omega_p^4}{4} + c^4q^4} \qquad (1.22)$$

It is important to note that the wave vector q entering the energy dispersion relation of equation 1.22 is a 2D wave vector in the plane of the surface and hence for an ideal surface will not allow light to couple to SPPs.

By using the energy momentum dispersion curve equations (equations 1.21 and 1.22) it can be seen that a momentum mismatch occurs between the SPP momentum k_{SP} and the exciting photon k_0 (top-right graph in figure 1.2). To overcome this mismatch certain requirements are needed. The requirements for a propagating wave mode are that k is real with the real part of the metals' permittivity negative [57]. Hence, from equation 1.17 we can see that for these conditions to hold we must have $|\epsilon_2| > \epsilon_1$ and $\epsilon_2 < 0$. Also, two mechanisms which allow external radiation to couple to SPPs are: attenuated total reflection which provides the external radiation with an imaginary wave vector perpendicular to the surface [64, 65], and surface roughness features such as gratings or NPs (which provide the necessary momentum via Umklapp scattering [66]). As we are working with thin nano-layers of silver with surface roughness features, as well as Ag NPs, the latter is of more interest.

Perhaps the most important features to take from this section are the requirements for successful external radiation coupling to SPPs, i.e. polarisation, negative permittivity, and surface roughness. All these conditions can be achieved for Ag NP-air interface with the silver permittivity being negative across a large optical range. Further work highlighted in chapter 4 will also demonstrate the limitations of s-polarised and p-polarised light in creating SPPs.

1.5 Nanotechnology for cancer therapeutics

There has been a tremendous amount of recent research done on the use of NPs for advanced cancer therapeutics [67-75]. Nano-enhanced tumour destruction has great potential due to its non-invasive nature as well as the ability for the NPs to remain 'stealth-like' during cardio-vascular and cellular circulation. Due to their nano-dimensions and small size when compared to biological cells these NPs can remain inherently bio-inert: able to circulate the human body without inducing a serious immune response, and being able to penetrate far deeper into cells for potential deep drug-delivery applications.

Nano-enhanced thermal destruction of cancer cells via cellular hyperthermia has been demonstrated by using strong alternating magnetic fields to heat iron oxide NPs [67, 68] as well as using near-infrared light to heat gold nanoshells [69, 70]. Single-walled carbon nanotubes (SWNTs) and gold NPs have also been used to induce cellular hyperthermia via non-invasive radiofrequency (RF) fields [71-73]. Ultra-short single-walled carbon nanotubes (US-SWNTs) loaded with gadolinium [74, 75] have also found use as a contrast agent for advanced magnetic resonance (MRI) imaging, offering the potential for single cellular imaging techniques.

The key driving force behind much of the cancer treatment research is the potential for these NPs to simultaneously offer certain key advantages such as enhanced diagnostic ability through higher resolution cellular imaging, and advanced treatment via non-invasive techniques such as cellular hyperthermia or deep drug-delivery. One such group leading the way in advanced cancer therapeutics via nanotechnology is a collaborative effort between Prof. Lon J. Wilson (Rice University, Houston) and Dr. Steven Curley (MD Anderson Cancer Center, Houston).

The Wilson research laboratory program is specifically aimed at bringing carbon nanotechnology to the field of biology and medicine. Fullerenes, endohedral metallofullerenes, and US-SWNTs (20 nm) are being externally chemically derivatized to make them biocompatible and cell-specific through peptide antibody targeting. These nanostructures are also being internally loaded with materials of interest for diagnostic and therapeutic purposes such as iron oxide (Fe_2O_3) and gadolinium (Gd^{3+}) for MRI contrast agents, iodine (I_2) molecules for X-ray computed tomography (CT) imaging, and alpha-particle radionuclides (Ac-225 and At-211) for alpha-autoimmunity of single-cell cancers.

The Curley group is focused on the development of a number of procedures including RF ablation of liver tumours or the use of novel therapies to treat hepatocellular cancer or colorectal cancer liver metastases. Their most recent work, based on the invention of John Kanzius, involves the RF ablation of cancer tumours through the use of SWNTs and gold NPs. *In vivo* experiments involving the direct intratumoral injection of SWNT suspensions into rabbits bearing hepatic VX2 tumours, combined with RF heating, have shown complete tumor necrosis after 48 hrs [73]. Furthermore, *in vitro* injection of gold NP suspensions into human gastrointestinal cancer cells have shown that RF induced heating is lethal to these cancer cells [72]. These nano-materials are now being functionalized for direct tumour targeting for *singular cellular cancer destruction*, something which must successfully be accomplished for a *true* cancer cure.

A short 2-month internship was established for the author to investigate the use of Ag NPs for thermal destruction of cancer cells via RF heating in comparison to recent published work on the heating rates of gold NPs [76]. Experimental parameters and apparatus are fully discussed in detail in chapter 3.

1.6 Project objectives and overview

Throughout this work a series of experiments and theoretical considerations were performed to achieve several pertinent goals. First, the evaporation of silver onto ε-Si substrates via direct thermal evaporation was investigated for the development of a portable-probe technique for ε-Si surface enhanced Raman spectroscopy using ε-Si substrates of thickness 9 nm, 17.5 nm, and 42 nm. These fulfilled a fundamental grant requirement (Science Foundation Ireland is gratefully acknowledged for support through grant number 05/IN/I656).

These samples were characterised via micro-Raman spectroscopy, UV-VIS spectroscopy, and scanning electron microscopy (SEM) to determine SERS enhancements as well as the plasmonic origins behind such an enhancement. SERS enhancement factors were also calculated. The results of these experiments are highlighted in chapter 4 entitled ‘Sticky-SERS’- a term coined by this author.

Due to inherent hardware and repeatability obstacles surrounding the synthesis of silver thin films via evaporation, this same application was then investigated using an alternative approach to increase productivity, reproducibility, and above all ease-of-use within the semiconductor industry. Silver NPs were synthesised via a chemical polyol process and directly deposited onto the same ε-Si substrates and analysed for ε-Si SERS enhancement via micro-Raman Spectroscopy. This technique was found to be a vast improvement over the Sticky-SERS technique. Several batches of citrate capped Ag NP solutions were also purchased from a commercial supplier and tested in comparison to our own Ag NPs. NP morphology and structure was investigated via SEM and UV-VIS. The results to these series of experiments are discussed in chapter 5 entitled ‘SOL-SERS’.

Theoretical and practical parameters associated with growth of silver thin-films via direct thermal evaporation as well as growth of Ag NPs via the polyol process were highlighted in detail in chapter 2 whilst chapter 3 essentially describes in detail the characterisation equipment used: SEM, Micro-Raman Spectroscopy, UV-VIS, RF Heating, and ICP-OES.

In the spirit of the interdisciplinary nature of nanoscience, the author then sought to explore the use of Ag NPs for advanced hyperthermic cancer treatments (previously discussed) as part of an international cross-disciplinary collaboration.

The capacitively-coupled RF heating rates of commercially purchased, citrate capped Ag and Au NPs of size 20 nm, 40 nm, 60 nm, and 80 nm were characterised by the author at our collaborators' facility at Rice University, Houston, Texas, and applied to the RF heating apparatus at M.D. Anderson. Characterisation techniques include transmission electron microscopy (TEM, performed by Miss Sophia Phounsavath, Chemistry Department, Rice University) UV-VIS, and inductively coupled plasma optical emission spectroscopy (ICP-OES). The main objectives of this section were; to investigate whether Ag NPs could be used as thermal heat sources; to what extent do the as-purchased buffer solutions contribute to heat production; can a theoretical framework be developed which would calculate the minimum amount of Ag NPs needed within a cell for cellular hyperthermia to take place?

Finally, Appendix A provides supplementary TEM and ICP-OES characterisation data of the NPs used in chapter 6 while Appendix B attempts to give a preliminary explanation into the NP related heating mechanism for aqueous sodium chloride solutions.

1.7 References:

[1] C. Ren, Y. Song, Z. Li, G. Zhu, *Anal. Bioanal. Chem.* **2005**, 381, 1179.

[2] H. Li, Z. Cui, C. Han, *Sensors and Actuators B* **2009**, 143, 87.

[3] A. Taheri, M. Noroozifar, M. Khorasani-Motlagh, *Journal of Electroanalytical Chemistry* **2009**, 628, 48.

[4] Y-Q Chena, C-J Lub, *Sensors and Actuators B* **2009**, 135, 492.

[5] W. Ngeontaea, W. Janrungroatsakula, P. Maneewattanapinyoa, S. Ekgasit, W Aeungmaitrepiroma, T. Tuntulani, *Sensors and Actuators B* **2009**, 137, 320.

[6] G. Naja, P. Bouvrette, S. Hrapovic, J. H. T. Luong, *Analyst* **2007**, 132, 679.

[7] Y. Ma, N. Li, C. Yang, X. Yang, *Anal. Bioanal. Chem*. **2005**, 382, 1044.

[8] F. Feng, G. Zhi, H. S. Jia, L. Cheng, Y. T. Tian, X. J. Li, *Nanotechnology* **2009**, 20, 295501.

[9] M. Muniz-Miranda, N. Neto, G. Sbrana, *Journal of Molecular Structure* **2003**, 651–653, 85.

[10] J. V. Zoval, P. R. Biernacki, R. M. Penner, *Anal. Chem*. **1996**, 68, 1585.

[11] A. Kudelski, *Chem. Phys. Letts.* **2005**, 414, 271.

[12] J. Yao, Z. Liu, Y. Liu,Y. Wang, C. Sun, G. Bartal, A. M. Stacy, X. Zhang, *Science*, **2008**, 321.

[13] S. M. Orbonsa, D. Freeman, B. Luther-Davies, B. C. Gibson, S. T. Huntington, D. N. Jamieson, A. Roberts, *Physica B* **2007**, 394, 176.

[14] J. L. Elechiguerra, J. L. Burt, J. R. Morones, A. Camacho-Bragado, X. Gao, H. H. Lara, M. J. Yacaman, *Journal of Nanobiotechnology* **2005**, 3:6.

[15] M. M. Kemp, A. Kumar, S. Mousa, E. Dyskin, M. Yalcin, P. Ajayan, R. J. Linhardt, S. A Mousa, *Nanotechnology* **2009**, 20, 455104.

[16] J. Tian, K. K. Y. Wong, C-M Ho, C-N Lok, W-Y Yu, C-M Che, J-F Chiu, P. K. H. Tam, *ChemMedChem* **2007**, 2, 129.

[17] K. Kneipp, Y. Wang, H. Kneipp, L. T. Perelman, I. Itzkan, R. R. Dasari, M. S. Feld, *Phys. Rev. Letts*. **1997**, 78, 9, 1667.

[18] P. L. Stiles, J. A. Dieringer, N. C. Shah, R. P. Van Duyne, *Annu. Rev. Anal. Chem*. **2008**, 1, 601.

[19] B. S. Atiyeh, M. Costagliola, S. N. Hayek, S. A. Dibo, *Burns* **2007**, 33**,** 2, 139.

[20] Y. Qin, *International Wound Journal* **2005**, 2**,** 2, 172.

[21] M. H. Hermans, *The American journal of nursin*g **2006**, 106, 12, 60.

[22] Colloidal Silver Products. National Center for Complementary and Alternative Medicine. December 2006. http://nccam.nih.gov/health/silver/, retrieved **02-11-2010.**

[23] Eighty First Annual Meeting of the British Medical Association". **1913**, *BMJ* **2**: 1282.

[24] Mike Adams, 'Antibacterial silver products finally begin to emerge after years of FDA opression', August 7th, 2009, http://www.naturalnews.com/010761.html, retrieved **02-11-2010**.

[25] P. L. Pereira, J. Trübenbach, M. Schenk, J. Subke, S. Kroeber, I. Schaefer, C. T. Remy, D. Schmidt, J. Brieger, C. D. Claussen, *Radiology* **2004**, 232, 482.

[26] A. P. O'Rourke, D. Haemmerich, P. Prakash, M. C. Converse, D. M. Mahvi, J. G. Webster, *Expert Rev Med Devices* **2007**, 4, 4, 523.

[27] J. Joosten, T. Ruers, *Critical Reviews in Oncology/Hematology* **2007**, 62, 2, 153.

[28] Y-S Chen, Y-C Hung, I. Liau, G. S. Huang, *Nanoscale Res. Lett.*, **2009**, 4, 858.

[29] Bai, P. C. Auth, **S.** Balakrishnan, M. Bost, *Electron Devices Meeting, IEDM Technical Digest. IEEE International* **2004**, 657–660.

[30] C-C Lin, L-W Lai, C-Y Lin, T-Y Tseng., *Thin Solid Films* **2006**, 515, 8005.

[31] A. Asenov, *VLSI Tech. Dig. Tech. Pap*. **2007**, 86–87.

[32] D. A. J. Moran, K. Kalna, E. Boyd, F. McEwan, H. McLelland, L. L. Zhuang, C. R. Stanley, A. Asenov, I. Thayne, ESSDERC '03: *33rd Conference on European Solid-State Device Research*, 16-18 September, 315, **2003**.

[33] D. J. Paul, *Adv. Mater*. **1999**, 11, 191.

[34] M. T. Currie, C. W. Leitz, T. A. Langdo, G. Taraschi, E. A. Fitzgerald, D. A. Antoniadis' *J. Vac. Sci. Technol. B* ***2001***, 19, 2268.

[35] D. K. Nayak, S. K. Chun, *Appl. Phys. Lett*. **1994**, 64, 2514.

[36] G. Abstreiter, H. Brugger, T. Wolf, *Phys. Rev. Lett*. **1985**, 54, 2441.

[37] C. Himcinschi, I. Radu, R. Singh, W. Erfurth, A. P. Milenin, M. Reiche, S. H. Christiansen, U. Gösele, *Materials Science and Engineering B* **2006**, 135, 184.

[38] J. Parsons, E. H. C. Parker, D. R. Leadley, T. J. Grasby, A. D. Capewell, *Appl. Phys. Lett*. **2007**, 91, 063127.

[39] P. Dobrosz, S. J. Bull, S. H. Olsen, A.G. O'Neill, *Surface & Coatings Technology* ***2005***, 200, 1755.

[40] W. M. Chen, P. J. McNally, G. D. M. Dilliway, J. Bonar, T. Tuomi, A. F. W. Willoughby, *J. Mater. Sci.: Mater. in Elec.* **2003**, 14, 455.

[41] Ingrid de Wolf, *Semicond. Sci. Technol*. **1996**, 11, 139.

[42] P. A. Flinn, G. A. Waychuna, *J. Vac. Sci. Technol. B* **1988**, 6, 1749.

[43] A. Armigliato, R. Balboni, I. De Wolf, S. Frabboni, K. G. F. Janssens, J. Vanhellemont, *Inst. Phys. Conf. Ser*. 1993, 134, 229.

[44] K. Kimoto, K. Usami, H. Sakata, M. Tanaka, *Japan., J. Appl. Phys*. **1993**, 32, L211-L213.

[45] D. J. Lockwood, J.-M. Baribeau, *Physical Review B*, **1992**, 45, 15, 8565.

[46] L. H. Wong, C. C. Wong, J. P Liu, D. K. Sohn, L. Chan, L. C. Hsia, H. Zang, Z. H. Ni, Z. X. Shen, *Japanese Journal of Appl. Phys*. **2005**, 44, 11, pp. 7922-7924.

[47] Martin Moskovits, *Reviews of Modern Physics*, **1985**, 57, 3.

[48] S. Nie, S. R. Emory, *Science*, **1997**, 275, 1102.

[49] M. Fleischmann P. J. Hendra, A. J. McQuillan, *Chem. Phys. Lett*. **1974**, 26, 163.

[50] D. L. Jeanmaire, R. P. Van Duyne, *J. Electroanal. Chem*. **1977**, 84, 1.

[51] M. G. Albrecht, J. A. Creighton, *J. Am. Chem. Soc.* ***1977***, 99, 5215.

[52] A. Campion, P. Kambhampati, *Chemical Society Reviews* **1998**, 27, 241.

[53] D. D. Tuschel, J. E. Pemberton, J. E. Cook, *Langmuir*, **1986**, 2**,** 4, 380.

[54] A. Feofanov, A. Ianoul, E. Kryukov, S. Maskevich, G. Vasiliuk, L. Kivach, I. Nabiev, *Anal. Chem.* **1997**, 69, 18, 3731.

[55] H. Wei, J. Li, Y. Wang, E. Wang, *Nanotechnology* ***2007***, 18, 175610.

[56] S. E. Hunyadi, C. J. Murphy, *J. Mater. Chem*. **2006**, 16, 3929.

[57] M. Moskovits, *J. Raman. Spectros*. **2005**, 36, 485.

[58] S. J. Lee, Z. Guan, H. Xu, M. Moskovits, *J. Phys. Chem. C* **2005**, 111, 49, 17985.

[59] L. Zhu, C. Georgi, M. Hecker, J. Rinderknecht, A. Mai, Y. Ritz, E. Zschech, *J. Appl. Phys*. **2007**, 101, 104305.

[60] N. Hayazawa, H. Watanabe, Y. Saito, S. Kawata, *J. Chem. Phys*. **2006**, 125, 244706.

[61] N. Hayazawa, M. Motohashi, Y. Saito, S. Kawata., *Appl. Phys. Letts.* **2005**, 86, 263114.

[62] J. M. Pitarke, V. M. Silkin, E. V. Chulkov, P. M. Echenique, *Rep. Prog. Phys*. **2007**, 70, 87.

[63] N. W. Ashcroft, N. D. Mermin, *Solid State Physics* **1976**, (Philadelphia: Saunders).

[64] A. Otto, *Z. Phys.* ***1968***, 216, 398.

[65] E. Kretschmann, H. Raether, *Z. Naturf.* A. **1968**, 23, 2135.

[66] Y-Y Teng, E.A. Stern, *Phys. Rev. Lett.* **1967**, 19, 511.

[67] R. Hergt, R. Hiergeist, I. Hilger, W. A. Kaiser, Y. Lapatnikov, S. Margel, U. Richter, *J. Magn. Magn. Mater*. **2004**, *270,* 345, 357.

[68] V. S. Kalambur, E. K. Longmire, J.C. Bischof, *Langmuir* **2005**, 23, 12329.

[69] L. R. Hirsch, R. J. Stafford, J. A. Bankson, S. R. Sershen, B. Rivera, R. E. Price, J. D. Hazle, N. J. Halas, J. L. West, *P. Natl. Aacd. Sci. USA* **2003**, 100, 13549 (2003).

[70] A. M. Gobin, M. H. Lee, N. J. Halas, W. D. James, R. A. Drezek, J. L. West, *Nano Lett.* **2007**, 7, 1929.

[71] S. A. Curley, P. Cherukuri, K. Briggs, C. R. Patra, M. Upton, E. Dolson, P. Mukherjee, *J. Exp. Ther. Oncol.* **2008**, 7, 313 (2008).

[72] C. J. Gannon, C. R. Patra, R. Bhattacharya, P. Mukerjee, S. A. Curley, *J. Nanobiotechnol.*, **2008**, 6, 2.

[73] C. J. Gannon, P. Cherukuri, B. I. Yakobson, L. Cognet, J. S. Kanzius, C. Kittrell, R. B. Weisman, M. Pasquali, H. K. Schmidt, R. E. Smalley, S. A. Curley, *Cancer* **2007**, 110, 2654.

[74] J. Ananta, L. J. Wilson, "Gadonanostructures as MRI Contrast Agents," invited book chapter in *Chemistry of Carbon Nanocarbons*, **2009**, in press.

[75] K. B. Hartman, S. Laus, R. D. Bolskar, R. Muthupillai, L. Helm, E. Toth, A. E. Merbach, L. J. Wilson, *Nano Lett*. **2008**, 8, 415.

[76] C. H. Moran, S. M. Wainerdi, T. K. Cherukuri, C. Kittrell, B. J. Wiley, N. W. Nicholas, S. A. Curley, J. S. Kanzius, P. Cherukuri, *Nano Res* **2009**, *2*, 400.

Chapter 2

Silver Nanoparticle Synthesis Techniques

2.1 Introduction

As was previously discussed in chapter 1 it has been reported that silver thin films can successfully be used as a viable SERS probe for Raman characterization of nm-thin ε-Si surfaces grown on SiGe virtual substrates [1a]. In line with this work we attempted to grow Ag thin films onto our 9, 17.5, and 42 nm ε-Si samples using a physical vapour deposition system (direct thermal evaporation). Although this evaporation technique is a simple and cost-effective approach to perform SERS analysis of ε-Si layers, it was found to have several drawbacks such as repeatability, pressure fluctuations, and unstable currents. Also, the hardware configuration was deemed to be too small to accommodate the larger 300 mm silicon wafers which are now currently on the market (that is of course, if this technique was to be used in such an industrial setting). This technique was then compared to an alternative chemical synthesis approach where NPs were instead grown in solution using the so-called ‘polyol’ process and subsequently deposited onto the ε-Si samples.

This chapter details specifically with the experimental and operating procedures of each technique as well as highlighting several aspects associated with the optimal experimental operating procedures for SERS-viable NP growth. It also gives a background into the physical mechanism behind NP growth (of both techniques) as well as highlighting the ‘pros and cons’ associated with each technique.

2.2 Direct thermal evaporation

Direct thermal evaporation (DTE) is a commonly used physical vapour deposition technique for thin film deposition onto a variety of substrates. In essence a source material is placed either in a boat, crucible or wire coil heating element and heated to evaporation point by passing a high current through the heating element. Evaporate evaporation rate is directly influenced by heating element temperature which is controlled by varying the current: allowing for quick and easy implementation with low costs. All elements are cased within a low pressure vacuum system by means of a thick, glass chamber, the pressure of which is controlled via a series of rotary and diffusion pumps.

Upon reaching evaporation point the source molecular species or atoms will then be ejected, filling up the evacuated space with subsequent condensation upon the chamber walls and substrate. Critical to a successful homogenous substrate coating are uniform heating and temperature distribution of the source material, non-oxidization and contamination of the boat source, high purity of source material, and general cleanliness and dirt-free environment of the evaporation chamber.

Several techniques have been employed for Ag crystalline thin film synthesis. These include, but are not limited to, high-temperature magnetron sputtering [1.b], radio-frequency sputtering under oxygen [2], and inert-gas condensation processes [3]. These techniques are essentially different to DTE in that they use a different mode of evaporation and a different gas-pressure environment; usually at ambient or high pressures with a mixture of inert gases such as helium, argon, krypton, or a reactive gas such as oxygen. Considering DTE at low pressure has already been shown to successfully allow for ε-Si SERS enhancements via Ag thin film deposition [4], and due to its inherent ease-of-use with low implementation costs this technique was considered more favorable.

Throughout this work evaporations took place on an Auto 306 Edwards evaporator (automated system, base pressure 1 x 10^{-6} mbar). The generic system diagram is shown in figure 2.1. A water-cooled FTM6 quartz thickness monitor can also be used in conjunction with the evaporation system but was neglected due to reproducibility issues (discussed later). Under normal operating conditions a rotary pump is used to remove air from the chamber until reaching a pressure of 0.2 mbar at which point the diffusion pump activates allowing a minimum pressure of approximately 7.0 x 10^{-7} mbar to be reached. A chilled water supply is needed to maintain adequate cooling of the diffusion pump which uses organic silicone oil (Dow Corning) for correct operation. As the backing pressure lowers to 0.2 mbar the silicon oil is heated and reaches boiling point to form a high velocity vapour jet which diffuses with the gaseous species from the chamber in a downward manner transporting them to the pump outlet where they condense and are exhausted by the rotary pump [5, 6]. The oil droplets are cooled via the water supply and start another cycle. Liquid nitrogen is also added to the system before deposition to ensure correct diffusion pump operation by reducing backstreaming effects: migration of minute traces of oil which move towards pump inlet.

In order to create thin films of isolated NPs the system had to be modified using a fully adjustable substrate holder as shown in figure 2.2. This holder allowed the source-to-substrate distance to be altered (5 cm – 22 cm) as well as the deposition angle: 0^{o} to 90^{o} corresponding to the parallel and perpendicular deposition position, respectively. This was created in line with work by Stöckle *et al.* [7] who demonstrated precise control of NP morphology by altering the distance from source-to-substrate. In line with previous

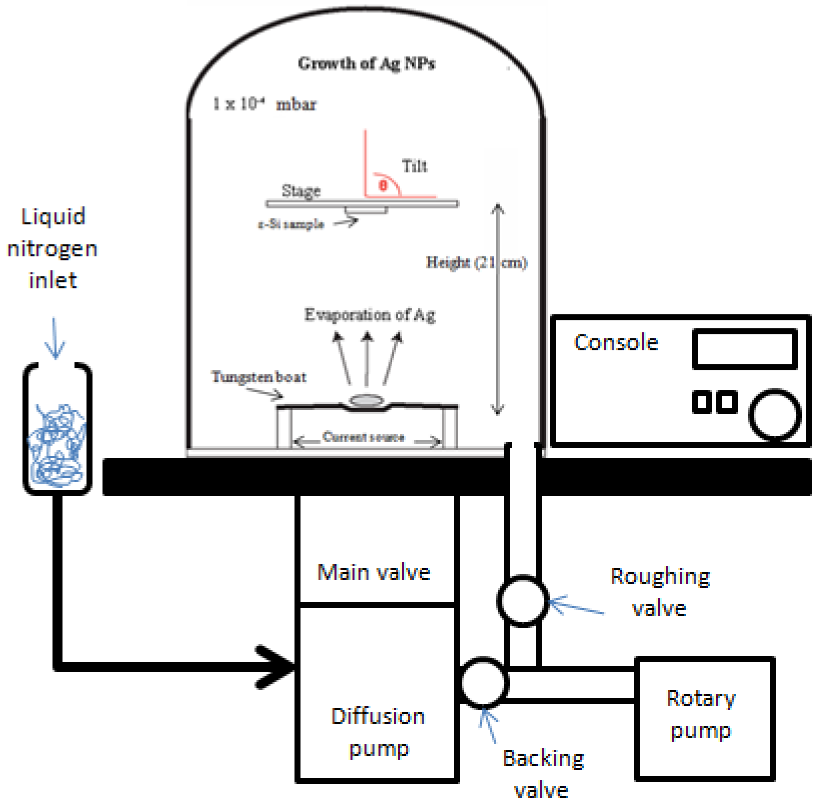

Figure. 2.1: Edwards Auto 306 system diagram.

ε-Si SERS work reported by Hayazawa *et al.* [4] we used a source-to-substrate distance of 21 cm for correct thin film morphology.

A relatively high evaporation pressure of 1 x 10^{-4} mbar was also used in line with work by Stöckle *et al.* [7] as this reduces the energy of particles arriving at the substrate surface due to airborne collisions. A reduction in particle energy is needed for more stable, isolated NP growth. It must be stated at this point that a considerable amount of time was spent trying to produce accurate and repeatable measurements on the evaporator. This proved to be extremely troublesome due to three main factors.

Factor 1: <u>Unstable Current</u>

For several repeated runs the evaporation boat current and source material weight (silver nanopowder) were manually kept constant by the user (30 A and 120 mg, respectively).

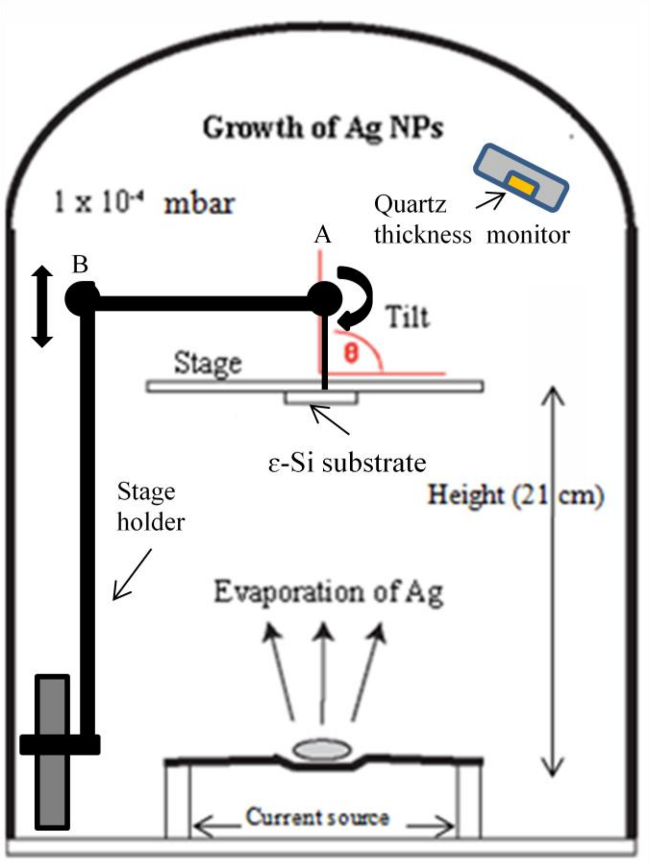

Figure. 2.2: Schematic of evaporation chamber with modified stage holder. Angle and height between substrate and current source and be adjusted via A and B, respectively.

The current could be kept constant by adjusting the current dial on the console window until the analogue current display read 30 A. It should be noted that the amount of dial rotation needed to reach 30 A for each experiment varied from run-to-run suggesting persistent systematic irregularities. This ultimately led to varying evaporation rates (determined by the quartz crystal thickness monitor) for identical experimental setups. This may have been caused by either surface oxidation of the exposed conducting surfaces, material contamination, or systematic errors which still occurred even after strict cleaning procedures were employed: the chamber would be wiped down and cleaned via ethanol and acetone before each use and the metal contacts were filed-down to expose fresh, unburnt metal contacts.

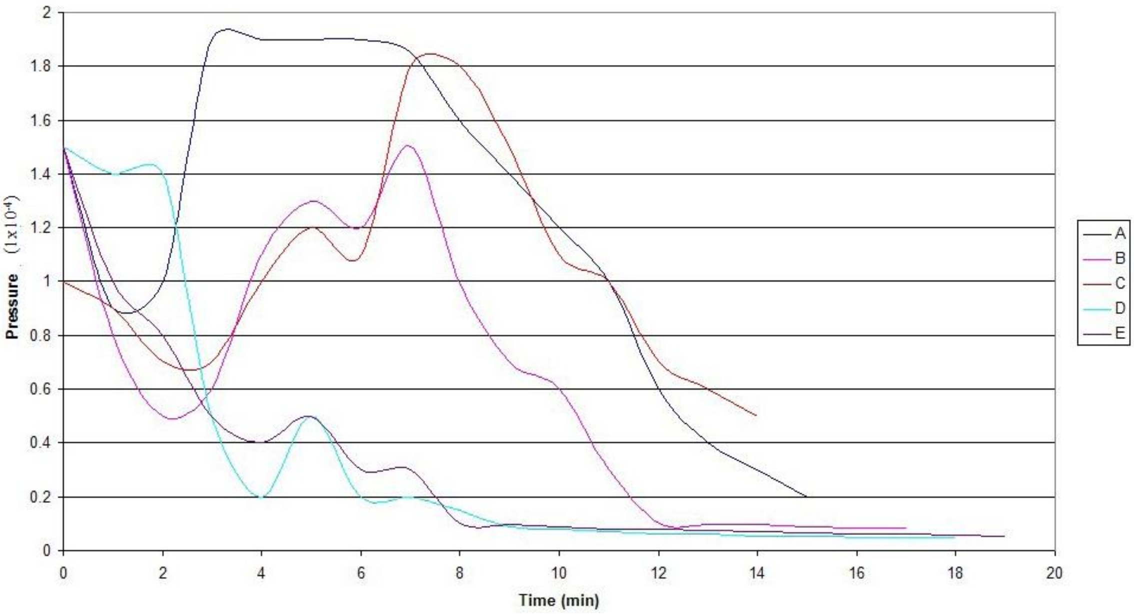

Figure 2.3: Chamber pressure versus time for five identical evaporations; A, B, C, D, and E, using a constant current (30 A), source material weight (120 mg), and evaporation starting pressure (1x10^{-4} mbar).

.Factor 2: <u>Pressure Fluctuations.</u>

Several evaporations, at a constant current, were performed at 1.4 x 10^{-3} mbar as the starting pressure. However, for each evaporation, the pressure versus time profile was different; i.e. pressure fluctuations versus time were different for each experiment which could cause changes in the evaporation rate (figure 2.3). As it has already been reported that thin film morphology is directly related to pressure [7] these irregularities were extremely disruptive. It is thought that pressure fluctuations were most likely due to irregular heating patterns due to unstable current fluctuations where the heated Ag element would cause variations in the environmental partial pressure (increasing the pressure for an increase in heat).

Factor 3: Thickness Monitor (Quartz Element)

The thickness monitor was calibrated for Ag NP deposition onto ε-Si using thickness measurements obtained from atomic force microscopy data but gave inaccurate readings for each evaporation; i.e. the displayed thickness monitor thickness and AFM height data disagreed. This could be attributed to general mechanical and electrical fluctuations described by factors one and two but also to the fact that Ag NP growth kinetics could be slightly different on a quartz substrate (active element in thickness monitor) as opposed to a ε-Si substrate. Also, the quartz element was situated at a different position than the ε-Si substrate (fig. 2.2) which would ultimately result in different surface coating coverage, as will be discussed in section 2.2.

To conclude, although a precise cause or set of causes were specifically identified, we found that the solution to these reproducibility problems was to evaporate at a low rate (approximately 0.5 nm/s) until the glass bell jar turned a deep purple/blue colour (controlled by means of direct visual inspection although a hand-held UV-VIS spectrometer with attached fiber optic probe could be used in future studies if deemed necessary). The series of colour changes during Ag NP formation occurred in the following order: yellow, orange, red, purple, blue, and finally bulk silver colour which covered an absorption spectrum of approximately 420 - 520 nm (also to be discussed later).

2.3 Evaporation rate & nucleation kinetics.

The first experimental analysis of mercury evaporation phenomena, performed by Hertz in1882, concluded that the observed evaporation rates were; not limited by insufficient heat supplied to the surface of the molten evaporate, and were proportional to the difference between the mercury equilibrium pressure and the hydrostatic pressure acting upon the evaporate, at a given temperature. This led to the basic equation for the rate of evaporation [6]:

$$\Phi_e = \frac{\alpha_e N_A (P_e - P_h)}{(2\pi MRT)^{1/2}} \qquad (2.1)$$

where Φ_e is the evaporation flux (number of atoms/molecules per m^2/s), α_e is the coefficient of evaporation (value between 0 and 1), P_e is the equilibrium pressure of the material, P_h is the hydrostatic pressure acting upon the evaporate, M and T are the molecular mass and absolute temperature of the material, respectively, and R is the gas constant. It should be noted that maximum evaporation is reached for a perfect vacuum; i.e. where P_h is equal to 0.

Once reaching evaporation temperature, the molecular species will be ejected from the surface and condense upon the substrate and chamber walls. If we consider the substrate as a plane parallel to the surface and model the surface as a point source we can show that the film thickness, *d*, at any length, *l*, from the origin can be evaluated via the following equation [6]:

$$d = \frac{\bar{M}_e \cos\theta}{4\pi\rho r^2} = \frac{\bar{M}_e h}{4\pi\rho r^3} = \frac{\bar{M}_e h}{4\pi\rho(h^2 + l^2)^{3/2}} \qquad (2.2)$$

where $\bar{M}_e$ is the total evaporated mass, θ is the deposition or receiving angle, h is the height between substrate and source, ρ is density of the deposit, and *l* is the substrate displacement length from origin (where evaporation emission angle, ϕ, is zero). Note that $r = (h^2 + l^2)^{1/2}$. The results from this equation, as well as the schematic

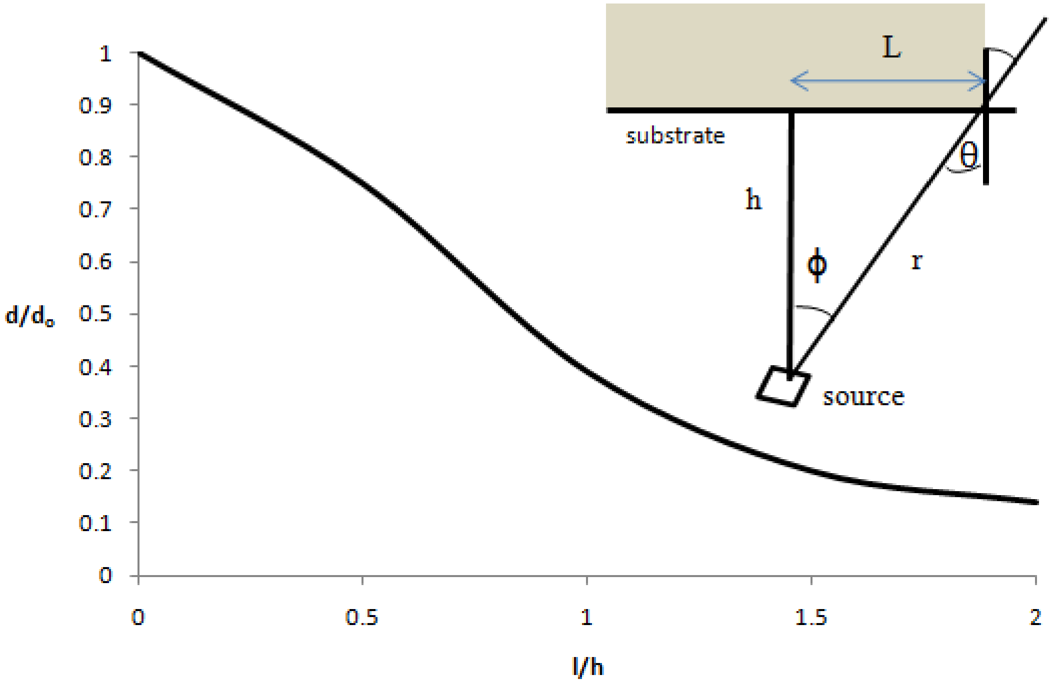

Figure 2.4: Film thickness uniformity (d/d$_o$) for a point source as a function of substrate geometry (l/h). Also shown is geometry of evaporation onto parallel substrate. Re-produced from [6].

illustration, are shown in figure 2.4. As can be seen, maximum film thickness (d_o) is observed directly above the source material, where $l = 0$. This thickness decreases as the substrate is moved away from the origin. This most likely explains why the thickness of the Ag thin film on ε-Si surfaces (determined from AFM) differed from that shown by the quartz crystal element and why there were colour gradients observed on the glass chamber walls.

There are several atomic processes which take place at the substrate surface once the atoms/molecules arrive. These include re-evaporation, surface diffusion, adsorption, inter-diffusion and 2D and 3D nucleation. On an ideal flat surface, where the surface is represented as an atomically sharp interfacial demarcation between condensed-phase and gas-phase atoms, inter-diffusion and capture at defect sites such as steps and cracks would not occur.

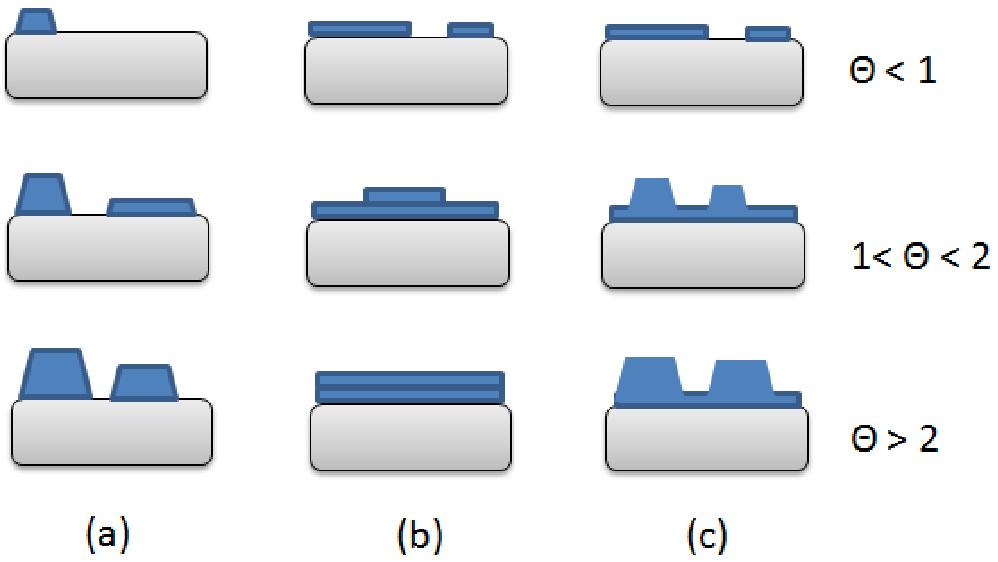

Figure. 2.5: Three modes of thin-film growth: (a) Volmer-Weber growth, (b) Frank-van der Merwe growth, (c) Stranski-Krastanov growth. Each growth mode is shown for different amounts of surface coverage, Θ (re-produced from [9]).

Observations of film formation have shown that there are three basic crystal growth modes: Volmer-Weber (island) mode; Frank-van der Merwe (layer) mode; and the Stranski-Krastanov (layer plus island) mode. These three growth modes are illustrated in figure 2.5. For the Volmer-Weber mode, small clusters are directly nucleated on the substrate surface and then grow into islands of the condensed phase. This is due to the molecules/atoms being more strongly bound to each other than the substrate and is displayed by many systems such as metals on insulators. The Frank-van der Merwe growth mode displays completely opposite characteristics as the atoms are bound more strongly to the substrate. This causes the initial arriving atoms to condense and form a monolayer on the surface with the second monolayer being slightly less tightly bound. Finally, the Stranski-Krastonov growth mode exhibits an intermediate case. After forming the first monolayer (or few monolayers) further island growth is unfavorable and islands are formed on top of this layer. It is thought that any factor which disturbs the monotonic decrease in binding energy, characteristic of layer growth, may be the cause of this growth formation [8]. From further SEM evidence give in chapter 4 combined with previously published data from Stöckle *et al.* [7] it is thought that island growth is preferable for maximum SERS enhancements and is indeed illustrated in SEM micrograph data [section 4.4]. Further information regarding surface nucleation kinetics can be sought in the literature [10 - 14].

2.4 Chemical synthesis (polyol process)

The direct thermal evaporation method for Ag NP synthesis may be relatively cheap and easy to do for lab research but for commercial applications, where bulky and expensive evaporators are not present, another technique must be sought. As the diameters of commercial evaporator chambers would have to be larger than the standard 300 mm silicon wafers, practicality issues will inevitably arise. The evaporation technique also has severe limitations such as repeatability, limited NP morphology, deposition and pressure control. Hence, it is imperative that any alternative techniques overcome these issues and can be applied to a variety of experiments. One such method is chemical synthesis.

Colloidal chemical synthesis methods are a ‘bottom-up’ approach and can be used to produce a wide range of NP shapes and sizes, albeit on a sub-mg quantity. Evaporation methods may allow for a large thin film NP coverage over a selected surface but have limited control over NP homogeneity - which is an imperative factor as the electrical, optical, and magnetic properties of these nanocrystals are strongly dependent on their dimensions (mono-disperse, with a size distribution of <5% is of key importance) [15].

A variety of chemical processes have been reported for the preparation of Ag NPs including thermal decomposition of organic solvents [16], chemical and photoreduction in reverse micelles [17-19], and chemical reduction of silver ions with [20] and without [21] stabilizing agents. Most of these techniques allow for the creation of spherical Ag NPs with a size range < 100nm. However, the best procedure by far (in the opinion of this author) for full Ag morphology control, which in turn allows for full exploitation of optical and electronic properties, is the so-called ‘polyol process’ [22-24].

The polyol process involves the preparation of metallic powders by reduction of inorganic compounds in liquid polyols. Polyols are a class of alcohols containing multiple hydroxyl groups and are primarily used in food science (as sugar alcohols) and polymer chemistry due to their multiple hydroxyl functional groups available for organic reactions. Originally developed by Fiévet *et al.* [22], it is a simple solution-phase method towards the synthesis of metallic and alloy colloidal NPs. In general, the reaction involves the reduction of an inorganic salt (the precursor) by a polyol (the reducing agent) such as ethylene glycol (EG) at an elevated temperature (usually 140 – 170°C). By introducing stabilizing agents such as poly(vinylpyrrolidone) (PVP) a variety of NP morphologies can be created whose plasmonic response can be tuned for specific applications. In the case of silver the following morphologies have been created via the polyol process: spherical, cubic, cuboctahedra, triangular, pentagonal, nanobeams, nanorods, nanorice, nanobars, and bipyramidal [22-24].

The generic experimental setup first used by myself is shown in figure 2.6. In a typical synthesis, 5 ml of anhydrous EG was heated at 160^{o}C for 1-hour (allows enough time for oxygen to react with EG to create the reducing agent glycoaldehyde, GA). During

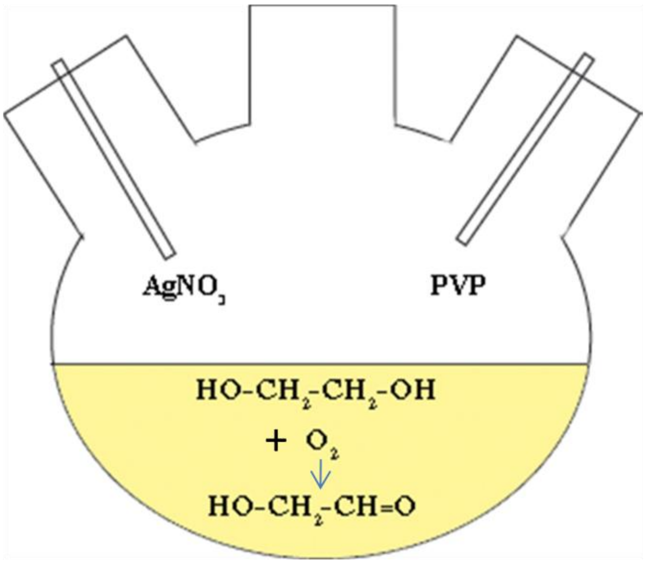

Figure 2.6: Generic experimental chemical schematic for polyol process.

this time 163 mg silver nitrate ($AgNO_3$, 0.25 Molar, (M)) was added to and dissolved in 3 ml EG, whilst 162 mg PVP (0.25 M) was added to and dissolved in 3 ml EG. These two solutions were then injected simultaneously into the hot 6 ml EG solution via a two-channel syringe pump at a rate of 0.375 ml/min. The reaction mixture is then continually heated at 160^{o}C for approximately 10 – 45 mins depending on the morphology required. Once the solution was cooled the supernatant was filtered out by centrifugation (1:1 ratio of solution to acetone) then repeated with water several times to remove excess EG. The remaining sample could then be examined via SEM by allowing a small droplet to be placed onto a silicon substrate then waiting until the water had evaporated at room temperature.

The main factors influencing NP morphology are: ratio of PVP to $AgNO_3$, reducing agent temperature, reaction time, and EG to GA conversion. Before describing the experimental setup in more detail (which is a modified version of the generic setup described previously) the fundamental mechanism behind Ag NP growth will first be addressed.

2.5 Solution based nanoparticle growth kinetics:

To prepare highly uniform, monodisperse nanocrystals it is necessary to induce a single nucleation event and to prevent additional nucleation during the subsequent growth process. Upon injection of the $AgNO_3$ solution, silver ions are reduced to atoms, which in turn merge together to form monomers [15] which are the minimum subunit of the bulk crystal. The concentration of these monomers increases over time until a maximum level (supersaturation) is reached where burst nucleation occurs, i.e. the degree of supersaturation is high enough to overcome the energy barrier for spontaneous nucleation, thus resulting in the formation and accumulation of stable nuclei [15]. Once a maximum supersaturation level is reached the rate of monomer consumption from nucleation and growth exceeds the rate of monomer supply until it reaches a level where net nucleation is zero. Below this level the system enters the growth stage in which nucleation is effectively stopped. Nucleated particles which are smaller than the critical radius, r_c, (the minimum stable radius that will not dissolve in solution) dissolve back into solution and form monomers which diffuse and precipitate onto larger particles (Otswald ripening).

The thermodynamic interpretation of the homogenous nucleation energy barrier can be modelled via equation 7 [15]. The Gibbs free energy*(units expressed as joules, J) of formation of spherical crystals with radius r from the solution with supersaturation, S, is given by equation 2.3 where γ is the surface energy per unit area and ΔG_v is the free energy change between the monomers in the solution and unit volume of bulk crystal ($r \rightarrow \infty$).

---

* *Gibbs free energy is a measure of the maximum available work that can be derived from any system under conditions of constant temperature (T) and pressure (P) and is given by: G = H – T*S, where H is the system enthalpy, T the temperature and S the entropy [25].*

$$\Delta G = 4\pi r^2\gamma + \frac{4}{3}\pi r^3 \Delta G_v \quad (2.3)$$

ΔG_v is negative as long as the solution is supersaturated ($\Delta G\nu = (-RT\ln S)/V_m$ where V_m is the molar volume of bulk crystal) releasing energy as it moves to a lower, more thermodynamically favourable and stable energetic state. The maximum Gibbs free energy available is when the radius is equal to the critical radius, r_c, where ΔGv is maximum. The free energy necessary to then subsequently form a stable nucleus is referred to as the critical free energy (ΔG_c) and is highlighted in equation 2.4.

$$\Delta Gc = \frac{16\pi\gamma^3}{3(\Delta G_v)^2} \qquad (2.4)$$

The rate of increase of number of particles, *N*, can then be written in the Arrhenius* form in terms of ΔG_c and is shown in equation 2.5:

$$\frac{dN}{dt} = A \exp\left[-\frac{\Delta Gc}{kT}\right] \qquad (2.5)$$

where *A* is the pre-exponential factor, *k* is Boltzmann's constant, and *T* is temperature. It should also be stated that for particles with dimensions where there is an increase in the ratio of surface to volume atoms, there is a strong driving force to minimise the surface free energy (γ) via reconstruction of the surface or crystal structure (through phase transitions [26] or lattice contractions [27]). Most silver nuclei hence incorporate twin boundary defects because such defects enable a lower surface energy. As these nuclei grow, changes in the defect structure become too costly relative to the available thermal energy and they become stuck in a given morphology. Also, by introducing various stabilisation agents such as PVP, cetyltrimethylammonium (CTAB), and cetyltrimethylammonium tosylate (CTAT) which possess preferred binding and

---

* *Arrhenius equation describes the temperature dependence of the rate of a chemical reaction in terms of the rate constant, k, gas constant, R, temperature, T, and activation energy, E_a:* $k = Ae^{-E_a/RT}$

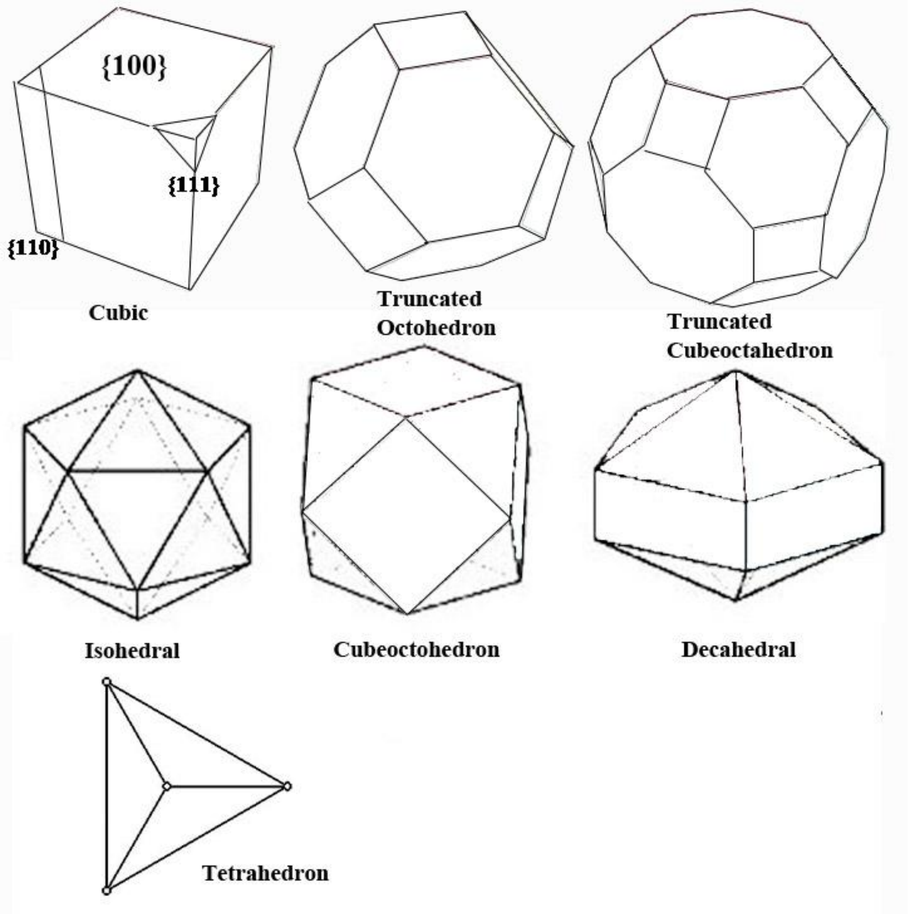

Figure 2.7: Possible Ag NP morphologies. Also shown is the {100}, {110}, and {111} Miller planes [20, 21].

adsorption onto selective crystal facets [28-30] the facet growth rates can be controlled to allow selective morphologies to be created. Figure 2.7 illustrates some examples.

Using the polyol process for formation of Ag nanocubes as an example [23, 31] the fast nucleation and growth of Ag seeds reduces the time available for twin defects to form. In turn, since twinning is only favourable when the surface energy of the {100} facets is greater than that of the {111} facet (twinning is more energetically favourable in this configuration) the presence of PVP can serve to reduce the driving force for twin formation through its selective interaction with the {100} planes yielding preferential growth on the {111} faces: resulting in nanocube formation.

As Ag nanocubes have maximum absorbance around around 488 nm [23] which is the Raman excitation source used throughout this project, and have excellent self-assembly characteristics [23, 31] we will focus on ideal experimental growth conditions and apparatus for such morphology.

2.6 Chemical synthesis components and setup

Although EG is by far the most commonly used reducing agent, others such as diethylene glycol as well as mixtures of the two have been used. First synthesized in 1859 by French chemist Charles-Adolphe Wurtz it subsequently went on to replace water as an aircraft engine coolant in World War I as well as being an ingredient in the explosive ethylene glycol dinitrate. It also finds uses in the plastics industry for the manufacturing of polyester fibres and resins, as well as acting as a specimen preservative. EG is mainly produced via the reaction of ethylene oxide with water according to the following chemical equation:

$$C_2H_4O + H_2O ==> HOCH_2CH_2OH$$

and can be catalysed by either acids or bases or at neutral pH under elevated temperatures. The ability of EG to reduce metal ions depends primarily on the conversion of EG to GA in the polyol process [32] where it has recently been shown that heating EG in air results in its oxidation to GA, a reductant capable of reducing most noble metal ions.

These results illustrate a strict time requirement in enabling a specific volume of EG to convert to GA, i.e. if a specific volume of EG has not been given enough time (and energy via temperature) to react with atmospheric oxygen to produce GA then the NP growth mechanism will invariably be altered leading to different nanostructures.

Silver nitrate ($AgNO_3$) and PVP are used as the precursor and stabilizing agent, respectively. Silver nitrate, also known as lunar caustic, is a soluble versatile precursor to many other silver compounds. The stable phase of silver nitrate at room temperature and pressure is orthorhombic. It belongs to the class 222, and space group* $P2_12_12_1$ with a = 10.125 (2), b = 7.335 (2) and c = 6.992 (2) Å [25]. It is used in the polyol process as an inorganic salt, which is reduced to atomic species by the reducing agent GA.

PVP is a water-soluble polymer made from the monomer N-vinylpyrrolidone. In solution it has excellent wetting properties and can absorb up to 40% of its own weight in water. It has found use as a coating for high-quality ink jet printer paper as well as inks due to its exceptional ability to bind to polar molecules. In relation to the use of

PVP within the polyol process it has been shown that both the oxygen and nitrogen atoms of the pyrrolidone can promote the adsorption of PVP chains onto the surface of silver [23]. Also, it has been suggested that the interaction strengths between PVP and different crystallographic facets of a silver lattice were substantially different, and could therefore induce anisotropic growth for silver (a solid which is highly isotropic in structure).

Critical to the successful generation of Ag NPs is the reaction temperature and time. A wide-range of reduction rates can be accessed by slight temperature reduction. Hence, by controlling the reaction temperature the time for burst nucleation is altered by changing the levels of Ag supersaturation. For temperatures around 150°C the time to

- *Space groups, in crystallography, define the symmetry of a crystal structure and can have 230 types. They are made from combinations of translational symmetry of the unit cell, point group operations, and the screw axis and grid plane operations.*

reach maximum supersaturation point will be slightly longer than at 160°C (as described previously in Arrhenius form, equation 2.5). Also, the growth time will be altered, being longer for lower temperatures and shorter for higher temperatures due to different conversion values.

It has been reported that the reaction time (once $AgNO_3$ and PVP has been injected into the EG solution) for successful Ag nanocube growth can vary from 15 minutes to 24 hours [15, 22-24]. However, by careful literature scrutiny, this time can be significantly reduced to 7 – 15 minutes by following the procedure by Siekkinen *et al.* [31]. As this is the experimental procedure used by this author for polyol Ag NP synthesis for ε-Si SERS characterisation it shall now be dealt with in more detail.

The experiments by Siekkinen *et al.* [31] have enabled the rapid synthesis of monodisperse nanocubes 25 nm – 45 nm in length. This reaction time has been significantly shortened by adding trace amounts of sodium sulfide (Na_2S). Sulfide species are known to interact very strongly with silver, such as the creation of Ag_2S when silver exists at concentrations above the 1 μM level with trace sulfides in aqueous systems. Also, Ag_2S NPs have been shown to catalyze the reduction of Ag^+ in a mechanism analogous to the autocatalytic reduction of silver clusters by drastically reducing the reduction potential compared to that of free Ag^+ [33, 34]. At this enhanced rate, the evolution of silver nanocubes is dominated by the fast kinetic growth of single-crystal seeds. As a result, they were able to effectively limit the formation of twinned seeds and minimize the size distribution of resultant single-crystal cubes by creating a more simultaneous nucleation event, allowing all silver nanocubes to grow to the same size. The experimental setup used in this study is shown in figure 2.8.

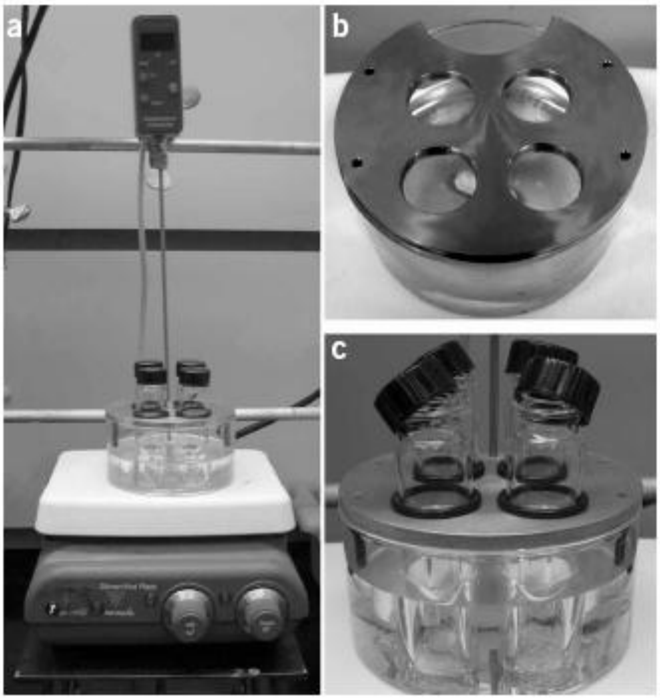

Figure 2.8: Experimental setup.

As shown in figure 2.8, four borosilicate vials (24 ml) 23 mm by 85 mm (O.D. by length) are immersed in a silicone oil bath (Dow Corning 200R Fluid, 50CST) at 150^{o}C and are filled with 6 ml of EG (including a single stir-bar for each vial, 15 x 6 mm, VWR International, 333004302) and heated for 1h (or until enough EG has been converted to GA). Note, the size of the vials and stir bars must be exact as changing the shape has led to different NP morphologies presumably due to a change in EG to GA conversion). The stir-bars are spun at approximately 260 – 350 r.p.m. Whilst the EG is being heated, approximately 140 mg of PVP (MW ~ 55,000, Aldrich, 856568) is added to 7 ml of EG and agitated with a vortex mixer. For the $AgNO_3$ solution, 120 mg of $AgNO_3$ (Aldrich, 209139) is added into 2.5 ml of EG and again, agitated with a vortex mixer and covered in tin foil, until injection into EG reductant to prevent optical degradation. Also, a 3 mM solution of Na_2S (Aldrich) in EG was made up and injected into each one of the four vials (after 1h EG heating) and heated for 8 minutes. The amount of 3 mM Na_2S solution injected into each one of the vials was 70 µL 80 µl, 90 µl and 100 µl respectively as slight changes in concentration yield different NP morphologies.

After this stage 1.5 ml of the PVP solution was injected into each vial as well as 0.5 ml of the $AgNO_3$ solution (immediately after, not before). Each vial then goes through a series of colour changes until after approximately 10 minutes the sample appears dark ruddy-red with the NP meniscus residing on the inner lining of the vials. After the specific reaction time (approximately 10 - 15 mins) the samples are then immediately transferred to a room-temperature water bath for rapid cooling. In order to image these samples via SEM each sample is divided into twelve 1.5 ml centrifuge tubes (half-full) and filled up with acetone (approximately 1:1 ratio) then spun-down at 1500 g overnight. The supernatant is then removed and samples filled with deionized water and centrifuged again (for 3 hours) after being agitated in an ultra-sonicator water bath. The supernatant is removed again with the water procedure being repeated several times. The final sample is a brown or green or yellow ochre-like colour (depending on reaction time). These samples are then stored in a 20 ml vial, covered in tin-foil and placed in a box in a refrigerator (2 – 4 ^{o}C), ready for analysis and characterisation.

2.7 Conclusion

This chapter discussed the two techniques which were employed to fabricate thin films of Ag NPs that were to be used as viable ε-Si SERS probes. In particular, Ag thin films created via a physical vapour deposition technique (direct thermal evaporation) as well as solution based Ag NPs formed via the polyol process (a chemical synthesis procedure) were discussed in detail including experimental apparatus, operating procedures, and requirements. Nanoparticle growth and nucleation kinetics – both in solution and from vapour phase condensation – were also highlighted with particular reference given to chemical synthesis optimisation for growth of Ag nanocubes.

Although the evaporation technique allowed for the successful fabrication of a relatively homogenous coating of Ag NP thin films onto ε-Si and glass substrates, the procedure had repeatability limitations due to pressure fluctuations, unstable currents, and experimental thin film thickness control. Also, if this technique were to be used in conjunction with standard 300 mm ε-Si wafers, a larger system, in particular a larger glass bell jar, would inevitably have to be used.

This led to the investigation into an alternative chemical synthesis technique called the polyol process which involved the growth of Ag NPs in solution from Ag salts and polymers (PVP) with trace amounts of Na_2S for fast Ag reduction times. Although a particular shape, the Ag nanocube, was sought the final result was a relatively homogenous suspension of Ag NPs, of a roughly spherical morphology. The Ag NP diameters for sample-to-sample could be directly controlled by altering the reaction time. By dropping approximately 10 µl of this 10 ml suspension onto the ε-Si sample to be investigated and letting it dry, potentially one thousand SERS experiments could be run from one Ag solution sample. This technique was also very easy to perform and involved minimal experimental costs and preparation time. The viability of each technique to allow for successful ε-Si SERS enhancements are discussed in chapters 4 and 5.

2.8 References:

[1.a] N. Hayazawa, M. Motohashi, Y Saito, S. Kawata, *Appl. Phys. Letts*. **2005**, 86, 263114.

[1.b] R. Chandra, P. Taneja, J. John, P. Ayyub, *NanoStructured Materials* **1999**, 11, 8, 1171.

[2] L. S. Kibis, A. I. Stadnichenko, E. M. Pajetnov, S. V. Koscheev, V. I. Zaykovskii and A. I. Boronin, *App. Surf. Sci*. **2010**, Article in Press.

[3] A. Simchi, R. Ahmadi, S. M. Seyed Reihani, A. Mahdavi, *Materials and Design* **2007**, 28, 850.

[4] N. Hayazawa, M. Motohashi, Y. Saito, S. Kawata, *Appl. Phys. Letts*. **2005**, 86, 263114.

[5] M. E. Joaquim, Santovac Fluids, INC. and Bill Foley, Varian, INC., Vacuum Technologies "Inside a vacuum diffusion pump" **2010**, *www.xtronix.ch/pdf/Diffusion%20Pump.pdf.*

[6] M. Ohring, "The Materials Science of Thin Films: deposition and Structure", 2nd edition, Academic Press, **2002**, pg. 58, 70, 97, 357, 360.

[7] R. M. Stöckle, V. Deckert, C. Fokas, R Zenobi, *Society for Applied Spectroscopy* **2000**, 54, 11, 1577.

[8] J. A. Venables, G. D. T. Spiller, M Hanbücken, *Rep. Prog. Phys.* **1984**, 47, 339.

[9]Stranski-Krastaov growth, taken from http://en.wikipedia.org/wiki/Stranski%E2%80%93Krastanov_growth#cite_note-venables2000-0, last uploaded on **02/11/2010**.

[10] D. L. Smith "Thin-Film Deposition: Principles & Practice", McGraw-Hill, **1995**.

[11] Z. Zhang, M. G. Lagally, *Science* **1997**, 276, 5311, 377.

[12] L. I. Maissel, M. H. Francombe, 'An Introduction to thin Films', Gordon and Breach Science Publishers, **1973**.

[13] H. S. Halwa, 'Handbook of Thin Film Materials: Nanomaterials and Magnetic Thin Films', Academic Press, **2002**.

[14] L. B Freund, S. Suresh, 'Thin Film Materials: Stress, Defect Formation and Surface Evolution', Cambridge University press, **2003**.

[15] J. Park, J. Joo, S. G. Kwon, Y. Jang, T. Hyeon, *Angew. Chem. Int. Ed.* **2007**, 46, 4630.

[16] K. Esumi, T. Tano, K. Torigoe, K. Meguro, *Chem. Mater*. **1990**, 2, 564.

[17] F. Mafuné, J-Y Kohno, Y. Takeda, T. Kondow , *J. Phys. Chem. B* **2000**, 104, 8333.

[18] H. H. Huang, X. P. Ni, G. L. Loy, C. H. Chew, K. L. Tan, F. C. Loh, J. F. Deng, G. Q. Xu, *Langmuir* **1996**, 12, 909.

[19] M. P. Pileni, *Prog. Colloid Polym. Sci*. **1993**, 93, 1.

[20] N. Toshima, T. Yonezawa, K. Kushihashi, *J. Chem. Soc. Faraday Trans*. **1993**, 89, 2537.

[21] L. M. Liz-Marzan, A. P. Philipse, *J. Phys. Chem*. **1995**, 99, 15120.

[22] F. Fievet, J. P. Lagier, B. Blin, B. Beaudoin, M. Figlarz, *Solid State Ionics* **1989**, 32/33, 198.

[23] B. Wiley, Y. Sun, B. Mayers, Y. Xia, *Chem. Eur. J*. **2005**, 11, 454.

[24] Y. Sun, Y. Xia, *Science* **2002**, 298, 2176.

[25] S. C. Mohr, C. J. Cleveland, "Gibbs free energy." In: Encyclopedia of Earth. Eds. Cutler J. Cleveland (Washington, D.C.: Environmental Information Coalition, National Council for Science and the Environment), **2007**.

[26] (a) R. C. Garvie, *J. Phys. Chem*. **1978**, 82, 218; (b) H. Zhang, J. F. Banfield, *J. Phys. Chem. B* **2000**, 104, 3481.

[27] (a) C. B. Murray, D. J. Norris, M. G. Bawendi, *J. Am. Chem. Soc*. **1993**, 115, 8706 (b) C. B. Murray, C. R. Kagan, M. G. Bawendi, *Annu. Rev. Mater. Sci*. **2000**, 30, 545.

[28] C. J. Johnson, E. Duhardin, S. A. Davis, C. J. Murphy, S. Mann, *J. Mater. Chem*. **2002**, 12, 1765.

[29] B. Nikoobakht, M. A. El-Sayed, *Chem. Mater*. **2003**, 15, 1957.

[30] C. Ni, P. A. Hassan, E. W. Kaler, *Langmuir* **2005**, 21, 3334.

[31] A. R. Siekkinen, J. M. McLellan, J. Chen, Y. Xia, *Chem. Phys.Letts*. **2006**, 432, 491.

[32] S. E. Skrabalak, B. J. Wiley, M. Kim, E. V. Formo, Y. Xia, *Nano Lett*. **2008**, 8, 7, 2077.

[33] A. Kryukov, N. Zin'chuk, A. Korzhak, S. Kuchmii, *Theor. Exp. Chem*. **2001**, 37, 355.

[34] A. Kryukov, A. Stroyuk, N. Zin'chuk, A. Korzhak, S. Kuchmii, *J. Mol. Cat*. **2004**, 221, 209.

Chapter 3

Characterisation Techniques

3.1 Introduction

Several analytical and elemental characterisation technologies were used throughout this work to examine the SERS, optical, compositional, and morphological properties of both Ag NPs and thin films. The primary characterisation tool utilised for SERS characterisation was micro-Raman spectroscopy (μ-Raman) which works on the principle of detecting the vibrational response of ε-Si/SiGe lattice optical phonons excited by a 488 nm excitation laser source. The surface plasmon polariton response of Ag NPs and thin films were analysed using Ultraviolet – Visible spectroscopy (UV-VIS) which detects the absorption properties of a sample as a function of excitation wavelength. Morphological features of Ag NPs and thin films were investigated via the use of scanning electron microscopy and transmission electron microscopy (SEM and TEM, respectively) which works on the principle of high-energy electron-matter interactions which are detected to build up a visual picture of the samples. Finally, composition analysis of Ag and Au NP solutions (i.e. detecting the concentration of Ag or Au in a solution) were performed using inductively-coupled plasma optical emission spectroscopy (ICP-OES) which involves ionizing the sample via an inductively-coupled plasma source and detecting the optical emission (which is elementally specific and proportional to concentration) of each sample in solution. The operating theory, principles and parameters of each characterisation device are now given in more detail.

3.2 Micro-Raman spectroscopy (μ-Raman)

Raman spectroscopy is an analytical light scattering technique used for analysing the intrinsic, internal properties of a variety of substances such as molecules, crystals, powders and liquids. A single monochromatic light source excites and interacts with phonons or molecular vibrational modes in the sample resulting in the energy of a fraction of the scattered laser photons being shifted up or down. By comparing the energies of the incident and scattered photons, the vibrational, rotational and low-frequency modes can be discovered.

Raman spectroscopy is an extremely versatile and non-destructive spectroscopic technique and has been used extensively since its discovery in 1928 by Indian physicist Sir C.V. Raman [1]. The underlying theory states that when a photon of known wavelength interacts with a molecule three types of scattering processes occur: Rayleigh scattering, Stokes scattering, and Anti-Stokes scattering. In Rayleigh scattering, photons with the same energy as the incident photons are elastically scattered from the atom. The atom is simply excited to a virtual energetic state by an incoming photon and emits a photon of the equivalent energy when returning to its ground state. There is however a certain percentage of scattering in which the scattered photon energy is not equal to the incident photon energy. This is known as Raman scattering (Stokes and anti-Stokes scattering) where the energy shift during such a scattering process is either due to phonon emission from photon energy transfer to the lattice (Stokes) or absorption of a phonon by the photon (anti-Stokes). In Stokes and anti-Stokes scattering the energy and momentum conservation laws must be satisfied, i.e.:

$$\hbar\omega_{scattered} = \hbar\omega_{incident} \pm \hbar\omega_{phonon} \qquad (3.1)$$

$$k_{scattered} = k_{incident} \pm k_{phonon} \qquad (3.2)$$

where $h\omega_{scattered}$ and $h\omega_{incident}$ are the scattered and incident photon energies respectively and $h\omega_{phonon}$ is the energy of the phonon vibration, $k_{scattered}$ and $k_{incident}$ are the wave vectors of the scattered and incident photons respectively, and k_{phonon} is the wave vector for the phonon vibration [2].

The vibrations within a crystal lattice can be thought of as quantized collective motions in the forms of waves, rather than individual atoms, and are referred to as normal modes or phonons. Each possible vibration j of the lattice is characterised by a wavevector Q_j and a frequency ω_j. The vibration amplitude, at position r, is hence given by:

$$Q_j = A_j \exp\left[\pm i\left(q_j \cdot r - \omega_j t\right)\right] \qquad (3.3)$$

where Q_j is the normal coordinate of the vibration [3]. The interaction between incident photons and phonons is indirect and is instead mediated by electronic interband transitions. Raman scattering only occurs when these interband transitions are influenced by lattice vibrations, which in turn cause a variation in the electrical susceptibility χ of the crystal. The influence of this vibration on the susceptibility tensor can be described by expanding χ into a Taylor series with respect to the normal coordinate of the vibration Q_j [4]:

$$\chi = \chi^{(0)} + \sum_{\mathrm{j}} \chi^{(1)} Q_j + \cdots = \chi_0 + \sum_{\mathrm{j}} \left(\frac{\partial \chi}{\partial Q_j}\right)_0 Q_j + \cdots \qquad (3.4)$$

The first term will give rise to Rayleigh scattering, the second to first-order Raman scattering, and the third to second-order Raman scattering where two phonons are involved: the transverse optical (TO) phonon and the longitudinal optical (LO) phonon.

The elements of $\chi^{(1)}$essentially define whether a normal vibration Q_j is Raman active or not and are referred to as components of the Raman tensor. For silicon, in the orthonormal coordinate system x = [100], y = [010], and z = [001], the Raman tensors have the form:

$$R_x = \begin{pmatrix} 0 & 0 & 0 \\ 0 & 0 & d \\ 0 & d & 0 \end{pmatrix}, R_y = \begin{pmatrix} 0 & 0 & d \\ 0 & 0 & 0 \\ d & 0 & 0 \end{pmatrix}, R_z = \begin{pmatrix} 0 & d & 0 \\ d & 0 & 0 \\ 0 & 0 & 0 \end{pmatrix} \qquad (3.5)$$

For back scattering from a (001) surface, R_x and R_y correspond to the TO phonons polarized along the x and y, respectively, and R_z to the LO phonon polarized along z [3]. For back scattering from a (100) surface, R_x corresponds to the LO phonon [4]. All samples used throughout this work are in the (100) surface configuration.

When a molecule interacts with an electromagnetic field a transfer of energy from the field to the molecule only occurs if Bohr's frequency condition is satisfied [1]; i.e.;

$$\Delta E = hv = h\frac{c}{v} = hc\tilde{v} \qquad (3.6)$$

where ΔE is the difference in energy between the two quantized states, h is Plank's constant (6.62 x 10^{-34} J.s), c is the velocity of light, and $\tilde{v}$ is the wavenumber. Hence, for Rayleigh scattering, an incident photon of energy $E_{INC} = hc\tilde{v}$ would result in a Rayleigh scattered energy of $\mathrm{E}_{\mathrm{RAY\,LEIGH}} = hc\tilde{v}$ which is equal to the incident photon energy. For Stokes scattering of the same incident energetic photon, the Stokes scattered energy would be $E_{STOKES} = hc\tilde{v} - \tilde{v}_{vib}$, where $\tilde{v}_{vib}$ is the first excited vibrational level. This shows that upon being excited by an incident photon, the energy of the molecule is returned to an excited vibrational level which results in a photon of lower energy $(hc\tilde{v} - \tilde{v}_{vib})$ and a longer wavelength photon being emitted. For anti-Stokes scattering, if an atom already exists in an excited vibrational state (due to thermal energy) and is further excited by an incident photon of energy $E_{INC} = hc\tilde{v}$, the molecule will be excited to a higher virtual state than that of Rayleigh and Stokes

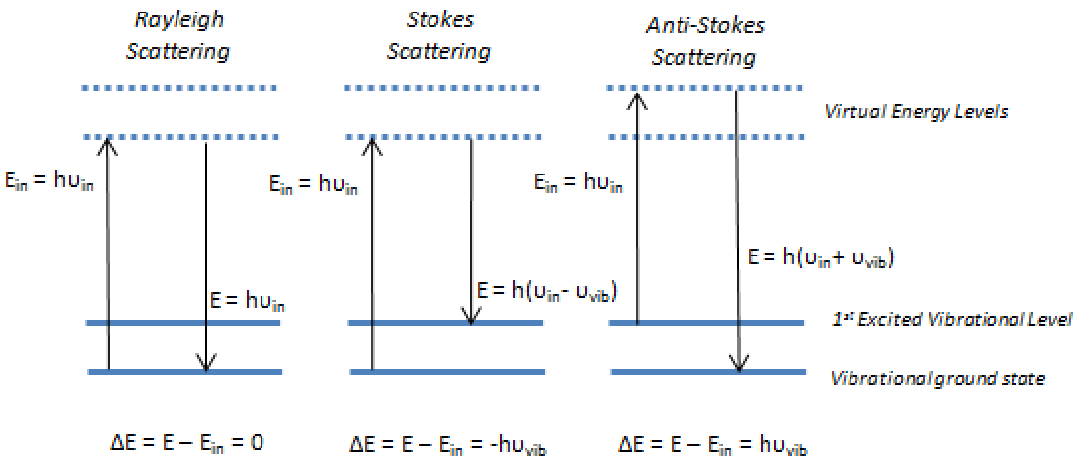

Figure 3.1: Energy diagram for Rayleigh, Stokes, and Anti-Stokes scattering. Reproduced from [1].

scattering, and will eventually return to its ground vibrational state emitting a photon of energy $E_{ANTI-STOKES} = hc\tilde{v} + \tilde{v}_{vib}$, which has a larger wavelength than Stokes scattering. These processes are illustrated in figure 3.1.

When dealing with phonons, Raman scattering typically involves the destruction of a photon with frequency ω_i (from an incident light source) and the creation of a photon with frequency ω_s. When an incident photon interacts with an electron, an electron-hole pair is created with the electron going from the ground state $|0\rangle$ to a higher state $|l\rangle$. This electron then drops to a state $|m\rangle$ by electron-phonon interaction where a photon of frequency ω_j is created (or annihilated in anti-Stokes). By recombination of the electron-hole pair a photon of frequency ω_s is emitted, where $\omega_s = \omega_i - \omega_j$ (or $\omega_s = \omega_i + \omega_j$ for anti-Stokes) [3]. This process is illustrated in figure 3.2.

The Maxwell-Boltzmann distribution law states that the population ratio of the v=1 and v=0 vibrational levels are given by [5]:

$$\frac{P_{v=1}}{P_{v=0}} = e^{-\Delta E/kT} \qquad (3.7)$$

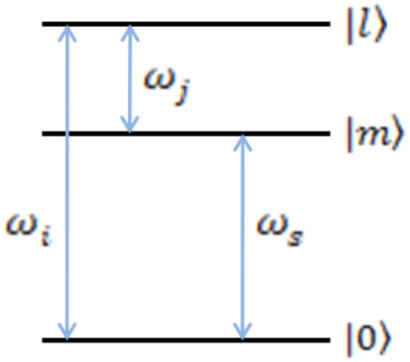

Figure 3.2: Energy level diagram for first-order Stokes scattering.

where ΔE is the energy difference between the two quantized states, k is Boltzmann's constant and T is the absolute temperature. However, in accordance with this distribution law, at room temperature the number of molecules existing in the excited state (v=1) will be much lower than the number of molecules existing in the ground state (v=0). For this reason, the stronger Stokes scattering lines are most often used for Raman analysis but anti-Stokes scattering may be used when fluorescence interference becomes problematic [6].

Throughout this work, Raman measurements were performed on a Jobin Yvon LabRam HR800 µRS system in backscattering geometry using a 488 nm Ar^+ laser excitation at room temperature. A 50x objective was used which allowed a minimum spot size diameter of approximately 4 µm. A liquid nitrogen cooled charged coupled device (CCD) detector was used to detect the Raman signals via the same objective. A confocal hole of 200 µm and a grating of 2400 g/mm were chosen for Raman measurements. The equipment was calibrated first using the 520.07 cm^{-1} Raman peak from a strain-free, reference silicon substrate. Raman peak positions were found to an accuracy of 0.04 cm^{-1} by fitting the original experimental spectrum with a Gauss/Lorentz function using the software provided by the equipment manufacturer. If there were any changes to the

Raman setup (i.e. with the addition of s-type and p-type polarisers) these will be highlighted at the beginning of each subsequent chapter.

3.3 Scanning electron microscopy (SEM)

Scanning electron microscopy is a high energy, electron microscopy technique capable of producing nanometer scale resolution images of bulk samples by performing a raster scan pattern over the sample surface. Movement of an electron beam across a sample surface generates backscattered electrons (BSE), secondary electrons (SE), Auger electrons (AE), low-loss electrons (LLE) and characteristic x-rays, all of which can be used to assess topological, compositional and conductivity parameters.

Unlike Transmission Electron Microscopy (TEM) which provides sub-nm resolution images of single NPs, SEM allows quick and easy determination of bulk sample properties. Depending on the quality of the instrument in use, a high-quality SEM image can be formed in approximately 2 – 20 minutes with a resolution of 1 to 20 nm.

The operating principles of SEM are illustrated in figure 3.3 (using a Hitachi S-4700 beam column as an example [7, 8]). The electron source is the electron gun from which high energy electrons (determined by beam accelerating voltage) are accelerated down the vertical column which are then manipulated via a series of electromagnetic condenser and objective lenses to help maintain tight control of focus (determined by probe coverage angle) and beam diameter. The beam also passes through a series of apertures (micron-size holes in film) from which they interact with the specimen whose position and orientation (rotation, tilt) is controlled by an X, Y, Z stage. The specimen signals are then acquired by the detector and analysed to form a high-resolution image

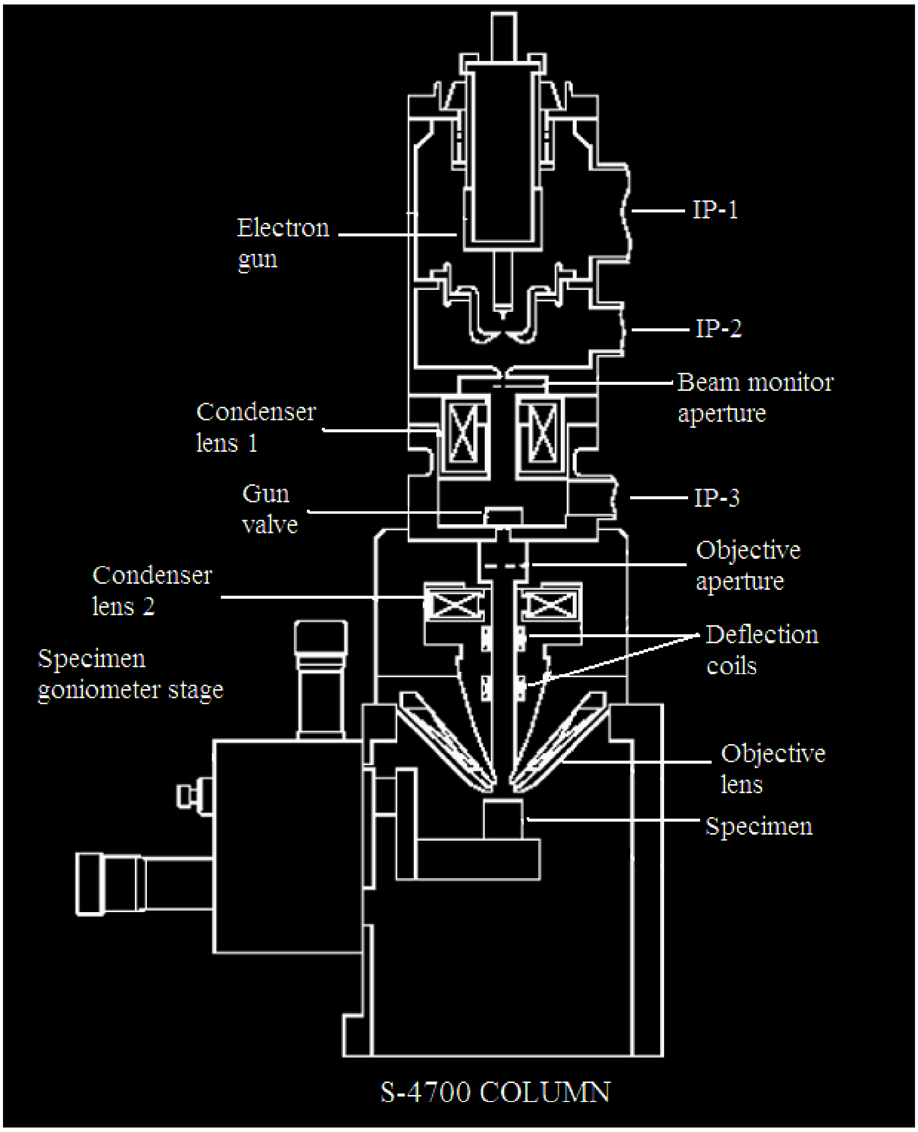

Figure 3.3. System schematic of Hitachi S-4700 SEM beam column [from 7].

of the specimen. All of these parts are maintained under a low pressure vacuum system of the order of 1.0 x $10^{-5 \text{ to } -11}$ mbar.

Electrons are produced via a thermionic, Schottky or field-emission cathode and are accelerated through a cathode-anode potential difference of typically 0.1 keV to 50 keV. At the smallest beam cross section of the gun, the beam is demagnified by a two or three stage electron lens system so that an electron probe of diameter 1 – 10 nm carrying an electron probe current of 10^{-9} to 10^{-12} A is formed at the specimen surface. This probe diameter can be increased for higher probe currents of ~10^{-8} A.

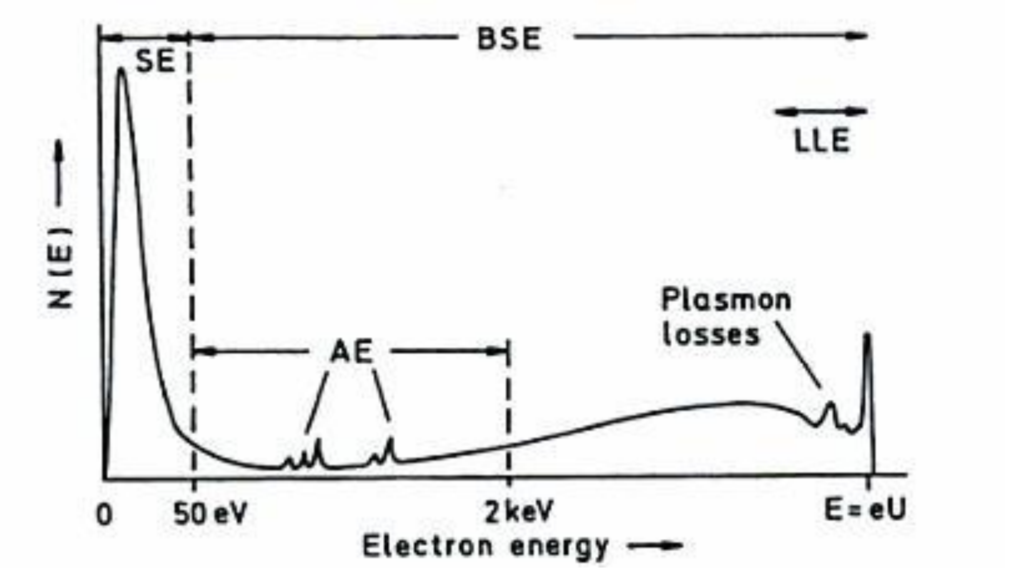

Figure. 3.4 Bremsstrahlung energy diagram for impact of electrons with specimen under SEM. Energy spectrum of electrons emitted consists of SE, LLE, BSE, and peaks of AE's. Taken from [9].

Upon hitting the specimen, electrons are mainly subjected to elastic and inelastic scattering of various energies. The overall energy spectrum, referred to as the Bremsstrahlung* energy diagram, as seen in figure 3.4, is caused by contributions from BSE's with $E_{BSE} > 50$ eV, SE's with $E_{SE} < 50$ eV, LLE's with energy losses of a few hundreds eV, as well as AE and plasmon loss peaks.

Secondary electrons and AE's are highly susceptible to elastic and inelastic collisions and can leave the specimen only from a very thin surface layer (~ nm thick). They are also generated by BSE on their way back through a larger region of the surface in addition to the narrow primary electron beam hitting the surface. Secondary electrons can be generated to such high energy levels that the excited electrons can overcome their work function before being decelerated to the Fermi level. Secondary electrons can also be collected relatively easily by means of a positively biased collector grid due to their low exit energy and as such are the most important electrons for image formation.

- Bremsstrahlung radiation: radiation caused by deceleration (the word is German for braking radiation) when passing through the field of atomic nuclei (external bremsstrahlung).

In regards to Auger electron production, upon ionization of an inner shell due to electron bombardment, the de-excitation energy can be converted to an x-ray of quantum $h\nu = E_2 - E_1$ [9] or can be transferred to another atomic electron – leaving the specimen as an AE with kinetic energy $E_2 - E_1$ less the energy necessary to overcome the ionization energy and work function.

For BSE, the broad spectrum exhibited between 50 eV and the primary electron beam energy ($E = eU$ where U is the operating voltage [9]) is caused by the deceleration of electrons that have suffered multiple energy losses and have undergone multiple large-angle scattering. They are ejected in straight trajectories and are not affected by electrostatic collision fields: detectors such as scintillators, semiconductors and channel plates have to be mounted with a large solid angle of collection.

All scanning electron microscopy (SEM) measurements were taken on the following systems: (i) Carl Zeiss EVO® LS 15 operating at 17 kV with a 5.5 mm working distance; (ii) FEI Quanta 400 ESEM operating at 20 kV with a working distance of 9.3 mm; and (iii) Hitachi Ultra-high Resolution STEM S-550, operating in transmission mode, at 20 kV at a working distance of 0.7 to 0.8 mm, with the S-550 offering the greatest resolution. SEM particle counting measurements were taken via the SEM system analysis software.

3.4 Transmission electron microscopy (TEM)

Transmission electron spectroscopy (TEM) is similar in nature to SEM except it allows for increased sample imaging resolution (individual crystal planes can even be seen) as it operates at a significantly higher voltage: routine instruments run at 100 – 200 kV, medium voltage instruments operate at 200 – 500 kV, whilst in high-voltage electron microscopy (HVEM) the acceleration voltage reaches 500 kV – 3 MV. Similar to SEM,

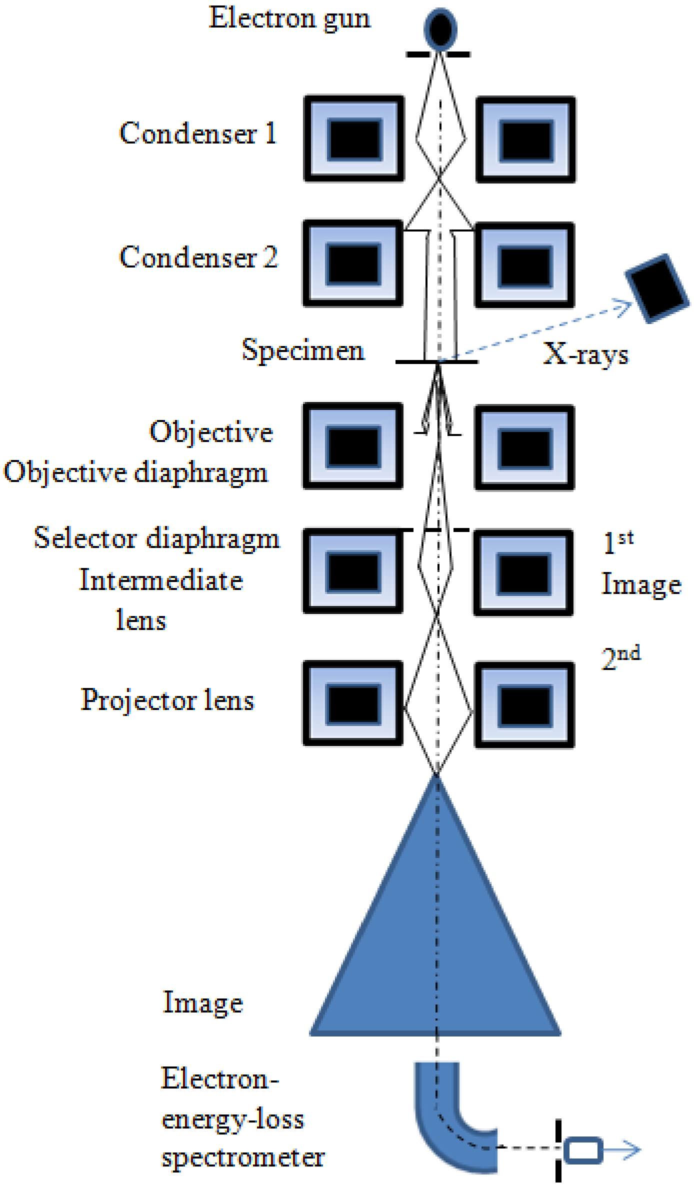

Figure 3.5: Schematic electron ray path for TEM equipped for additional x-ray and electron loss spectroscopy. Reproduced from [10].

electrons are emitted in the electron gun via Schottky or field emission and interact with sample electrons via elastic or inelastic scattering (the sample must be approximately 10 – 100 nm thin, depending on the density and composition of the sample itself.

Figure 3.5 is a schematic electron ray path for a TEM equipped for additional x-ray and electron loss spectroscopy (reproduced from [10]). The TEM can operate in bright or dark field contrast mode by either intercepting the electrons scattered through angles larger than the objective aperture (or by interference between the scattered wave and the incident wave at the image point) or by tilting the primary beam or hollow-core illumination so that the primary beam falls on the objective diaphragm [11]. The use of bright or dark-field imaging in crystalline structures gives rise to diffraction contrast which can be used to image crystal defects. Also, when Bragg-diffracted beams pass through the aperture, crystal structure imaging reveals projections of atomic periodicity. TEM can also be operated in scanning transmission mode (STEM) by means of a three or four-stage condenser-lens system with resolution determined by the electron-probe diameter (0.2 – 10 nm) [10].

Transmission electron microscopy can also be used as a powerful analytical probe tool via x-ray microanalysis and electron energy-loss spectroscopy (EELS). X-ray microanalysis in TEM mainly relies on energy dispersive Si (Li) or highly pure germanium detectors. However, Si (Li) detectors, with a resolution of ~150 eV, have the inherent disadvantage that neighbouring characteristic energy lines are less well dispersed within the energy spectra and the analytical sensitivity is poorer than in a wavelength-dispersive spectrometer [10].

An EELS, with a CCD array, can allow for a large range of energy losses to be recorded in parallel. These losses can be captured either with a magnetic prism behind the final image or with an imaging energy filter inside the column of the microscope. Electron energy-loss spectroscopy has greater collection efficiency than x-rays due to their low fluorescence yield, isotropic emission, and small solid acceptance angle of the detector, which means therefore it can be employed as a superior elemental analysis tool [11].

Although an extensive range of experiments and analytical information can be captured on the TEM, within this report only the imaging capabilities were used to image Ag and Au NPs of diameters 20, 40, 60, and 80 nm. Throughout this work, TEM images were performed on a JEOL 1230 high contrast transmission electron microscope (HC-TEM) operating at 120 kV. Samples were prepared by depositing aqueous solutions of Ag/Au NPs onto carbon PELCO® TEM grids (Ted Pella, Inc.) and allowing them to dry overnight.

3.5 Ultra-Violet visible absorption spectroscopy (UV-VIS)

Ultra violet – visible absorption spectroscopy (UV-VIS) is a spectroscopic technique for determining the absorption as a function of wavelength for a specific sample (thin film or organic solution, etc) across the near ultra-violet to visible optical spectrum (~250 nm to ~1500 nm).

For thin silver films and NPs, it has been shown that small atoms, ions, and clusters of silver have characteristic absorption bands within the visible spectrum [12]. High-energy (192 nm to 225 nm) bands are attributed to the partially forbidden $4d^{10}$- $4d^9 5s^1$ excitation of Ag^+[13] whilst there are a number of bands across the range of 250 nm to 330 nm which are ascribed to $4d^{10}5s^1$ - $4d^9 5s^1 5p^1$, $4d^{10}5s^1$ - $4d^9 5s^1 6p^1$, or $5s^1$ - $5p^1$ atomic resonance transitions in Ag^0 [14-16]. The growth of Ag atoms and ions into Ag_n clusters ($n < 7$) gives several other absorption bands (Ag_n clusters can be considered as multi-atomic molecules with s-s* and n-s* transitions between the molecular orbits corresponding to absorption bands at 330 nm to 360 nm and 440 nm to 540 nm [16-18]).

Absorption bands around 350 nm to 380 nm are attributed to clustering of Ag_n clusters resulting is clusters of size ~1 nm. As these cluster sizes increase in diameter (> 10 nm) the main broad peak seen around 400 nm to 500 nm is attributed to surface plasmon polariton resonance (SPP) absorption [19, 20]. Several other plasmon absorption peaks can appear in the spectrum depending on the shape and distribution of the NPs.

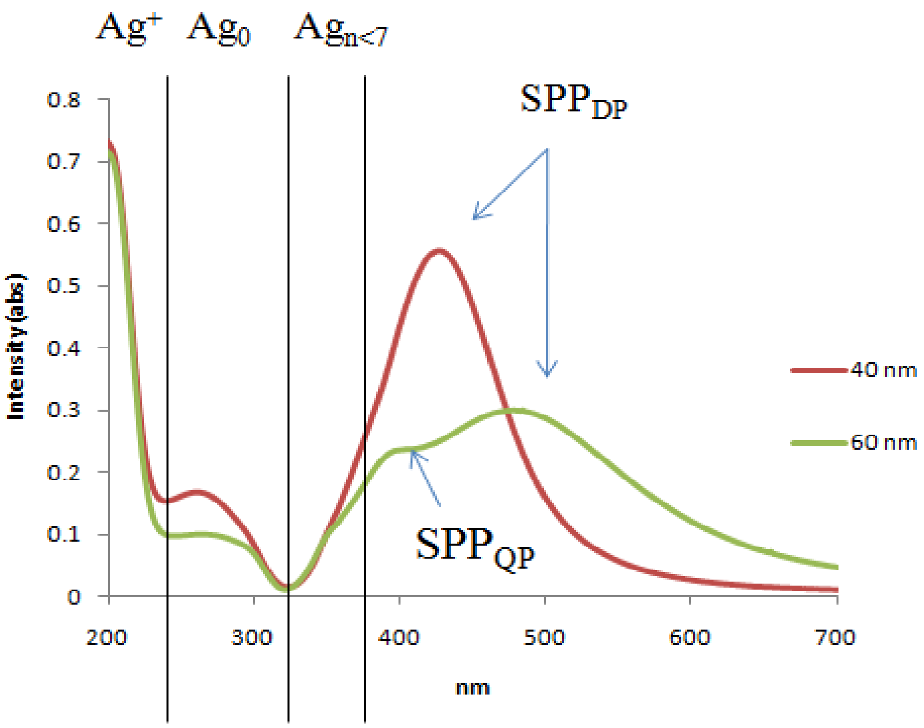

Figure 3.6: UV-VIS spectra for Ag NPs 40 nm and 60 nm in diameter (suspended in water). Shown are areas relating to absorption of Ag^+, Ag_o, small silver clusters ($Ag_{n<7}$), and surface plasmon polariton dipole and quadrupole resonance (SPP_{DP} and SPP_{QP} respectively).

For small particles, much smaller than the excitation wavelength of light, only dipolar plasmon modes are excited and are size independent within the dipole approximation [21] – a reduction in particle radius only results in a general broadening of the plasmon peak. As the particle increases in size (> 50 nm) scattering effects become prevalent with the plasmon resonance peak becoming red-shifted and broader [22]. For larger particles, where the extinction coefficient explicitly depends on the NP size [21], the plasmon bandwidth is increased and red-shifted – leading to an inhomogeneous polarization of the NP by the magnetic field. This broadening is also increased due to the excitation of different multipole modes (which peak at different energies) but mainly stems from radiative losses where the oscillating mode cannot be trapped in the particle and couples to propagating light [23, 24].

Quadrupole resonance can also appear in the UV-VIS spectrum as a high energy shoulder on the main plasmon peak [21, 25]. As larger particle sizes become relatively comparable to that of the wavelength of incident light the incident field is sufficiently inhomogeneous across the extension of the particle to allow coupling along the *xz* plane, allowing for a mixing effect to take place between dipole and quadrupole modes. Also, as particles increase in size, the main contribution to extinction for wavelengths above approximately 600 nm comes from scattering, with almost zero absorption [22]. Hence, this spectroscopic technique is an extremely fast and efficient method of characterising the plasmonic response of silver thin films and NPs (figure 3.6).

When analysing UV-VIS data, great care must be taken not to confuse the two terms absorbance and absorption. Absorbance refers to the mathematical quantity of light transmittance through a sample whilst the term absorption refers to the physical process of absorbing light. Absorbance is given by the following equation:

$$A_\lambda = -log_{10}(I/I_0) \qquad (3.8)$$

where I_0 is the incident light intensity and I is the transmitted light intensity, i.e. the intensity of light at a specific wavelength that has travelled through the sample [26].

Absorption spectra throughout this work were recorded on a Perkin Elmer Lambda 40 UV-VIS spectrometer at room temperature in the wavelength range of 200 – 900 nm with a resolution of 1nm or on an Agilent 8435 UV-VIS spectrometer across the wavelength range 200 nm to 1800 nm, using 1 nm increments, with an acquisition time of 20 s using a 5 ml quartz cuvette.

3.6 Inductively coupled plasma optical emission spectroscopy (ICP-OES)

Inductively coupled plasma optical emission spectroscopy (ICP-OES) is a spectroscopic technique capable of determining elemental compositional analysis across the whole periodic table [27]. It has an inherent capability of being able to analyze extremely low concentration levels of chemical and inorganic solutions, providing measurements from low (μ/ml) to high (mg/l) concentrations [28]. It uses an inductively coupled plasma to produce excited atoms and ions that emit electromagnetic optical emissions at wavelengths characteristic to particular elements. The intensity of the optical emission is proportional to the elemental concentration and many elements can simultaneously be analysed at once.

In principle, inductively coupled plasma is used to ionize the sample whilst an optical emission spectrometer is used to separate and detect the constitutional sample elements. In order to create the plasma, in most cases, argon gas is passed through a quartz torch which is housed in an induction coil into which high power radio frequency (RF) energy is applied, generating an alternating current within the magnetic field. Most commercial instruments use an RF source between 27.1 MHz to 40 MHz [27, 28]. If a spark is then applied to the gas, ionization occurs as electrons are stripped from the argon gas atoms and become trapped in the sustained magnetic fields, becoming accelerated in closed circular paths. Further electrons are stripped from the argon atoms, due to rapid electron collisions, causing a chain reaction effect with the plasma existing for as long as the RF field is applied. The sample is then introduced into the centre of the plasma, usually as a mist of liquid formed by passing the sample through a nebulizer* where the sample is then excited, producing optical emissions at wavelengths inherent to the individual element (figure 3.7).

- Nebulizer – A device which converts liquids to a fine spray of droplets by passing gas (oxygen, nitrogen, etc.) through the liquid.

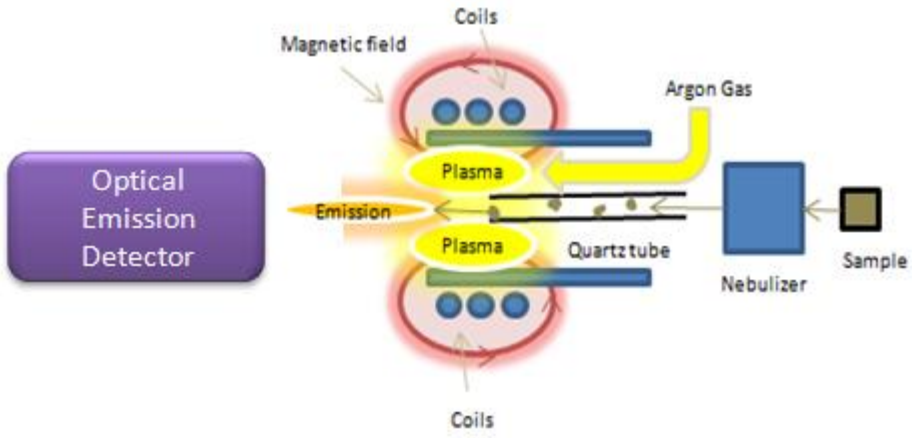

Figure 3.7: ICP-OES system schematic.

These emissions are then separated into different wavelengths, inside the optical emission chamber, with the corresponding wavelength intensities measured via an array of photomultiplier tubes, and are then captured using high resolution semiconductor photo detectors such as CCDs. Finally, the ICP-OES outputs the sample concentration.

In this report, ICP-OES was used to determine Ag and Au NP concentrations (explained in more detail in chapter 6) which could then be diluted to specific concentration values. All ICP-OES measurements were taken on a Perkin Optima 4300 DV inductively coupled plasma optical emission spectrometer with concentric nebulizer and cyclonic spray chamber.

Probably the most important part of the ICP-OES characterisation procedure is sample preparation which utilises ICP-OES standards (Ag or Au for Ag and Au NP solutions respectively) as a reference before sample measurements on NP solutions can take place. This calibration procedure is now discussed, using silver as an example.

Using an ICP-OES Ag standard [(356565, Sigma): 100 ml, 10,015 µg/ml of Ag in 1-2% wt nitric acid (HNO_3)] calibration samples of various concentrations were prepared for the ICP-OES. Using standard micro-pipette techniques 500 µl of a 70 % nitric acid solution was added to 100 µl of the ICP-MS Ag standard and boiled until completely dry. A further 500 µl of a 70 % nitric acid solution was then added and boiled until completely dry. The dried remains were then rinsed with a 1 % nitric acid solution and collected in a 10 ml glass funnel, then made up to 10 ml with the same 1% nitric acid solution. This solution has a concentration of 100 mg/l (from ICP-OES Ag standard data) which can then be diluted to 10 mg/l and 1 mg/l (and so on) by pipetting 1 ml of the solution into 9 ml of the 1 % nitric acid solution, and so on (each time reducing the concentration by a factor of 10).

Final concentrations used for ICP-OES calibration were 0.1, 0.5, 1, 5, and 10 mg/l. Before examining the concentration levels of Ag NP solutions, all organic matter had to first be removed. This was achieved by boiling 100 µl of the Ag NP solutions in 1000 µl of nitric acid. The dried matter was then rinsed with a 1% wt HNO_3 solution and made up to a 10 ml volume.

Given the concentration of each Ag NP sample the correct amount of solution could be withdrawn and diluted with the correct amount of water to make a 6 ml solution at a concentration of 6.5 mg/l (using 6 ml at 6.5 mg/l purely as an example). The following equation [29, 30] is used to make such a solution (using a 20 nm Ag NP solution as an example):

$$M_1 . V_1 = M_2 . V_2 \qquad (3.9)$$

$$41.1\, ppm \, . V_1 = 6.5\, ppm \, . \, 6\, ml$$

$$V_1 = 0.948\, ml$$

$$Ag_{20nm\_con} = 0.948\, ml + 5.052\, ml\, H_2O = 6\, ml\ @\ 6.5\, mg/l$$

Hence, given that a 20 nm Ag solution has a concentration of 41.1 mg/l, we would need to dilute 0.948 ml of the solution in 5.052 ml of water to make a 6 ml solution with a silver concentration of 6.5 mg/l.

3.7 Conclusions

In this chapter the underlying theory and operating principles and parameters of each of the elemental and analytical characterisation instruments used throughout this work were discussed in detail. These included micro-Raman spectroscopy, scanning electron and transmission electron microscopy, Ultraviolet-Visible spectroscopy, and inductively-coupled plasma optical emission spectroscopy.

3.8 References

[1] J. R. Ferraro, K. Nakamoto, C. W. Brown "Introductory Raman Spectroscopy". 2nd Edition, Academic Press, pp. 1-5, **2003**.

[2]B. G. Yacobi "Semiconductor materials: an introduction to basic principles", Kluwer academic/Plenum publishers, pg. 187, **2003**.

[3] Ingrid De Wolf, *Semicond. Sci. Technol*. **1996**, 11, 139.

[4] K. F. Domdrowski, "Micro-Raman Investigation of Mechanical Stress in Si Device Structures and Phonons in SiGe", PhD thesis, **2000**.

[5] S. Perkowitz, "Optical Characterization of Semiconductors, Infrared, Raman and Photoluminescence Spectroscopy", Academic Press, pp. 23, **1993**.

[6] E. Smith, G. Dent "Modern Raman Spectroscopy: A Practical Approach", John Wiley & Sons Ltd., **2005**.

[7] B. Hafner, "Scanning Electron Microscopy Primer", **2007**, University of Minnesota, Characterisation Facility, www.charfac.umn.edu/sem_primer.pdf.

[8] Hitachi website, http://www.hht-eu.com/cms/3171.html, last accessed **21-01-2011.**

[9] L. Reimer "Scanning electron microscopy: physics of image formation and microanalysis", 2nd Edition, Springer. pp.1-5, **1998**.

[10] L. Reimer, H. Kohl, 'Transmission electron microscopy: physics of image formation', 5th Edition, Springer, **2008**.

[11] D. B. Williams, C. B. Carter, 'Transmission electron microscopy: a textbook for materials science', 2nd Edition, Springer, **2009**.

[12] A. N. Pestryakov, A. A. Davydov, *Journal of Electron Spectroscopy and Related Phenomena* **1995**, 74, 195.

[13] J. Texier, J.J . Hastrelter, J. L. Hall, *J. Phys. Chem*. **1983**, 87, 4690.

[14] J. Hormes, G. Happel, *J. Chern. Phys*. **1983**, 8(4).

[15] V. I. Srdanov, D.S. Pesic, *J. Mol. Spectrosc*. **1981**, 90, 27.

[16] G. A. Ozin, H. Huber, *Inorg. Chem*. **1978**, 17, 155.

[17] M. R.V. Sahyun, Growth and Properties of Metal Clusters, *Proc. 32nd Meet. Soc. Chem. Phys*. **1980**, Amsterdam, p. 379.

[18] S. A. Mitchell, G. A. Kenney-Wallace, G.A. Ozin, *J. Am. Chem. Soc*. **1983**, 103, 6030.

[19] D. Fornasiero, F. Grieser, *J. Phys. Chem*. **1987**, 87, 3213.

[20] R. Jin, Y. W. Cao, C. A. Mirkin, K. L. Kelly, G. C. Schatz, J. G. Zheng, *Science* **2001**, 294.

[21] S. Link, M. A. El-Sayed, *J. Phys. Chem. B* **1999**, *103*, 8410-8426.

[22] J. Rodrıguez-Fernandez, J. Perez-Juste, F. J. Garcıa de Abajo, L. M. Liz-Marzan, *Langmuir* ***2006***, *22*, 7007.

[23] G. C. Papavassiliou, *Prog. Solid State Chem.* **1980**, *12*, 185.

[24] C. F. Bohren, D. R. Huffman, *Absorption and Scattering of Light by Small Particles*; Wiley: New York, **1983**.

[25] H. Jia, J. Zeng, W. Song, J. An, B. Zhao, *Thin Solid Films* ***2006***, 496, 281.

[26] B. J. Clark, T. Frost, M.A. Russell, "UV Spectroscopy: techniques, instrumentation, and data handling", Chapman and Hall, 1993.

[27] H. E. Taylor, "Inductively Coupled Plasma-Mass Spectroscopy: Applications and Techniques" Academic Press, pp.1-5, **2001**.

[28] S. Nelms, "Inductively Coupled Plasma Mass Spectrometry handbook", Blackwell Publishing, pp. Preface & 1-6, **2005**.

[29] M. S. Silberberg, "Principles of General Chemistry" McGraw-Hill, **2007**.

[30] W. A. Masterton, C. N. Hurley, "Chemistry: principles and reactions", sixth edition, Brooks-Cole Cengage Learning, **2008**.

Chapter 4

Sticky-SERS (Thermal Evaporation)

4.1 Introduction & Aims

As previously discussed in chapter 1 ε-Si engineering can be incorporated into transistor fabrication processes to enhance transistor operating performances such as increased operating speed and reduced power consumption. In order to effectively characterise these ε-Si layers, grown on SiGe virtual substrates, a variety of techniques and processes have been investigated. None however possess the ability to analyse both ε-Si and SiGe peaks, *simultaneously* on a sub-µm length scale, using a completely non-destructive approach. Although micro-Raman studies have shown excellent results, adhering to the requirements just stated, so far only expensive UV laser sources with their inherent shallow penetration depths have been capable of probing the nm-thin ε-Si epilayers [1a, 1.b]. Larger wavelength sources such as 514.5 nm propagate deep into the bulk SiGe substrate and overshadow the relatively weak ε-Si signal (software deconvolution and destructive etching techniques have been used to determine ε-Si values using these excitation sources [1.c]). These limitations provide good reasons for the use of SERS enhancements (discussed in section 1.3) such as those recently documented by Hayazawa *et al*. [1.d] which effectively confine light to the upper layer of the ε-Si and increase the probability and intensity of Raman scattering from the ε-Si optical phonons.

In this chapter, the direct thermal evaporation technique previously described in section 2.1 has been utilized to deposit and grow uniform Ag thin films on top of ε-Si layers of thickness 9, 17.5, and 42 nm. The ability for these films to act as effective SERS probes, offering the simultaneous peak determination of both ε-Si and SiGe peaks, was investigated by means of a micro-Raman system operating with a 488 nm excitation source. These Ag thin films were also analysed via UV-VIS and SEM instruments (discussed in sections 3.3 and 3.5, respectively) as well as p-type and s-type polarization filters loaded into the micro-Raman system to analyse the plasmonic response of these films which would help indicate the necessary surface roughness features and surface plasmon polariton absorption profiles needed for ε-Si SERS effects to take place – as discussed in section 1.4. Post measurement mathematical strain determination then followed.

Specific aims relevant to this chapter are as follows:

1) Can Ag thin films deposited onto ε-Si substrates of various thicknesses, fabricated using direct thermal evaporation techniques, be successfully utilised for ε-Si SERS enhancements?
2) If SERS enhancements are visible, to what extent do Raman system artefacts and Ag thin film morphologies influence the intensity and spectral position of the observed ε-Si peaks.
3) Can strain calculations be used to determine strain values from sample-to-sample?
4) Can a relative mathematical enhancement factor model be derived to assess enhancement factors from sample-to-sample?
5) What limitations does this technique possess?

4.2 Sample preparation

Strained-silicon samples of thickness 17.5 nm of size 0.8 mm by 0.8 mm with (100) surface orientation were cleaved from a 150 mm p-type $Si_{0.8}Ge_{0.2}$ strained silicon (ε-Si) wafer. Single pieces of similar size ε-Si samples of thickness 9 nm and 42 nm were also used for tests (30 % and 20 % Ge, respectively). All samples, including microscope cover glass slips (Thermo Scientific) of size 22 mm by 22 mm (number 1 thickness), were loaded onto the evaporation stage located 21 cm vertically above the tungsten boat evaporation source. All samples were first cleaned with a De-ionised (DI) water wash; Decon™ scrub; acetone dip; then final DI water wash to remove organic contaminants and grease. Evaporation took place on an Edwards evaporator system.

Approximately 120 mg of Ag nanopowder (< 100 nm, Sigma Aldrich, #576832) was used as the evaporation source and loaded into a tungsten boat (Testbourne, ME4.005W). The Ag nanopowder was evaporated (at an evaporation current of 36 A) and deposited onto the substrates once the vacuum chamber pressure reached 1.0×10^{-4} mbar. By altering the evaporation exposure time Ag nanoparticle growth on the substrates could be controlled and optimised for maximum SERS ε-Si enhancement, as described in chapter 2. Micro-Raman results for maximum SERS enhancement are analysed first and given in section 4.2. Factors impacting maximum SERS enhancement such as plasmonic resonance, structural, and optical properties are then discussed with reference to SEM, and UV-VIS absorption in subsequent sections.

4.3 Strained-silicon SERS optimisation results

Before the addition of Ag NPs via evaporation a Raman spectrum was taken for the 9 nm, 17.5 nm, and 42 nm ($Si_{0.7}Ge_{0.3}$, $Si_{0.8}Ge_{0.2}$, and $Si_{0.8}Ge_{0.2}$, respectively) ε-Si samples. SERS enhancement in relation to s- and p-polarized light was also investigated via the use of s- and p-polarization filters. The effect of focal plane control on SERS enhancement was also investigated by changing the focusing plane across a range of values from +5 µm to - 40 µm. These measurements were then compared to non-SERS ε-Si samples.

Figure 4.1 depicts the average Raman spectra for 9, 17.5, and 42 nm ε-Si samples (data represents a total of 300 scans at 20 accumulations for each point, 5 points per sample, and three samples) and includes a standard non-strained silicon spectrum for reference. As can be seen an increase in Ge concentration results in a greater red-shifting of the SiGe peak. These SiGe Raman peaks, including standard deviation, are located at approximately 498.25 ± 0.38 cm^{-1}, 506.55 ± 0.21 cm^{-1}, and 505.90 ± 0.15 cm^{-1} for ε-Si of thickness 9 nm, 17.5 nm, and 42 nm. The respective corresponding Si-Si Raman modes are located at approximately 507.64 ± 0.37 cm^{-1}, 512.52 ± 0.27 cm^{-1}, and 511.96 ± 0.21 cm^{-1}. Peak fitting was done via a double Lorentian peak fit using both the SiGe and ε-Si Raman peaks to an accuracy of 0.04 cm^{-1}. From careful literature scrutiny these SiGe and ε-Si peak positions are reasonable [1-6].

After evaporation, each sample was analysed at several different random locations via micro-Raman spectroscopy. Data shown represents a total of 300 scans (20 accumulations for each point, 5 points per sample, and three samples). The results for the17.5 nm sample are shown in figure 4.2. As can be seen there is an obvious SERS enhancement of the 17.5 nm ε-Si layer when compared to bare 17.5 nm ε-Si, for the

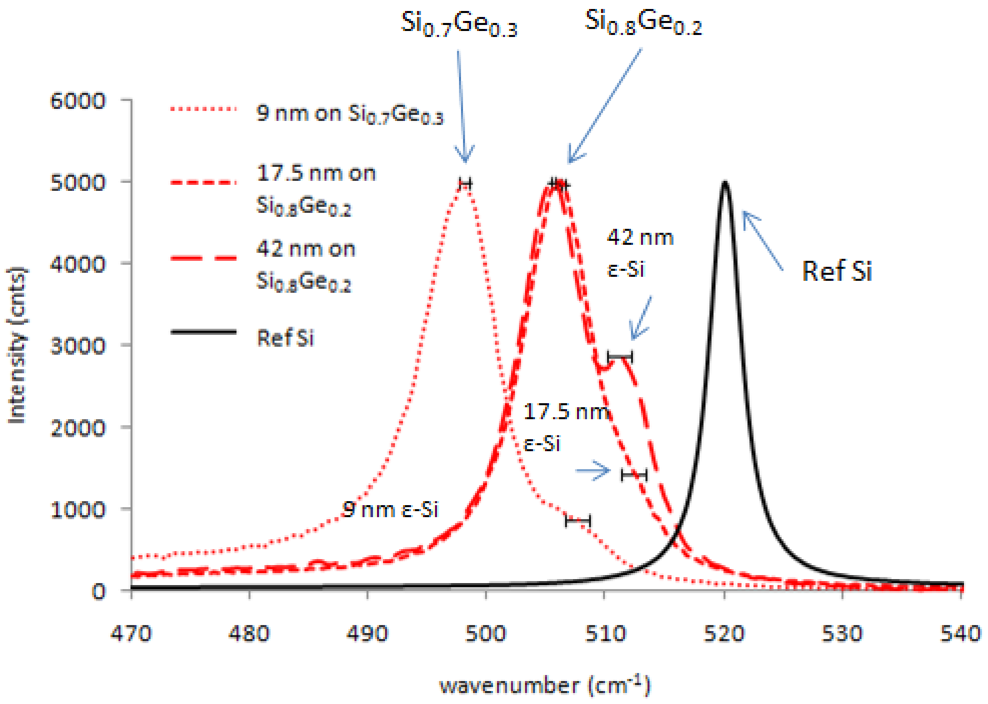

Figure. 4.1: Raman spectrum for 9, 17.5, and 42 nm ε-Si samples. A reference non-strained silicon peak is also shown (black). Data represents a total of 300 scans (20 accumulations for each point, 5 points per sample, and three runs). An increase in Ge concentration results in a greater red-shifted SiGe peak compared to standard silicon. Although a ε-Si peak can be seen at approximately 511.96 cm^{-1} for ε-Si of thickness 42 nm it is extremely difficult to locate accurate ε-Si peaks for ε-Si thickness 9 nm and 17.5 nm. Standard deviation bars are also shown for SiGe and Si-Si peaks. Excitation source was 488 nm.

four random sample points shown (although far more points were analysed (over 20) the spectra depicted are the best SERS enhancements across all experimental runs). The average SERS SiGe peak was found to be 506.98 ± 0.33 cm^{-1} with a corresponding SERS ε-Si peak located at 512.9 ± 0.37 cm^{-1}. The SiGe peak is only slightly shifted with respect to the non-SERS peak (506.55 ± 0.21 cm^{-1}) by an amount of 0.43 cm^{-1} which is almost equal to the difference when comparing the non-SERS and SERS ε-Si peaks located at 512.52 ± 0.27 cm^{-1} and 512.9 ± 0.37 cm^{-1}, respectively: the difference in this

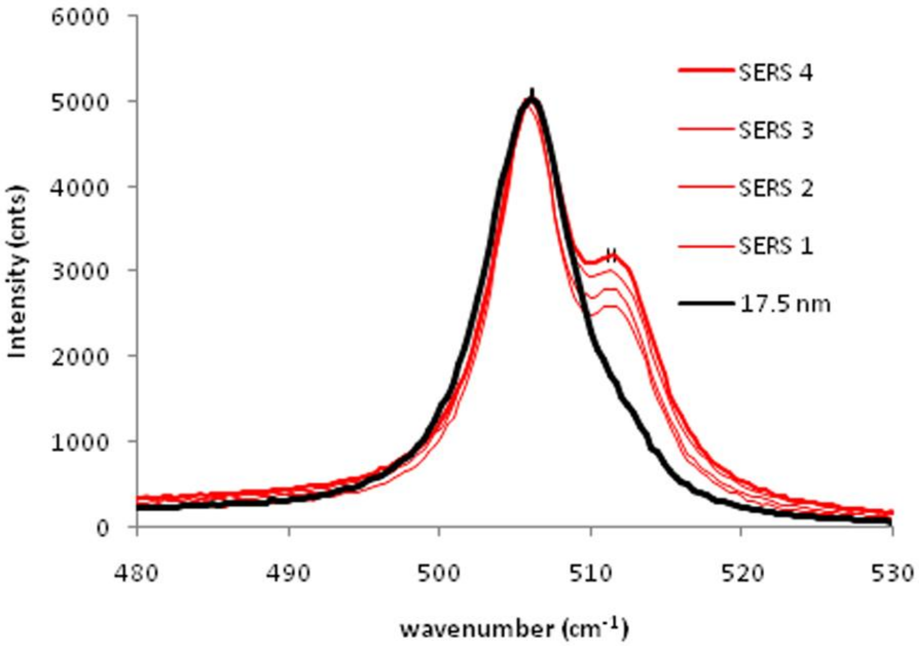

Figure. 4.2: 17.5 nm strained-silicon SERS enhancement at 4 random locations. All samples have been intensity normalised to a SiGe peak intensity of 5000 counts. Data represents a total of 300 scans (20 accumulations for each point, 5 points per sample, and three runs). SiGe peaks for non-SERS and SERS conditions were located at 506.55 ± 0.21 cm^{-1} and 506.98 ± 0.33 cm^{-1}, respectively. ε-Si peaks for non-SERS and SERS conditions were located at 512.52 ± 0.27 cm^{-1} and 512.9 ± 0.37 cm^{-1}, respectively.

case being 0.38 cm^{-1}. For the case of 17.5 nm ε-Si samples it seems that SERS enhancements only offer a slightly more accurate peak determination, with the previous Lorentzian peak fitting algorithms being sufficient to give a good estimate of the ε-Si peak position. Considering the user has to manually locate the peaks of interest for the peak-fitting software to work, this technique is limited by the accuracy of the user's peak placement. The SERS condition however, leaves no room for doubt as to where the ε-Si peaks reside as they are clearly enhanced within the full Raman spectra. Hence, the SERS technique is far more accurate due to the ability to accurately pick out the specific ε-Si peaks which are a direct result of *SERS enhancement.*

We can then use the peak positions to assess strain values via equation 4.1 [7]:

$$\sigma_{xx} = \sigma_{yy} = \frac{-\Delta_{\omega}}{4} \pm \frac{SD}{4} \quad (\mathrm{GPa}) \quad (4.1)$$

where σ_{xx} and σ_{yy} are the in-plane biaxial strains in the x and y direction, respectively, and Δ_{ω} is the Raman peak position shift between bulk non-strained silicon and ε-Si, and *SD* is the standard deviation. Substituting the value of 512.9 ± 0.37 cm^{-1} into equation 4.1, and using 520.07 cm^{-1} for bulk silicon, we would get a strain value of 1.79 ± 0.0925 GPa. If instead we used the non-SERS ε-Si peaks of 512.52 ± 0.27 cm^{-1} we would get a strain value of 1.88 ± 0.0675 GPa. Considering the maximum resolution obtained during the course of these experiments was ± 0.15 cm^{-1} (for 42 nm SiGe peak) the lowest strain variation possible for this case would be ± 0.0375 GPa. This is comparable to using neon emission line adjustments to reduce the error margin to ± 0.1 cm^{-1} [7]. It should be noted that neon line adjustments were not used in these experiments due to potential plasma line interactions with the SiGe and ε-Si peaks across the range 490 cm^{-1} to 530 cm^{-1} [8] as well as potential problematic fluorescence issues associated with UV excitation of silver NPs [9].

Considering the 17.5 nm SERS ε-Si variations were 0.0925 GPa which is almost three times as large as the best possible system resolution of ± 0.0375 GPa, this *could* suggest that the variation in strain peaks for the 17.5 nm SERS ε-Si peaks are in fact due to *nanoscale strain variations*. Hence, this SERS technique could effectively allow for nanoscale strain variation characterisation across the whole sample from point-to-point.

On the contrary, it has been argued that shifts in the SERS spectrum of ε-Si could be explained by the chemical effects such as the existence of silver atoms close to silicon atoms [10] or due to temperature induced localised laser heating of the sample [11]. The former speculation involves Raman shifts of over 10 cm^{-1} for adenine molecule ringbreathing modes exhibited by Tip-enhanced Raman spectroscopy (TERS) and is thought to occur due to the deformation of adenine molecules by silver atoms of the metallic tip. The latter argument involves laser heating of micro-thin, boron doped, silicon cantilevers where an increase in temperature would result in a shift of the TO phonon band to a lower wavenumber with an increase in half-bandwidth, as a result of decreased phonon relaxation times – sufficient to produce shifts of around 0.2 cm^{-1} which is equivalent to maximum permissible system resolution.

In their experiment the heating effects were only substantial across the 3 μm thin cantilever structure, and not the bulk silicon sample itself (the thickness of the structures used throughout this report were ~ 3 mm). They also used large, continuous exposure times of 200 s to 600 s, instead of the 30 s exposure times used within this report. Hence, considering the e-Si Raman peak shifts in this report are larger than that attributed to heating effects and that the structural and experimental characteristics are completely different from that of TERS experiments [10] it could be said that observed ε-Si peak shifts from point-to-point are not a direct result of heating or chemical effects but are either due to actual strain variations from point-to-point or from other system limitations.

Also, research by Himcinschi *et al.* [5] have demonstrated strain variations across large areas (40 μm^2) of bulk ε-Si (as well as 150 nm x 150 nm and 150 nm x 750 nm ε-Si pillars) by as much as 60 – 80 x 10^{-3} %. Hence, although these percentages are lower

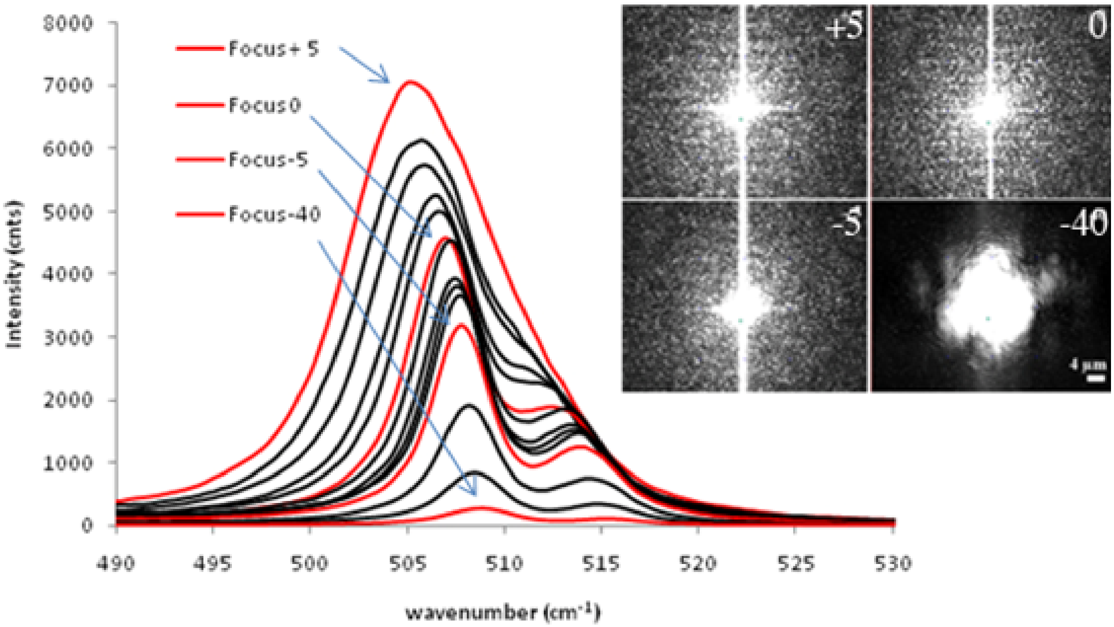

Figure. 4.3: SERS SiGe and ε-Si peak shifts as a function of focal height (+ 5µm to - 40 µm) for a SERS active 17.5 nm thick ε-Si sample. Photos for focal height of + 5 µm, 0 µm, -5 µm, and - 40 µm are shown in the top right. A shift in focal height from + 5 µm to – 40 µm results in an attenuation and a blue shift for both the SiGe and ε-Si peaks. Black lines are Raman spectra for z-height in-between labelled spectra (red lines). Data represents a total of 300 scans (20 accumulations for each point, 5 points per sample, and three runs).

than the calculated values shown previously, it does give evidence that *there can be strain variations on the nanoscale*. One final system artefact that needs to be ruled out before a true conclusion can be made is Raman peak shifts resulting from focal plane defocusing.

Under normal Raman operating procedures before a scan may commence the laser light has to be brought into focus on the sample. A tight focal spot is reached on the ε-Si sample once the laser target resembles a cross-hair target on the sample itself. An example of this is shown in the top-right hand corner of figure 4.3, which also includes a focus spot image for out-of-focus laser spots at z-heights of + 5 µm, - 5 µm, and - 40 µm. As can clearly be seen a more intense cross-hair pattern is reached for a z-height of 0 µm which results in a laser spot size of approximately 4 µm. Also shown in figure 4.3 is the actual SERS Raman data for a 17.5 nm thick ε-Si sample.

As the focal plane is gradually reduced across the range + 5 µm, + 4 µm, +3 µm, +2 µm, +1 µm, 0 µm, -1 µm, -2 µm, -3 µm, -4 µm, -5 µm, - 10 µm, - 20 µm, and – 40 µm, both the SiGe and ε-Si peaks are attenuated in intensity and blue shifted (in figure 4.3 red lines are labelled and represent z-heights of + 5 µm, 0 µm, - 5 µm, and + 40 µm while the black lines are Raman spectra for z-heights of + 4 µm, +3 µm, +2 µm, +1 µm, -1 µm, -2 µm, -3 µm, -4 µm, - 10 µm, and - 20 µm).

Using the values for the 17.5 nm SERS ε-Si peaks located at +1 µm, 0 µm, and -1 µm (506.54 cm^{-1}, 506.94 cm^{-1}, and 507.34 cm^{-1}, respectively) we can see that a 1 µm change in z-height corresponds to ~ 0.4 cm^{-1} difference in peak position. Also, if this effect is linear then the amount which the ε-Si peak has shifted by will equal the SiGe peak shift. This is indeed confirmed by first choosing a reference SiGe reference peak of 506.55 cm^{-1} from non-SERS 17.5 nm samples and then normalising the defocused SiGe peaks to this position. The amount of peak shifting needed to fit to the 506.55 cm^{-1} SiGe peak is then applied to the ε-Si peaks to obtain an average value.

This normalised ε-Si peak value was found to be 512.61 ± 0.34 cm^{-1} which is very close to the non-SERS value of 512.52 ± 0.27 cm^{-1}. This suggests that although focus height does indeed result in a peak shift for both the SiGe and ε-Si peaks these are in fact *linear effects* with the amount of SiGe and ε-Si peak shifting being *proportional* to each other. The physical effect of these peak shifts are unknown and although they have been documented elsewhere [12] with far less deviation (± 0.4 cm^{-1} as opposed to ± 0.05 cm^{-1} reported in the literature [12] across the range -1 µm < z < 1 µm) they also follow a different pattern in that the peak position is constantly blue-shifted as the defocusing goes from positive to negative, within this experiment. Considering this author had extensive experience with maintaining tight control over the focal plane within the range -1 µm < z < 1 µm, from this evidence, it would seem more favourable to only highlight any nanoscale strain variations for which the standard deviation is greater than ± 0.4 cm^{-1} associated with defocusing which equates to a strain variation of ± 0.1 GPa

A counter argument against these statements would be that the distribution and homogeneity of the SERS active substrate could also induce Raman peak fluctuations. In this case, the thin layer of silver NPs covering the ε-Si substrates could cause intensity and peak position variations due to activation and deactivation of certain so called SERS hot-spots (areas which are more SERS active than others due to homogeneity variations).

However, in Raman spectroscopy, the scattered intensity is linear with the incident field intensity which is magnified at the NP surface due to the SERS effect - so called SERS hot-spots would simply increase the overall SERS effect, providing a greater enhancement factor of the analyte being investigated (in this case the thin ε-Si layers). This would also be the case for non-homogenous surface coverage. This is further elucidated in equation 4.2 [13]:

$$EF = \frac{|E_{out}|^2 . |E'_{out}|^2}{|E_0|^4} = 4|g|^2|g'|^2 \qquad (4.2)$$

where E_{out} and E_0 are the radiated and incident electromagnetic fields respectively, E'_{out} is the field evaluated at the scattered frequency which is Stokes-shifted by the vibrational frequency of the strained-silicon, g' is the Stokes-shifted value of g which is defined by:

$$g = \frac{\varepsilon_{in} - \varepsilon_{out}}{(\varepsilon_{in} + 2\varepsilon_{out})} \qquad (4.3)$$

where ε_{in} and ε_{out} are the dielectric constants of the metal nanoparticle and external environment (in this case air), respectively [13].

As the enhancement factor, *EF*, is the magnitude of increase in Raman scattering cross-section of analytes in close proximity to a SERS active substrate any variation in the terms involves in equation 4.2 would simply increase or decrease this factor. This has also been shown experimentally using the SERS spectra of pyridine absorbed onto silver films over nanosphere samples coated with various thicknesses of alumina [13]. As the alumina thickness gradually increases from 0 nm to 4.8 nm the spectra gradually decreases from a SERS maximum, showing enhanced SERS peaks, to the bulk pyridine Raman spectra. This is effectively due to a gradual decrease in the enhancement factor. Even though the SERS peaks may attenuate, *their relative Raman peak positions do not*. However, it must be stated that excessive thermal gradients and heating effects associated with laser illumination of the Ag thin films may actually change the nano/micro environment which would alter both the dielectric functions of the Ag thin films and the surrounding air molecules resulting in a change of value for the enhancement factor.

It should also be worth mentioning that variations in ε-Si peak intensities, not peak positions, are also highly dependent on the following equation:

$$I_{SERS} = \left(\frac{a + r}{a}\right)^{-10} \qquad (4.4)$$

where I_{SERS} is the intensity of the Raman mode, a is the average size of the field-enhancing features on the surface, and r is the distance from the surface to the absorbate [14]. This equation shows that for nm-thin layers of silicon surface oxide, the SERS intensity will drop due to the r^{-10} distance dependence. Although maximum SERS enhancement would most likely arise from treating the ε-Si with a hydrogen fluoride (HF) dipping procedure to remove native oxide layers it is not necessary in this case as any techniques used throughout this project should inherently remain non-destructive.

Hence, although Raman ε-Si peak intensities are dependent on the enhancement factor, their peak position should be completely *independent* and rely solely on the *vibrational modes in the ε-Si*. Therefore this seems to suggest ε-Si peak shifts are not dependent on SERS substrates and SERS substrate variations across the sample. The remaining ε-Si samples (17.5 nm and 42 nm think) were then analysed for SERS enhancements.

The results for the 9 nm thick ε-Si sample are shown in figure 4.4. As can be seen, there is an obvious SERS enhancement of the 9 nm ε-Si peak. The SERS ε-Si peak is located at 508.39 ± 1.022 cm^{-1} compared to the non-SERS ε-Si peak located at 507.64 ± 0.37 cm^{-1}. This is somewhat larger than the non-SERS peaks but is a far more accurate value considering a visible non-SERS ε-Si peak was almost non-existent and almost completely overshadowed by the bulk substrate – which makes peak fitting an arduous process. This does however (again) emphasise the sensitivity of SERS effects and the corresponding ability to easily perform Raman characterisation on both the SiGe and ε-Si peaks simultaneously using a high resolution 488 nm Ar^+ excitation source. In fact, this is the first time ever (known to this author) that SERS enhancements have successfully been accomplished for a 9 nm ε-Si thickness. It is also worth pointing out the difference in ε-Si peak intensities which as described earlier are most likely due to

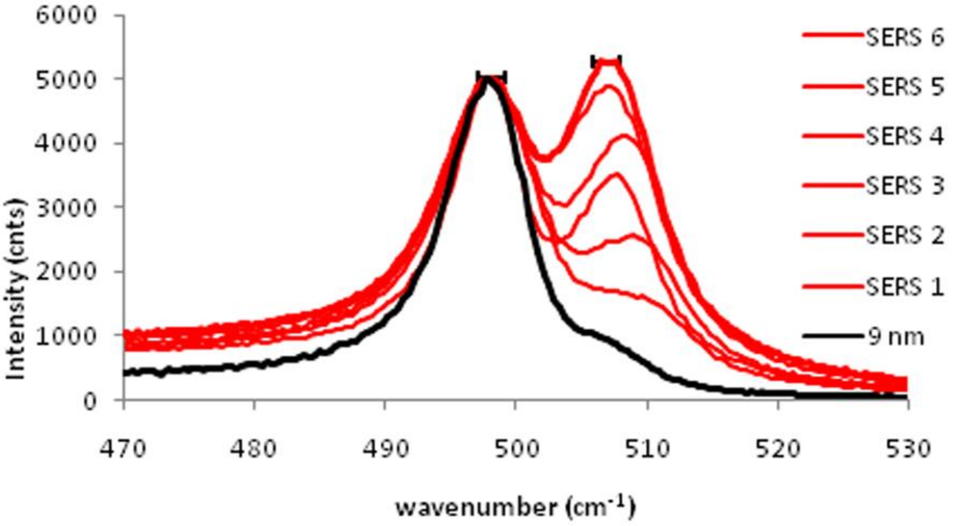

Figure. 4.4: 9 nm ε-Si SERS enhancement at 6 random locations. All samples have been intensity normalised to a SiGe peak intensity of 5000 counts. SiGe peaks for non-SERS and SERS conditions were located at 498.25 ± 0.38 cm^{-1} and 498.20 ± 1.00 cm^{-1}, respectively. ε-Si peaks for non-SERS and SERS conditions were located at 507.64 ± 0.37 cm^{-1}and 508.39 ± 1.022 cm^{-1}, respectively. Data represents a total of 300 scans (20 accumulations for each point, 5 points per sample, and three runs).

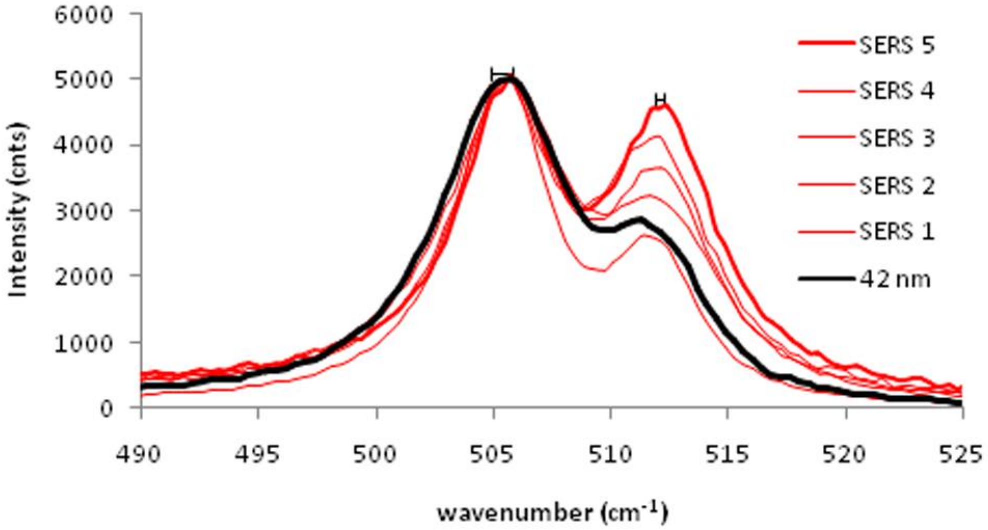

Figure. 4.5: 42 nm ε-Si SERS enhancement at 5 random locations. All samples have been intensity normalised to a SiGe peak intensity of 5000 counts. Scan time was 30 s at 20 accumulations. SiGe peaks for non-SERS and SERS conditions were located at 505.90 ± 0.15 cm^{-1} and 506.09 ± 0.45 cm^{-1}, respectively. ε-Si peaks for non-SERS and SERS conditions were located at 511.96 ± 0.21 cm^{-1} and 511.32 ± 0.63 cm^{-1}, respectively. Data represents a total of 300 scans (20 accumulations for each point, 5 points per sample, and three runs).

Sample	SiGe (cm^{-1})	SERS SiGe (cm^{-1})	ε-Si (cm^{-1})	SERS ε-Si (cm^{-1})	ε-Si Strain (Gpa) SERS
9 nm	498.25 ± 0.38	498.20 ± 1.00	507.64 ± 0.37	508.39 ± 1.022	2.92 ± 0.25
17.5 nm	506.55 ± 0.21	506.98 ± 0.33	512.52 ± 0.27	512.9 ± 0.37	1.79 ± 0.0925
42 nm	505.90 ± 0.15	506.09 ± 0.45	512.52 ± 0.27	512.9 ± 0.37	2.1875 ± 0.157

Table 4.1: SiGe and e-Si peak positions (non-SERS and SERS) for 9 nm, 17. 5nm and 42 nm e-Si samples. Also shown are calculated strain values for ε-Si SERS spectra.

nano-scale silicon oxide formation and non-homogeneous surface coverage of silver nanoparticles.

Using equation 4.1, the 9 nm thick ε-Si SERS sample has strain values of 2.92 ± 0.25 GPa (compared to 3.1075 ± 0.09 GPa for the non-SERS case). As the strain variation is larger than ± 0.1GPa, this could be evidence for strain fluctuations from point-to-point as described earlier. Analysis of the 42 nm ε-Si sample also shows significant SERS enhancements.

As can be seen in figure 4.5 there is an obvious SERS enhancement of the 42 nm ε-Si layer when compared to bare 42 nm ε-Si, for the five random sample points investigated. The non-SERS SiGe and ε-Si Raman peaks are located at 505.90 ± 0.15 cm^{-1} and 511.96 ± 0.21 cm^{-1}, respectively whilst the SERS SiGe and ε-Si Raman peaks are positioned at 506.09 ± 0.45 cm^{-1} and 511.32 ± 0.63 cm^{-1}, respectively.

Using equation 4.1, this corresponds to the 42 nm thick ε-Si SERS sample having a strain value of 2.1875 ± 0.157 GPa. As the variation is larger than ± 0.1 GPa as previously mentioned, this could also be possible evidence for strain fluctuations from point-to-point. All peak positions and corresponding strain values are highlighted in table 4.1.

4.4 SERS enhancement factor calculations

Calculations for determining the enhancement factor (EF) in SERS complexes is currently a contentious issue [15]. First of all, EFs were thought to arise from an increase of the surface area on which the analyte being investigated resided i.e. the surface area of nano-roughened silver thin films would be greater than a continuous flat silver film, resulting in an increase number of probed analytes [16].

However, this is not the case as EFs arise from the apparent increase in Raman cross section of the molecule: an increase in the probability that a molecule will emit a Raman photon [17]. For a true EF calculation regarding ε-Si enhancement via SERS several steps must be performed [15]. Using a known, fully calibrated compound such as Rhodamine 6-G (whose non-SERS Raman cross section has been fully analysed) as a reference the non-SERS Raman cross section of the ε-Si must first be calculated, then the characterisation of the scattering volume must be performed. This will lead finally to a true ε-Si SERS EF. This is not an easy task as several aspects such as laser excitation profile (laser intensity as a function of position, which is often non-uniform) and detection efficiency profile (often a function of the experimental setup) must first be calibrated. However, although steps are underway to develop a more accurate EF for ε-Si, we will adopt the following equation for rapid EF estimations:

$$EF = \frac{I_{SERS}\,/N_{surf}}{I_{NRS}/N_{vol}} \qquad (4.5)$$

where I_{SERS} is the surface-enhanced Raman intensity, N_{surf} is the number of molecules bound to the enhancing silver substrate, I_{NRS} is the normal Raman intensity, and N_{vol} is the number of molecules in the excitation volume [18]. In the case of ε-Si where we use thin ε-Si layers as opposed to actual molecules we can model our sample by changing

N_{surf} to the number of ε-Si atoms affected by the total evanescent near-field emitted from the NP layer across the sampling area (equal to the 4 µm laser spot size) as well as changing N_{vol} to the number of ε-Si atoms in the excitation volume – where the actual probe volume would include attenuation of the 488 nm Raman laser source due to silver absorption. In this model, we are assuming that the Ag NP thin film is essentially trapping the incident light and amplifying it in the near-field. Any ε-Si in close proximity to these near-field interactions will have a greater probability of Raman scattering which would in turn increase the ε-Si Raman signal.

The total depth to which the ε-Si atoms are affected by the total evanescent near-field omitted from the NP layer can be estimated to be 5 nm from published data [19]. Although we cannot directly calculate this value, careful literature scrutiny shows this to be a good estimate. In order to calculate the number of ε-Si atoms which are affected by this field, values for the SiGe lattice constants must first be calculated. This is found via equation 4.6 where *x* is the Ge concentration [20].

$$aSi_{1-x}Ge_x = 0.5431 + 0.01992x + 0.0002733\,x^2\;(nm) \qquad (4.6)$$

As silicon has a face-centered diamond cubic crystal structure with 8 atoms per unit cell [21] the total number of atoms per m^3 can be directly calculated for each sample. This allows the value of N_{surf} and N_{vol} to be calculated. I_{SERS} and I_{NRS} can be taken from measured Raman data spectra. These values are highlighted in table 4.2.

As can be seen from table 4.2 the calculated EFs are extremely small when compared to such reported values as 10^6 - 10^9 [13]. This is most likely due to the difference in modelling parameters (i.e. atoms as opposed to molecules) as well as the fact that only a

variable	9 nm	17.5 nm	42 nm
$aSi_{1-x}Ge_x$	0.5491 nm	0.5471 nm	0.5471 nm
N_{surf}	3.795 x 10^8 atoms	3.836 x 10^8 atoms	3.836 x 10^8 atoms
N_{vol}	6.831 x 10^8 atoms	1.343 x 10^9 atoms	3.223 x 10^9 atoms
I_{NRS}	968.02	1796.91	2545.87
I_{SERS}	5270.01	3192.29	4578.75
EF	**9.79**	**6.22**	**15.1**

Table 4.2. Values for enhancement factor calculations.

small section of the available near-field is actually interacting with the ε-Si layers. Also, as there will be no ε-Si in close proximity to any so-called ‘SERS hot-spots’ (which are primarily confined to nm gaps between adjacent NPs located on the plane parallel to the ε-Si surface) the near-field interactions with the ε-Si surface will be significantly reduced. These figures do however serve as a figure of qualitative relative merit for each SERS enhancement, and is the first time, known to this author, that an attempt has actually been made to model ε-Si SERS enhancement factors.

4.5 Plasmonic Considerations

As previously discussed in section 1.4 there are certain requirements in order for external radiation to couple to surface-plasmon polaritons (SPP). These requirements state that SPP modes will only propagate along a metal-dielectric interface if the light is p-polarised (electric field normal to the interface); the metal permittivity (ε_2) must satisfy the conditions where $\varepsilon_2 < 0$ and $|\epsilon_2| > \epsilon_1$ (where ϵ_1 is the permittivity of air and ε_2 is the permittivity of the NPs); and the momentum mismatch between SPP and the excitation photon must be overcome through the use of gratings and surface roughness via Umklapp scattering.

Hence, to verify that ε-Si SERS enhancements were plasmonic in origin and not just from general signal attenuations from the absorption coefficients of silver (which would effectively reduce the laser penetration depth and increase the amount of ε-Si present in the signal) we tested the 9 nm thick ε-Si sample using both p-polarised and s-polarised Raman filters, and SEM. These results indeed confirm the plasmonic origin of ε-Si enhancements via SERS.

Figure 4.7 compares both normal and SERS enhanced 9 nm thick ε-Si using p-polarised light (includes normal, un-polarised 9 nm ε-Si spectrum). Although a definite SERS enhancement is visible at approximately 508.39 ± 1.02 cm^{-1} it is still nowhere near the maximum enhancement shown previously in figure 4.4 which had a ε-Si peak intensity greater than 5000 counts. This is most probably due to a reduction in laser intensity from use of polarisation filters, as well as a change in sampling point.

In figure 4.8 we can definitely see that no SERS enhancement is observed at all for the use of s-polarised light. The Raman signal is attenuated across the whole bandwidth and only a small SiGe peak is barely visible. It does show however a finer resolution of the ε-Si peak before evaporation (under s-polarised light). Again, this is most likely due to laser power reduction which in turn would alter the silicon penetration depth with the ε-Si surface making up a larger percentage of the probed volume. What figure 4.7 and 4.8 confirm however is the plasmonic nature of the SERS enhancement as only the p-polarised light conditions show an enhanced ε-Si Raman signal.

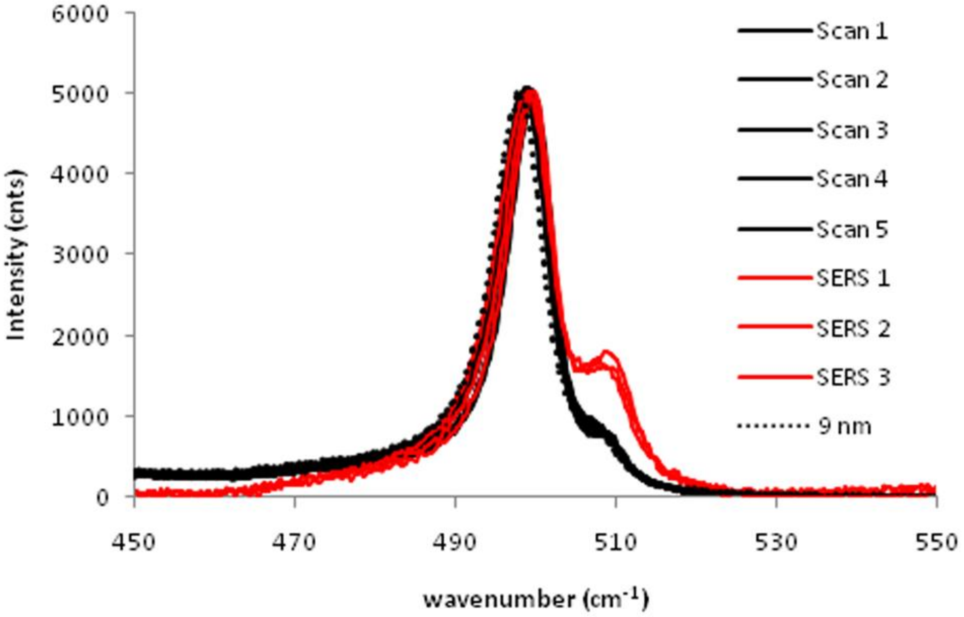

Figure 4.6: Raman spectra of 9 nm thick ε-Si using un-polarised light (9 nm), and p-polarised light (SERS 1 to 3 depict 9 nm ε-Si signal after evaporation, scan 1 to 5 depict normal signal before evaporation). Data represents a total of 300 scans (20 accumulations for each point, 5 points per sample, and three samples).

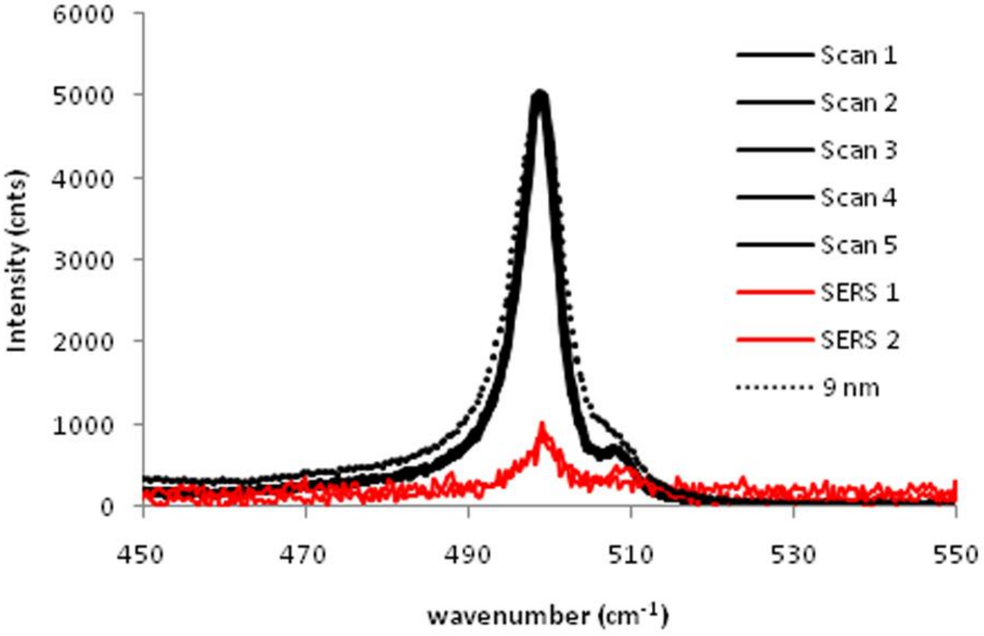

Figure 4.7: Raman spectra of 9 nm thick ε-Si using un-polarised light (9 nm), and s-polarised light (SERS 1 to 2 depict 9 nm ε-Si signal after evaporation, scan 1 to 5 depict normal signal before evaporation). Data represents a total of 300 scans (20 accumulations for each point, 5 points per sample, and three samples).

The sample was also investigated under SEM. All SEM measurements were taken on a Carl Zeiss EVO LS 15 with a scanning voltage of 17 kV at 5.5 mm working distance. These results are depicted in figure 4.9. Both figures clearly show a good, homogeneous coating of NPs across the 9 nm thick ε-Si sample. In the top figure it is easy to see the difference between the NP surface (left of the image) and the darker, flatter ε-Si surface (right of image). The bottom figure illustrates a larger area of NP coverage. Further analysis shows that these NPs vary in shape and size but remain within the dimensions of approximately 40 – 50 nm. The surface coverage and morphology is similar to results by Hayazawa *et al*. [22].

Finally, a UV-VIS spectrum was taken of the Ag thin film deposited onto a small glass slide (1 cm by 1 cm) located as close to the ε-Si sample as possible. As depicted in figure 4.10 there is clear evidence of a broad plasmon resonance peak located at ~ 540 nm. Although the morphology could not be investigated via means of SEM or atomic force microscopy, AFM (SEM cannot be used with untreated glass slides and AFM measurements caused the Ag thin film to be etched), we can assume a general match with the Ag thin films on ε-Si as they were very co-evaporated close together and are made roughly of the same material (Si versus SiO_2 although the ε-Si surface will in fact have a nm-thin coating of SiO_2 due to atmospheric surface oxidation).

On another note, as a final point of interest, it was found that prolonged exposure to Raman scans over a period of 42 minutes caused a general decrease in ε-Si SERS intensity. Figure 4.11 depicts ε-Si SERS enhancements as a function of scan time. As soon as a single scan had been completed (scan settings were 30 s for 20 accumulations) another scan was initiated straight away. As can be seen in figure 4.11 as the total scan time progressed the SERS enhancements dropped quite substantially until the SERS

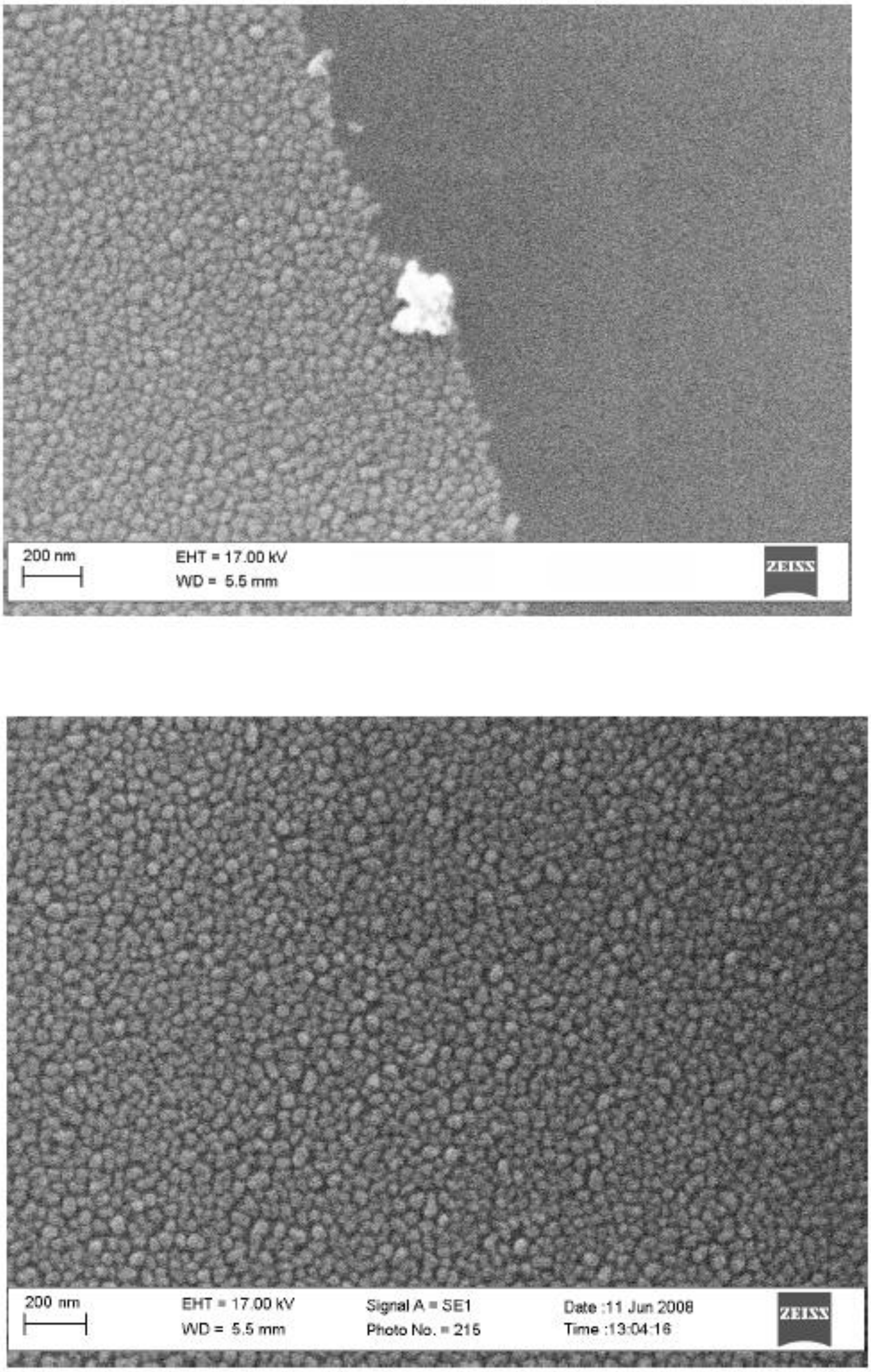

Figure 4.8: SEM micrographs of Ag nanoparticle growth on 9 nm thick ε-Si via direct thermal evaporation. The SEM at the top depicts the Ag NPs (left) and bare ε-Si (right) interface. The image at the bottom highlights the uniformity of the NP coating, made up of Ag NPs approximately 40 - 50 nm in width.

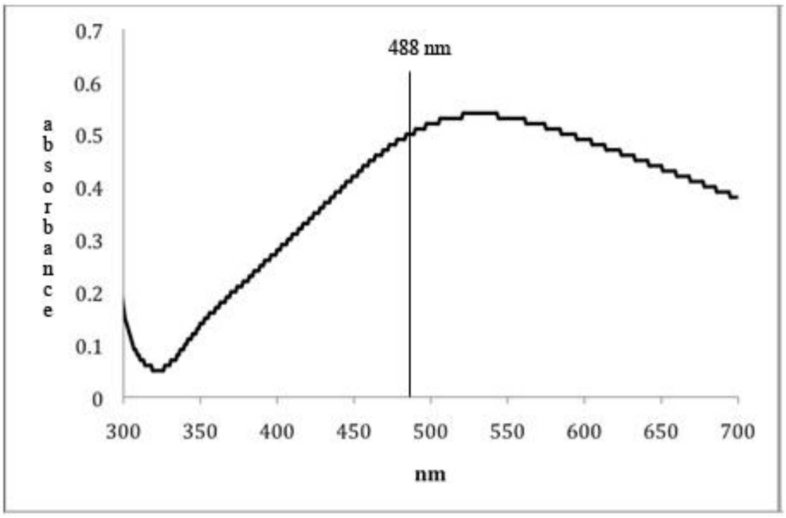

Figure 4.9. UV-VIS data for Ag NPs on glass slide (co-evaporated simultaneously with 17.5 nm thick ε-Si sample).

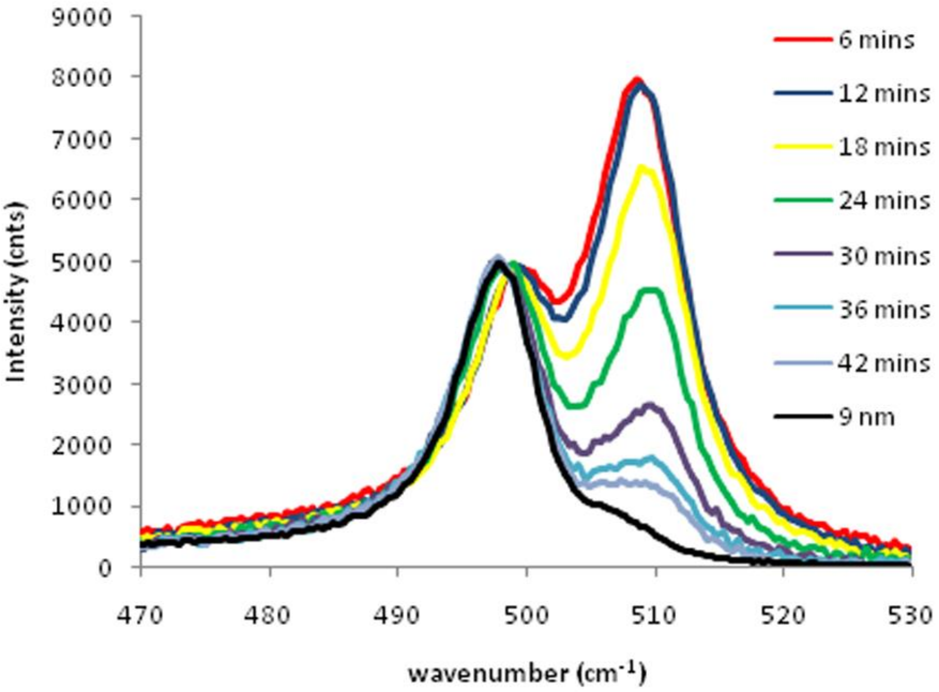

Figure 4.10: μ-Raman spectroscopy data for 9 nm ε-Si sample for multiple scans, on the same spot, across a 60 minute time interval. Data represents a total of 300 scans (20 accumulations for each point, 5 points per sample, and three runs).

intensity was just above that of a normal 9 nm ε-Si sample. A general red-shift of the Si-Ge peak is also evident where the red-shift seems dependent on the total scan time. The SiGe is first located at approximately 498.94 cm^{-1} for a scan time of 6 minutes, then left-shifts a total of 1.20 cm^{-1} to a new SiGe position of 497.74 cm^{-1} for a scan time of 42 minutes. It is thought that this shifting and lowering of ε-Si SERS enhancement could be due to plasmonic NP heating as both gold and silver NPs have been shown to be photonically heated for applications such as cancer-cell destruction via cellular hyperthermia [23].

4.6 Conclusions

The surface plasmon polariton response of Ag thin films deposited by means of a direct thermal evaporation technique was utilised for the SERS enhancement of ε-Si samples of thickness 9, 17.5, and 42 nm using a 488 nm Raman excitation laser. Although clear enhancements were visible, it is though that slight peak position variations from point-to-point are mainly the result of systematic limitations stemming from uneven focal planes, as well as Ag thin film thickness variations. It is also thought that intensity variations from point-to-point are also the result non-uniform Ag deposition and nm-thin SiO_2 surface layers caused from atmospheric surface oxidation of the ε-Si layer. By examining the morphological and optical properties of the Ag thin-films via SEM, and UV-VIS it is suggested that these enhancements are plasmonic in origin – causing the incident light field to be confined to the Ag thin films, enhancing the ε-Si Raman scattering within an estimated proximity of < 5 nm. Also, the use of s-type and p-type polarisation filters again confirmed a plasmonic origin as ε-Si SERS effects were only visible for p-polarised light, which was to be expected from theoretical considerations given in section 1.4 involving optical excitation of surface plasmons.

An attempt to quantify the enhancement factor using a modified enhancement factor equation given in previous work was also given. Even though these values were significantly smaller than that published in the literature, a set of causes was given to explain these attenuations and are most likely the result of non-interactions with SERS hotspots. It should also be highlighted that prolonged Raman characterisation exposure results in a gradual attenuation of the ε-Si SERS signal. We believe this to be due to excessive heating of the Ag thin film which may cause morphological variations and possible leaching of Ag atoms into the ε-Si structure. Future work should be spent trying to examine the extent and destructive nature of this effect, possibly via a combination of SEM and secondary ion mass spectroscopy.

Although this chapter clearly demonstrates that Ag thin films *can* be used as an effective SERS probe for ε-Si Raman enhancement, another alternative technique is highly sought after as direct thermal evaporation, although being a relatively cheap method, has significant limitations such as repeatability, pressure fluctuations, unstable current, and hardware size. Also, another technique which is more ‘portable’ and easy to setup would be highly desirable within the semiconductor industry.

4.7 References:

[1.a] C. Himcinschi, I. Radu, R. Singh, W. Erfurth, A.P. Milenin, M. Reiche, S.H. Christiansen, U. Gösele, *Materials Science and Engineering B* **2006**, 135, 184.

[1.b] W. M. Chen, P. J. McNally, G. D. M. Dilliway, J. Bonar, T. Tuomi, A. F. W. Willoughby, *J. Mater. Sci.: Mater. in Elec.* **2003**, 14, 455.

[1.c] P. Dobrosz, S. J. Bull, S. H. Olsen, and A. G. O'Neill, *Surface & Coatings Technology*, **2005**, 200, 1755.

[1.d] N. Hayazawa, M. Motohashi, Y. Saito, S. Kawata, *Appl. Phys. Letts*. **2005**, 86, 263114.

[1.e] Evans Analytical Group "AN 395, Semiconductor stress measurements by Raman spectroscopy", (2007), http://www.eaglabs.com/files/appnotes/AN395.pdf, last accessed **24/05/2010**.

[2] W. M. Chen, P. J. McNally, G. D. M. Dilliway, J. Bonar, T. Tuomi and A. F. W. Willoughby, *Journal of Materials Science: Materials in Electronics* **2003**, 14, 455.

[3] S. Nakashima, T. Mitani, M. Ninomiya, K. Matsumoto, *J. Appl. Phys*. **2006**, 99, 053512.

[4] P. Dobrosz, S. J. Bull, S. H. Olsen, A.G. O'Neill, *Surface & coatings technology* **2005**, 200, 1755.

[5] C. Himcinschi, I. Radu, R. Singh, W. Erfurth, A.P. Milenin, M. Reiche, S. H. Christiansen, U. Gösele, *Materials science and engineering B*, **2006**, 135, 184.

[6] J. McCarthy, T. S. Perova, R. A. Moore, S. Bhattacharya, H. Gamble B. M. Armstrong, *Scanning* **2004**, 26, 235.

[7] K. Horan, A. Lankinen, L. O'Reilly, N.S. Bennett, P. J. McNally, B. J. Sealy, N. E. B. Cowern, T.O. Tuomi, *Materials Science and Engineering: B* **2008**, 154, 118.

[8] Ingrid de Wolf, *Semicond. Sci. Technol*. **1996**, 11, 139.

[9] Z. Jian, Z. Xiang, W. Yongchang, *Microelectronic Engineering* **2005**, 77, 58.

[10] H. Watanabe, Y. Ishida, N. Hayazawa, Y. Inouye, S. Kawata, *Physical Review B* **2004**, 69, 155418.

[11] M. A. LourençO, D. J. Gardiner, V. Gouvernayre, M. Bowden, J. Hedley, D. Wood *J. Mater. Sci. Letts*. **2000**, 19, 771.

[12] K. F. Dombrowski, PhD Thesis "*Micro-Raman Investigation of Mechanical Stress in Si Device Structures ad Phonons in SiGe*", **2000**.

[13] P. L. Stiles, J. A. Dieringer, N. C. Shah, R. P. Van Duyne, *Annu. Rev. Anal. Chem*. **2008**, 601, 26.

[14] B. J. Kennedy, S. Spaeth, M. Dickey, K. T. Carron, *J. Phys. Chem. B* **1999**, 103, 3640.

[15] E. C. Le Ru, E. Blackie, M. Meyer, P. G. Etchegoin, *J. Phys. Chem. C* **2007**, 111, 13794.

[16] M. Fleischmann, P. J. Hendra, A. McQuillan, *J. Chem. Phys. Lett.* **1974**, 26, 163.

[17] M. G. Albrecht, J. A. Creighton, *J. Am. Chem*. **1977**, 99, 5215.

[18] A. D. McFarland, M. A. Young, J. A. Dieringer, R. P. van Duyne, *J. Phys. Chem. B* **2005**, 109, 22, 11279.

[19] A. Ogura, K. Yamasaki, D. Kosemura, S. Tanaka, I. Chiba, R. Shimidzu1, *J. Journal Appl. Phys*. **2006**, 45, 4B, 3007.

[20] D. J. Paul, *Semicond. Sci. Tech.* **2004**, 19, R75–R108.

[21] W. C. O'Mara, *Handbook of Semiconductor Science Technology*, William Andrew Inc, p.349 – 352, **2008**.

[22] N. Hayazawa, M. Motohashi, Y. Saito, S. Kawata, *Appl. Phys. Letts*. **2005**, 86, 263114.

[23] L. R. Hirsch, R. L. Stafford, *P. Natl. Acad*. Sci. USA, **2003**, 100, 13549.

Chapter 5

Sol-SERS (Chemical Synthesis)

5.1 Introduction & Aims

As previously discussed in chapter 1 ε-Si engineering can be incorporated into transistor fabrication processes to enhance transistor operating performances such as increased operating speed and reduced power consumption. In order to effectively characterise these ε-Si layers, grown on SiGe virtual substrates, a variety of techniques and processes have been investigated. None however possess the ability to analyse both ε-Si and SiGe peaks, *simultaneously* on a sub-µm length scale, using a completely non-destructive approach. Although micro-Raman studies have shown excellent results, adhering to the requirements just stated, so far only expensive UV laser sources with their inherent shallow penetration depths have been capable of probing the nm-thin ε-Si epilayers [1a, 1.b]. Larger wavelength sources such as 514.5 nm propagate deep into the bulk SiGe substrate and overshadow the relatively weak ε-Si signal (software deconvolution and destructive etching techniques have been used to determine ε-Si values using these excitation sources [1.c]). These limitations provide good reasons for the use of SERS enhancements (discussed in section 1.3) such as those recently documented by Hayazawa *et al*. [1.d] which effectively confine light to the upper layer of the ε-Si and increase the probability and intensity of Raman scattering from the ε-Si optical phonons.

In the previous chapter, the direct thermal evaporation technique previously described in section 2.1 was utilized to deposit and grow uniform Ag thin films on top of ε-Si layers of thickness 9, 17.5, and 42 nm. Although it was shown that this method could in fact produce reasonable ε-Si SERS signals, due to systematic limitations such as repeatability problems, pressure fluctuations, and unstable current etc., another more ‘portable’ technique was sought.

As already discussed in section 2.4 Ag NPs can be synthesised in solution via the so called polyol process which involves heating a mixture of silver nitrate ($AgNO_3$) and poly(vinylpyrrolidone (PVP) in a hot, ethylene glycol solution with trace amounts of sodium disulfide (Na_2S). By changing the ratio of $AgNO_3$ to PVP as well as the reaction time and temperature a variety of NP morphologies can be created where although a cubic morphology was preferred only general spherical morphologies were realised (as will be seen from SEM images).

The ability for these Ag NPs (directly deposited onto the ε-Si and allowed to dry at room temperature) to act as effective SERS probes, offering the simultaneous peak determination of both ε-Si and SiGe peaks, was investigated by means of a micro-Raman system operating with a 488 nm excitation source. Commercially available citrate capped Ag NPs were also tested in comparison.

All Ag NPs were subsequently analysed via UV-VIS and SEM instruments (discussed in sections 3.3 and 3.5, respectively) to analyse the plasmonic response of these Ag NPs which would help indicate the necessary surface roughness features and surface plasmon polariton absorption profiles needed for ε-Si SERS effects to take place – as discussed in section 1.4. Post measurement mathematical strain determination then followed.

Specific aims relevant to this chapter are as follows:

1) Can PVP and citrate-capped Ag NPs deposited onto ε-Si substrates of various thicknesses be successfully utilised for ε-Si SERS enhancements?
2) If SERS enhancements are visible, to what extent does size and distribution contribute to the intensity and spectral position of the observed ε-Si SERS peaks.
3) Can strain calculations be used to determine strain values from sample-to-sample?
4) Can a relative mathematical enhancement factor model be derived to assess enhancement factors from sample-to-sample?
5) What limitations does this technique possess?

5.2 Sample Preparation

Selected Ag NP samples synthesised via the polyol process were used and tested on 9, 17.5, and 42 nm thick ε-Si on SiGe virtual substrates for SERS analysis and characterised using µ-Raman, SEM, and UV-VIS. In addition Ag NPs of diameters 20 ± 5 nm, 40 ± 5 nm, 60 ± 5 nm, and 80 ± 7 nm were purchased from Ted Pella, Inc., (Redding, USA) and subjected to the same procedures. These samples, synthesised via proprietary citrate reduction techniques [1], are shown in figure 5.1.

For the polyol process, four samples were chosen for ε-Si SERS analysis (figure 5.2). These samples vary in size and shape with some being fairly monodisperse whilst others displayed a blended range of Ag morphologies such as cubic, triangular, rod-like and octahedral (according to SEM micrographs). Although great care was taken in trying to

Figure 5.1: Ted Pella industrial samples 1 to 4 (reported diameters are 20 nm, 40 nm, 60 nm, and 80 nm) suspended in water with trace amounts of citrate. Concentration was reported to be ~ 20 mg/L from supplier.

Figure 5.2: Polyol samples 5 to 8 (left to right, respectively) suspended in HPLC water. Concentration is estimated to be ~80 – 110 mg/L.

achieve highly monodisperse cubic NPs the samples used represent the best achieved.

For deposition onto ε-Si substrates a small volume (approx 10 µl) was deposited using standard micro-pipette techniques and allowed to dry at room temperature. A bronze-like metallic thin film was observed on the substrates after the water had evaporated. These same deposition techniques were applied using the Ted Pella, Inc. industrial samples. If a greater surface coverage was needed for characterisation more solution was added to the substrate and allowed to dry.

Due to the high costs of the ε-Si samples all measurements were first performed on a 17.5 nm thick ε-Si (17.5 nm ε-Si on a 20 % Ge virtual substrate) sample taken from a 150 mm diameter, p-Si (100) wafer. This meant that potentially hundreds of tests could be carried out initially on extremely small 17.5 nm thick ε-Si samples (0.8 cm by 0.8 cm) until the Sol-SERS procedure had been optimised, after which measurements could then be taken on the 9 nm and 42 nm thick ε-Si samples which were extremely limited in number. Before the µ-Raman SERS results are shown SEM, and UV-VIS characterisation measurements are discussed to understand how the solutions compare to each other.

Structural properties were characterised via SEM and UV-VIS spectroscopy. All SEM measurements were taken on the following systems: a Carl Zeiss EVO® LS 15 operating at 17 kV with a 5.5 mm working distance, a FEI Quanta 400 ESEM operating at 20 kV with a working distance of 9.3 mm or a Hitachi Ultra-high Resolution SEM S-550 operating at 20kV at a working distance of 0.7 to 0.8 mm. SEM particle counting measurements were taken via the SEM analysis software.

UV-VIS measurements were taken on an Agilent 8435 UV-VIS spectrometer across the wavelength range 200 nm to 1800 nm, 1 nm increment, with an acquisition time of 20 s using a 5 ml quartz cuvette. As the polyol samples were extremely reflective, deionised water was added to a small volume of the sample until the sample became more diluted and transparent – allowing a successful UV-VIS spectrum to be taken.

5.3 SEM & UV-VIS results

Figures 5.3 to 5.6 are SEM images of Ted Pella samples comprised of nominally 20 nm, 40 nm, 60 nm, and 80 nm diameter Ag NPs, respectively, taken on the JEOL ESEM.

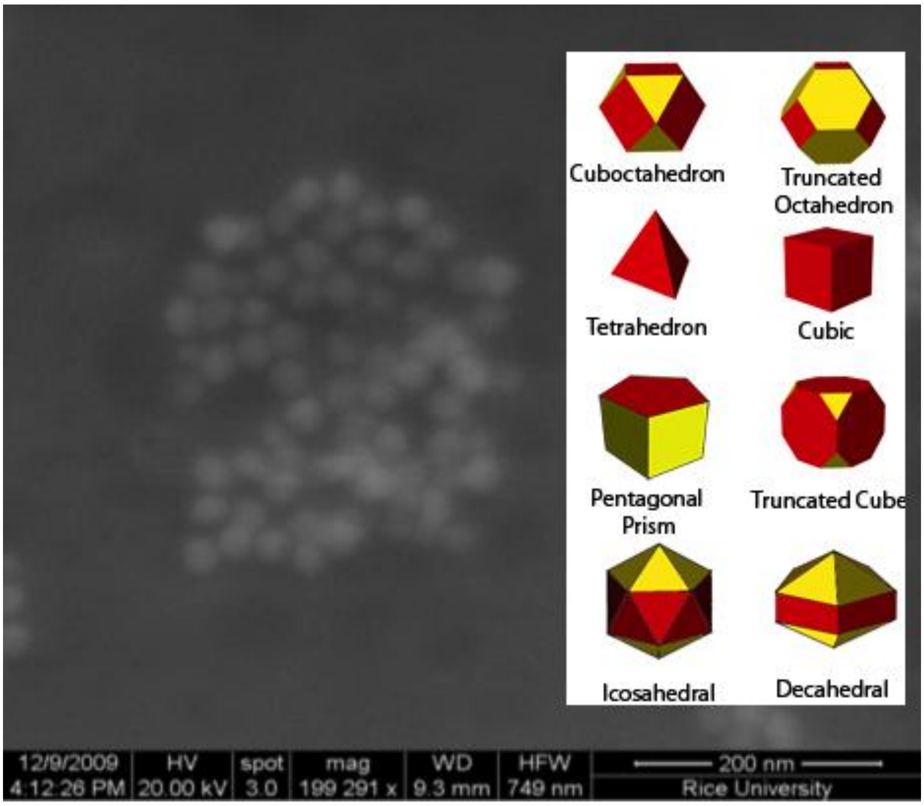

Figure 5.3: SEM (JEOL) micrograph of sample 1 (Ted Pella, 20 nm). Operating parameters & scale bar shown. Geometric shapes of most common Ag NP formations are also shown (right).

Using this SEM, imaging of 20 nm Ag NPs is just about possible – reaching the resolution limits of the JEOL SEM – and we can see fairly mono-disperse NPs covering the SEM sample holder. Although only one image is shown (for each sample) several images were taken so that an accurate measurement of average NP size and standard deviation could be determined.

From SEM image analysis shown in figure 5.3, sample 1 (20 nm) contained NPs of average size 26 ± 4 nm. From NP growth kinetics discussed in section 2 the main morphology available via chemical reduction techniques are either cuboctahedron, truncated cube, and tetrahedron single crystals or decahedral, icosahedral, and quasi-spherical multiple twinned particles (MTPs). From analysis of SEM images for sample 1 it is difficult to confirm exactly what structural characteristics are shown.

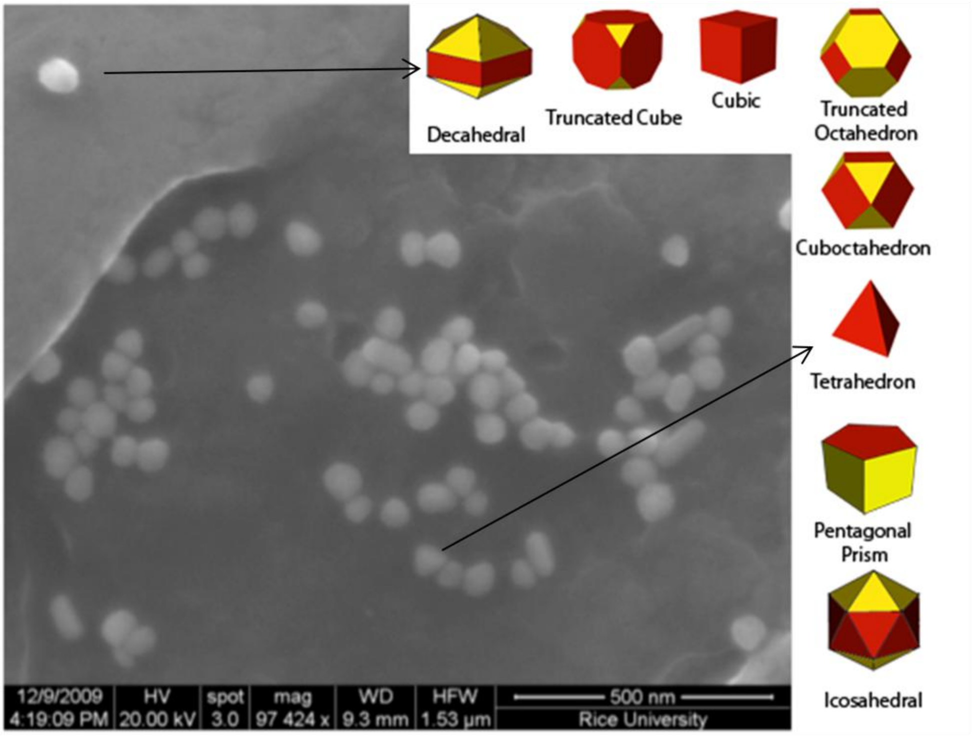

Figure 5.4: SEM (JEOL) micrograph of sample 2 (Ted Pella, 40 nm). Operating parameters & scale bar shown. Geometric shapes of most common Ag NP formations are also shown.

From analysis of SEM micrographs for sample 2 (40 nm) shown in figure 5.4 both truncated tetrahedrons and decahedral morphologies can be somewhat identified although the majority of the particles exhibit random structures which again, cannot easily be identified. There is also some evidence of small, ‘rod-like’ structures. Further SEM micrograph analysis gives an average NP diameter of approximately 49.6 ± 9 nm which is somewhat larger than 40 nm specified by Ted Pella, Inc.

From analysis of SEM micrographs for sample 3 (60 nm) shown in figure 5.5 we can clearly see some evidence of both decahedral and truncated octahedron structures although again it is too hard to distinguish strong morphological features, with the majority of the NPs exhibiting roughly spherical structures. The average particle size determined from particle counting software was found to be 76 ± 11 nm.

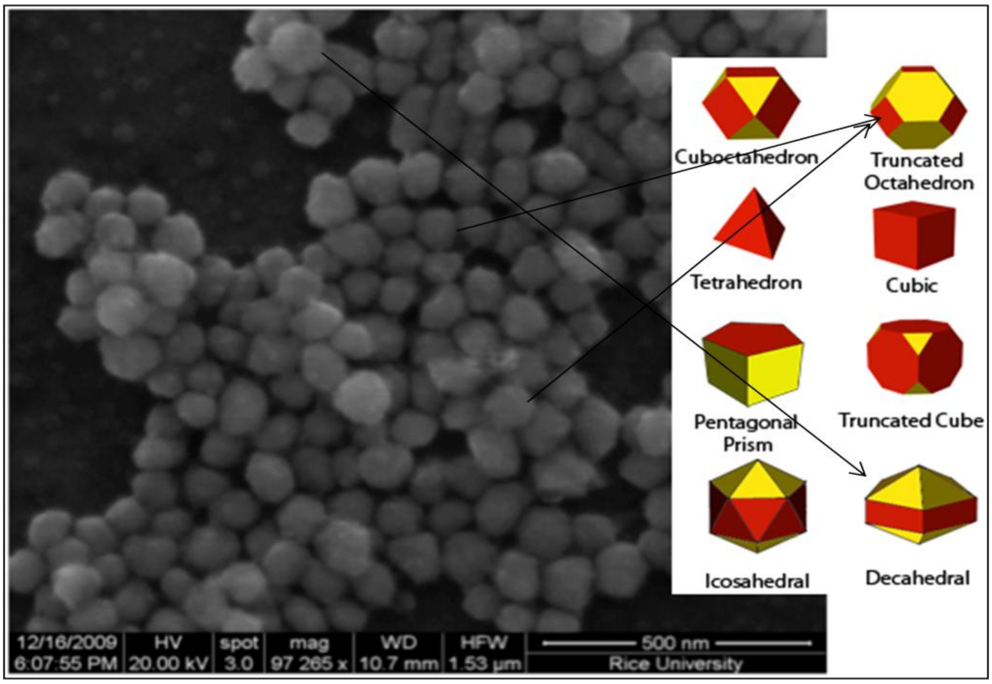

Figure 5.5: SEM (JEOL) micrograph of sample 3 (Ted Pella, 60 nm). Operating parameters & scale bar shown. Geometric shapes of most common Ag NP formations are also shown.

Finally, close examination of SEM micrographs for sample 4 (80 nm) shown in figure 5.6 reveals an average NP size range of 115 ± 20 nm which is much larger than the size quoted. There is also an ensemble of morphologies throughout the samples, with a lot of tetrahedron and triangular structures prevalent. There is also strong evidence of nano-rod formation with a large nano-rod of length approximately 1.4 µm clearly visible as well as smaller (~100 nm to 400 nm) nano-rods. In general, when examining NP morphologies throughout the Ted Pella, Inc., samples it is not sufficient to state that all samples have spherical morphologies or that one structure is prevalent. Each sample contains a blended range of morphologies which *roughly* look spherical in nature. The SEM characterisation does however give insight into the mean NP size and distribution which tend to deviate slightly (especially for 80 nm NPs) from the quoted size regime.

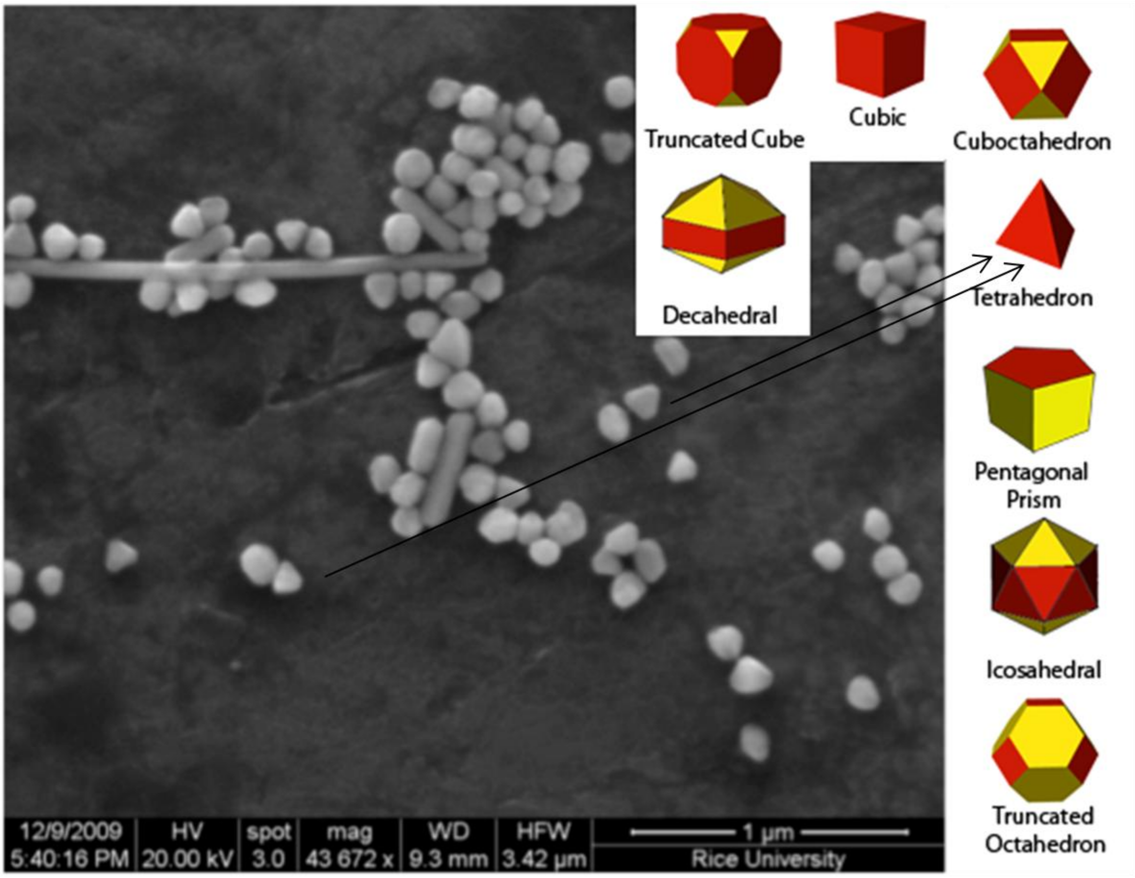

Figure 5.6: SEM (JEOL) micrograph of sample 4 (Ted Pella, 80 nm). Operating parameters & scale bar shown. Geometric shapes of most common Ag NP formations are also shown.

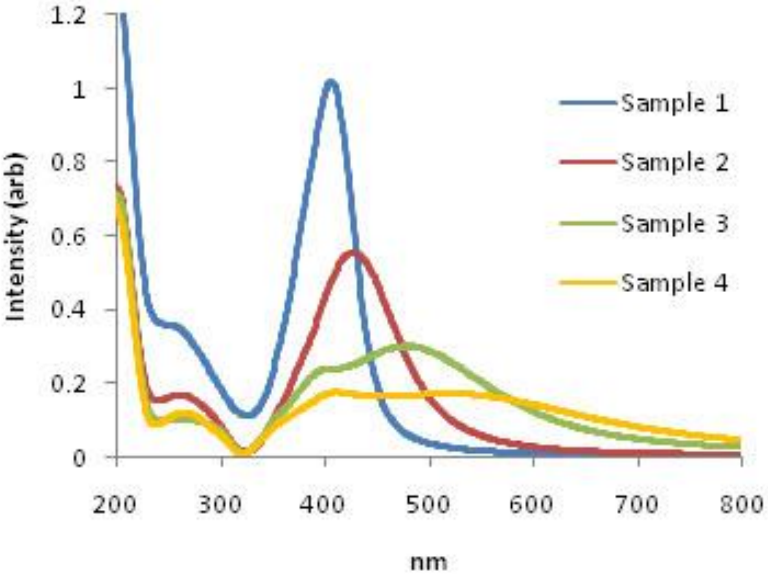

Figure 5.7: UV-VIS absorption spectra for samples 1 to 4 (Ted Pella silver NPs of diameter 26 ± 4 nm, 49.6 ± 9 nm, 76 ± 11 nm , and 115 ± 20 nm, respectively).

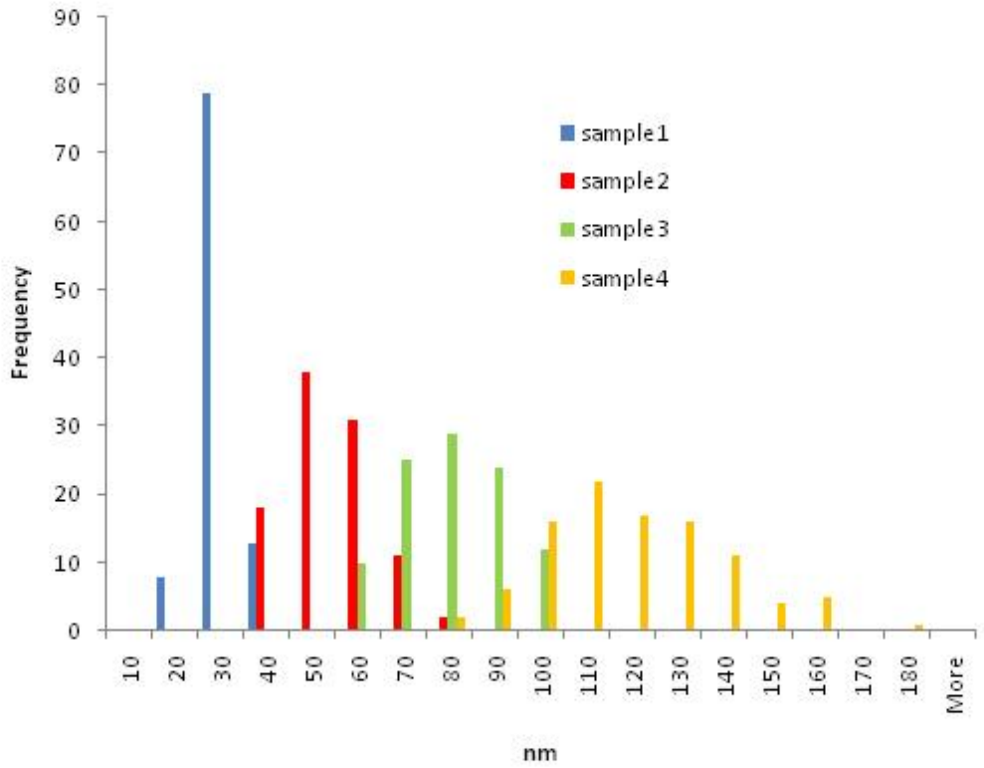

Figure 5.8: Histogram of particle sizes for samples 1 to 4.

The UV-VIS results and histogram profiles of the citrate-capped Ag NPs are shown in figures 5.7 and 5.8, respectively. It has been shown that small atoms, ions, and clusters of silver have characteristic absorption bands within the visible spectrum [4], highlighted in section 3.5. Using this information described earlier and from further analysis of figure 5.7 we can see that for all Ted Pella, Inc. samples, the small absorption peaks across the region of 250 nm to 300 nm are attributable to $4d^{10}5s^{1}$ - $4d^{9}5s^{1}5p^{1}$, $4d^{10}5s^{1}$ - $4d^{9}5s^{1}6p^{1}$, or $5s^{1}$ - $5p^{1}$ atomic resonance transitions in Ag^{0} [5-7]. A strong plasmon resonance peak is clearly observed for sample 1 and sample 2 located at approximately 406 nm and 427 respectively. From careful literature scrutiny it is though that both plasmon peaks stem from plasmon dipolar modes, with the slightly broader peak located at 427 nm resulting from an increase in particle size [8-12]. Samples 3 and 4 also display evidence of a red-shifted, broadened plasmon peak located at

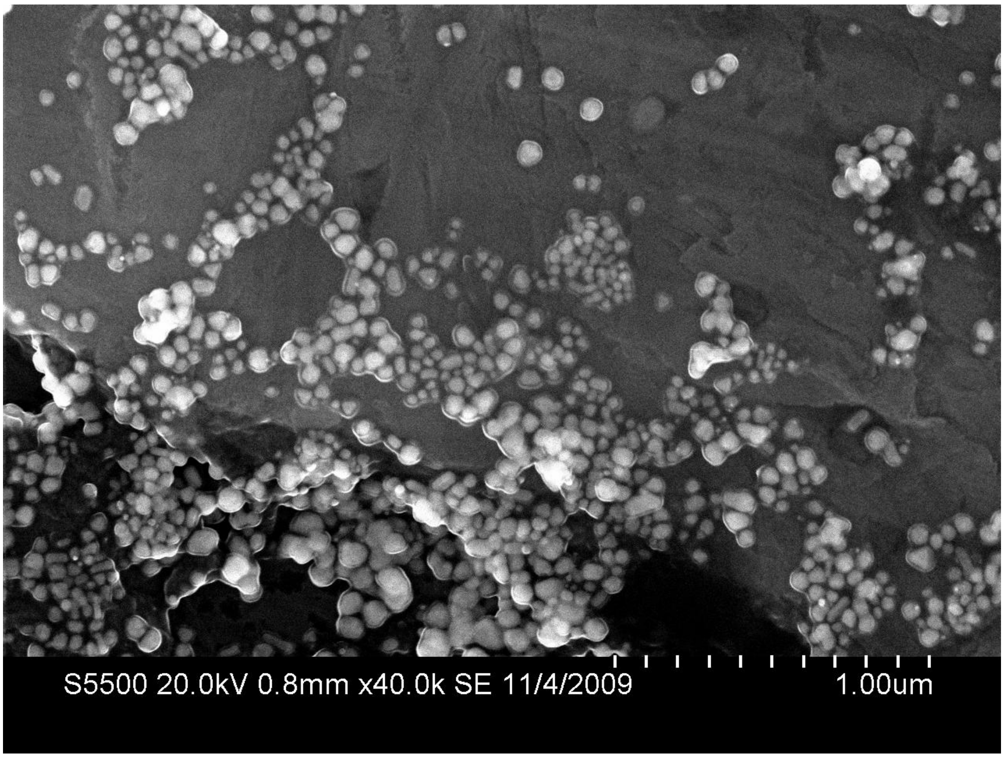

Figure 5.9: SEM (S-550) micrograph of sample 5 (polyol). Operating parameters & scale bar shown.

approximately 478 nm and 520 nm respectively as well as two small quadrupole modes located at approximately 404 nm and 412 nm, respectively. For wavelengths above 600 nm absorption is negligible due to an increase in scattering.

Using previously synthesised NPs via the polyol process (discussed in chapter 2) SEM analysis was found to give mean diameters of 33 ± 11 nm, 78 ± 19 nm, 80 ± 18 nm, and 147 ± 38 nm for samples 5 to 8, respectively. Figures 5.9 and 5.10 are SEM micrographs (using S-550 SEM) taken at 2 magnifications for polyol sample 5. After further analysis of samples 5 – 8, sample 5 was found to contain silver NPs of the smallest dimensions (33 ± 11 nm). The higher magnification image depicted in figure 5.10 shows the assortment of NP morphologies which include cubic, triangular, tetrahedronal, and truncated octahedron plus a variety of others not easily distinguishable. At this magnification we can also clearly see remnants of what is most

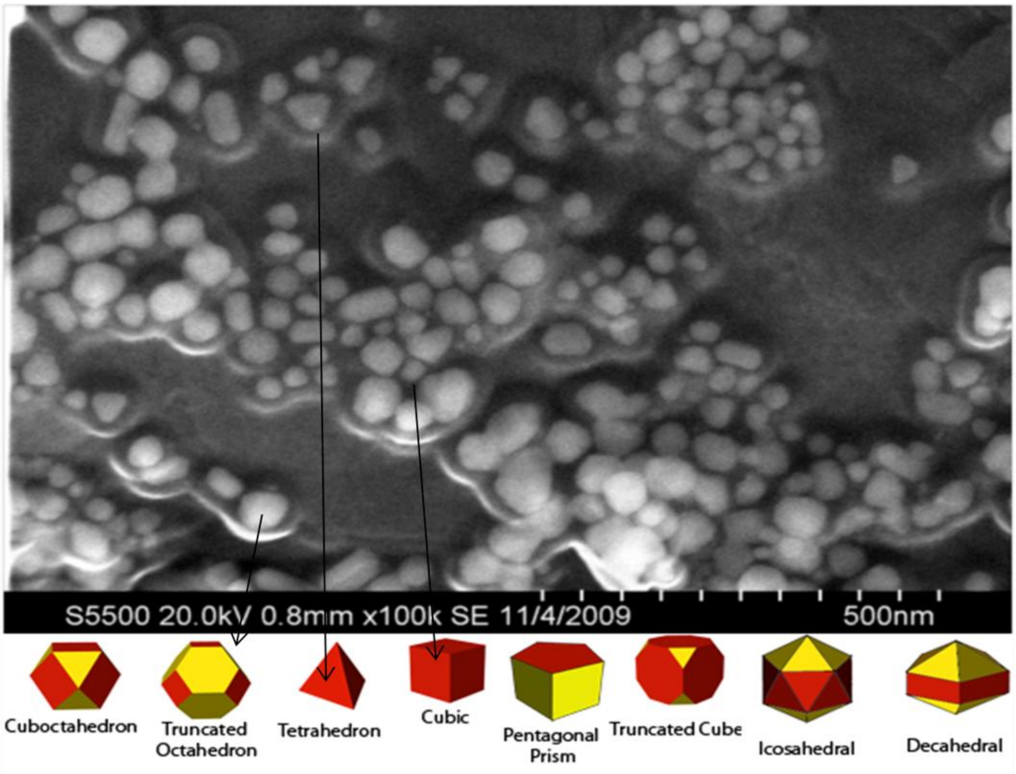

Figure 5.10. SEM (S-550) micrograph of sample 5 (polyol). Operating parameters & scale bar shown. Geometric shapes of most common Ag NP formations are also shown.

probably PVP or ethylene glycol that has not been evaporated during sample preparation. This is evident from the shiny, ‘liquid-like’ material covering the majority of the NPs – this can easily be removed however by an extra round of acetone and centrifugation.

Figures 5.11 and 5.12 depict SEM micrographs of sample 6 using both the Hitachi S-550 and Carl Zeiss SEM. The higher resolution power of the S-550 SEM is evident when comparing the two pictures as the NPs in figure 5.12 are more blurred. Particle counting software gives an average NP size of 78 ± 19 nm. Closer examination of NP morphology distribution again reveals a range of NP morphologies with no single shape being prevalent.

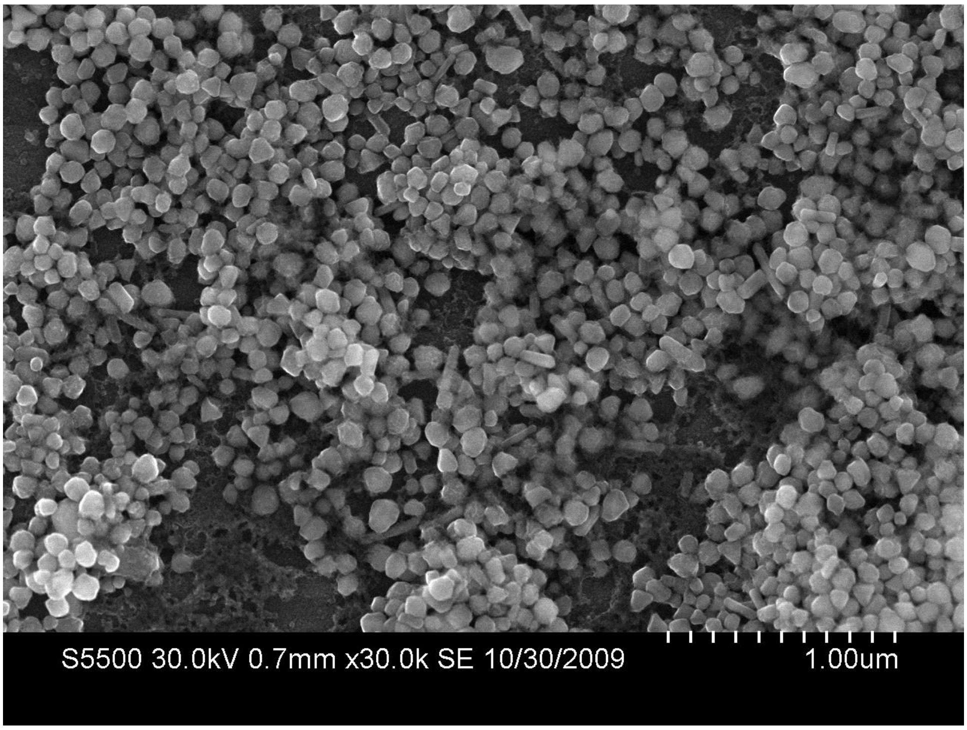

Figure 5.11. SEM (S-550) micrograph of sample 6 (polyol). Operating parameters & scale bar shown (1.00 µm scale bar, 100 nm per division).

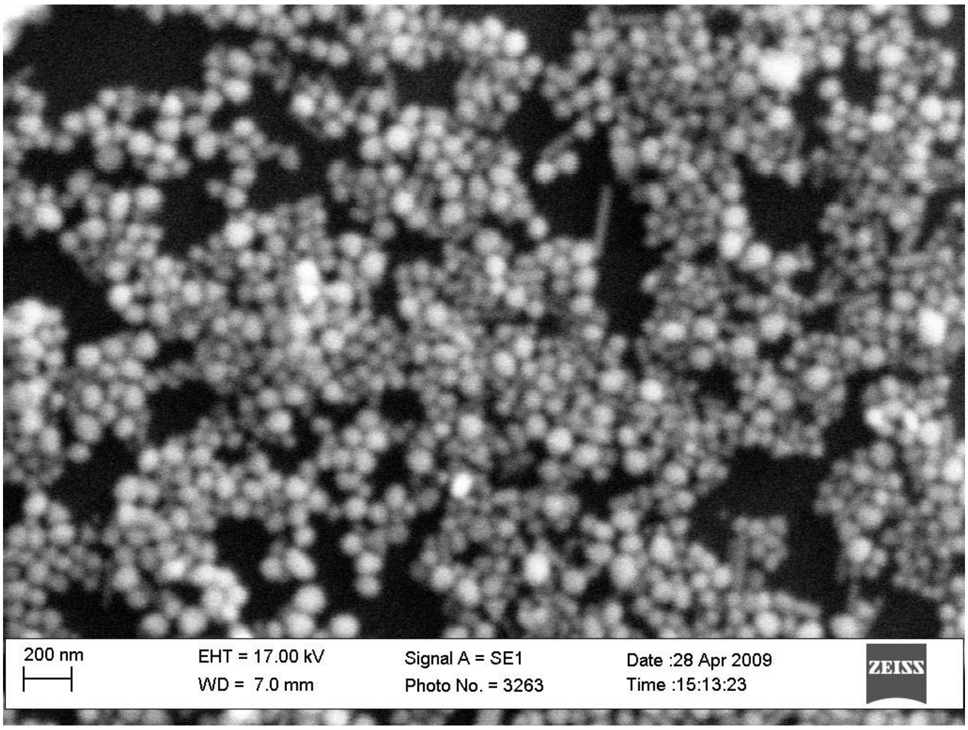

Figure 5.12. SEM (Zeiss) micrograph of sample 6 (polyol). Operating parameters & scale bar shown (200 nm).

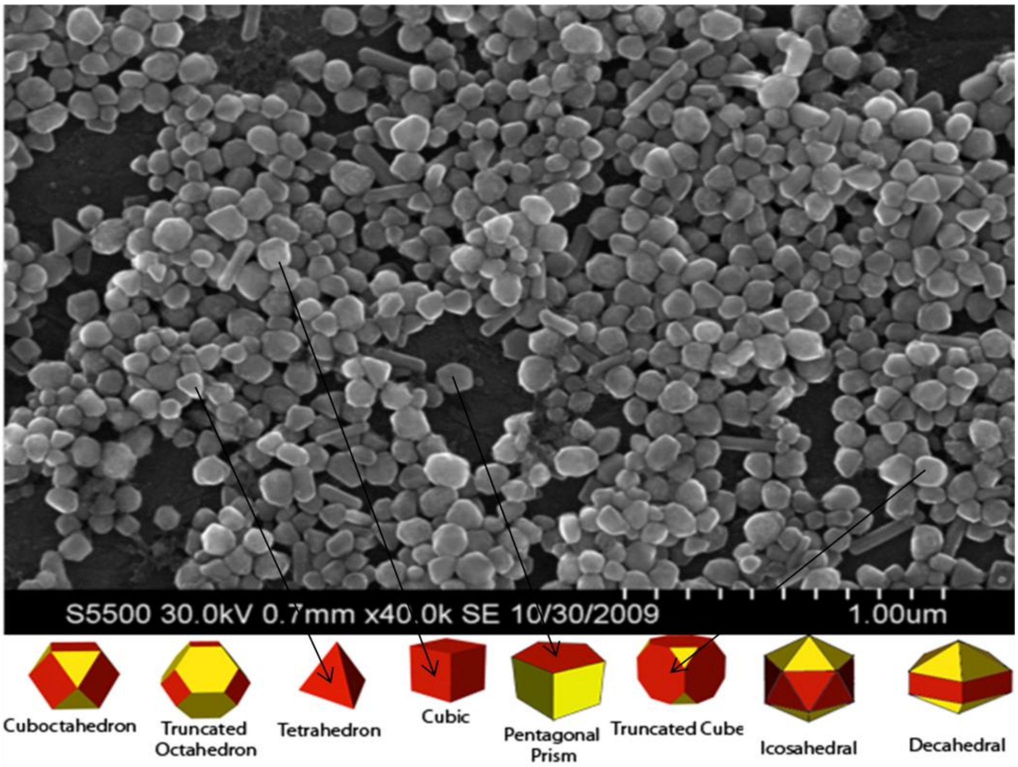

Figure 5.13. SEM (S-550) micrograph of sample 7 (polyol). Operating parameters & scale bar shown. Geometric shapes of most common Ag NP formations are also shown.

Figure 5.13 depicts an SEM (S-550) micrograph of sample 7 with an average NP size of 80 ± 18 nm, which is almost exactly that of sample 3 and 7. Morphological variations include cubic, tetrahedron, truncated cube and pentagonal prisms. Again, the overall sample structure is made of a mixture of non-defined morphologies. There are also some rod-like structures shown.

Finally, figure 5.14 illustrates an SEM micrograph of the largest polyol species, sample 8. These NPs have an average size of approximately 147 ± 38 nm and can be seen to be made up of truncated cubes and tetrahedrons including what looks like as decahedral and icosahedral structures – some with extended rod-like formation. What is interesting is the apparent ability for the NPs to seemingly 'self-assemble' into mosaic like patterns, reducing the free space available. This is similar to the literature [2] where pre-

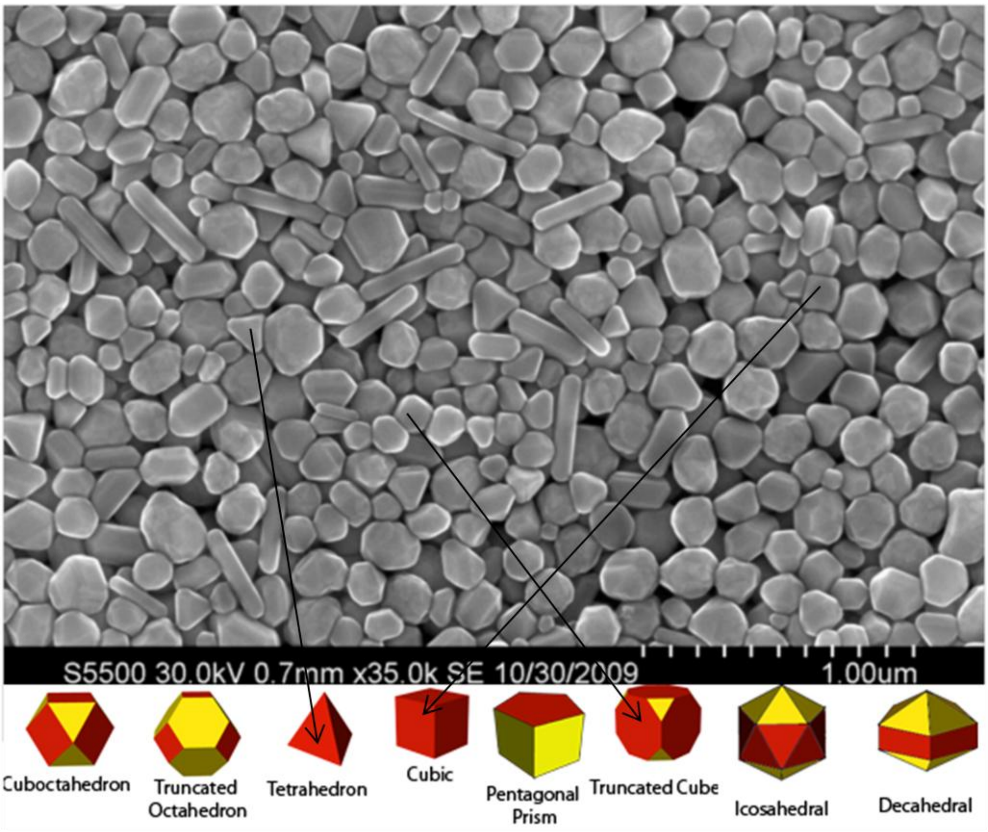

Figure 5.14. SEM (S-550) micrograph of sample 8 (polyol). Operating parameters & scale bar shown. Geometric shapes of most common Ag NP formations are also shown.

designed building blocks (e.g. molecules, nanocubes, etc.) spontaneously organize themselves into relatively stable structures (close to or at thermodynamic equilibrium state) through non-covalent interactions. Previous work has also shown the spontaneous, template-free organisation of silver NPs into dendritic, flower-like structures via aggregation of the NPs initiated in the liquid phase by diffusion limited aggregation [3].

The UV-VIS results and histogram profiles of the in-house synthesised, PVP-capped Ag NPs are shown in figures 5.15 and 5.6, respectively. Samples 5 to 7 all display small absorption peaks across the region of 250 nm to 300 nm, which are again attributed to $4d^{10}5s^1$ - $4d^95s^15p^1$, $4d^{10}5s^1$ - $4d^95s^16p^1$, or $5s^1$ - $5p^1$ atomic resonance transitions in Ag^0 [5-7]. However, there is a significant relative increase in absorption across this region

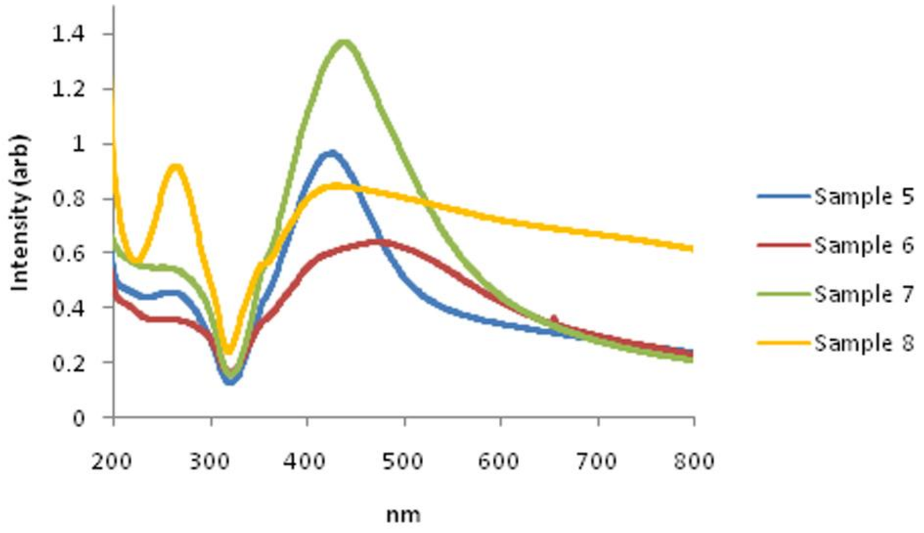

Figure 5.15: UV-VIS spectrum for samples 5 to 8 (polyol synthesised silver NPs of diameter 33 ± 11 nm, 78 ± 19 nm, 80 ± 18 nm, and 147 ± 38 nm respectively).

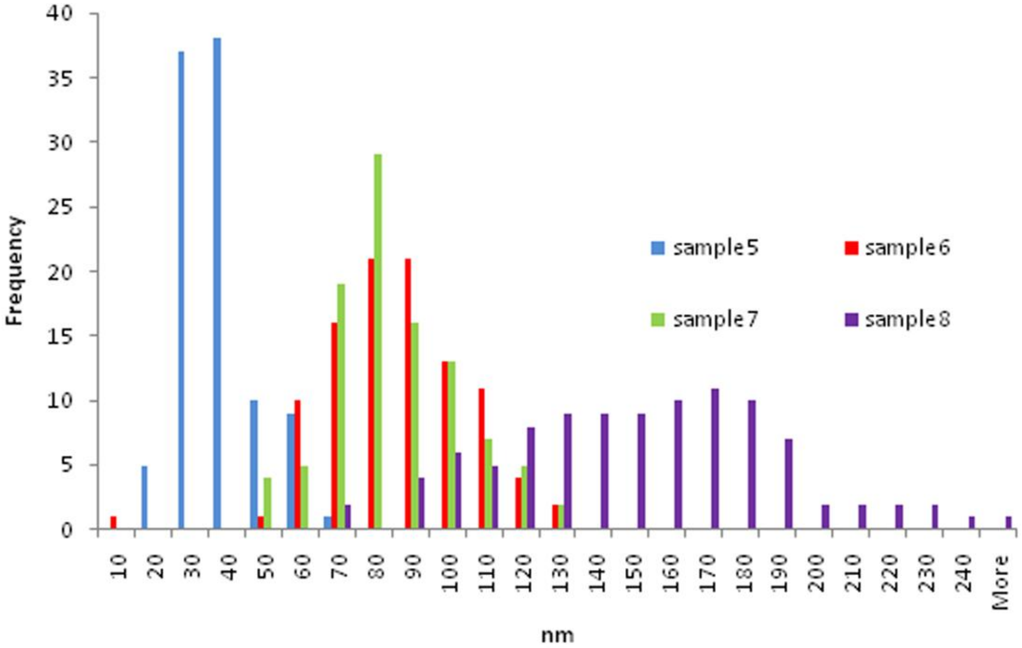

Figure 5.16: Histogram of particle sizes for samples 5 to 8.

for sample 8. Again, from the literature [8-12] it is thought that sample 5 displays a single dipolar peak at approximately 426 nm as well as a small quadrupole peak at approximately 360 nm which is different from quadrupole peaks shown for samples 3 and 4. Sample 7 is similar to sample 5 but has a larger and broader plasmon peak (439 nm) due to larger NPs. Sample 8 has an extremely broad plasmon peak located at approximately 425 nm and continues to have a high absorption factor across the full spectral range. There is also a large quadrupole plasmon mode located at approximately 360 nm, similar to samples 5 and 7. Sample 6 is of interest as there is evidence of a third peak located between the quadrupole (360 nm) and dipolar mode (472 nm), residing at approximately 410 nm. This new peak is most likely attributed to the out-of-plane dipolar resonance due to the assortment of NP morphologies, especially triangular [12, 13], as indicated by SEM images.

The evidence of higher energy quadrupole peaks compared to samples 3 and 4 is also evidence of the different morphology distributions throughout samples 5 to 8. The Ted Pella, Inc. samples are more regulated and contain a higher percentage of identical Ag NP morphologies (high mono-dispersion) when compared to the polyol samples, as well as a smaller deviation. This can also be confirmed by looking at the relative histogram charts, taken from SEM data analysis, associated with each sample. This can be seen in figures 5.8 and 5.16 for Ted Pella samples 1 to 4, and polyol synthesised samples 5 to 8, respectively.

In figure 5.8 it can clearly be seen that sample 1 (26 ± 4 nm) has the sharpest distribution profile with almost 80 % of its size distribution residing in the 20 to 30 nm region. Samples 2 to 4 (49.6 ± 9 nm, 76 ± 11 nm, and 115 ± 20 nm, respectively) generally have a broader profile which increases in width as the NP size increases. On the other hand, as demonstrated in figure 5.16, although sample 5 (33 ± 11 nm) has the sharpest profile for all the polyol samples, approximately 75 % of its size distribution is across the 20 to 40 nm region with the remainder across the 50 to 70 m region. This explains slight UV-VIS discrepancies between sample 1 and sample 5 where even though they have similar NP sizes (26 ± 4 nm, and 33 ± 11 nm, respectively) the larger distribution of particles for sample 5 causes a more broadened and red-shifted plasmon peak.

Finally, if samples 3, 6 and 7 are all comprised of same Ag NP morphologies their almost identical mean diameter (76 ± 11 nm, 78 ± 19 nm, 80 ± 18 nm) would result in almost identical UV-VIS absorption spectra. However, as can clearly be seen this is not the case. Samples 3 and 6 do however show similar UV-VIS profiles with major plasmon peaks located at 478 nm and 472 nm, respectively, (including quadrupole peaks located at 404 nm and 360 nm, respectively) but their corresponding histogram data demonstrates a generally broader size distribution for sample 6 which would explain the existence of a third out-of-plane dipolar peak located at ~ 410 nm as well as a shifting of the quadrupole peak. The case is slightly reversed when comparing samples 6 and 7, where although they display similar histogram distributions, their UV-VIS absorption spectra are completely different. Sample 7 displays a strong plasmon peak at approximately 439 nm (more reminiscent of the UV-VIS profile for smaller 20 nm to 40 nm Ted Pella, Inc. samples) while sample 6 displays both quadrupole and dipolar resonances as well as an out-of-plane resonance. Hence, this is a strong indication that NP *morphology* (i.e. cubic versus spherical, etc.) may be a key factor in determining plasmon resonance and could be concluded by comparing Ag NPs of different shapes with tighter mono-dispersion profiles – something which is outside the realm of this project.

To conclude SEM characterisation results, even though it is considerably difficult to define specific geometric morphologies and structural variations from sample-to-sample, the high-resolution SEM micrographs do however give an estimate at the mean NP size and standard deviation. This will become important when assessing any SERS enhancement factor relations, exhibited from sample to sample.

5.4 Micro-Raman SERS results

Raman measurements were performed on a Jobin Yvon LabRam HR800 µRS system with the setup previously described in chapter 4. Figure 5.17 depicts the Raman spectra for non-SERS 9, 17.5, and 42 nm thick ε-Si samples and includes a standard, non-strained silicon spectrum for reference. Peak positions are identical to that previously described in chapter 4.

A small droplet (~ 20 µl) of each Ag NP sample was applied to individual 17.5 nm ε-Si samples and allowed to dry a room temperature. This sample was then analysed via the micro-Raman optical microscope to find the area with the best Ag NP coverage. To determine so called SERS ‘hot-spots’ a technique was developed which performed a series of Raman xy maps so that certain areas could be examined more thoroughly. For each sample a 100 µm^2 area scan (50 points, 10 seconds at 30 accumulations) was first taken, mapped, then another 50 point scans was taken across a smaller area of 25 µm^2 where the highest SERS intensities were visible (figure. 5.18). This ultimately meant that the largest SERS enhancement across an area of 100 µm^2 could be found.

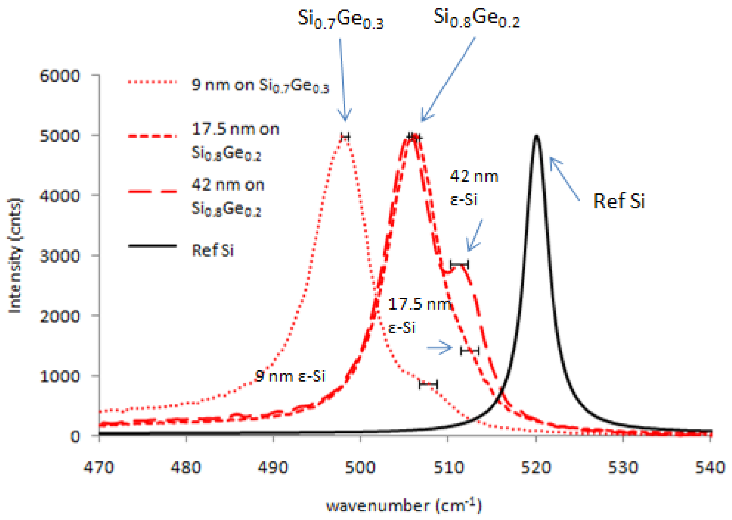

Figure. 5.17: Raman spectra for 9 nm, 17.5 nm, and 42 nm thick ε-Si samples. A reference non-ε-Si peak is also shown (black). Although ε-Si peaks can be seen at approximately 511.96 cm^{-1}for ε-Si of thickness 42 nm it is extremely difficult to locate accurate ε-Si peaks for ε-Si thickness 9 nm and 17.5 nm. Standard deviation bars are also shown for SiGe and ε-Si peaks.

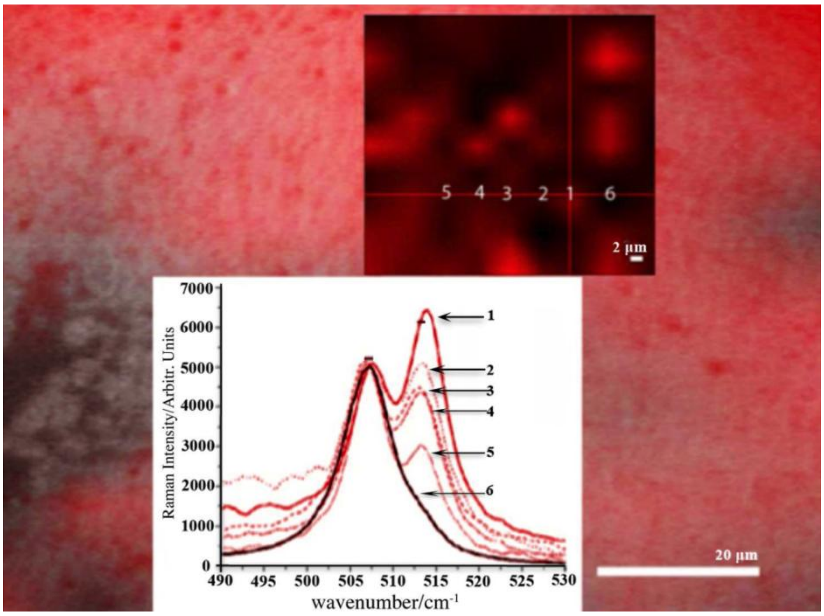

Fig. 5.18: Micro-Raman optical image of Ag NP coverage on 17.5 nm ε-Si (black-white image, 20 µm scale). Superimposed on top are areas of 17.5 nm SERS enhancements shown by varying red intensities. A smaller area was then scanned (top right hand corner, 2 µm scale) with SERS enhancements superimposed. Final Raman spectra of points 1 to 6 are shown in bottom right-hand spectrum. Point 1 is the largest SERS enhancement (thick red); point 6 is the non-SERS spectrum (black). SERS SiGe peak is located at 506.98 ± 0.33 cm^{-1} whilst the SERS ε-Si peaks are located at 513.33 ± 0.37 cm^{-1}. Standard deviation bars are also shown.

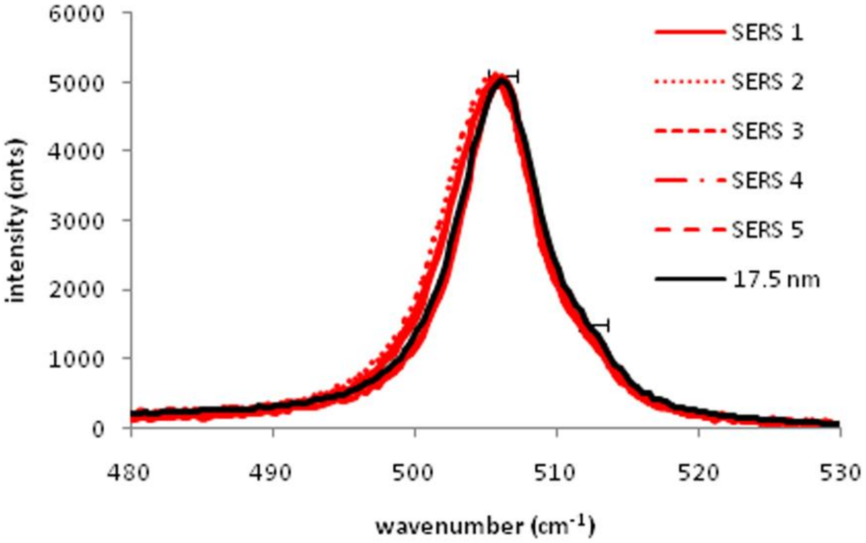

Figure 5.19: ε-Si SERS enhancements using sample 1 NPs of average size 26 ± 4 nm. SERS SiGe peak is located at 505.972 ± 0.29 cm^{-1}, whilst ε-Si peak is at 511.46 ± 0.19 cm^{-1}. Data represents a total of 90 scans (30 accumulations for each one of three experimental runs).

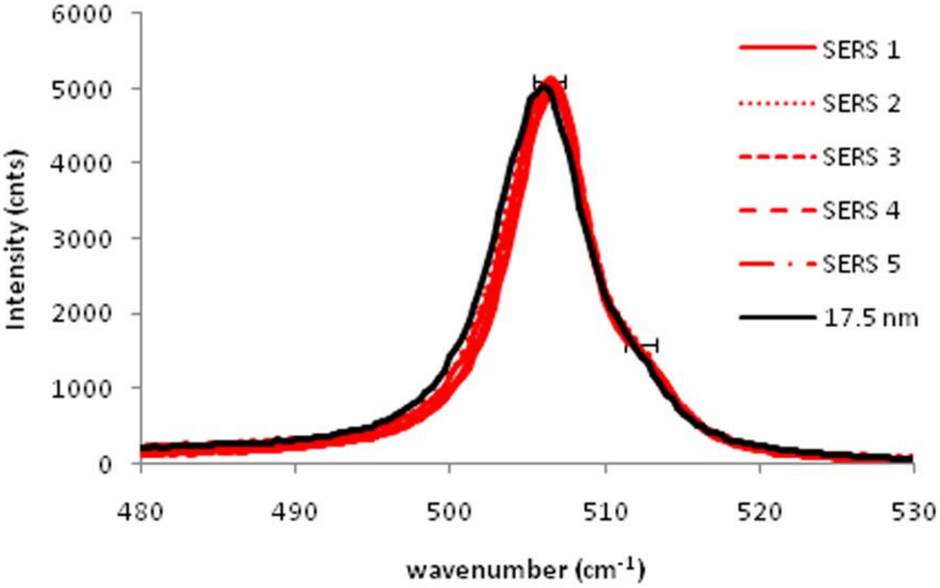

Figure 5.20: ε-Si SERS enhancements using sample 2 NPs of average size 49 ± 9 nm. SERS SiGe peak is located at 506.48 ± 0.13 cm^{-1}, whilst ε-Si peak is at 512.29 ± 0.16 cm^{-1}. Data represents a total of 90 scans (30 accumulations for each one of three experimental runs).

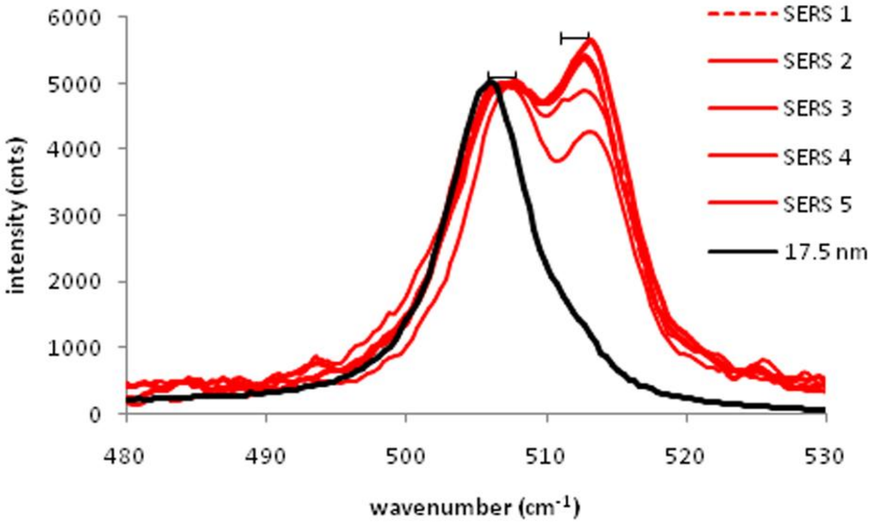

Figure 5.21: ε-Si SERS enhancements using sample 3 NPs of average size 76 ±11 nm. SERS SiGe peak is located at 507.28 ± 0.23 cm^{-1}, whilst ε-Si is at 512.91 ± 0.21 cm^{-1}. Data represents a total of 90 scans (30 accumulations for each one of three experimental runs).

This technique was applied to all samples investigated with approximately 4 – 6 maximum SERS enhancements depicted in the final Raman data where the data represents a total of 90 scans (30 accumulations for each one of three experimental runs). All data was first normalised to a SiGe peak intensity of 5000 counts. Figure 5.19 depicts the ε-Si Raman spectra obtained using sample 1 NPs of average size 26 ± 4 nm. As can be seen there is absolutely no SERS enhancement at all. This is also shown for the ε-Si Raman spectra using sample 2 NPs of average size 49 ± 9 nm (figure 5.20). It is not until we use sample 3 NPs of average size 76 ±11 nm that a strong SERS effect is confirmed.

As can be seen in figure 5.21 there is an obvious SERS enhancement of the 17.5 nm ε-Si layer when compared to bare 17.5 nm ε-Si. The non-SERS SiGe and ε-Si Raman peaks are located at 506.55 ± 0.21 cm^{-1} and 512.52 ± 0.27 cm^{-1}, respectively whilst the SERS SiGe and ε-Si Raman peaks are positioned at 507.28 ± 0.23 cm^{-1} and 512.91 ± 0.21 cm^{-1}, respectively.

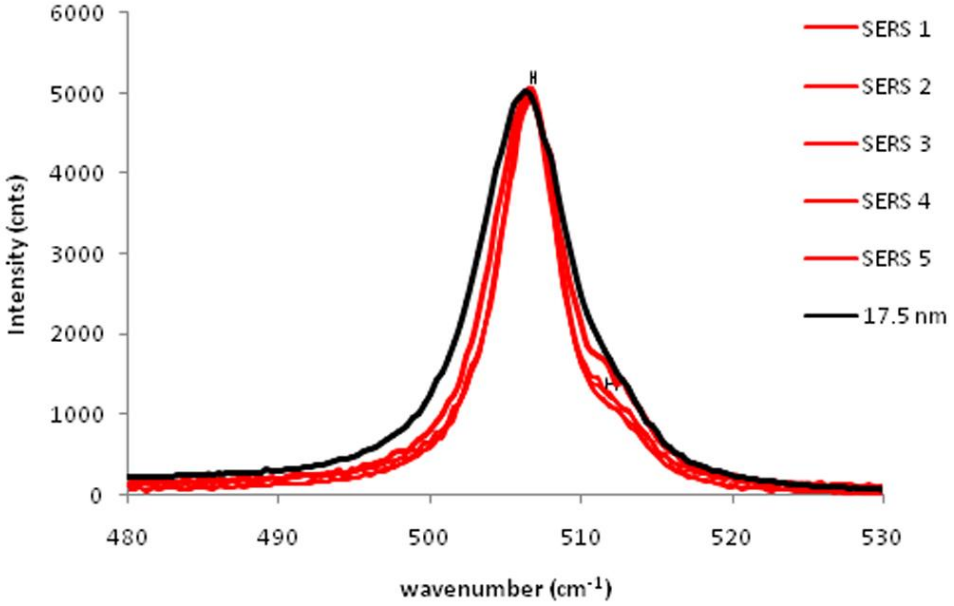

Figure 5.22: ε -Si SERS enhancements using sample 4 NPs of average size 115 ±20 nm. SERS SiGe peak is located at 506.61 ± 0.14 cm^{-1}, whilst ε-Si is at 512.09 ± 0.35 cm^{-1}. Data represents a total of 90 scans (30 accumulations for each one of three experimental runs).

The Raman spectra of the final Ted Pella, Inc. sample used (sample 4, of average size 115 ± 20 nm) is shown in figure 5.22. Again, similar to samples 1 and 2 there is very little evidence of SERS enhancements although the original ε-Si peak does however seem more *pronounced* if not actually *enhanced*. Hence, from a SERS analysis of Ted Pella, Inc. samples 1 to 4 it seems that only NPs of size 76 ± 11 nm are effective at producing a 17.5 nm ε-Si SERS effect. The synthesised polyol samples are now investigated using the same techniques.

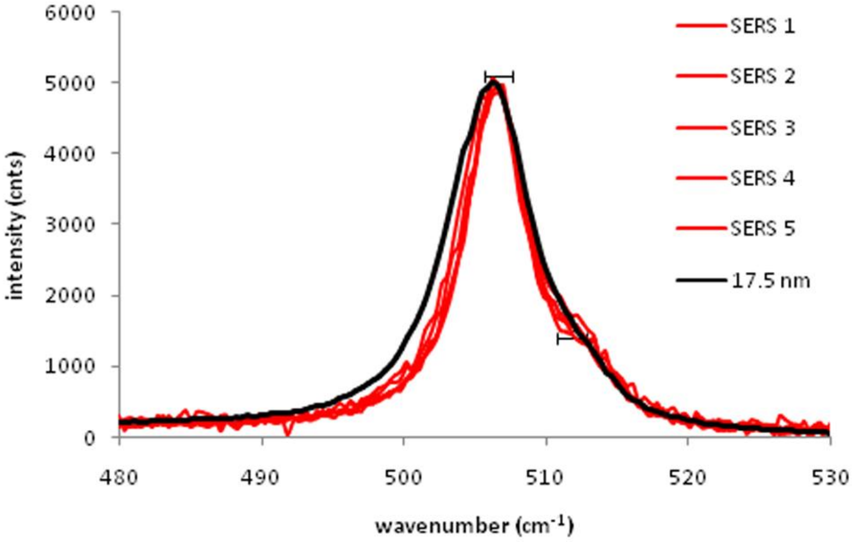

Figure 5.23: ε -Si SERS enhancements using sample 5 polyol stabilised Ag NPs of average size 33 ± 11 nm. SERS SiGe peak is located at 506.5 ± 0.12 cm^{-1}, whilst ε-Si is at 511.79 ± 0.27 cm^{-1}. Data represents a total of 90 scans (30 accumulations for each one of three experimental runs).

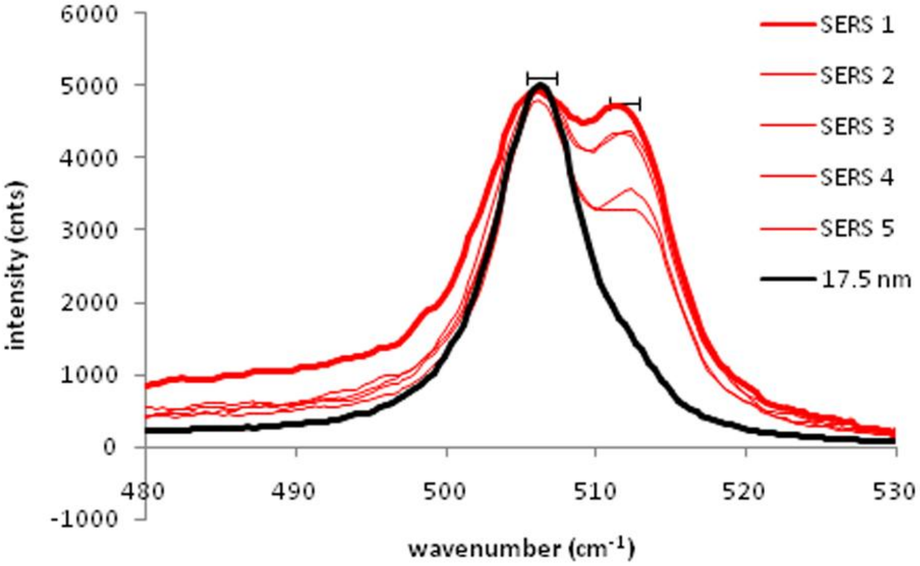

Figure 5.24: ε -Si SERS enhancements using sample 6 polyol stabilised Ag NPs of average size 78 ± 19 nm. SERS SiGe peak is located at 506.21 ± 0.13 cm^{-1}, whilst ε-Si is at 511.89 ± 0.35 cm^{-1}. Data represents a total of 90 scans (30 accumulations for each one of three experimental runs).

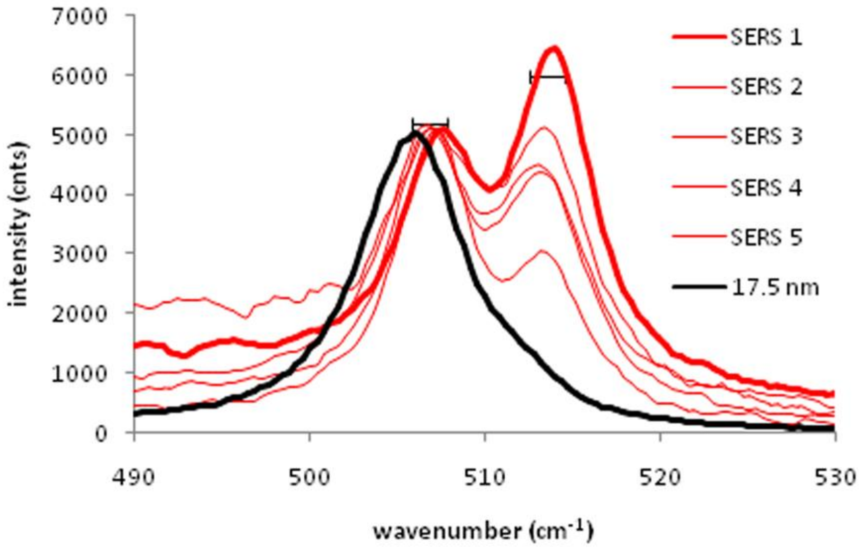

Figure 5.25: ε -Si SERS enhancements using sample 7 polyol stabilised Ag NPs of average size 80 ± 18 nm. SERS SiGe peak is located at 506.98 ± 0.33 cm^{-1}, whilst ε-Si is at 513.33 ± 0.37cm^{-1}. Data represents a total of 90 scans (30 accumulations for each one of three experimental runs).

Figure 5.23 depicts the ε-Si Raman data using sample 5 NPs of average size 33 ± 11 nm. While there does not seem to be any SERS evidence the original ε-Si peak does however seem more pronounced if not actually enhanced, which is similar to the case for sample 4.

There is strong evidence however of a SERS enhancement using sample 6 NPs of average size 78 ± 19 nm. As can be seen in figure 5.24 there is an obvious SERS enhancement of the 17.5 nm ε-Si layer when compared to bare 17.5 nm ε-Si. The non-SERS SiGe and ε-Si Raman peaks are located at 506.55 ± 0.21 cm^{-1} and 512.52 ± 0.27 cm^{-1}, respectively whilst the SERS SiGe and ε-Si Raman peaks are positioned at 506.21 ± 0.13 cm^{-1} and 511.89 ± 0.35 cm^{-1}, respectively. There is also an even greater SERS enhancement evident for sample 7.

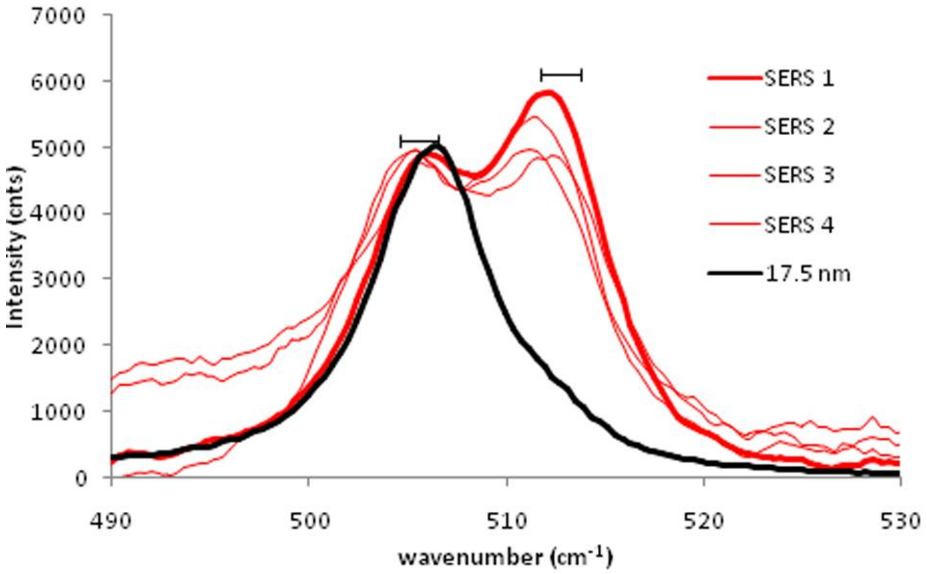

Figure 5.26: ε -Si SERS enhancements using sample 8 polyol stabilised Ag NPs of average size 147 ± 38 nm. SERS SiGe peak are located at 505.63 ± 0.3 cm^{-1}whilst ε-Si is at 511.75 ± 0.55 cm^{-1}. Data represents a total of 90 scans (30 accumulations for each one of three experimental runs).

The ε-Si Raman results using sample 7 NP of average size 80 ± 18 nm are shown in figure 5.25. The non-SERS SiGe and ε-Si Raman peaks are located at 506.55 ± 0.21 cm^{-1} and 512.52 ± 0.27 cm^{-1}, respectively whilst the SERS SiGe and ε-Si Raman peaks are positioned at 506.98 ± 0.33 cm^{-1} and 513.33 ± 0.37 cm^{-1}, respectively. The SERS enhancement associated with sample 7 is the greatest SERS enhancement across the whole range of samples and will subsequently be applied to the final 9 nm and 42 nm ε-Si samples. The results for the final sample (sample 8, average NP size 147 ± 38 nm) are first discussed and shown in figure 5.26.

The use of sample 8 NPs produces clear evidence of a SERS enhancement of the 17.5 nm thick ε-Si layer. The non-SERS SiGe and ε-Si Raman peaks are located at 506.55 ± 0.21 cm^{-1} and 512.52 ± 0.27 cm^{-1}, respectively whilst the SERS SiGe and ε-Si Raman

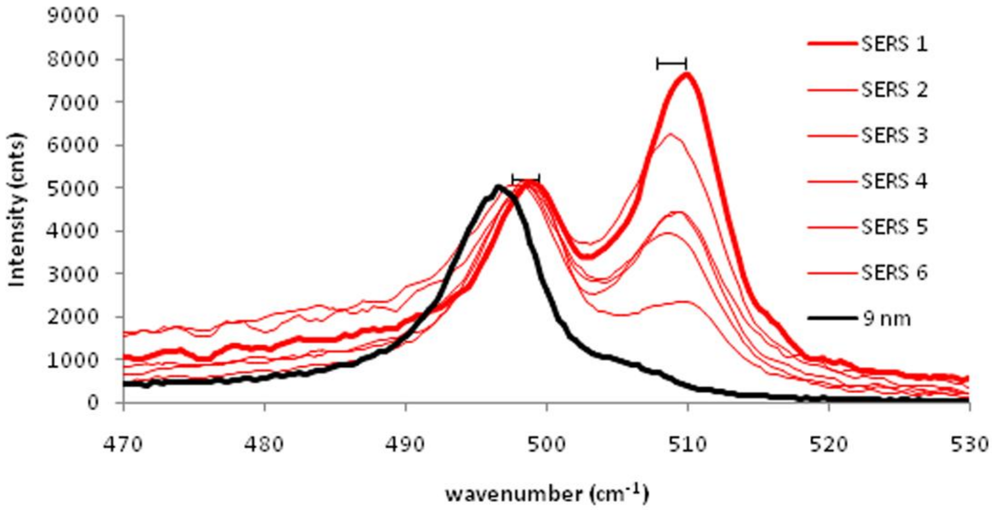

Figure 5.27: ε -Si SERS enhancements using sample 7 polyol stabilised Ag NPs of average size 80 ± 18 nm on 9 nm thick ε-Si. SERS SiGe peak is located at 498.49 ± 0.26 cm^{-1}, whilst ε-Si is at 509.21 ± 0.47cm^{-1}. Data represents a total of 90 scans (30 accumulations for each one of three experimental runs).

peaks are positioned at 505.63 ± 0.3 cm^{-1} and 511.75 ± 0.55 cm^{-1}, respectively. The SERS enhancement shown is almost equal to that produced using sample 6 NPs, which is interesting considering the size difference between the two samples (78 ± 19 nm versus 147 ± 38 nm).

From all samples evaluated the polyol synthesised NPs from sample 7 gave the greatest ε-Si SERS enhancement. These NPs were then applied to ε-Si samples of thickness 9 nm and 42 nm. These results are highlighted in figures 5.27 and 5.28, respectively. As can be seen in figure 5.27 the non-SERS SiGe and ε-Si Raman peaks are located at 498.25 ± 0.38 cm^{-1} and 507.64 ± 0.37 cm^{-1}, respectively whilst the SERS SiGe and ε-Si Raman peaks are positioned at 498.49 ± 0.26 cm^{-1} and 509.21 ± 0.47 cm^{-1}, respectively. Application of sample 7 NPs to 42 nm thick ε-Si also gives SERS enhancement which can be seen in figure 5.28.

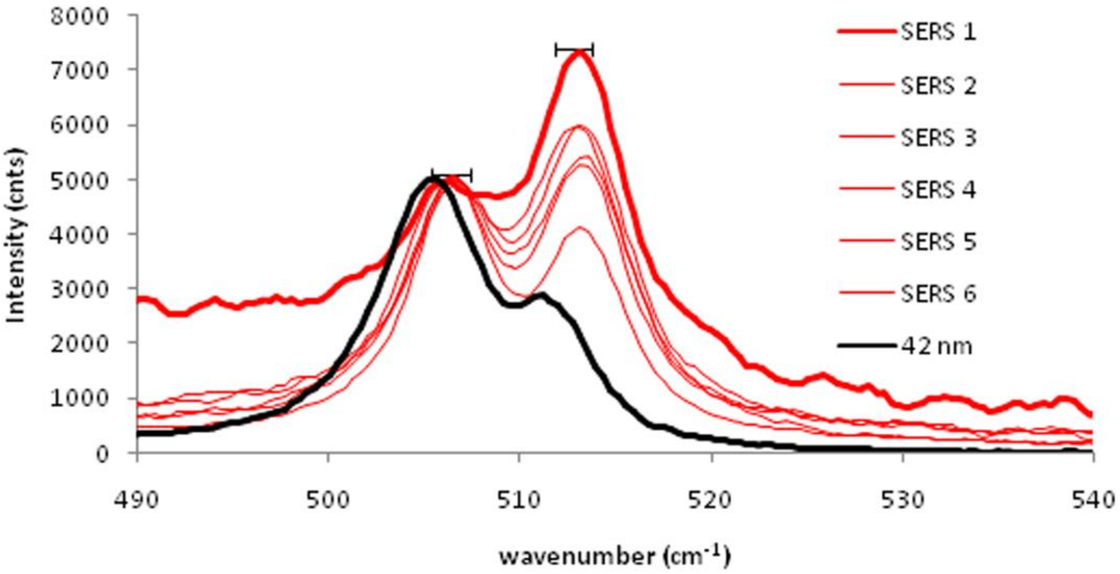

Figure 5.28: ε -Si SERS enhancements using sample 7 polyol stabilised Ag NPs of average size 80 ± 18 nm on 42 nm thick ε-Si. SERS SiGe peak is located at 506.46 ± 0.16 cm^{-1}, whilst ε-Si is at 513.26 ± 0.09 cm^{-1}. Data represents a total of 90 scans (30 accumulations for each one of three experimental runs).

As can be seen in figure 5.28 the non-SERS SiGe and ε-Si Raman peaks are located at 505.90 ± 0.15 cm^{-1} and 511.96 ± 0.21 cm^{-1}, respectively whilst the SERS SiGe and ε-Si Raman peaks are positioned at 506.46 ± 0.16 cm^{-1} and 513.26 ± 0.09 cm^{-1}, respectively. These findings are now summarised in table 5.1 for clarity. By making reference to section 4.2 which discussed among other things the extent to which ε-Si peak shifts are a function of nanoscale strain distributions as opposed to focal plane variations it was found that strain variations are only valid for standard deviations greater than ± 0.4 cm^{-1} which corresponds to strain deviations of ±0.1 GPa. From analysis of table 5.1 it can be seen that for the observed 17.5 nm ε-Si SERS enhancements (exhibited using samples 3, 6, 7, and 8) the average strain across all four samples is 1.9 GPa. This is slightly larger than 1.79 GPa (given in section 4.3 via the evaporation technique) although samples 3 and 7 gave almost equivalent values of 1.79 ± 0.052 GPa and 1.685 ± 0.092 GPa, respectively.

Sample	***Average NP size (nm)***	***17.5 nm SiGe (SERS)***	***17.5 nm ε-Si (SERS)***	***17.5 nm ε-Si Strain (GPa)***
1	26 ± 4	505.972 ± 0.29	n/a	n/a
2	49 ± 9	506.48 ± 0.13	n/a	n/a
3	76 ± 11	507.28 ± 0.23	512.91 ± 0.21	**1.79 ± 0.052**
4	115 ± 20	506.61 ± 0.14	n/a	n/a
5	33 ± 11	506.5 ± 0.12	n/a	n/a
6	78 ± 19	506.21 ± 0.13	511.89 ± 0.35	**2.045 ± 0.087**
7	80 ± 18	506.98 ± 0.33	513.33 ± 0.37	**1.685 ± 0.092**
8	147 ± 38	505.63 ± 0.3	511.75 ± 0.55	**2.08 ± 0.137**
		9 nm SiGe (SERS)	***9 nm ε-Si (SERS)***	***9 nm ε-Si strain (GPa)***
7	80 ± 18	498.49 ± 0.26	509.21 ± 0.47	**2.715 ± 0.117**
		42 nm SiGe (SERS)	***42 nm ε-Si (SERS)***	***42 nm ε-Si strain(GPa)***
7	80 ± 18	506.46 ± 0.16	513.26 ± 0.09	**1.70 ± 0.022**

Table 5.1: Summary of ε-Si SERS peaks and strain values for samples 1 to 8 applied to 17.5 nm thick ε-Si samples as well as sample 7 applied to 9 nm and 42 nm thick ε-Si samples. ε-Si SERS enhancement are only visible for samples 3, 6, 7, and 8 with sample 7 displaying the strongest SERS enhancement.

The strain exhibited for sample 7 NPs deposited onto 9 and 42 nm ε-Si samples was 2.715 ± 0.117 GPa and 1.70 ± 0.022 GPa, respectively. When comparing to values obtained in section 4.2 (2.92 ± 0.25 GPa and 2.1875 ± 0.157 GPa, respectively) we can see that the 9 nm values closely match but are a more varied for the 42 nm sample.

The exact nature of these variations is unclear but it could be due to chemical interactions between the Ag NPs and the ε-Si surface, as well as the r^{-10} distance dependence, explained in section 4.2. It could also be due to the interactions between Ag^+ ions and Ag_0 within the system – i.e. any remnant Ag^+ ions and Ag_0 atoms may precipitate out of the solution and create an atomic layer upon the ε-Si surface (we have already seen from UV-VIS solution analysis that the relative percentage of Ag^+ and Ag_0 varies from sample-to-sample.

Also, non-uniform coatings of citrate and PVP may have an influence on these strain variations. Considering each sample contains billions of NPs all of different shapes and sizes (as determined previously from SEM micrographs) it could be that NP size and morphology plays a vital part in attaining exact strain characteristics: which indeed is suggested considering no SERS enhancements were visible for Ag NP size < 76 ± 11nm. These results suggest that ε-Si SERS enhancements are a function of NP size as no SERS enhancements were evident for NP size 33 nm ± 11 nm. This is most likely due to a decrease in the electrical conductivity caused by a decrease in the electron mean free path length (55 nm for Ag [14]) which effectively reduces SERS enhancements; a fact recently illustrated by Praharaj *et al*. [15].

The important point to take from these micro-Raman spectra is that Ag NPs *can be used* as SERS probes, allowing micro-litre droplets of Ag NP suspensions to be used to characterise ε-Si samples of various thickness. This technique is far more efficient and portable than evaporation techniques and does not require bulky, expensive evaporation hardware, especially considering that a single 10 µl droplet can allow for thousands of accurate ε-Si SERS enhancement experiments. This technique is also highly reproducible – being accurate across three experimental runs using different samples.

5.5 SERS enhancement factor calculations

variable	**9 nm**	**17.5 nm**	**42 nm**
$aSi_{1-x}Ge_x$	0.5491 nm	0.5471 nm	0.5471 nm
N_{surf}	3.795 x 10^8 atoms	3.836 x 10^8 atoms	3.836 x 10^8 atoms
N_{vol}	6.831 x 10^8 atoms	1.343 x 10^9 atoms	3.223 x 10^9 atoms
I_{NRS}	968.02	1796.91	2545.87
I_{SERS}	7621.97	6444.01	8123.85
EF	**14.17**	**12.55**	**26.62**

Table 5.2. Calculated SERS enhancement values for sample 7 deposited onto 9 nm, 17.5 nm, and 42 nm ε-Si samples.

A full evaluation of specific methods for evaluating SERS enhancement factors (EFs) is given in section 4.4. To reiterate, we used the following equation to determine SERS EFs:

$$EF = \frac{I_{SERS}\ /N_{surf}}{I_{NRS}/N_{vol}} \qquad (5.1)$$

where I_{SERS} is the surface-enhanced Raman intensity, N_{surf} is the number of molecules bound to the enhancing silver substrate, I_{NRS} is the normal Raman intensity, andN_{vol} is the number of molecules in the excitation volume [14]. As can be seen from table 5.2 the calculated EFs are extremely small when compared to such reported values as 10^6 - 10^9 [14]. As previously stated in section 4.4 this is most likely due to the difference in modelling parameters (i.e. atoms as opposed to molecules) as well as the fact that only a small 2D section of the available near-field is actually interacting with the ε-Si layers. Also, as there will be no ε-Si in close proximity to any so-called ‘SERS hot-spots’ (which are primarily confined to nm gaps between adjacent NPs located on the plane parallel to the ε-Si surface) the near-field interactions with the ε-Si surface will be significantly reduced. These figures do however serve as a figure of qualitative relative merit for each SERS enhancement, and is the first time, known to this author, that an attempt has actually been made to model ε-Si SERS enhancement factors.

Conclusion:

The surface plasmon polariton response of PVP and citrate-capped Ag NPs across the size range 26 to 147 nm were utilised for the SERS enhancement of ε-Si samples of thickness 9, 17.5, and 42 nm using a 488 nm Raman excitation laser. SEM studies indicated that although the samples were relatively homogenous, they did display a slight blended range of morphologies with some samples displaying evidence of cubic, triangular, and rod-like structures. Overall the main morphology was found to be generally spherical. From UV-VIS optical characterisation we were able to confirm the general surface plasmon resonance peaks, which would generally red-shift and broaden for an increase in NP size. For the larger NPs, there was also evidence of quadruple plasmon resonance.

Similar to chapter 4, although clear SERS enhancements were visible, it is though that slight peak position variations from point-to-point are mainly the result of systematic limitations stemming from uneven focal planes, as well as PVP and citrate thickness variations. It was also noticed that SERS enhancement were size dependent, exhibiting no SERS enhancements for diameters < 76 nm. Careful literature scrutiny suggests this is most likely due to a decrease in the electrical conductivity caused by a decrease in the electron mean free path length which effectively reduces SERS enhancements.

Again, similar to chapter 4, it is also thought that intensity variations from point-to-point are also the result non-uniform Ag deposition and nm-thin SiO_2 surface layers caused from atmospheric surface oxidation of the ε-Si layer.

An attempt to quantify the enhancement factor using a modified enhancement factor equation given in previous work was also given. Even though these values were significantly smaller than that published in the literature, a set of causes was given to explain these attenuations and are most likely the result of non-interactions with SERS hotspots.

A rapid protocol was also developed to quickly assess maximum SERS enhancements across relatively large areas (100 μm^2) which will inevitably aid in reducing ε-Si characterization time and expenditure. Hence, this Sol-SERS technique is a cheap, rapid, portable-probe technique for accurate ε-Si characterization and seems to offer slightly better advantages when compared to the evaporation technique.

5.6 References

[1] J. DeMay 'The preparation and storage of colloidal gold sols', I*mmunocytochemistry*, gold probes, p 133 (received from Rick Giberson, Ted Pella associate), **2010**.

[2] M. Rycenga, J. M. McLellan, Y. Xia., *Adv. Mater*. **2008**, 20, 2416.

[3] A. L. Swatek, Z. Dong, J. Shaw Jr, M. R. Islam, *J. Experimental Nanoscience* **2010**, 5, 1, 10.

[4] A. N. Pestryakov, A. A. Davydov, *Journal of Electron Spectroscopy and Related Phenomena* **1995**, 74, 195.

[5] J. Hormes, G. Happel, *J. Chern. Phys*. **1983**, 78, 4.

[6] V. I. Srdanov, D. S. Pesic, *J. Mol. Spectrosc*. **1981**, 90, 27.

[7] G. A. Ozin, H. Huber, *Inorg. Chem*. **1978**, 17, 155.

[8] S. Link, M. A. El-Sayed, *J. Phys. Chem. B* **1999**, 103, 8410.

[9] J. Rodrıguez-Fernandez, J. Perez-Juste, F. J. Garcıa de Abajo, L. M. Liz-Marzan, *Langmuir* **2006**, 22, 7007.

[10] G. C. Papavassiliou, *Prog. Solid State Chem.* **1980**, 12, 85.

[11] C. F. Bohren, D. R. Huffman, *Absorption and Scattering of Light by Small Particles*; Wiley: New York, **1983**.

[12] H. Jia, J. Zeng, W. Song, J. An, B. Zhao, *Thin Solid Films,* **2006**, 496, 281.

[13] R. Jin, Y. W. Cao, C. A. Mirkin, K. L. Kelly, G. C. Schatz, J. G. Zheng, *Science* **2001**, 294.

[14] U. Kreibig, C.V. Fragstein, *Z. Physik*, **1969**, 224, 307-323.

[15] S. Praharaj, S. Jana, S. Kundu, S. Pande, T. Pal, *J. Colloid and Interface Science*, **2009**, 333, 699-706.

[16] A. D. McFarland, M. A. Young, J. A. Dieringer, R.P. van Duyne, *J. Phys. Chem. B* **2005**, 109, 22, 11279.

Chapter 6

Capacitively-coupled RF heating of silver and gold nanoparticles

6.1 Introduction

Silver nanoparticles (Ag NPs) which possess exceptional biological properties have been used to treat a variety of chronic afflictions and diseases such as cancer, acquired immunodeficiency syndrome (AIDS), Alzheimer's disease, and bacterial infections like methicillin-resistant Staphylococcus aureus (MRSA). To this end, such nanoparticles have recently been shown to block retinal endothelial cell permeability induced by both VEGF and IL-1β [1], inhibit HIV-1 virus binding to host cells [2], detect biomarkers optically for Alzheimer's disease [3], and possess natural antibiotic [4] and anti-angiogenic properties [5].

In regards to cancer therapy, the size-dependent optical, magnetic and electrical properties of a variety of magnetic, metallic and core-shell NP materials have been exploited to allow for proposed, next-generation cancer therapeutics centered on hyperthermic cellular necrosis [6-12]. These emerging cancer-heating nano-inspired technologies potentially permit targeted single cell–specific oncology, alleviating the need for often less than perfect cancer treatments such as proton-, chemo-, radio- and immunotherapy, as well as surgical resection.

Although tumor hyperthermia can be achieved via commonly-used invasive radiofrequency (RF) ablation techniques, they have disadvantages such as 1) relatively large needle diameters (1.6 to 2.5 mm) and restrictive penetration depth due to organ proximities and short electrode lengths (1.5 – 2.5 cm), 2) extensive tissue charring in close proximity to the active electrodes, 3) non-uniform tumor heating profiles which ablates healthy cells but not always all the malignant cells, and 4) tumor size and consistency problems [13-15].

An alternative RF approach, currently under development in our laboratories [6-8, 12, 16] uses a non-invasive, full-body penetrating, capacitively-coupled RF field combined with cell-internalized NP thermal agents for targeted, localized heating of tumors by RF-hyperthermia at any stage of tumor development and metastatic cycle. Using this RF technique, it has recently been shown that gold nanoparticles (Au NP) of a variety of sizes and concentrations, suspended in their buffer solutions, are thermal agents [6], and that intracellular Au NPs promote thermal ablation of human hepatocellular, colorectal, and pancreatic cancer cell lines [7,8]. In a similar manner, single-walled carbon nanotubes have also been shown to be RF thermal agents and have been used to treat rabbits bearing hepatic VX2 tumors [12]. Thus, this RF heating technique is a new complimentary technique to other cancer hyperthermia methodologies such as magnetic heating by iron oxide [9] or plasmonic heating by Si/Au core-shell NPs using infrared radiation [10,11].

In this work, we compare the heating performance of buffer-free Ag NPs and Au NPs in the RF field and propose a model to explain the heat production and its concentration dependency for the first time.

6.2 J. Kanzius RF heating apparatus

As previously mentioned, several samples of buffer-free Ag and Au NP solutions were subjected to RF heating using a high power, capacitively-coupled system to assess

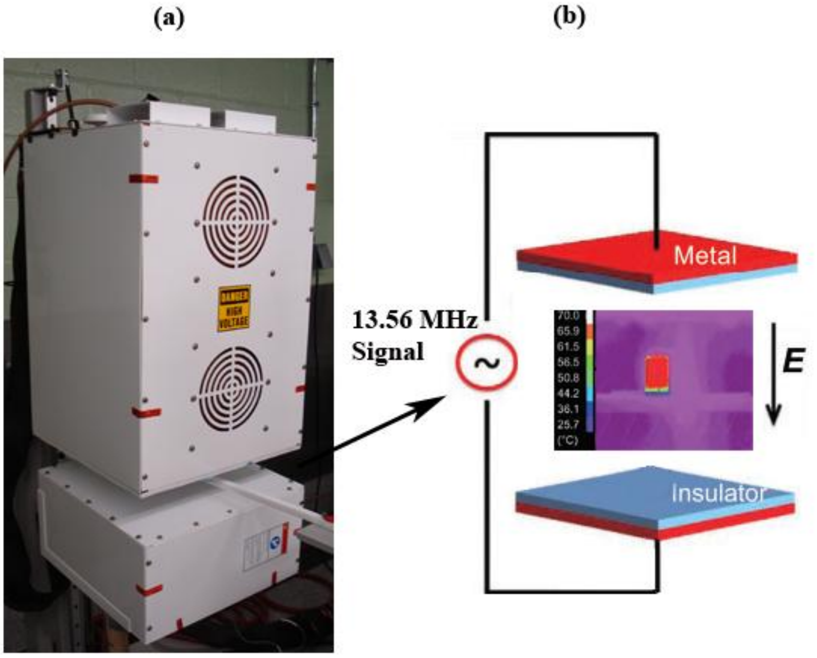

Figure 6.1 (a) Prototype of the RF J. Kanzius heating system. The metal chassis (top white box) contains high voltage matching circuits to efficiently produce RF fields between the electrodes. The nanoparticle suspensions are placed on a Teflon® sample holder located within the 7.5 cm gap between the top and bottom chassis. (b) Diagram of the capacitively-coupled RF heating system. Operating parameters are: operational frequency 13.56 MHz, magnitude of the electric field strength across copper electrodes (red) and Teflon® insulating layers (light blue) is 15 kVm^{-1}, RF generator power is 600 W. As the sample is heated, thermal emissions are recorded via a thermal digital camera, with the output similar to the sample picture which shows a temperature of approximately 65 ^{o}C

heating rates as a function of NP composition and size. Figure 6.1 shows the 13.56 MHz capacitively-coupled RF heating system (Therm Med, LLC, Inc., Erie, PA, USA) including an example digital thermal image obtained from an experiment.

The RF generator is connected to a high Q coupling system (Therm Med, LLC) that has a transmitting (T_x) head, a receiving (R_x) head, and coupling circuitry. The T_x and R_x heads and the contained coupling circuitry are mounted on a swivel bracket, allowing the RF field to be oriented in either a horizontal or vertical direction. The distance between the heads is adjustable, and the RF field is generated between the T_x and R_x

heads. The coaxial coupling circuitry in the T_x and R_x heads produces a focused electromagnetic field with a useful diameter of 30 cm and with a peak intensity of 7 cm from the central axis of the T_x and R_x heads. Each time the RF field is activated, the heads are checked, and the coupling circuit is fine-tuned to assure that there is no power reflected back through the coupling circuit.

The electromagnetic field strength between the T_x head and R_x head was established in a Faraday shielded room to exclude any interference from external RF sources. The field strength was measured at low power using an isotropic field monitor and probe (models FM2004 and FP2000, respectively; Amplifier Research Inc., Souderton, PA, USA); a Hewlett-Packard Spectrum Analyzer (model 8566B; Agilent, Santa Clara, CA, USA) was connected simultaneously to the system through a directional coupler to accurately measure transmitted power. The field strengths measured at low generator output powers were then used to estimate field strengths at the various RF generator output powers that were used in our experimental studies. We set the power at 600 W for all experiments.

A cylindrical quartz cuvette (1.2 cm diameter, 1.7 cm height) containing 1.3 ml of aqueous colloid was positioned on a thin (~0.5 cm) horizontal Teflon® platform located 0.42 cm from the Tx head. All suspensions were exposed to 600 W of RF generator power resulting in a total RF field of 15 kVm^{-1} although the actual field across the cuvette was far less due to the relative permittivity of water. Experiments were powered off once the sample reached 70 ^{o}C (to prevent electrical arcing) or after 120 s. Reflected RF power was monitored and minimized by impedance matching during RF exposure. Thermal imaging of the cuvette was monitored and recorded using an infrared camera (Amber Engineering Inc., Goletta, CA, USA). Each sample was run a total of five times.

6.3 Sample preparation and characterization

Ag and Au NPs of diameters 20, 40, 60, and 80 nm were purchased from nanoComposix™ (San Diego, CA, 92111) and Ted Pella, Inc. (Redding, CA, 96049), respectively. Each sample was divided between 1.5 ml polypropylene centrifuge tubes and spun-down at 10,000 r.p.m. for 10 minutes (20 min for 20 nm NPs) to remove the aqueous buffers, since it was observed that the buffers themselves exhibited heating properties (see section 6.4). The transparent buffers were collected and stored, while the resulting NPs were re-dispersed in HPLC water via sonication. This process was repeated twice to remove any residual buffer material. The resulting NP samples were stored in polypropylene centrifuge tubes and used for the RF experiments within 12 hours.

Sample concentrations were determined using inductively coupled plasma optical emission spectroscopy (ICP-OES) performed using a Perkin Elmer Optima (Waltham, MA) 4300 DV ICP-OES instrument with concentric nebulizer and cyclonic spray chamber. For ICP-OES sample preparation, the Au and Ag NP samples were digested with $HClO_3$ and HNO_3, respectively ($HClO_3$ could not be used for Ag due to the formation of silver chloride) to remove organic contaminants. The Au and Ag NP samples were then re-suspended in 10 ml of aqua regia and 1% HNO_3, respectively, before ICP-OES analysis. Once concentrations had been determined, volumes of the original samples were diluted to concentrations of 0.5, 5.0, and 50 mg/l and then subjected to the RF heating experiment within 12 hours of sample preparation. Characterization of the samples using UV-VIS spectroscopy was performed before and after RF exposure using an Agilent 8435 UV-VIS spectrometer. Nanoparticles (before and after RF exposure) were also imaged using a JEOL 1230 (Peabody, MA) high contrast transmission electron microscope (HC-TEM) operating at 80 kV. Samples were

Sample (Ag or Au)	Manufacturer quoted size (nm)	Actual size from TEM (nm)	ICP-OES concentration (mg/l)
20 nm (Ag)	*20 ± 2.4*	*20.1 ± 2.5*	*105.8*
40 nm (Ag)	*41.9 ± 3.6*	*41.2 ± 4*	*119.9*
60 nm (Ag)	*61.2 ± 5.3*	*62.5 ± 6.1*	*123.6*
80 nm (Ag)	*79.6 ± 8.6*	*80.1 ± 8.6*	*150.7*
20 nm (Au)	*20.3 ± 1.6*	*17.3 ± 1.9*	*100.6*
40 nm (Au)	*40.3 ± 3.2*	*39.4 ± 4.3*	*71.6*
60 nm (Au)	*58.3 ± 4.7*	*61.1 ± 6.8*	*59.9*
80 nm (Au)	*81.3 ± 6.5*	*83.4 ± 7.4*	*75*

Table 6.1: Characterisation data for Ag and Au NPs. The manufacturers' quoted diameter and distribution is compared to actual TEM particle counting measurements (100 particles were counted). Also shown is ICP-OES data which was used to create samples of concentrations 0.5, 5, and 50 mg/l.

prepared by drop-casting aqueous solutions of the NPs onto carbon PELCO® TEM grids (Ted Pella, Inc.) and allowing them to dry overnight.

For comparison to previously published results [6] the entire experiment was repeated with Au NPs of similar diameter purchased from Ted Pella, Inc. (Redding, CA, USA). These Au NPs contained trace amounts of tannic acid, citrate, and potassium carbonate due to the citrate synthesis process [17] and were also removed from their buffers. All supporting ICP-OES and TEM data can be found in Appendix A and are summarized in table 6.1. The ICP-OES data for the buffers (both Au and Ag) are not shown as these concentrations were found to be *lower* than the background signal used for calibration (1% HNO_3 in HPLC for silver and 1% 1:3 ratio of HNO_3:HCl in HPLC for gold, as previously described in section 3.6) which would indicate negligible traces of silver and gold – indicating that the Ag/Ag NPs had been completely removed from their buffers.

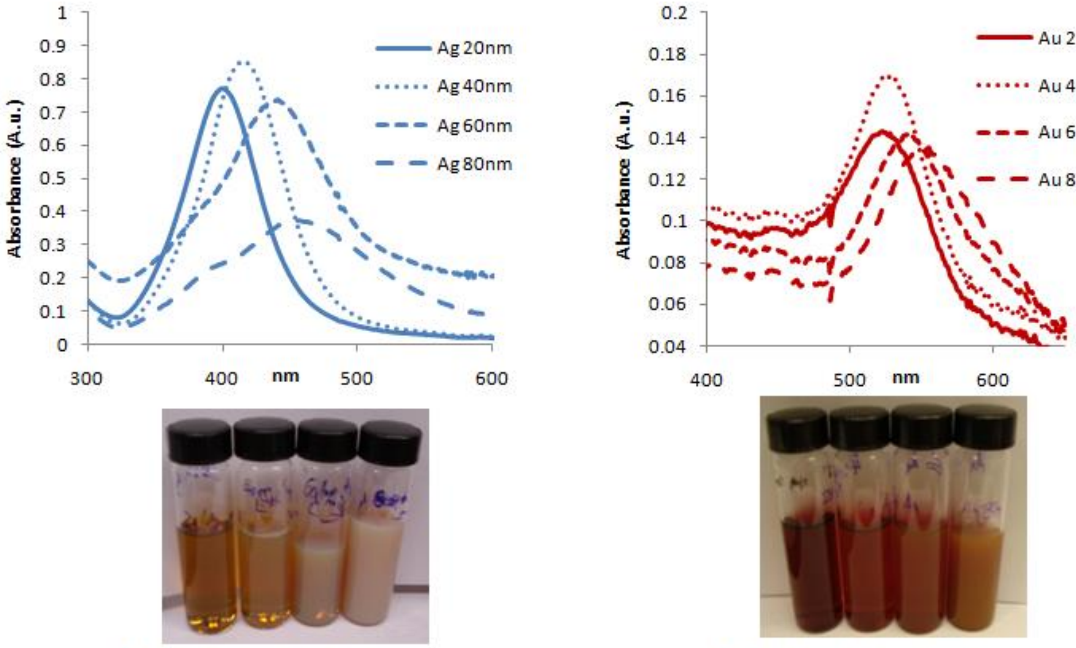

(Ag) 20, 40, 60 80 nm

(Au) 20, 40, 60 80 nm

Figure 6.2: UV-VIS spectra of Ag and Au NPs (top left and top right, respectively) of diameter 20, 40, 60, and 80 nm used in RF heating experiments. Also shown below each UV-VIS spectra are sample photographs.

It should be noted that nanoComposix™ was chosen as the preferred Ag NP supplier over Ted Pella, Inc. NPs (which were used throughout chapter 5) as there was a 3 month back log for several NP sizes and it had been shown that for 80 nm NPs the actual sizes and distributions were irregular with strong evidence of rod-like formation (previously shown in section 5.3) which would ultimately effect the heating results. NanoComposix™ also had extensive characterization schemes (UV-VIS, TEM, metal concentration, zeta-potential, etc.) aiding them to achieve greater mono-dispersity and accuracy – which is evident in table 6.1. Ted Pella, Inc. NPs were however used as the Au NP supplier as these were the NPs already incorporated into cellular studies within the Curley lab group at M.D. Anderson. Also, none of the PVP synthesized Ag NPs used throughout chapter 5 were RF treated as these had a different capping agent (PVP versus citrate) and could therefore not be compared to previous work on Au NPs. Future work will however assess RF heating rate as a function of NP surface functionalization.

Figure 6.2 depicts the UV-VIS spectra and photographs of all NP samples. The size-dependent plasmon peak position of each sample correlates well with the literature [18-20] as well as the manufacturer's documentation. For Ag NP solutions a UV-VIS spectra was only clearly visible for concentrations of 0.5 and 5 mg/l as 50 mg/l concentrations caused the spectra to saturate. For Au NP solutions the 0.5 mg/l concentration was too low for a clear spectrum allowing for only concentrations of 5 and 50 mg/l to be clearly visible (see Appendix A for data).

It must be highlighted from the outset that the RF heating properties of HPLC water were found to be extremely sensitive to container contaminations. From preliminary investigations it was found that borosilicate glass vials could not be used for experiments as they were introducing unknown contaminants which contributed to relatively large amounts of heat production (see figure 6.3). Contaminations were not due to air quality, vial cap materials (aluminium, paper, Teflon®), washing procedures, or manufacturer, as can be seen in figure 6.3. Although the source of these contaminants is unknown it is estimated that the release of boron from borosilicate glass could be the culprit as previous work has documented the slow release of µg quantities of boron from borosilicate glass over a period of 171 days [21]. It could also be due to trace amounts of sodium which, as will be documented in Appendix B, releases relatively large amounts of heat for NaCl solutions. Whatever the case, only polyethylene or polypropylene containers were used throughout these experiments to eliminate any unwanted sources of error.

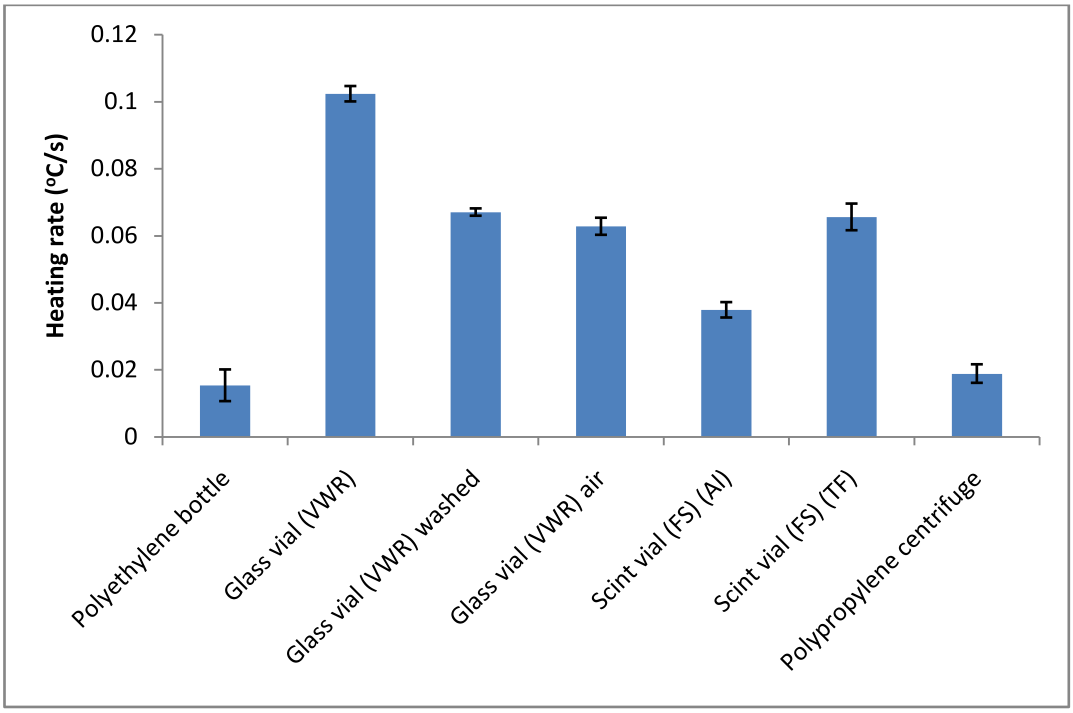

Figure 6.3: Heating rate of HPLC water in a variety of glass and plastic containers. Glass vials purchased from VWR international were subjected to different air qualities (lab air vs. clean room air), washing procedures (HPLC rinse) and as-purchased conditions (cap material was paper). Glass scintillation vials (Scint vial, Fisher Scientific, FS) were also tested with Teflon® (TF) and aluminium caps (Al). Polyethylene bottles and polypropylene centrifuge tubes were found to exhibit minimal contamination evidence.

6.4 RF heating results

Figure 6.4 compares the heating rates of Ag and Au buffer solutions versus the as-purchased solutions (i.e. NPs suspended in buffers). As can directly be seen the *buffers* are the main source of heat within the RF field! This graph is of *fundamental* importance as it completely contradicts claims made by Moran *et al*. [6] that Au NP solutions exhibit size-dependent heating under the influence of an RF field. This claim simply cannot be justified as they neglected to take into account the heating effects from the buffers themselves. This also places enormous doubt on recent studies by Gannon *et al*. [8] who documented the complete hyperthermia destruction of Heb3B and Panc-1

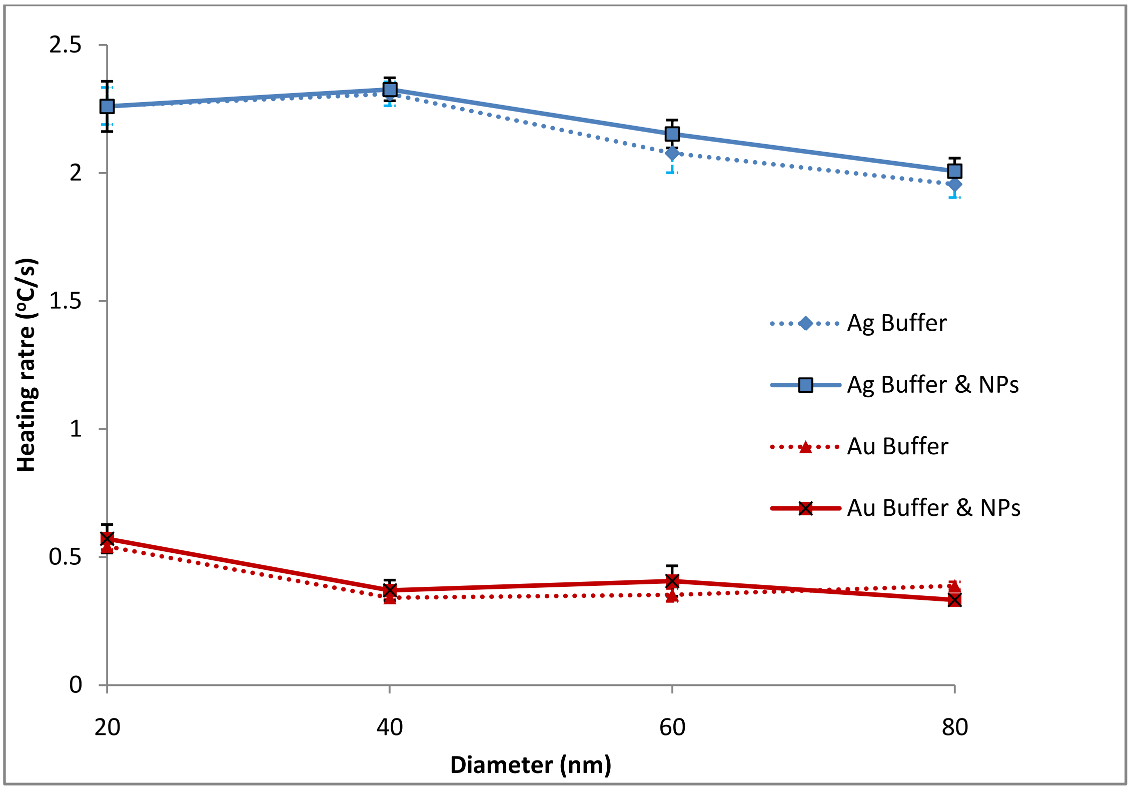

Figure 6.4: Heating rates of Ag and Au buffers versus as-purchased solutions (i.e. NPs suspended in buffers) for a concentration of 5 mg/l. This graph is of fundamental importance as it shows that buffer solutions are the main source of heat within an RF field, not the NPs themselves.

human cancer cell lines via Au NPs of diameter 5 nm, internalised within the cells. Although they state that RF-induced heating is lethal to these cells they *did not* fully separate the Au NP buffer from the solution. With regards to their Au NP synthesis procedure (in brief) 50 ml of aqueous solution containing 4.3 mg of solid sodium borohydride was added to 100 ml of 100 μmol/l aqueous solution of tetrachloroauric acid under vigorous stirring for at least 12 hours. Gold NPs particles were then filtered through a 0.22 μm filter. The key element here is the filter technique where although NPs smaller than 0.22 μm pore size would pass straight through, the *buffer* would also pass through – thereby being present in the final solutions exposed to *in vitro* cellular experiments.

Currently, the understanding of the physical mechanism behind the heating of buffers in an RF field is unclear. However, it does tie in with recent work performed by the inventor of this apparatus, the late John Kanzius, and fellow colleague, the late Rustum Roy [22], with experiments in demonstrating the effect of RF radiation on the structure and subsequent dissociation of water to yield hydrogen and oxygen. They were literally able to show combustion of salt water. Using NaCl-H_2O concentrations ranging from 0.1 to 30% NaCl placed in a 300 W RF field (with an identical apparatus to that reported in this chapter) the continuous combustion of salt water was exhibited for as long as the RF field was active. Although previous work has shown the generation of hydrogen and oxygen via electrolysis [23, 24] and photo-catalysis of various oxides [25] as well as the more 'exotic' research surrounding the structure of water in regards to residual RF field oscillations [26] and 'magnetic memory effects', it is claimed by Roy and Kanzius [22] that none of these effects can account for the reactions involved with the dissociation of water into H_2 and O_2 exhibited with their experimental setup. This 'hydrogen-oxygen' dissociation effect was also observed by myself and is shown in figure 6.5 for the 40 nm Ag buffer solution as an example (figure 6.5). As can be seen, once the RF field is turned on the hydrogen and oxygen by-products can be ignited by a small flame and will continue to combust for as long as the RF machine is active.

As previously mentioned, the current mechanism behind heat and hydrogen-oxygen production from buffer and salt solutions is still as of yet unknown; however an attempt to understand this mechanism is given by this author in Appendix B as it lies outside the main objectives of this chapter – the investigation into whether Ag NPs can be used for RF heat sources and if so how do they compare to gold; the extent to which the as-purchased Ag/Au buffer solutions contribute to the heating effects; and the physical

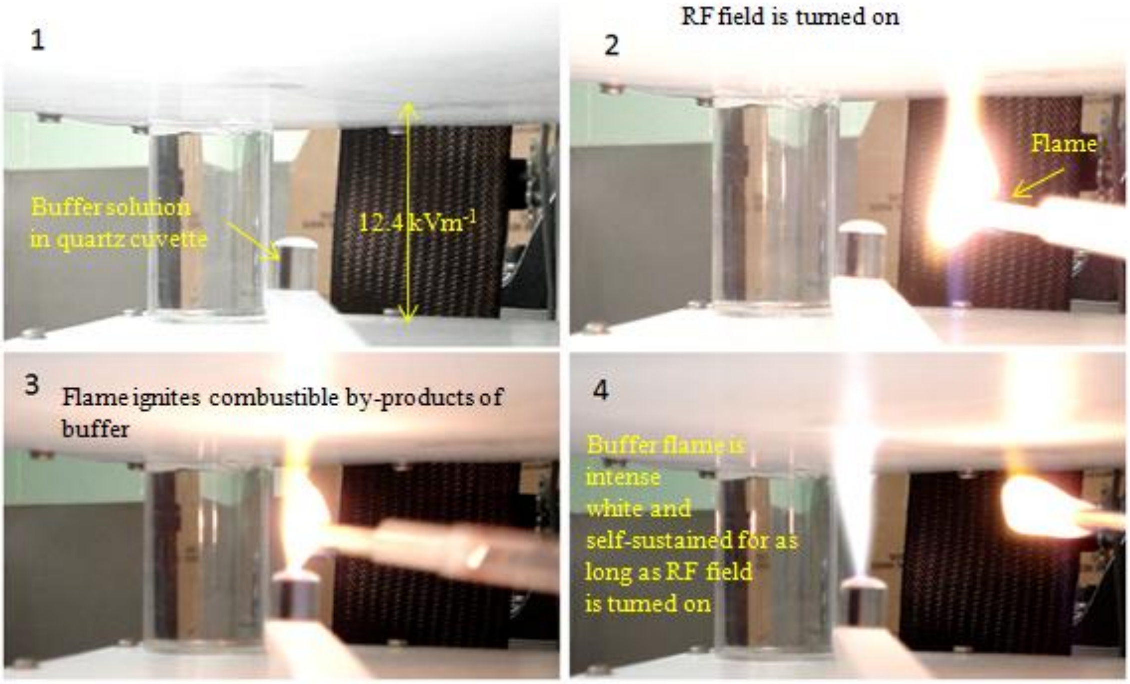

Figure 6.5: Hydrogen-oxygen dissociation effect. Upon activation of the RF apparatus, a small flame ignited the 40 nm Ag buffer solution which continued to combust until the RF field was turned off. As can be seen in figure 4 an intense bright white flame emanates from the buffer surface. Electric field strength is 12.4 kVm^{-1}.

mechanism behind heat production to estimate threshold concentrations of Ag/Au NPs needed for full cancer cell hyperthermia. Figure 6.6 answers the main investigative objective of this chapter, namely to provide evidence that *buffer-free Ag and Au NPs do indeed heat up in an RF field*. To the author’s knowledge this is the first time this has been documented and strongly suggests that silver of nanoparticle dimensions (which has been approved by the FDA) can be used as an alternative RF heat source for cancer cell hyperthermia.

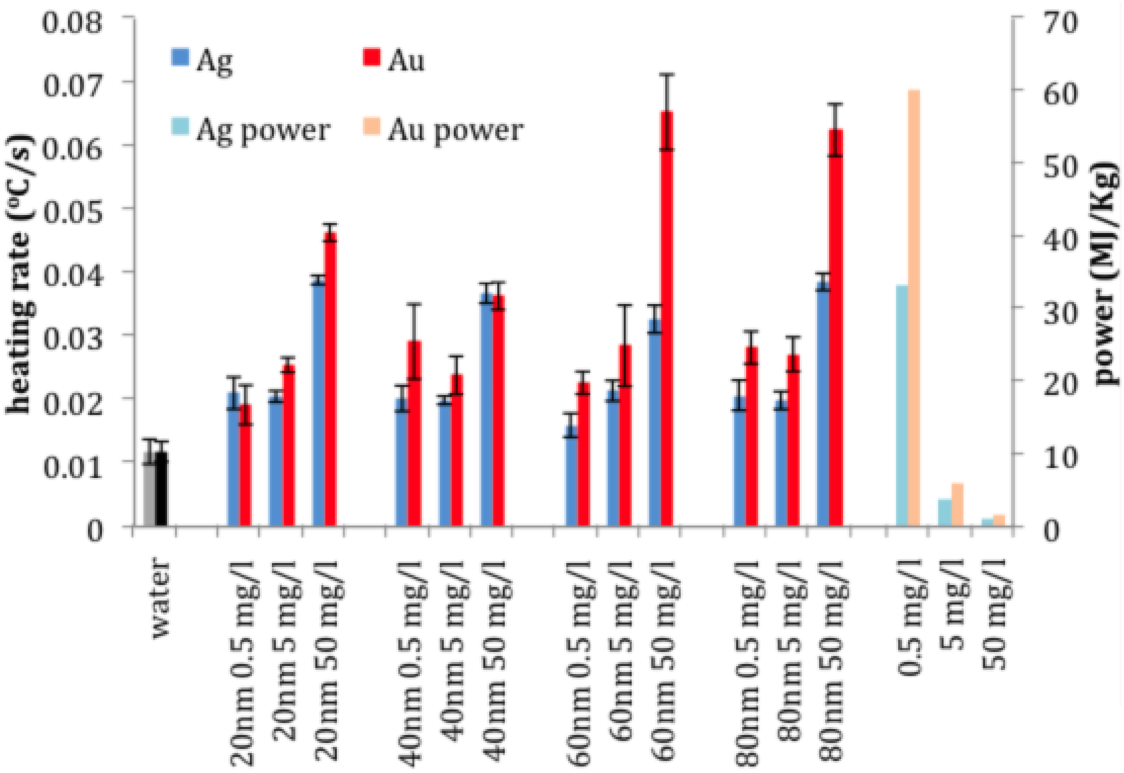

Figure 6.6: Heating rates of Ag and Au NPs (blue and red columns, respectively) as a function of diameter and concentration. Grey and black columns are heating rates of the HPLC water controls taken on the day of the experiments. Thermal power dissipation (MJ.kg^{-1}) for the Ag and Ag NPs (light blue and orange, respectively), as a function of concentration, are also shown on the secondary right-hand side Yaxis.

Figure 6.6 depicts experimental heating rates (^{o}C.s^{-1}) for the Ag and Au NPs as a function of diameter and concentration (blue and red columns, respectively), as well as thermal power (mega joule, MJ) dissipated per kilogram (MJ.kg^{-1}) as a function of concentration. The heating rates for the HPLC water controls were essentially identical and are shown as grey and black columns, respectively. It can be seen that all NP samples possessed heating rates greater than that of the HPLC water in which the NPs were suspended. As well as being relatively size-independent, heating rates were generally proportional to concentration, especially when comparing heating rates for the 0.5 and 50 mg/l samples. Also, as the concentration was increased, the power dissipation (calculated using size-independent average heating rates) was significantly

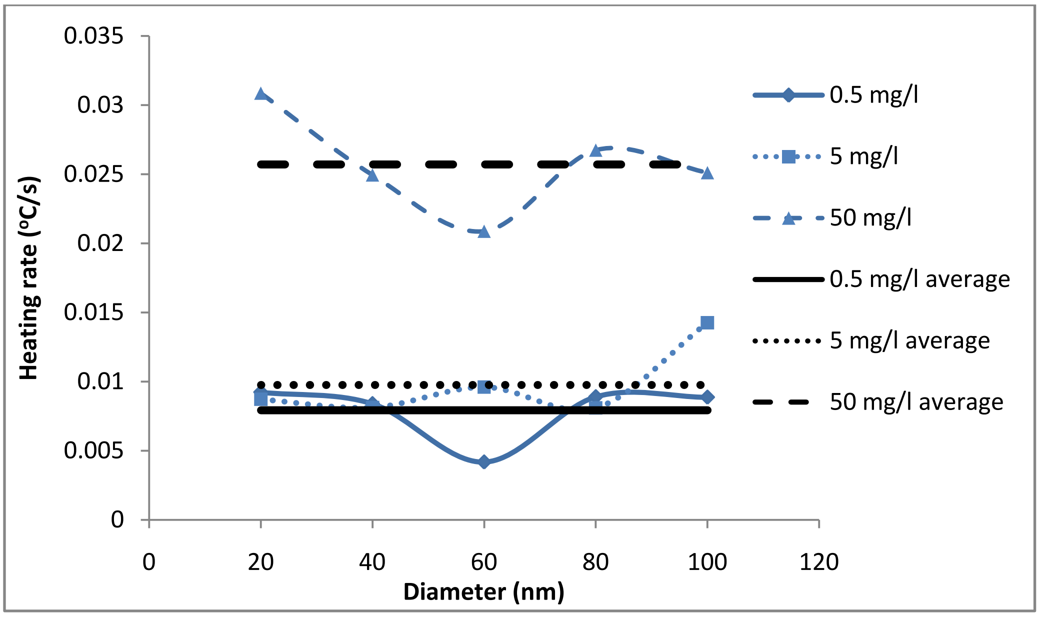

Figure 6.7: Heating rate versus Ag NP diameter for 0.5, 5, and 50 mg/l concentrations. Also shown are the *average* heating rates as a function of concentration which assumes no size dependence heating effects. As can be seen the average heating rate is directly proportional to concentration.

decreased, which was an unexpected result. It should also be noted that Au NP heating rates were generally slightly greater than for Ag NPs of equivalent size and concentration.

One can also observe from the data in figure 6.6 that, although a direct correlation between concentration and heating rate can be seen when comparing concentrations of 0.5 mg/l and 50 mg/l the case is somewhat unclear when comparing 0.5 mg/l and 5 mg/l concentrations. A linear increase between heating rate and concentration can be seen (for example) for 60 nm Ag NPs as well as for 20 nm and 60 nm Au NPs. The other samples either display a similar heating rate when comparing 0.5 mg/l and 5 mg/l (as in 20 nm, 40 nm, and 80 nm Ag NPs as well as 80 nm Au NPs) or a decrease in heating rate (as in 40 nm Au NPs). This effect will be discussed further in section 6.4 as it is thought that NP aggregations may be reducing the surface interactions between Ag-H_2O

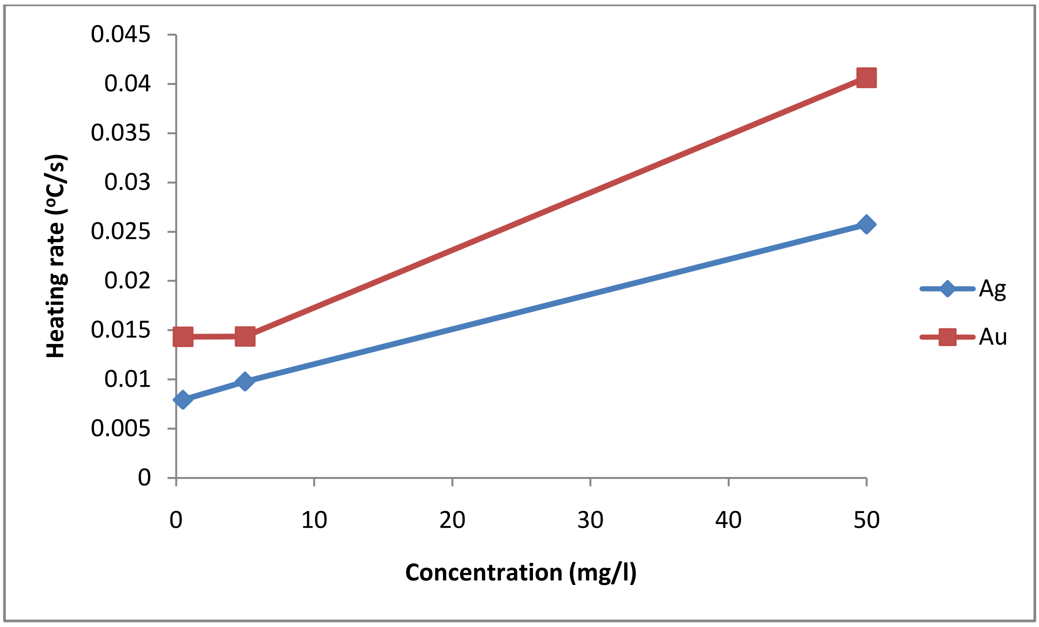

Figure 6.8: Average heating rate versus concentration curves for Ag and Au NPs.

phonon coupling resulting in decreased heating efficiency. However, since the *magnitude* of heat production as a function of size is roughly similar, notwithstanding no evidence of size dependent heating for 60 and 80 nm Au NPs with concentrations of 50 mg/l, the average values of heating rates were taken for each sample and are shown in figure 6.7 (using Ag as an example). This graph (also derived for Au NPs but not shown) allows the heating rate versus concentrations curve to be determined, which can be used to compare Ag and Ag heating rates and is shown in figure 6.8.

As can be seen in figure 6.8 although the heating rate versus concentration curve shows a linear dependence for Ag NPs the case is slightly different for the Au NP curve due to the similarities between 0.5 mg/l and 5 mg/l concentration heating rates. The Au NP heating rates are however greater than for Ag NPs which is surprising as recent theoretical work by Moran *et al.* [6] predicted an *increase* in heat production for an *increase* in sample conductivity – as Au is less conductive than Ag the results shown in figures 6.7 and 6.8 are contrary to this prediction.

This now brings us to the theoretical part of this chapter. A theory will be fully developed to account for how much heat can be produced per NP which will ultimately allow for the final objective: to assess the heat production per NP in order to estimate the minimum amount of NPs needed within a cell to allow hyperthermia to occur.

6.5 Theoretical analysis

For small, metallic NPs, their one electron energy levels are discrete and have not yet formed quasicontinuous energy bands (the valence electrons cannot be continuously accelerated by an external electric field but are able to change their energy only through transitions between quantized eigenstates [27, 28]). The mean spacing between energy levels will effectively become broadened for NPs under a critical diameter where quantum size effects become prevalent. For NP diameters larger than this critical diameter, the conduction band is quasicontinuous (as in the bulk metal) and its conductivity can be classically modelled using the mean free path effect.

Previous work by Kreiberg *et al.* [27, 28] have shown that for Ag quantum size effects are prevalent for atomic densities below 400 atoms per NP (diameters approximately 1.9 to 4.8 nm). Hence, as we are working with Ag NPs of diameter 20 to 80 nm quantum size effects can be neglected. We can also apply the same logic to Au NPs due to their similarity in structure.

In order to assess the conductivity for each material we can use the Drude equation for free electron gas theory [29]:

$$\sigma = \left(\frac{ne^2 l}{m_e V_F}\right) \qquad (6.1)$$

where n is the electron density per unit volume (5.856 x 10^{28} and 5.901 x 10^{28} for Ag and Au, respectively [30, 31]), e is the electron charge (1.602 x 10^{-19} C), l is the electron

NP diameter (nm)	Ag: m.f.p. (nm)	Au: m.f.p. (nm)	Ag: σ (S/m)	Au: σ (S/m)
20	8.36	7.9	$9.923\text{x}10^{6}$	$9.381\ \text{x}10^{6}$
40	14.3	38	$1.697\text{x}10^{7}$	$4.512\ \text{x}10^{7}$
60	51	38	$6.301\text{x}10^{7}$	$4.512\ \text{x}10^{7}$
80	51	38	$6.301\text{x}10^{7}$	$4.512\ \text{x}10^{7}$

Table 6.2: Calculated mean free path (m.f.p.) and conductivity (σ) for Ag and Au NPs used in experiments.

mean free path, m_e is the electron mass ($9.109\text{x}10^{-31}$ kg) and V_F is the Fermi velocity ($1.39\text{x}10^{6}$ ms^{-1}[30] and $1.4\ \text{x}10^{6}$ [31] for Ag and Au, respectively).

For noble metal particles with dimensions smaller or equivalent to the mean free path of the conduction electrons, their dielectric constants differ from that of bulk metals. The mean free path, l_∞, of the conduction electrons in bulk material can be calculated as:

$$l_\infty = V_F . \tau_s \qquad (6.2)$$

where V_F is the Fermi velocity and τ_s is the relaxation time – the average electron collision time caused by phonons, impurities and lattice defects. For particle dimensions smaller than the bulk mean free path length (52 and 38 nm for Ag and Au, respectively [28, 32]) an alternative equation must be used as the collisions of the conduction electrons with the particle surface become more frequent, effectively reducing the mean free path. This is given by:

$$l(R)^{-1} = l_\infty^{-1} + R^{-1} \qquad (6.3)$$

where R is the NP radius, and l_∞ is the bulk mean free path length [27, 28]. For Ag this equation must be used for NPs of diameter 20 and 40 nm, whilst for Au is would only be used for diameters of 20 nm or less. Using equations 6.1 to 6.3, table 6.2 depicts the calculated m.f.p.‘s and conductivity for both Ag and Au NPs. We now develop a model to describe internal heating processes.

The classical approach towards a mathematical description of conductive and displacement current density theory refers to Ampère's law for the current density developed in a material such that:

$$\nabla \times \mathbf{H} = \sigma\mathbf{E} + \frac{\partial \mathbf{D}}{\partial t} \qquad (6.4)$$

and

$$\nabla \times \mathbf{H} = \sigma\mathbf{E} + j\omega\varepsilon_0\varepsilon_r\mathbf{E} \qquad (6.5)$$

where ∇ is the curl operator, H is the magnetic field intensity, E is the electric field intensity, D is the electric flux density, σ is the conductivity, ε_0 is the permittivity of free space, ε_r is the relative permittivity or dielectric constant, and ω the angular frequency [33]. Using the expression for the current density established due to the presence of an electric field

$$\boldsymbol{J} = \sigma\mathbf{E} \qquad (6.6)$$

which represents the first right hand side term of equations 6.4 and 6.5. It is important to note that J represents the combined loss of all possible mechanisms in the medium such as ionic conduction, dielectric relaxation, and Maxwell-Wagner polarization losses [34]. The second terms in equations 6.4 and 6.5 represent the displacement current density ($\partial\mathbf{D}/\partial t$) and is the dominant mechanism of electrical conduction in dielectric materials.

A complex permittivity, ε, under the influence of a time-varying electromagnetic field must be introduced when dealing specifically with a conductive material, metal or dielectric, hence:

$$\varepsilon = \varepsilon_0(\varepsilon' - j\varepsilon'') \qquad (6.7)$$

where ε' is the relative dielectric constant and ε'' is the relative dielectric loss factor [33]. As mechanisms such as dipolar relaxation, and ionic conduction, etc. are all fundamentally different from each other an equation needs to be derived which takes this fact into account. By using the most general form of Ampère's law applied to a dielectric with conductivity we get the following equation:

$$\mathbf{J}_{\mathrm{t}} = \sigma_d \mathbf{E} + \varepsilon_0(\varepsilon' - j\varepsilon'')j\omega\mathbf{E} \qquad (6.8)$$

where $\mathbf{J_t}$ $(= \nabla \times \boldsymbol{H})$ represents an abbreviation of the generic current density. Rearranging equation 6.8 gives:

$$\mathbf{J}_{\mathrm{t}} = (\sigma_d + \varepsilon_0\omega\varepsilon'')\mathbf{E} + j\omega\varepsilon_0\varepsilon'\mathbf{E} = \sigma_e\mathbf{E} + j\omega\varepsilon_0\varepsilon'\mathbf{E} \qquad (6.9)$$

where σ_e is the effective conductivity given by:

$$\sigma_e = \sigma_d + \varepsilon_0\omega\varepsilon'' \qquad (6.10)$$

It is now clear that effective conductivity is a result of two different mechanisms: dipolar relaxation ($\varepsilon_0\omega\varepsilon''$) and and dielectric conductivity (σ_d) [35]. The physical difference lies in the fact that the former involves the 'rotation-like' motion of dipoles in the presence of a high frequency electric field whilst the latter concerns the 'drift' of ionic species under the same applied field.

The importance of equation 6.9 is that it can be used as a basis for deriving a unified approach to electromagnetic heating since it can be applied to either dielectrics or metals by using suitable assumptions. For metallic materials, where the dominant loss mechanism for induction or ohmic heating is due to the metallic conductivity (denoted σ_m), the displacement current is negligible. On the other hand, for a conductive dielectric material the dominant loss mechanisms are due to dielectric conductivity (σ_d)

and the part of the displacement current which is in phase with the applied electric field, i.e. the $\varepsilon_0 \omega \varepsilon''$ term.

Metaxas *et al*. [35] have shown that by incorporating a mathematical parameter K which depends upon the material under consideration, and taking $j\omega\varepsilon_o$ as a common factor in equation 6.9 as well as reverting to the generic case by replacing σ_d with σ we get:

$$\mathbf{J}_\mathrm{t} = (\sigma + \varepsilon_0 \omega \varepsilon'')\mathbf{E} + j\omega\varepsilon_0\varepsilon'\mathbf{E} = j\omega\varepsilon_o K\mathbf{E} \qquad (6.11)$$

where K is given by:

$$K = \frac{[\varepsilon - j(\sigma/\omega)]}{\varepsilon_o} = \varepsilon' \left[1 - j\left\{\frac{\sigma}{\omega\varepsilon_0\varepsilon'} + \frac{\varepsilon''}{\varepsilon'}\right\}\right] = \varepsilon' - j\varepsilon_e'' \qquad (6.12)$$

where ε_e'' is the effective relative loss factor. This parameter K contains all the necessary information through which the nature of the conductive material can be established. For example, for a metallic material $\sigma = \sigma_m$, $\sigma_m/\omega\varepsilon_0\varepsilon' \gg 1$ and $\varepsilon'' = 0$, equation 6.12 now yields:

$$K_{metal} = -j\sigma_m/\varepsilon_0\omega \qquad (6.13)$$

whilst for a dielectric material with no ionic loss mechanism, $\sigma = \sigma_d = 0$ and equation 6.12 now becomes:

$$K_{dielectric} = (\varepsilon' - j\varepsilon'') \qquad (6.14)$$

Hence, in electromagnetic heating, using the above equations for specified cases where the nature of the material is known we can successfully evaluate the current density. In order to equate calculated current density to power, which is required when evaluating the heating mechanism and power generated for single Ag and Au NPs, we need to make use of additional analysis.

The time average power dissipated in a material per unit volume p_v is given by [35]:

$$p_v = \frac{1}{2} Re(\boldsymbol{E}.\boldsymbol{J}^*) \qquad (6.15)$$

Therefore using equation 6.11 and substituting in equation 6.15 gives:

$$p_v = \frac{1}{2} Re(\sigma_e \boldsymbol{E}.\boldsymbol{E}^* - j\omega\varepsilon_0\varepsilon' \boldsymbol{E}.\boldsymbol{E}^*)$$

$$p_v = \frac{1}{2}\, \sigma_e \boldsymbol{E}.\boldsymbol{E}^* = \frac{1}{2}\, \sigma_e |E^2| \qquad (6.16)\ (dielectrics)$$

where $\sigma_e = \sigma + \omega\varepsilon_0\varepsilon''$ and $|E|$ is the magnitude of the electric field strength. Equation 6.16 is the case used when calculating the power dissipated in *dielectric* materials. For *metallic* materials where equation 6.11 gives $J = \sigma_m \boldsymbol{E}$, we have:

$$p_v = \frac{|\sigma_m \boldsymbol{E}|^2}{2\sigma_m} \qquad (6.17)\ (metals)$$

with σ_m =metallic conductivity.

Therefore, we now have two equations which can be used to determine the power dissipated within a metal or dielectric in the presence of an electric field. The heating rate per NP can now be derived using the standard equation for heat energy and the volume of the NP shape. Using the equation for heat energy:

$$Q = m.c.\Delta T \qquad (6.18)$$

where Q is the heat energy (*J*), m is the mass (*kg*), c is the specific heat capacity (J/kg.K), and ΔT is the difference in temperature (*K*) [33] we can express the amount of heat generated within each NP by modifying the power equation stated by Metaxas *et al.* [35] shown in equation 6.17:

$$p_v = \frac{|\sigma_m \boldsymbol{E}|^2}{2\sigma_m} = m.c.\Delta T \qquad (6.19)$$

Therefore;

$$\frac{dT}{dt} = \frac{|\sigma_m \boldsymbol{E}|^2}{2\sigma_m V.c} \qquad (6.20)$$

where m has been replaced by volume, V (as 1ml = 0.001 kg). As this equation relates to the temperature produced per unit volume the temperature produced per NP can be derived by multiplying equation 6.20 by the NP volume (spherical morphology is assumed):

$$\frac{dT}{dt} = \left[\frac{|\sigma_m \boldsymbol{E}|^2}{2\sigma_m V.c} \ \left(\frac{4}{3}\,\pi r^3\right).n\right] (6.21)$$

where n is the total number of NPs present in the specified volume. Finally, equation 6.21 is verified via dimensional analysis (shown in equation 6.22) to have units of K.s^{-1}.

$$\left[\frac{dT}{dt}\right] = \left[\frac{|\sigma_m E|^2}{2\sigma_m.V.c} \ \left(\frac{4}{3}\pi r^3\right).n\right] = \frac{m^2.kg.s^{-3}}{kg.(m^2.s^{-2}.k^{-1})} = \frac{s^{-1}}{k^{-1}} = \boldsymbol{K.s^{-1}} \qquad (6.22)$$

With regards to the electric field strength (Vm^{-1}) inside the 1.3 ml cuvette, the previously measured external field strength of the RF heating device, with a 7 cm air spacer layer, was found to be 12.4 kVm^{-1} [8]. This is however effectively reduced by the permittivity of water (80.3 at 20 ^{o}C [36]) and subsequently becomes 154 Vm^{-1}. We can now apply equation 6.21 to the *average* experimental data shown in figure 6.7.

Figures 6.9 and 6.10 depict the theoretical heating rate per Ag or Au NP compared to average experimental heating rate per NP (experimental heating rates per NP were calculated by dividing average heating rates by amount of NPs present in 1.3 ml of solution (calculated from ICP-OES data). Nanoparticle data is shown in Appendix A.

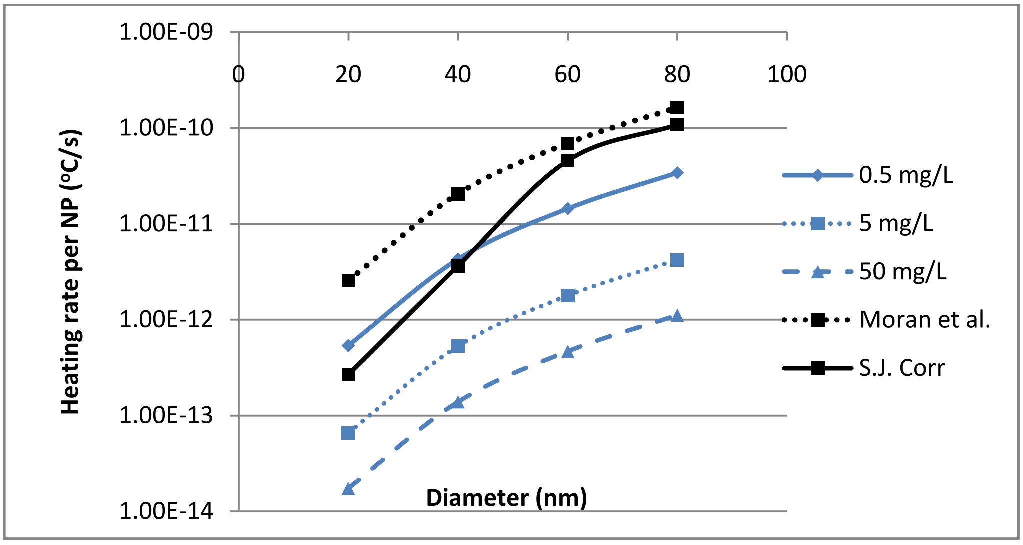

Figure 6.9: Heating rate per NP versus NP diameter for Ag experimental studies of 0.5, 5.0, and 50 mg/l concentrations. Also shown is theoretical calculated heating rate based on proposed model by Moran *et al*. [6] compared to equation 6.21. Experimental results exhibit a decrease in heating efficiency as concentration is increased.

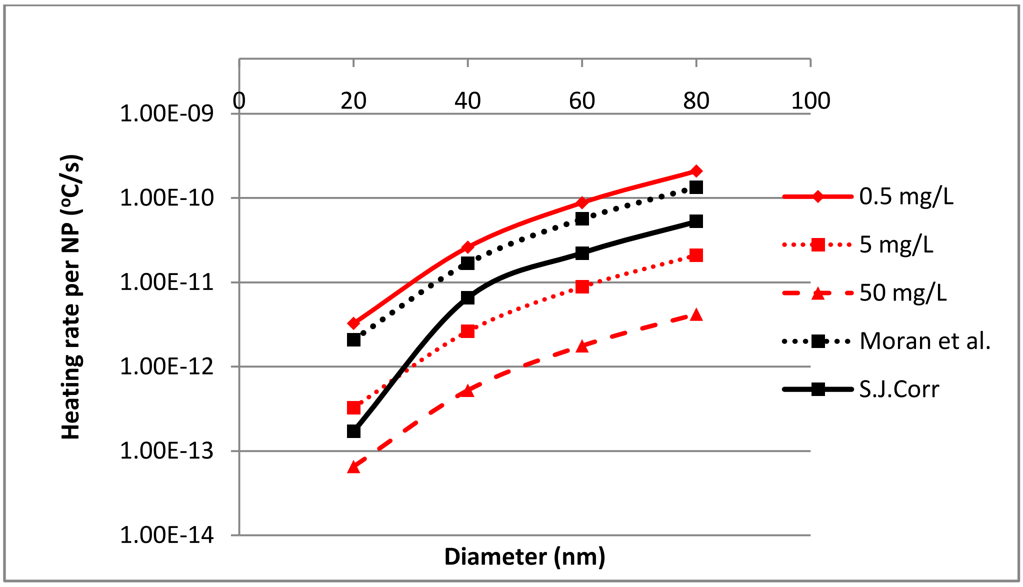

Figure 6.10: Heating rate per NP versus NP diameter for Au experimental studies of 0.5, 5.0, and 50 mg/l concentrations. Also shown is theoretical calculated heating rate based on proposed model by Moran *et al*. [6] compared to equation 6.21. Experimental results exhibit a decrease in heating efficiency as concentration is increased.

From evaluating the heating rate per NP of both Ag and Au NPs shown in figures 6.9 and 6.10 it can clearly be seen in both cases that as the concentration is increased there is a decrease in the heating rate for each NP across the full size regime. This would indicate a decrease in *heating efficiency* and is thought to arise from a combination of attenuation factors due to NP aggregation as well as thermodynamic issues as will be discussed. It can also be seen that as NP dimensions are increased so too is the heating rate. Also, in both cases there are good matches between theory and experiment for 0.5 mg/l concentration values using the approach of Moran *et al*. [6] However the author's theoretical model described herein, using a reduced conductivity, is more accurate for Ag NPs of diameters less than 60 nm.

By looking at aggregation states of NPs from TEM images of NPs in as-purchased buffers and in HPLC water after the centrifugation procedure had been performed it is evident that the NPs are clearly aggregating to a higher extent after removal from their buffers. This is shown in figures 6.11 and 6.12. Aggregation is most likely due to the excess removal of the negatively charged citrate from the NP surface which would result in a less stable suspension – NPs would therefore aggregate. Obviously, as the concentration of NPs is increased so too would the amount of aggregate which would effectively reduce the surface area for Ag-H_2O phonon coupling – resulting in decreased heating efficiency as concentrations are increased. Conclusive proof of these aggregate states would come from a combination of Cryo-TEM (which uses freezing techniques combined with TEM to give a 'snap-shot' of the NPs in solution) as well as Zeta-potential measurements which would indicate the surface charge and hydro dynamic radius of the NPs. Although such equipment was not available at the time of these experiments future work will involve these characterisation techniques.

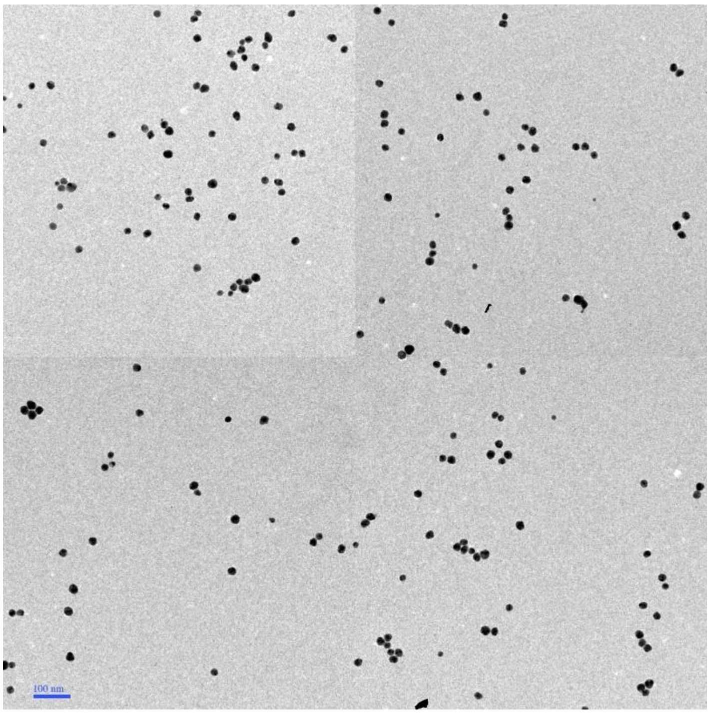

Figure 6.11: TEM image of 20 nm Ag NPs dispersed in as-purchased buffer solutions. Scale bar is 100 nm.

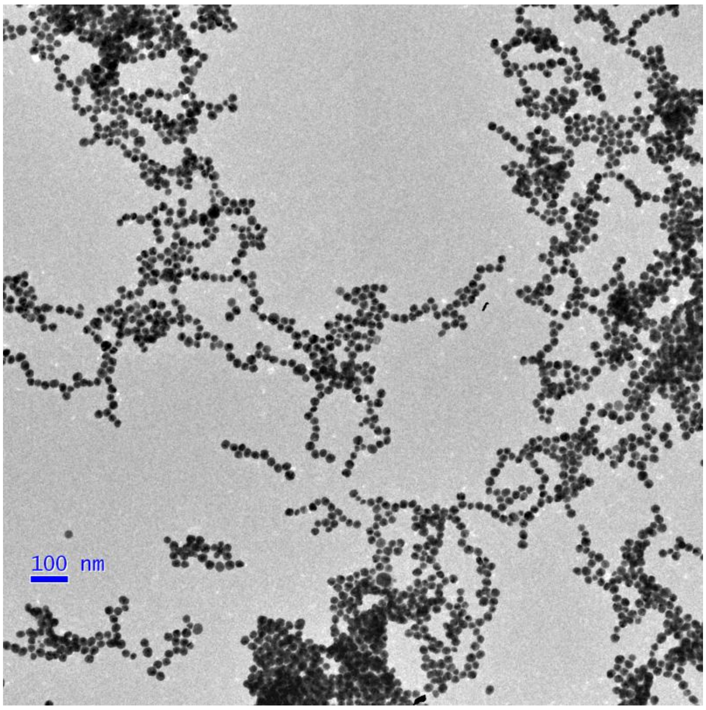

Figure 6.12: TEM image of 20 nm Ag NPs dispersed in HPLC after centrifugation procedure. Scale bar is 100 nm. NPs are aggregating most probably due to citrate removal during centrifugation procedure.

It should also be mentioned that as Ag and Au have far greater thermal conductivities than water (417 W/m.K and 314 W/m.K [37.a] for Ag and Au, respectively versus 0.026 W/m.K for water [37.b]) a proportion of heat production pumped into the water by the NPs could inevitably be reabsorbed by the NPs themselves – which would result in an overall net reduction in NP-H_2O heat dissipation and a decrease in the heating rate and heating efficiency as concentration increases. This point is now discussed further

Investigations into electron dynamics within NPs excited by femtosecond laser pulses [38-40] have generally exhibited three photophysical processes: electron-electron (e-e) scattering, electron-phonon (e-ph) scattering, and phonon-phonon (ph-ph) coupling. Accelerated electrons will oscillate and thermalize almost instantly (femto seconds) under the influence of an external incident electromagnetic wave (e-e scattering) and will transfer their kinetic energy to the underlying lattice through e-ph interactions. Finally, through ph-ph coupling at the NP solution interface heat will be transferred into the surrounding medium, which is regulated by the thermal boundary conductivity h_{BD} [41] which is defined as the ratio of heat flow Q per unit area A across the interface to the temperature discontinuity ΔT at the interface ($h_{BD} = Q/A\,\Delta T$).

Although we are not dealing herein with the optical excitation of Ag NPs we can neglect e-e scattering and instead start at e-ph interactions through the polarization of the Ag NP under the influence of an external electric field (Gauss's law) which will re-distribute the electrons to create an internal electric field equal in magnitude but opposite in polarity to the applied external field [42].

In metallic Ag NPs of diameter ~10 nm it has been shown [38] that photoexcited electrons relax to generate heat within 1 ps, while the heat-diffusing distance from the heat source can be modelled via the bi-exponential decay ultrafast lensing response which consists of two constant time parameters, τ_1 and τ_2. The former time constant is associated with molecular-scale heat conduction across the interfacial layer (~0.49 to 1.1 nm) whilst the latter represents heat conduction across the electric double layer (~2.5 to 7.7 nm).

The heat transfer rate across these layers also depends on the thermal boundary conductivity which is dependent on the number of carriers (phonons) incident at the interface, the energy carried by each phonon, and the probability that each phonon is transmitted across the interface [41]. Hence, as a phonon dispersion mismatch will occur for a Ag NP-H_2O interface (which will ultimately influence the heat transfer rate) any NPs in close proximity (within the heat-diffusion distance of 0.49 to 7.7 nm) will *increase* the thermal boundary conductivity and the *probability* of ph-ph coupling between adjacent Ag NPs due to equivalent phonon energies. This proximity effect will also reduce the available surface area for Ag NP – H_2O phonon coupling.

In essence, the RF induced heat within the NP will be more likely to be reabsorbed by adjacent Ag NPs than couple to the bulk water, which would attenuate the efficiency and effectiveness of Ag NP-H_2O radiative heat transfer. Evidence recently documented by N. Zeng *et al.* [40] has theoretically shown larger temperature distributions around Ag NP aggregates when compared to single isolated NPs which would suggest that the heat energy is coupling to Ag NPs in close proximity more effectively than single, isolated NPs. It is also worth considering the interactions of water molecules adjacent to the Ag NP surface to see if any electric field screening effects are prevalent. This is now discussed.

To further elucidate the point mentioned a physical picture of the interactions of water molecules on the surfaces of citrate stabilized Ag and Au NPs both at equilibrium conditions (no external electric field) and active conditions (RF exposure) must be presented. This is illustrated in figure 6.13. Considering first the Ag NPs under steady

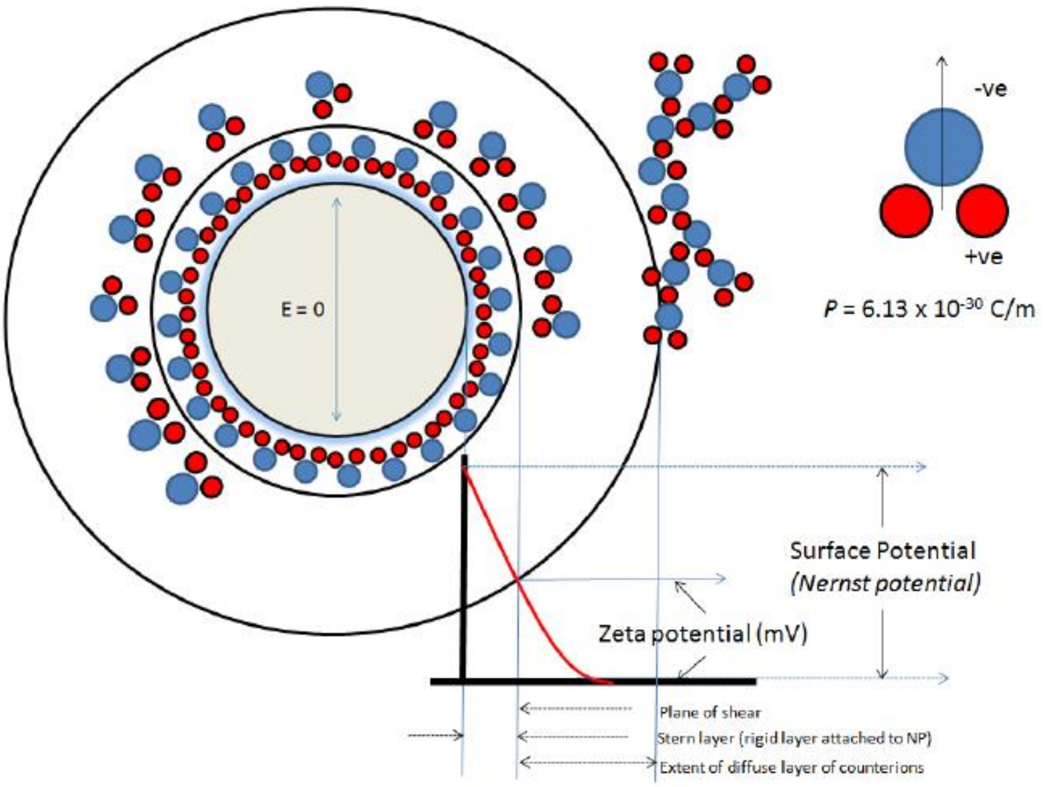

Figure 6.13: Illustration of the surface interaction of water molecules on an Ag NP under equilibrium conditions (no external electric field). Electric field within Ag NP is zero (Gauss law) and electron charge density is evenly distributed across the surface. Water molecules will become polarized over the NP surface (Stern layer) with degree of polarization and layer thickness linearly decreasing. This creates an electric double-layer. The electric potential between edge of Stern layer and diffuse layer is known as the zeta-potential. Also shown is molecule of water with polarization orientation from positive to negative.

state (equilibrium) conditions, the net volume charge density within the conducting NP is zero. As the electrons are free to move within the conductor they are constantly ‘feeling’ repulsive forces and will inherently move to minimize this interaction which leads to surface charge accumulation. This surface charge effectively reduces the internal electric field to zero (Gauss’s law) [42]. The surface charge will also induce polarization of adjacent water molecules in close proximity to the NP surface – which is further enhanced due to the negative charge nature of the citrate surfactant.

Water is a polar molecule (top-right, figure 6.12) with a dipole moment of 6.3 x 10^{-30} C/m (equal to 1.885 D, Debye) [43]. Even though there are an equal number of positive and negative charges within a water molecule their spatial arrangement and asymmetry causes a finite charge separation (0.0039 nm) which in turn induces a permanent dipole moment with the hydrogen and oxygen atoms being the positive and negative terminals, respectively.

When water molecules come into contact with a charged surface (or a Ag NP with surface charge) they orientate themselves to align their positive ends with the negative surface charge and effectively ‘stick’ to the NPs. This forms a layer known as the Stern layer. The negative charge present on the NP surface essentially dictates the concentration of counter ions within the Stern layer (which may be several layers thick) as well as the concentration of counter ions in close proximity. This forms a double-layer which is made of two parts: the Stern layer and an outer region (diffuse layer) where a balance of electrostatic forces and random thermal interactions determines the concentration of counter ions. Although the electric potential between the inner and outer region of the Stern layer falls off sharply and linearly, the electric potential across the diffuse layer (which terminates when the electric potential is zero) decays exponentially. The electric potential across this region is celled the zeta potential (fig. 6.13) and can be experimentally measured. Outside this diffuse layer the water molecules are in a state of random motion, creating hydrogen bonding networks with one another. We now examine the case then an electric field (square wave, 13.56 MHz) is applied to the system.

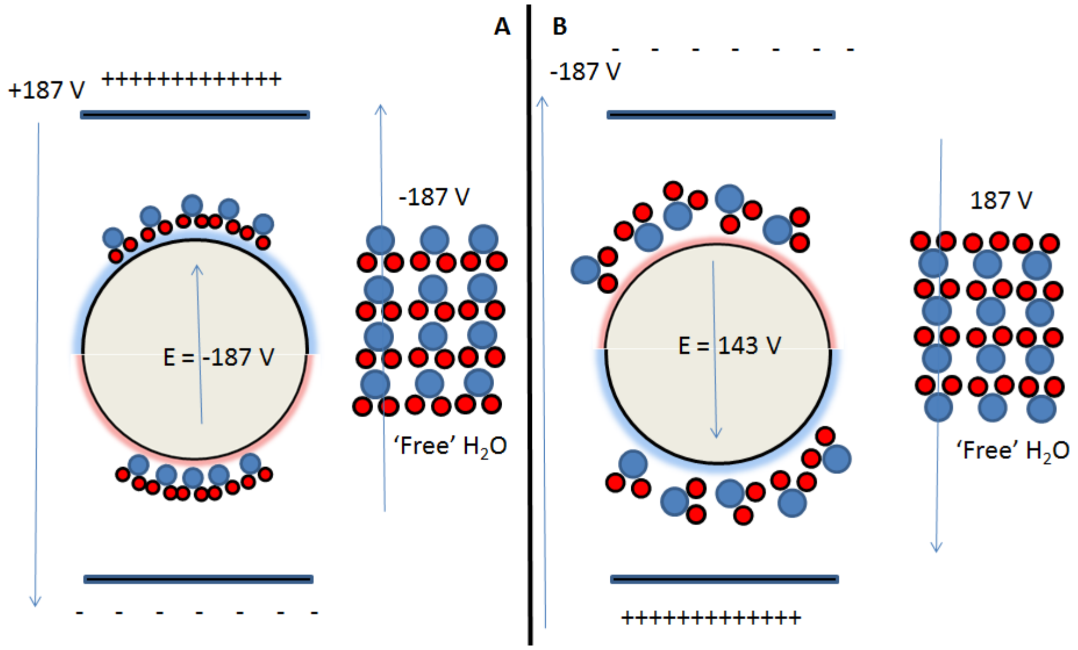

Figure 6.14: Illustration of Ag NP/water interactions in an applied electric field.

As can be seen in figure 6.14 upon applying an external field to the system the electric field within the Ag NP will be equal in magnitude but opposite to the external field (Guass's law). Hence, the external electric field effectively polarizes the NP creating areas of condensed negative and positive charge (top and bottom, respectively). The water molecules across the Stern layer will re-orientate from their equilibrium conditions to match the positive and negative surface charge areas on the NP surface. External 'free' water molecules outside the diffusion layer will align almost instantaneously (relaxation time of polarization process is 9.6 x 10^{-12} s [36]). However when the field is reversed although the external 'free' water molecules re-align almost instantaneously the water molecules across the Stern layer *take longer to re-align due to the water-NP surface interactions*. In effect this *reduces* the electric field 'seen' by the NP and ultimately may reduce the heating rate by a very small fraction. However, due to the relatively large period of each successive 13.56 MHz RF wave (~36 ns) it is estimated by the author that the re-orientation of the citrate attached water molecules will happen within a relatively short time frame, comparable to that of ‘free’ water molecules.

To summarize, it is suggested that heating rates are concentration dependent due to the presence of aggregates which increase the thermal boundary conductivity by increasing the probability of NP –NP phonon coupling across the heat diffusion layer rather than NP-H_2O phonon coupling. In essence, any heat produced within the NPs would more likely be reabsorbed by adjacent NPs in close proximity (nm) rather than diffuse throughout the bulk water. As concentration increases, aggregation states increase resulting in an increase in NP-NP coupling with a decrease in observed heating rates. It has also been shown that ‘residual capacitance effects’ due to an increase in water re-orientation times from NP surface citrate bound water molecules may also attenuate the electric field across the NP – this effect is thought to be relatively weak and considered negligible.

Although possible reasons behind a concentration dependent decrease in heating rate have been given we can still use equation 6.21 in evaluating the final objective of this section (calculating the minimum number of NPs needed for successful cancer cell hyperthermia) as the difference between the results for 0.5 mg/l concentrations and equation 6.21 are very close and less than an order of magnitude (other concentrations can subsequently be modelled by introducing an attenuation factor which is proportional to concentration – omitted in this report as we are only interested in achieving the greatest heating efficiency possible, which was observed for a concentration of 0.5 mgl)

Using Ag and Au NPs of diameter 20 nm (for cellular studies the smaller size is more likely to internalize within the cell structure) we can plot equation 6.21 as a function of HPLC volume – this is the real advantage of this equation in that any volume of solution and any number of NPs can be taken and calculated for heating rates. Figure

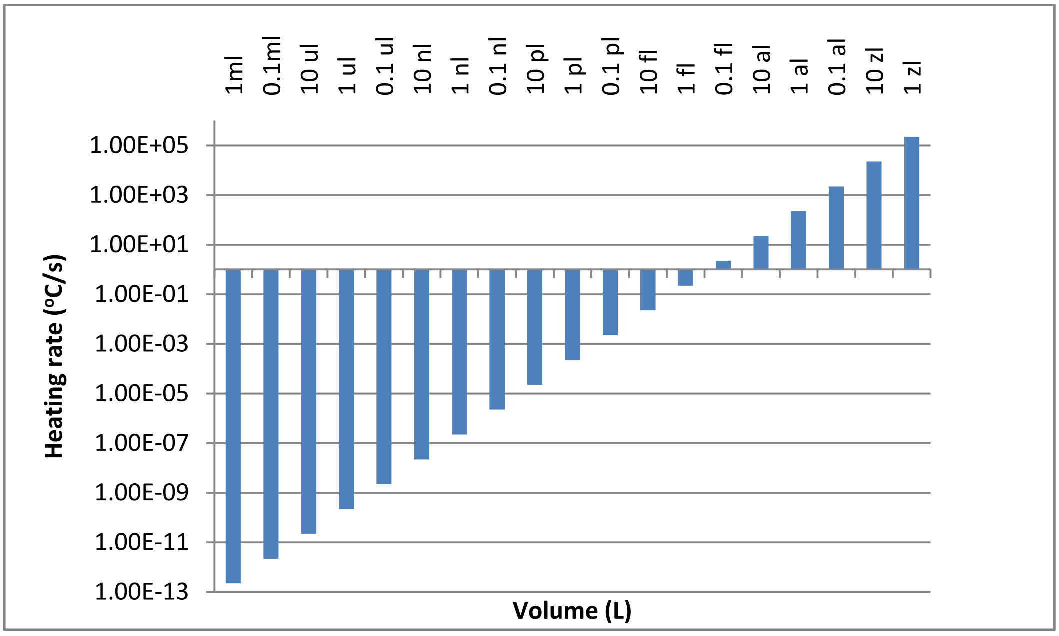

Figure 6.15: Heating rate per 20 nm Ag NP suspended in a variety of HPLC water volumes (1 milli-litre (ml), micro-litre (μl), nano-litre (nl), pico-litre (pl), femto-litre (fl), atto-litre (al), and zepto-litre (zl)). As can be seen, a 20 nm Ag NP situated in a water volume of 0.1 fl would result in a volumetric temperature increase of 2.2 ^{o}C which is almost enough for hyperthermia to take place (an increase of ~ 10 ^{o}C is needed for cellular hyperthermia).

6.15 illustrates this data and shows that for a volume of 0.1 femto-litre (fl) the heat increase will be 2.22 ^{o}C and will continue to increase by an order of magnitude for an order of magnitude decrease in volume. As an increase of 10 ^{o}C is needed for hyperthermia to take place, which is attainable for a volume of 10 al, this would suggest that a single Ag NP of diameter 20 nm could be used as an effective single-cellular hyperthermic agent.

Although l0 al seems like an extremely small volume, this would equate to a spherical water particle of radius 133 nm which is comparable to the dimensions of the 20 nm Ag NP itself. This is further illustrated in figure 6.16 which plots the temperature increase per fixed volume of water (10 al, 1 al, 0.1 al, and 1 zl) whose volume has been modelled

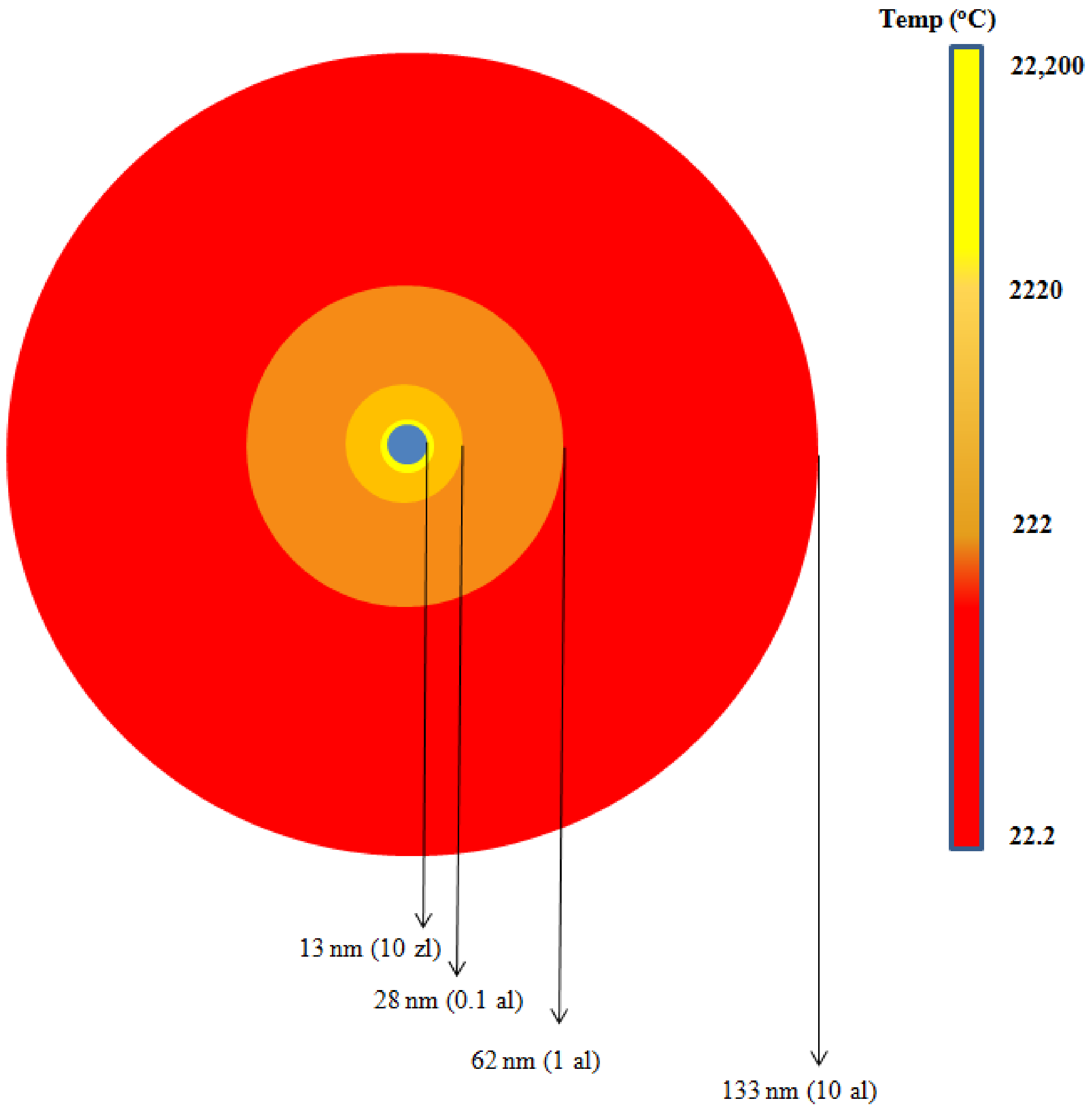

Figure 6.16: Heat production versus volume (for a 20 nm Ag NP) using equation 6.21. A water volume of 10 al would exhibit a temperature increase of 22.2 °C within one second which would be enough to induce cellular hyperthermia within this volume.

as purely spherical. What is extremely interesting is the temperature increase in close proximity to the NP; i.e. for a 10 zl water volume the temperature increase would be approximately 22,200 °C. Although this temperature is extremely unlikely in physical systems (due to fast thermal gradients and heat dissipation into the surrounding volume) TEM evidence of 20 nm Ag NPs after RF exposure does indeed suggest that the NP aggregates are fusing together – as if they are being melted to some degree in solution.

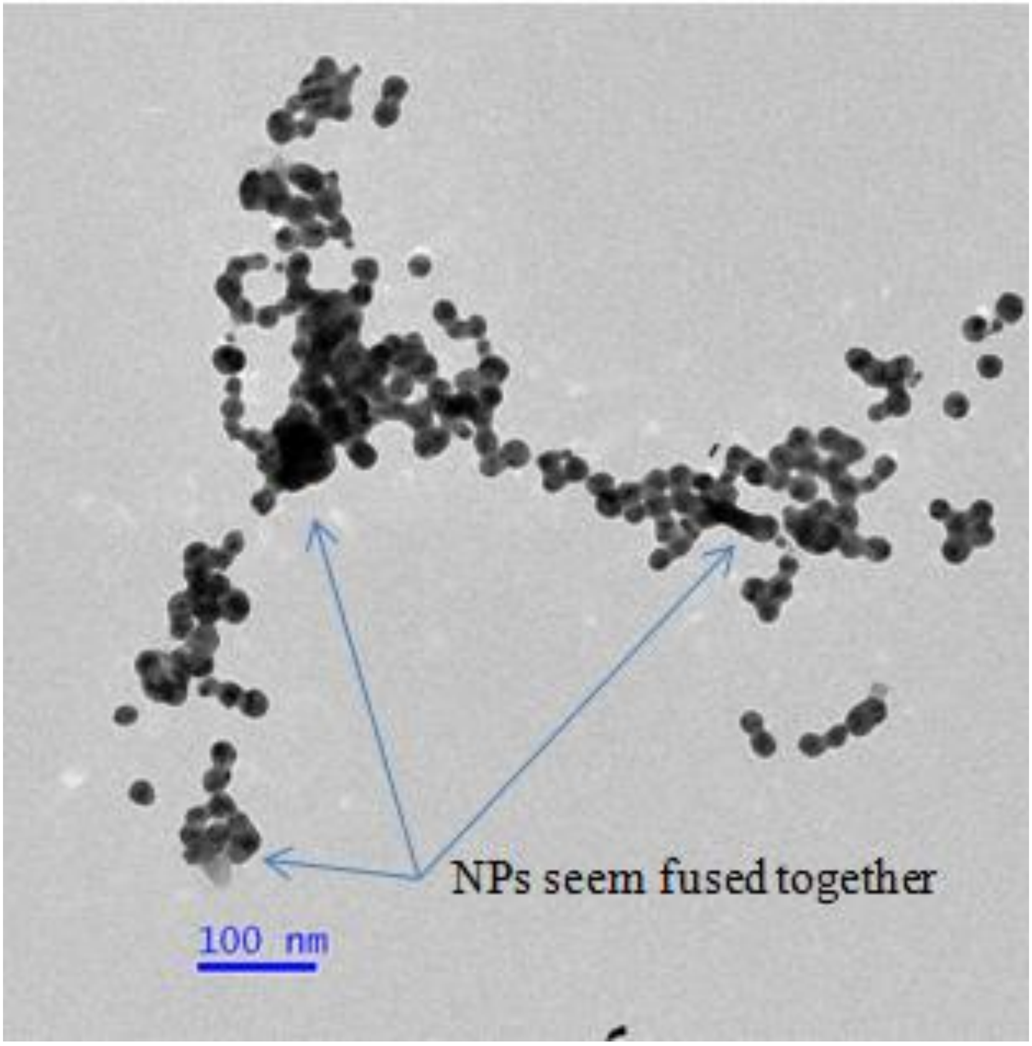

Figure 6.17: TEM image of 20 nm Ag NPs after RF exposure. The NPs seem almost fused together due to the presence of large heat production. Concentration was 5 mgl.

This is seen in figure 6.17. It should be noted that heat generated by NPs can be used to melt the NPs themselves and modify their shape [44, 45]. Hence, for this to occur the temperature in close vicinity must be comparable to the melting point of Ag (~961 ^{o}C)

6.6 Conclusions

In conclusion, it has been shown that the bulk of the heating rates of the as-purchased Ag and Au solutions are due to the buffer solutions, and not the NPs themselves. This contradicts recent claims made by Moran *et al.* and Gannon *et al.* [6, 8] as they did not take this fact into account. This may also elucidate the potential for developing new types of NPs for maximum heating efficacies; i.e. it could be the case that hollow Au/Ag nanocages filled with excess salts may be a far more efficient heating element.

It was also shown that Ag and Au NPs dispersed in ultrapure HPLC water do in fact exhibit low levels of heat production when compared to water alone and increase their heat production for an increase in sample concentration.

A modelling framework was also developed and successfully derived, via dimensional analysis, to allow heat production to be calculated per NP based on electric field strength, conductivity, specific heat capacity and volume of solution in which NPs are suspended in, as well as NP volume (which can easily be altered to accommodate different morphologies such as cubic, rod-like, triangular, etc.). This model also suggests that the heating efficiency is decreased as concentration is increased – several ideas were presented to account for this fact and include NP aggregation (which reduces Ag/Au-H_2O phonon interactions), difference in thermal conductivities, and residual capacitance effects due to ‘sticky’ interaction between water molecules and citrate capped NP surfaces. Finally, we used the volumetric heating model to estimate heat production within a variety of water volumes to estimate that for volumes lower than 0.1 fl enough heat may be produced to induce cellular hyperthermia within that specific volume.

6.6 References:

[1] S. Sheikpranbabu, K. Kalishwaralal, D. Venkataraman, S.H. Eom, J. Park, S. Gurunathan, *Journal of Nanobiotechnology* **2009**, 7:6.

[2] J. L. Elechiguerra, J. L. Burt, J. R. Morones, A. C. Bragado, X. Gao, H. H. Lara, M. J. Yacaman, *Journal of Nanobiotechnology* **2005**, 3:6.

[3] A. J. Haes, L. Chang, W. L. Klein, R. P. Van Duyne, *J. Am. Chem. Soc.*, **2005**, 127, 2264-2271.

[4] N. V. Ayala-Núñez, H. H. L. Villega, L. C. I. Turrent, C. R. Padilla, *Nanobiotechnology* **2009** 5:2–9,

[5] M. M. Kemp, A. Kumar, S. Mousa, E. Dyskin, M. Yalcin, P. Ajayan, R. J. Linhardt, S. A. Mousa, *Nanotechnology* **2009**, 20, 455104.

[6] C. H. Moran, S. M. Weinerdi, T.K. Cherukuri, C. Kittrell, B. J. Wiley, N. W. Nicholas, S. A. Curley, J. S. Kanzius, P. Cherukuri, *Nano Res* **2009**, 2, 400-405.

[7] S. A. Curley, P. Cherukuri, K. Briggs, C. R. Patra, M. Upton, E. Dolson, P. J. Mukherjee, *Exp. Ther. Oncol.* **2008**, 7, 313-326.

[8] C. J. Gannon, C. R. Patra, R. Bhattacharya, P. Mukerjee, S. A. Curley, *J. Nanobiotechnology* **2008**, 6:2.

[9] R. Hergt, R. Hiergeist, I. Hilger, W. A. Kaiser, Y. Lapatnikov, S. Margel, U. Richter, *J. Magn. Magn. Mater.* **2004**, *270*, 345–357.

[10] L. R. Hirsch, R. J. Stafford, J. A. Bankson, S. R. Sershen, B. Rivera, R. E. Price, J. D. Hazle, N. J. Halas, J. L. West, *P. Natl. Acad. Sci. USA* **2003**, *100*, 13549–1355.

[11] A. M. Gobin, M. H. Lee, N. J. Halas, W. D. James, R. A. Drezek, J. L. West, *Nano Lett.* **2007**, *7*, 1929–1934.

[12] C. J. Gannon, P. Cherukuri, B. I. Yakobson, L. Cognet, J. S. Kanzius, C. Kittrell, R. B. Weisman, M. Pasquali, H. K. Schmidt, R. E. Smalley, S. A. Curley, *Cancer* **2007**, 110, 2654-2665.

[13] P. L. Pereira, J. Trübenbach, M. Schenk, J. Subke, S. Kroeber, I. Schaefer, C. T. Remy, D. Schmidt, J. Brieger, C. D. Claussen, *Radiology*, **2004**, 232, 482-490.

[14] A. P. O'Rourke, D. Haemmerich, P. Prakash, M. C. Converse, D. M. Mahvi, J. G. Webster, *Expert Rev Med Devices*. **2007**, 4, 523-537.

[15] J. Joosten, T. Ruers, *Critical Reviews in Oncology/Hematology*, **2007**, 62, 153-163.

[16] *Website of Steven Curley, M.D. and Paul Cherukuri, Ph.D. http://www.rfnanocancer.com/60minutes.php* (accessed Dec 9th, **2010**).

[17] J. DeMay 'The preparation and storage of colloidal gold sols', i*mmunocytochemistry*, gold probes, pg. 133 (received from Rick Giberson, Ted Pella associate, via email).

[18] A. N. Pestryakov, A. A. Davydov, *Journal of Electron Spectroscopy and Related Phenomena* **1995**, 74, 195.

[19] J. Texier, J. J. Hastrelter, J. L. Hall, *J. Phys. Chem*. **1983**, 87, 4690.

[20] W. Haiss, N. T. K. Thanh, J. Aveyard, D. G. Fernig, *Anal. Chem*. **2007**, 79, 4215.

[21] R. H. Walter, R. M. Sherman, *J. Agric. Food Chem*. **1976**, 24, 6, 1245.

[22] R. Roy, M. L. Rao, J. S. Kanzius, *Mater. Res. Innov*. **2008**, 12, 1.

[23] S. Z. Baykara, *Int. J. Hydrogen Energy* **2004**, 29, 1459.

[24] E. A. Fletcher, R. L. Moen, *Science* **1977**, 197, 1050.

[25] A. Kudo, H. Kato, I. Tsuji, *Chem. Lett*. **2004**, 33, 1534.

[26] E. Chibowski, L. Holysz, *Coll. Surf. A*. **1995**, 101A, 99.

[27] U. Kreibig, *J. Phys. F: Met. Phys.* **1974**, 4, 999, 1014.

[28] U. Kreibig, C.V. Fragstein, *Z. Physik* **1969**, 224, 307.

[29] J. Singleton, "Band Theory and Electronic Properties of Solids" Oxford University Press **2004**.

[30] N. P. Singh, S. C. Gupta, B. R. Sooda, *Am. J. Phys*. **2002**, 70 (8).

[31] K-S Lee, M. A. El-Sayed, *J. Phys. Chem. B* **2006**, 110, 19220.

[32] W. Zhang, S.H. Brongersma, O. Richard, B. Brijs, R. Palmans, L. Froyen, K. Maex, *Microelectronic Engineering* **2004**, 76, 146.

[33] D. Cassidy, G. Holton, J. Rutherford "Understanding Physics Student Guide", Springer-Verlag, **2005**.

[34] T. Prodromakis, C. Papavassiliou, G. Konstantinidis, and C. Toumazou, *Micro & Nano Letters* **2009**, 4, 2, 80.

[35] A. C. Metaxas, *Foundations of Electroheat: A Unified Approach*, J. Wiley & Sons: New York, NY, **1996**.

[36] R. Buchner, J. Barthel, J. Stauber, *Chem. Phys. Lett*. **1999**, 306, 57.

[37a/b] R. B. Dinwiddie, R. J. Pylkki, P.E. West, 'Thermal conductivity contrast imaging with a scanning thermal microscope', Proceedings of the 22nd International conference on Thermal Conductivity, pg. 674[a], pp 724 [b], **1994**.

[38] A. Harata, J. Taura, T. Ogawa, *Jpn. J. Appl. Phys*. **2009**, 39, 2909.

[39] Y. Jiang, H-Y Wang, L-P Xie, B-R Gao, L. Wang, X-L Zhang, Q-D Chen, H Yang, H-W Song, H-B Sun, *J. Phys. Chem. C* **2010**, 114, 2913.

[40] N. Zheng, A. B. Murphy, *Nanotechnology* **2009**, 20, 375702.

[41] E.T. Swartz, R. O. Pohl, *Reviews of Modern Physics* **1989**, 61, 3.

[42] R. A. Serway, C. Vuille, J. S. Faughn, 'College Physics', 8th Edition, Brooks/Cole Cengage Learning, **2008**.

[43] J. K. Gregory, D. C. Clary, K. Liu, M. G. Brown, R. J. Saykally, *Science* **1997**, 275, 5301, pp. 814.

[44] A. L. Stepanov, *Rev. Adv. Mater. Sci* **2003**, 4, 123-38.

[45] A. Plech, V. Kotaidis, S. Grésillon, C. Dahmen, G. von Plessen, *Physical Review B* **2004**, 70, 195423.

7.1 Conclusions and future work

Application I: Strained-Silicon SERS

Surface enhanced Raman spectroscopy was successfully utilised to enhance the Raman scattering intensity for a variety of nm-thin ε-Si samples. The signal transducing NPs were fabricated using a physical vapour deposition system and alternatively via chemical synthesis. Strained-silicon samples of thickness 9 nm, 17.5 nm, and 42 nm grown on $Si_{0.7}Ge_{0.3}$, $Si_{0.8}Ge_{0.2}$, and $Si_{0.8}Ge_{0.2}$ virtual substrates, respectively, were used throughout this investigation.

Using a direct thermal evaporation source, Ag nanopowder was evaporated at a relatively high pressure using a source-to-substrate distance of 21 cm to optimise Ag NP growth upon the selected ε-Si samples. Optimised SERS enhancements were found for a Ag NP thin-layer of purple-blue colour. These samples were then investigated for SERS enhancement using a micro-Raman system with a 488 Ar^+ nm excitation source. For all samples SERS enhancements were visible. After discussing effects such as z-alignment, heating effects, SERS enhancement variations, as well as system limitations and error margins it was concluded that nanoscale strain variations from point-to-point are most likely due to system limitations, but there are certain samples however which display variations larger than these systematic error margins which may suggest the ability for this SERS technique to accurately characterise nanoscale strain variations.

Attempts were also made for the first time (known to this author) to accurately characterise the SERS enhancement factors for NPs deposited on inorganic ε-Si layers. The plasmonic origin of such SERS enhancements were also investigated using p- and s-polarised light, including high resolution SEM micrographs, to indeed show the plasmonic origin of such effects. It was also shown that for excessive, extended micro-Raman exposure times the SERS intensity almost completely vanishes over a period of approximately one hour – most likely due to heating effects. Future work should be focused on testing the non-destructive nature of such a technique via secondary ion mass spectroscopy – something which unfortunately could not be achieved by this author due to prolonged hardware failure.

The SERS enhancements for identical ε-Si samples were also documented using an alternative chemical synthesis approach as the evaporation technique was found to be too problematic, un-repeatable and most likely unusable in industrial settings. This alternative technique was found to be more efficient (one sample could be used for thousands of experiments), reliable, systematic, and reproducible.

To this effect, Ag NPs synthesised using proprietary citrate reduction methods were purchased from Ted Pella, Inc, and characterised using SEM and UV-VIS. SEM evidence showed that the average sizes and standard deviations of the samples were somewhat different from the values quoted by Ted Pella. SEM evidence also showed that the majority of NP morphologies were generally undefined and showed little resemblance to specific geometric shapes such as tetrahedrons, cubic, truncated cubic etc, with most samples consisting of ‘irregular spherical’ morphologies. Of all the samples investigated (26 ± 4 nm, 49.6 ± 9 nm, 76 ± 11 nm , and 115 ± 20 nm) only the size regime of 76 ± 11 nm showed any SERS activity via micro-Raman spectroscopy using a 488 Ar^+ excitation source. UV-VIS absorption measurements allowed us to determine the relative composition of each solution; i.e. Ag^+ ions, Ag^0, small Ag clusters, and plasmon resonance modes.

Silver NPs were also synthesised using the polyol process (PVP as the stabilizer) to create four samples with NP sizes of 33 nm ± 11 nm, 78 ± 19 nm, 80 ± 18 nm, and 147 ± 38 nm, and were subsequently evaluated for their SERS activity using micro-Raman spectroscopy with a 488 nm Ar^+ excitation source. Apart from the 33 nm ± 11 nm size regime all samples exhibited SERS enhancements with Ag NPs of size 80 ± 18 nm showing optimised SERS activity.

These results also suggest that ε-Si SERS enhancements are a function of NP size as no SERS enhancements were evident for NP sizes smaller than 49.6 nm. This was found to be most likely due to a decrease in the electrical conductivity caused by a decrease in the electron mean free path length which effectively reduces SERS enhancements.

A new, rapid protocol was also developed to help determine optimised SERS characterisation across a large area (100 µm by 100 µm). Future work should be focused on evaluating SERS activity as a function of NP morphology, i.e. use NPs with tighter and sharper distribution profiles, as well as to determine whether this technique is truly non-destructive using secondary ion mass spectroscopy – again, something which could not be done by this author due to prolonged hardware issues.

Application II: Capacitively-coupled radiofrequency heating

As-purchased nanoComposix™ and Ted Pella, Inc, Ag and Au NPs, respectively, were subjected to a 13.56 MHz capacitively-coupled RF heating system to evaluate their use as potential cancer therapeutic thermal agents. This was part of an international collaboration instigated by this author. Ag and Au NPs of diameter, 20 nm, 40 nm, 60 nm, and 80 nm were used. Characterisation procedures involved UV-VIS, TEM, and ICP-OES to determine the optical and structural morphologies of the samples as well as their concentrations, respectively. All samples were centrifuged to remove the NPs from their buffers with the final NPs being suspended in ultra pure HPLC water.

Using ICP-OES data the Ag/Au NP solutions of concentrations 0.5, 5, and 50 mg/L were exposed to the RF heating system. These samples were shown to exhibit heating rates larger than the bulk HPLC water heating rates which indicated conclusively that Ag NPs can be used as effective thermal agents for RF cancer therapeutic treatments. To the authors knowledge this is the first time ever that Ag NPs have been shown to heat under the influence of an RF field.

The heating rates of the buffer only and as-purchased Ag/Au NP samples (at a concentration of 5 mg/L) were also exposed to the RF field to elucidate to what extent the buffer contributes to heat production. These results explicitly showed that the buffers are a major source of heat production and must be removed to investigate the heating rates of the individual Ag/Au NPs samples. These results contradict claims made by Moran *et al*. [1] that Au NPs exhibit size dependent heating profiles as they neglected to take this buffer heating into account. This also casts doubts on recent cellular work by Gannon *et al.* [2] who showed the complete hyperthermic destruction of Heb3B and Panc-1 human cancer cell lines via Au NPs of diameter 5nm internalised within the cells. Although they state that RF-induced heating is lethal to these cells they *did not* fully separate the Au NP buffer from the solution. At this point it is still unclear whether Au NPs actualize cellular hyperthermia via RF heating although tests are underway.

A major effort was undertaken to develop and expand on theoretical aspects to attempt to explain the Ag/Au NP heating mechanism using a volumetric metallic heating model as a function of electric field strength, metallic conductivity (modified to account for a reduction in electron mean free path effects), number of NPs present in the solution and their dimensions, solution volume and specific heat capacity.

Relatively good matches are seen when comparing theoretical and experimental values (especially for Ag NPs) and indicate a decrease in heating efficiency for an increase in sample concentration – several ideas were presented to account for this fact and include NP aggregation (which reduces Ag/Au-H_2O phonon interactions), difference in thermal conductivities, and residual capacitance effects due to 'sticky' interaction between water molecules and citrate capped NP surfaces. Finally, we used the volumetric heating model to calculate heat production within a variety of water volumes to estimate that for volumes lower than 0.1 fl enough heat may be produced to induce cellular hyperthermia within that specific volume.

Future work should attempt to understand the heating mechanism of the buffers in the RF field (which has in fact been attempted in appendix B) which may ultimately led to more advanced NP design for optimal cancer hyperthermia thermal efficiency.

References:

[1] C. H. Moran, S. M. Wainerdi, T. K. Cherukuri, C. Kittrell, B. J. Wiley, N. W. Nicholas, S. A. Curley, J. S. Kanzius, P. Cherukuri, , *Nano Res* **2009**, 2, 5, 400.

[2] C. J. Gannon, C. R. Patra, R. Bhattacharya, P. Mukerjee, S. A. Curley, *J. Nanobiotechnology* **2008**, 6:2.

Appendix A: Chapter 6 supplementary data

The following figures (figures A.1 to A.8) are TEM micrographs of the HPLC suspended Ag and Au NPs, after the centrifugation process, used to obtain morphological characteristics and particle counting measurements outlined in section 6.1. Several more TEM micrographs were taken but omitted from this report.

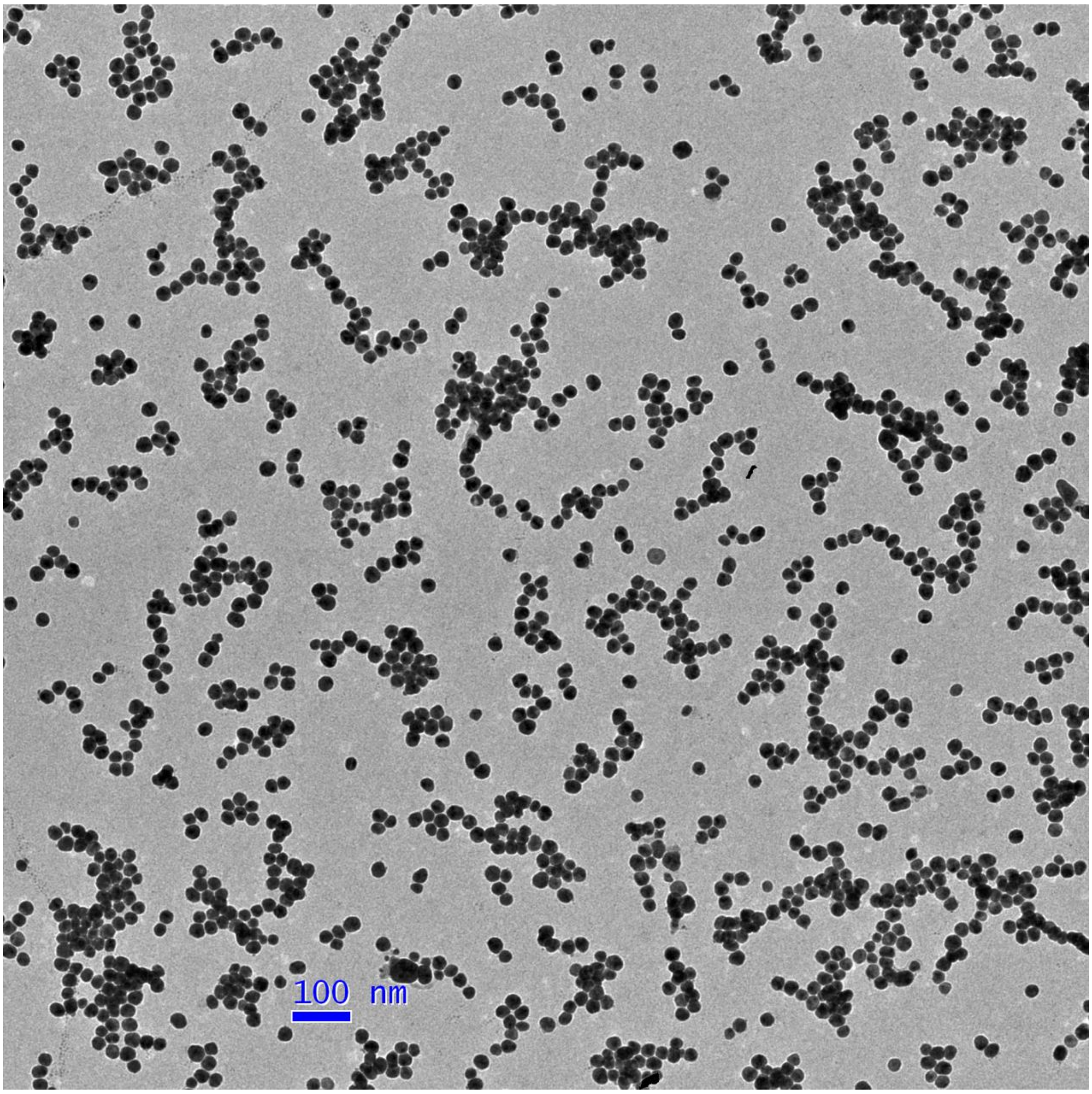

Figure A.1: Ag NPs of dimensions 20.1 ± 2 suspended in HPLC water, after centrifugation procedure. Scale bar is 100 nm.

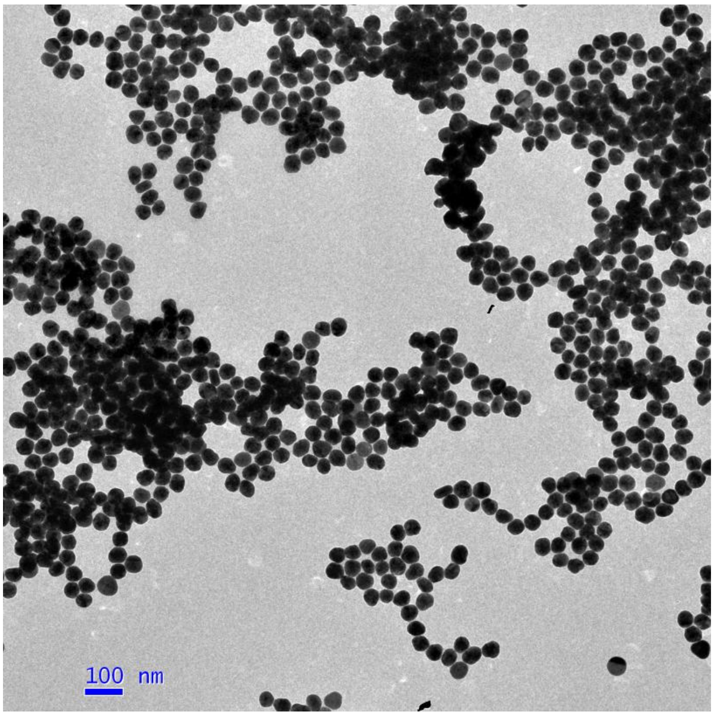

Figure A.2: Ag NPs of dimensions 41.2 ± 4 suspended in HPLC water, after centrifugation procedure. Scale bar is 100 nm.

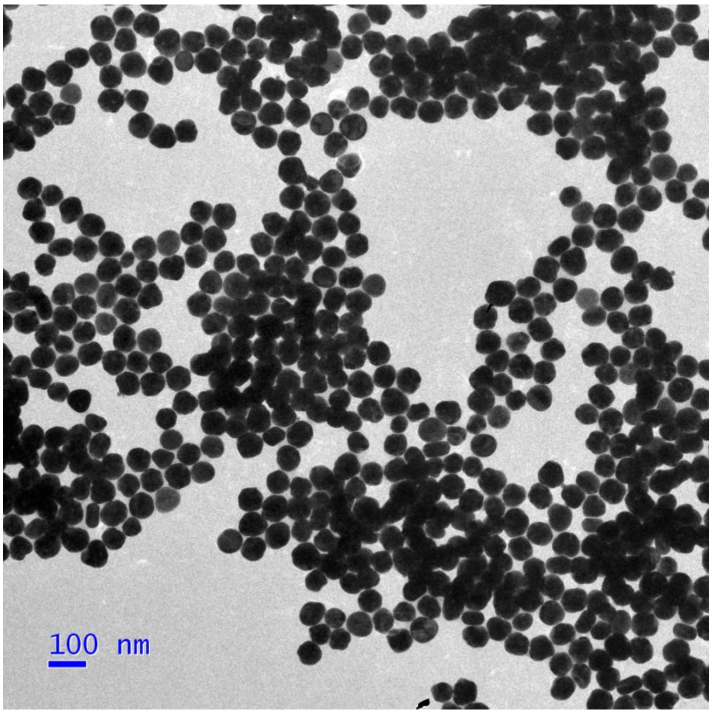

Figure A.3: Ag NPs of dimensions 62.5 ± 6.1 suspended in HPLC water, after centrifugation procedure. Scale bar is 100 nm.

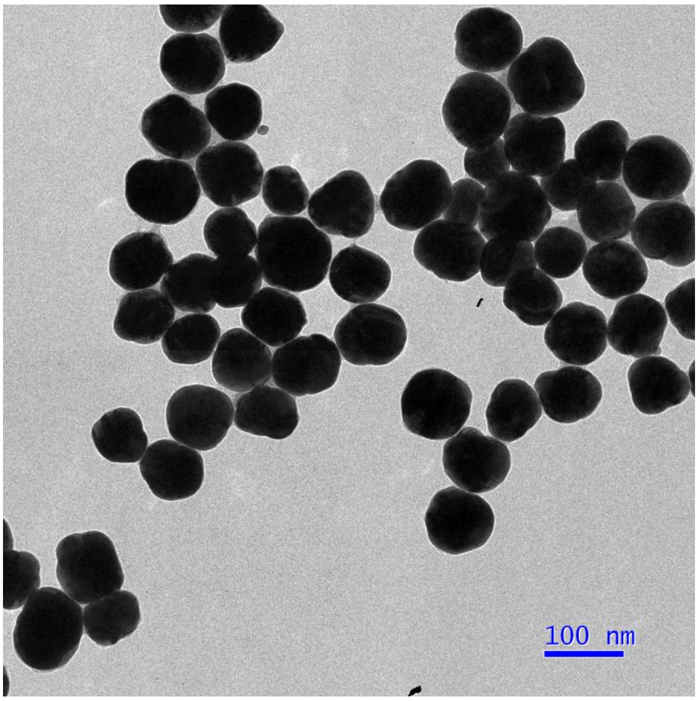

Figure A.4: Ag NPs of dimensions 80.1 ± 8.6 suspended in HPLC water, after centrifugation procedure. Scale bar is 100 nm.

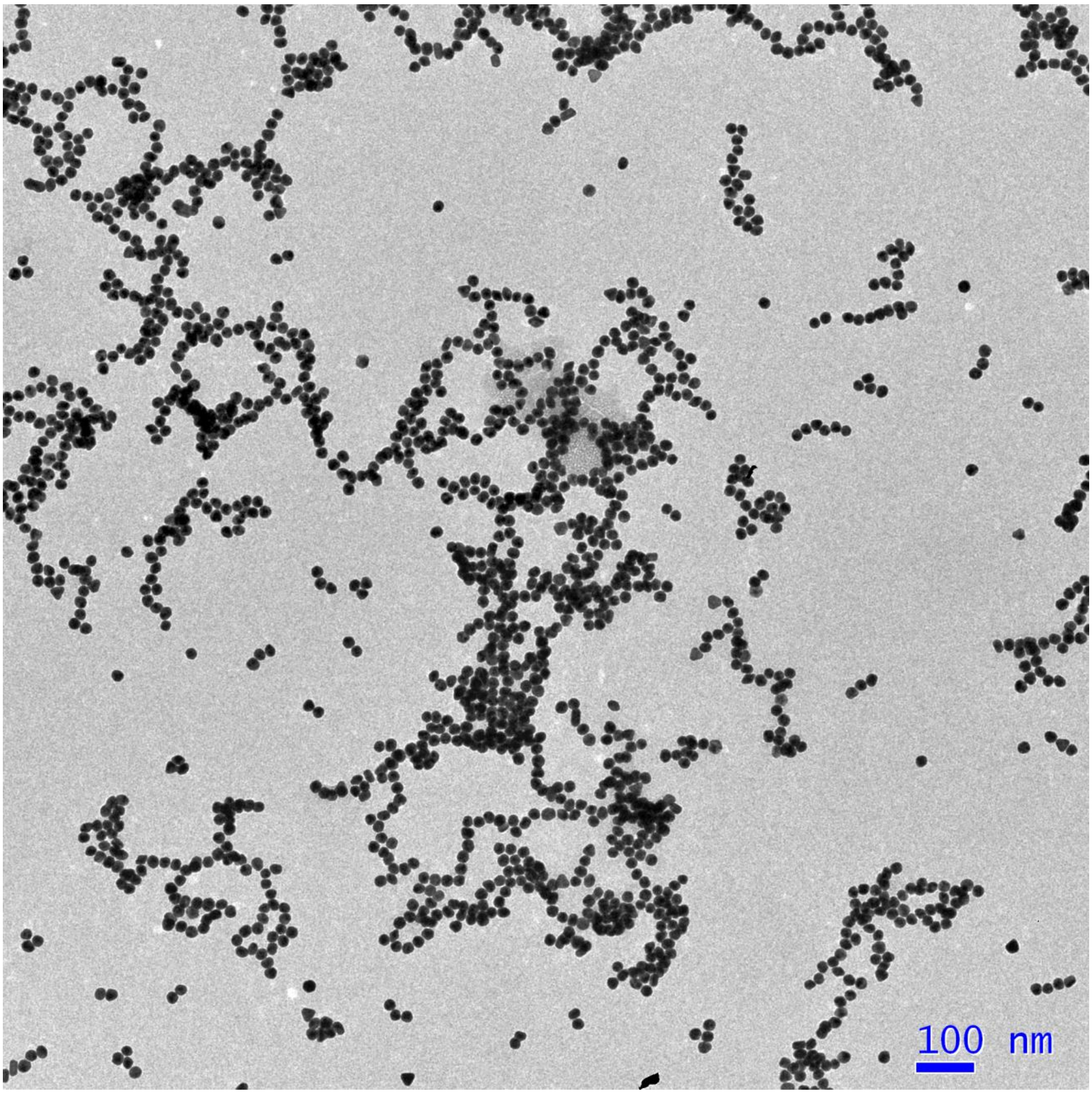

Figure A.5: Au NPs of dimensions 17.3 ± 1.9 suspended in HPLC water, after centrifugation procedure. Scale bar is 100 nm.

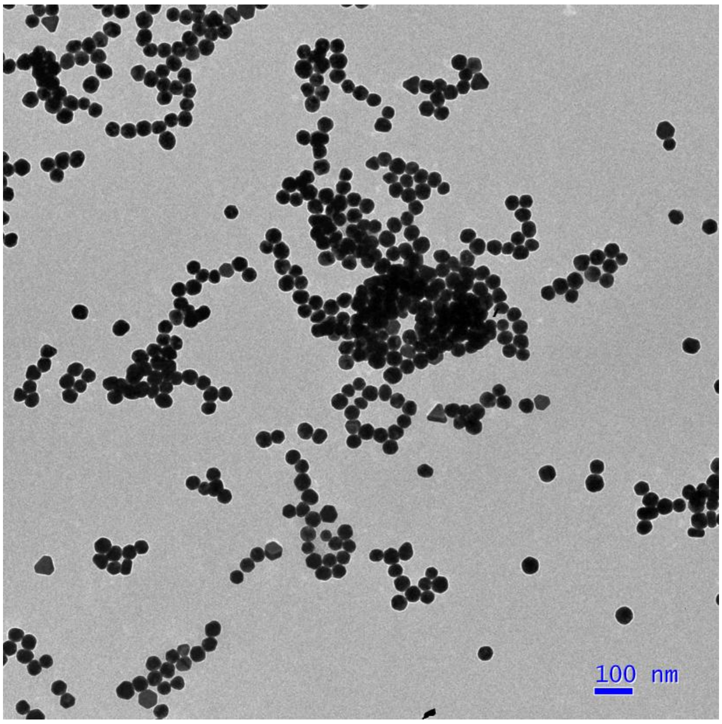

Figure A.6: Au NPs of dimensions 39.4 ± 4.3 suspended in HPLC water, after centrifugation procedure. Scale bar is 100 nm.

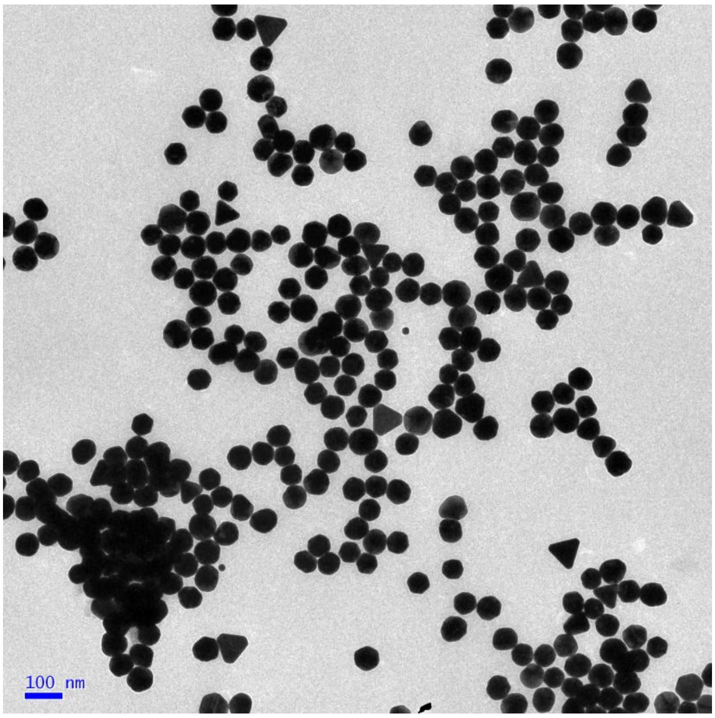

Figure A.7: Au NPs of dimensions 61.1 ± 6.8 suspended in HPLC water, after centrifugation procedure. Scale bar is 100 nm.

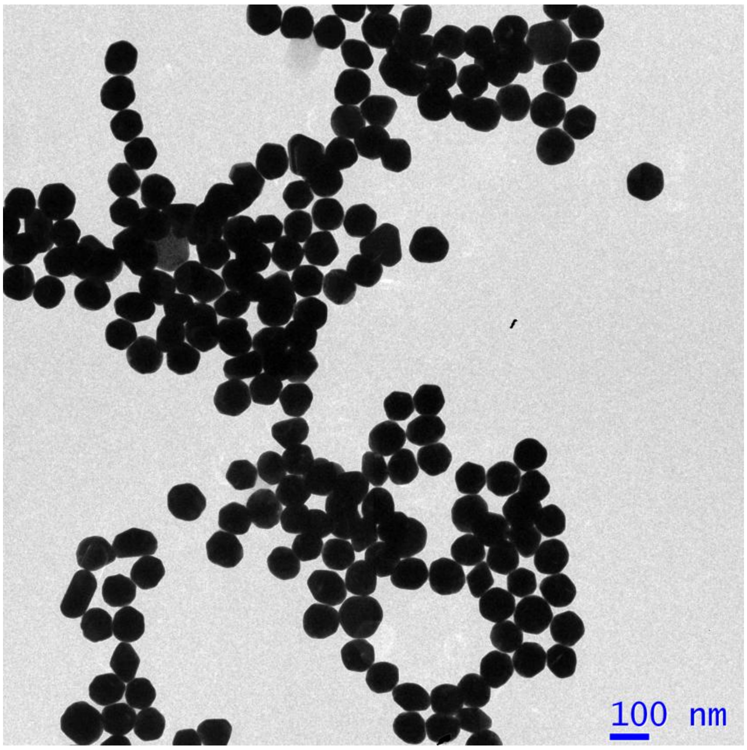

Figure A.8: Au NPs of dimensions 83.4 ± 7.4 suspended in HPLC water, after centrifugation procedure. Scale bar is 100 nm.

The following figures (fig. A.9 and A.10) depict the UV-VIS absorption spectra for 40 nm Ag/Au NPs dispersed in HPLC water. As can be seen for Ag NPs, adequate spectra can only be taken for concentrations of 0.5 and 5 mg/l. Concentrations at 50 mg/l cause the spectra to saturate. For Au NPs adequate spectra can only be taken for concentrations of 5 and 50 mg/l. Concentrations at 0.5 mg/l are too low to show plasmon absorption peaks.

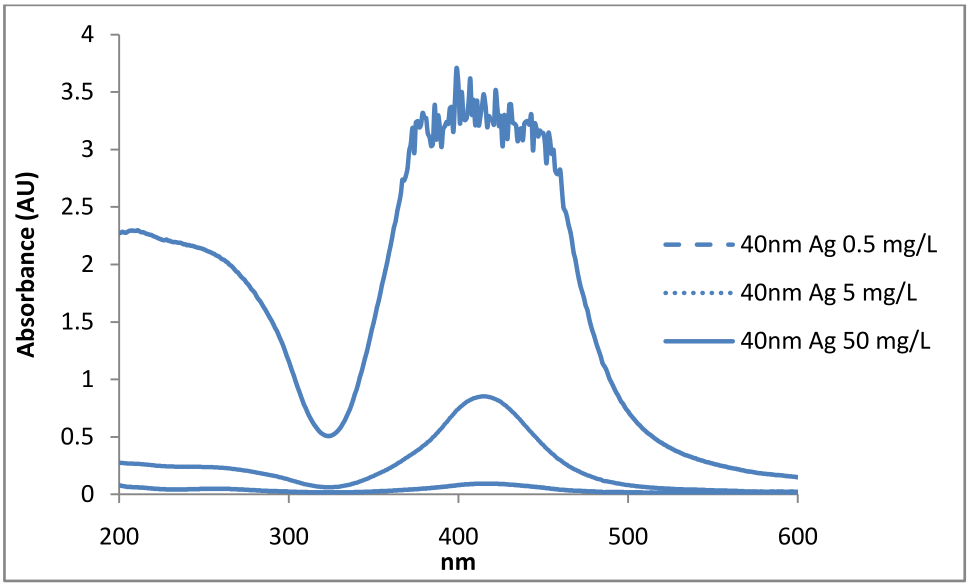

Figure A.9: UV-VIS spectra for 40 nm Ag NPs suspended in HPLC water for concentrations 0.5, 5, and 50 mg/l. As can be seen adequate spectra can only be taken for concentrations of 0.5 and 5 mg/l. Concentrations at 50 mg/l cause the spectra to saturate.

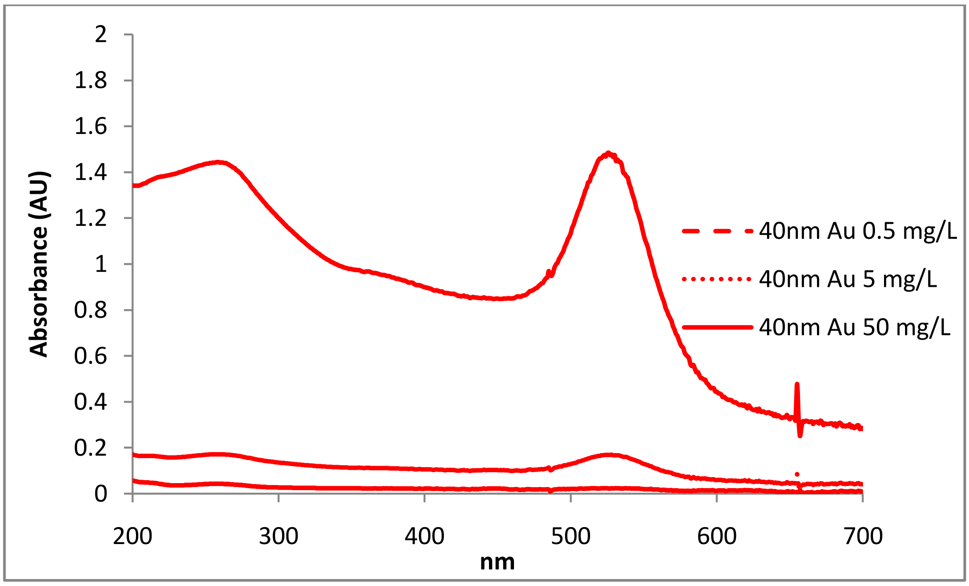

Figure A.10: UV-VIS spectra for 40 nm Au NPs suspended in HPLC water for concentrations 0.5, 5, and 50 mg/l. As can be seen adequate spectra can only be taken for concentrations of 5 and 50 mg/l. Concentrations at 0.5 mg/l are too low to show plasmon absorption peaks.

The following tables (A.1 to A.6) depict various data needed for full theoretical evaluations and are extracted from the ICP-OES data. For all the tables; column A is the concentration used (0.5, 5 or 50 mg/l); column B is the amount of material within the RF sample 1.3 ml volume expressed as mg per 1.3 ml; column C is identical to column B but expressed as kg per 1.3 ml; column D is the calculated spherical volume of the relevant NP (i.e. for diameters of 20 nm, 40 nm, 60 nm, or 80 nm); column E is the density of the material (10490 kg/m^3 and 19300 kg/m^3 for Ag and Au, respectively); column F is the calculated weight (in kg) of a single NP; column G is the calculated quantity of NPs present within 1.3 ml of RF solution (taken by dividing column C by column F); column H is the experimental heating rate (expressed as K.s^{-1}) of each solution after subtracting the bulk HPLC water heating rate; and finally column I is the calculated individual heating rate per NP (k.s^{-1}, calculated by dividing column H by column G). When using the *average* heating values for each concentration (i.e. rather than the *exact* experimental values as no size dependent heating was observed, as mentioned in section 6.2) all values in column H would be replaced by the single average concentration dependent value. Columns highlighted in blue or red (Ag and Au, respectively) indicate the main data for which the ICP-OES data was used to calculate.

0.5 mg/l	A	B	C	D	E	F	G	H	I
Ag	mg/L	mg/1.3ml	Kg/1.3ml	Volume	density	W/NP	# NPs	Heating rate	dT/dt (per NP)
20nm	0.5	0.00065	6.50E-10	4.19E-24	1.05E+04	4.40E-20	1.48E+10	9.23E-03	6.24E-13
40nm	0.5	0.00065	6.50E-10	3.35E-23	1.05E+04	3.51E-19	1.85E+09	8.40E-03	4.54E-12
60nm	0.5	0.00065	6.50E-10	1.13E-22	1.05E+04	1.19E-18	5.48E+08	4.19E-03	7.64E-12
80nm	0.5	0.00065	6.50E-10	2.68E-22	1.05E+04	2.81E-18	2.31E+08	8.90E-03	3.85E-11

Table A1: Theoretical evaluation data for Ag NPs at a 0.5 mg/l concentration.

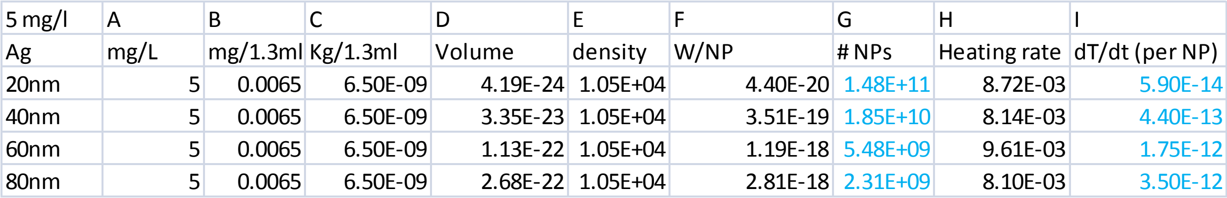

5 mg/l	A	B	C	D	E	F	G	H	I
Ag	mg/L	mg/1.3ml	Kg/1.3ml	Volume	density	W/NP	# NPs	Heating rate	dT/dt (per NP)
20nm	5	0.0065	6.50E-09	4.19E-24	1.05E+04	4.40E-20	1.48E+11	8.72E-03	5.90E-14
40nm	5	0.0065	6.50E-09	3.35E-23	1.05E+04	3.51E-19	1.85E+10	8.14E-03	4.40E-13
60nm	5	0.0065	6.50E-09	1.13E-22	1.05E+04	1.19E-18	5.48E+09	9.61E-03	1.75E-12
80nm	5	0.0065	6.50E-09	2.68E-22	1.05E+04	2.81E-18	2.31E+09	8.10E-03	3.50E-12

Table A2: Theoretical evaluation data for Ag NPs at a 5 mg/l concentration.

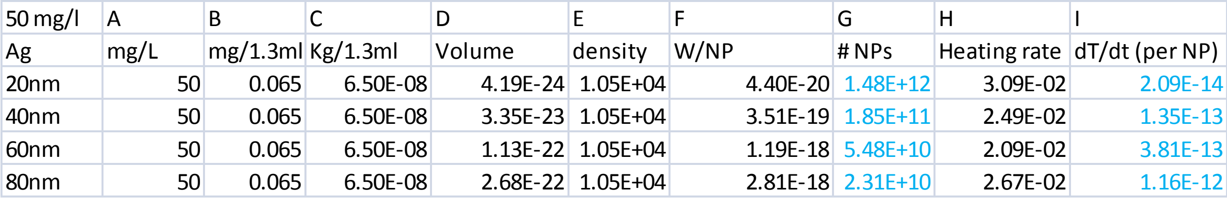

50 mg/l	A	B	C	D	E	F	G	H	I
Ag	mg/L	mg/1.3ml	Kg/1.3ml	Volume	density	W/NP	# NPs	Heating rate	dT/dt (per NP)
20nm	50	0.065	6.50E-08	4.19E-24	1.05E+04	4.40E-20	1.48E+12	3.09E-02	2.09E-14
40nm	50	0.065	6.50E-08	3.35E-23	1.05E+04	3.51E-19	1.85E+11	2.49E-02	1.35E-13
60nm	50	0.065	6.50E-08	1.13E-22	1.05E+04	1.19E-18	5.48E+10	2.09E-02	3.81E-13
80nm	50	0.065	6.50E-08	2.68E-22	1.05E+04	2.81E-18	2.31E+10	2.67E-02	1.16E-12

Table A3: Theoretical evaluation data for Ag NPs at a 50 mg/l concentration.

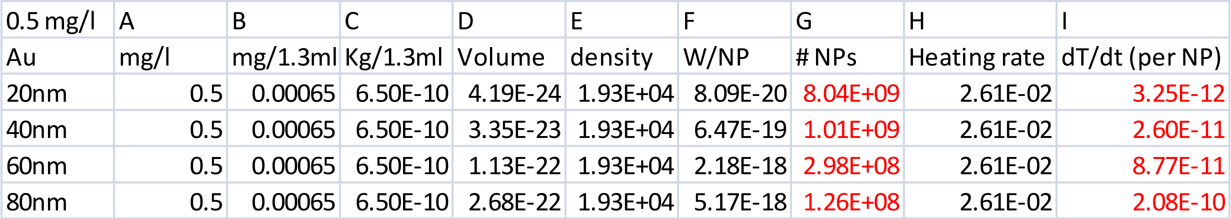

0.5 mg/l	A	B	C	D	E	F	G	H	I
Au	mg/l	mg/1.3ml	Kg/1.3ml	Volume	density	W/NP	# NPs	Heating rate	dT/dt (per NP)
20nm	0.5	0.00065	6.50E-10	4.19E-24	1.93E+04	8.09E-20	8.04E+09	2.61E-02	3.25E-12
40nm	0.5	0.00065	6.50E-10	3.35E-23	1.93E+04	6.47E-19	1.01E+09	2.61E-02	2.60E-11
60nm	0.5	0.00065	6.50E-10	1.13E-22	1.93E+04	2.18E-18	2.98E+08	2.61E-02	8.77E-11
80nm	0.5	0.00065	6.50E-10	2.68E-22	1.93E+04	5.17E-18	1.26E+08	2.61E-02	2.08E-10

Table A4: Theoretical evaluation data for Au NPs at a 0.5 mg/l concentration.

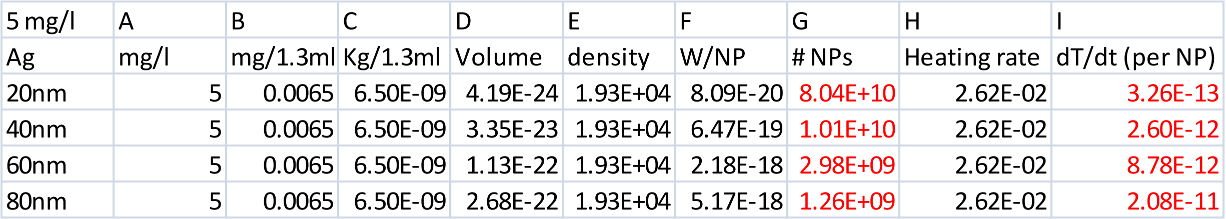

5 mg/l	A	B	C	D	E	F	G	H	I
Ag	mg/l	mg/1.3ml	Kg/1.3ml	Volume	density	W/NP	# NPs	Heating rate	dT/dt (per NP)
20nm	5	0.0065	6.50E-09	4.19E-24	1.93E+04	8.09E-20	8.04E+10	2.62E-02	3.26E-13
40nm	5	0.0065	6.50E-09	3.35E-23	1.93E+04	6.47E-19	1.01E+10	2.62E-02	2.60E-12
60nm	5	0.0065	6.50E-09	1.13E-22	1.93E+04	2.18E-18	2.98E+09	2.62E-02	8.78E-12
80nm	5	0.0065	6.50E-09	2.68E-22	1.93E+04	5.17E-18	1.26E+09	2.62E-02	2.08E-11

Table A5: Theoretical evaluation data for Au NPs at a 5 mg/l concentration.

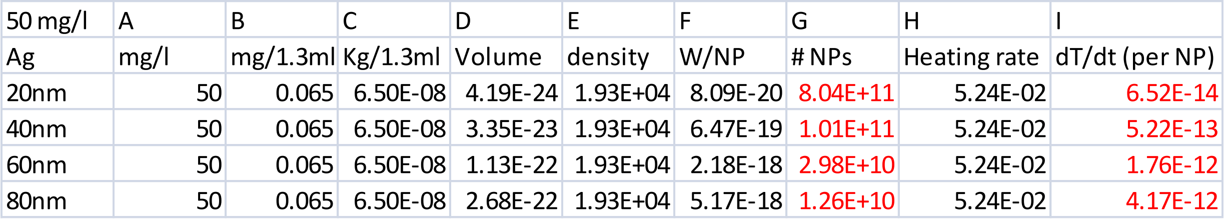

50 mg/l	A	B	C	D	E	F	G	H	I
Ag	mg/l	mg/1.3ml	Kg/1.3ml	Volume	density	W/NP	# NPs	Heating rate	dT/dt (per NP)
20nm	50	0.065	6.50E-08	4.19E-24	1.93E+04	8.09E-20	8.04E+11	5.24E-02	6.52E-14
40nm	50	0.065	6.50E-08	3.35E-23	1.93E+04	6.47E-19	1.01E+11	5.24E-02	5.22E-13
60nm	50	0.065	6.50E-08	1.13E-22	1.93E+04	2.18E-18	2.98E+10	5.24E-02	1.76E-12
80nm	50	0.065	6.50E-08	2.68E-22	1.93E+04	5.17E-18	1.26E+10	5.24E-02	4.17E-12

Table A6: Theoretical evaluation data for Au NPs at a 50 mg/l concentration.

Appendix B: Possible mechanism behind hydrogen-oxygen dissociation from aqueous NaCl solutions.

B.1: Introduction & electrolysis chemical pathways

Currently, an understanding of the physical mechanism behind the heating of buffers in an RF field remains elusive. However, as previously mentioned it does tie in with recent work [1] performed by the inventors of this apparatus with respect to their experiments which demonstrated the effect of RF radiation on the structure and subsequent dissociation of water to yield hydrogen and oxygen. They confirmed the existence of a salt water combustion process. Using NaCl-H_2O concentrations ranging from 0.1 to 30% NaCl placed in a 300 W RF field (an identical apparatus to that reported previously in this chapter 3) the continuous combustion of salt water was exhibited for the duration of the applied RF field. It is also thought by Roy and Kanzius [1] that none of the standard electrolysis methods [2, 3], or other methods for that matter [4,5] can account for the reactions involved with the dissociation of water in H_2 and O_2 exhibited with their experimental setup. An attempt to understand this mechanism is now given.

First of all, the chemical reaction pathways behind hydrogen-oxygen production via electrolysis are known [6]. The four fundamental equations which govern this mechanism are given by equations B.1 to B.4 (assuming the standard electrode configuration, shown in figure B.1).

$$2H_2O\,(l) + 2e^- \rightarrow H_2\,(g) + 2OH^-\,(aq) \quad (B.1)$$

$$2OH^- \rightarrow \tfrac{1}{2}\,O_2\,(g) + H_2O\,(l) + 2e^- \quad (B.2)$$

$$2H_2O\,(l) \rightarrow O_2\,(g) + 4H^+\,(aq) + 4e^- \quad (B.3)$$

$$4H^+ + 4e^- \rightarrow 2H_2\,(g) \quad (B.4)$$

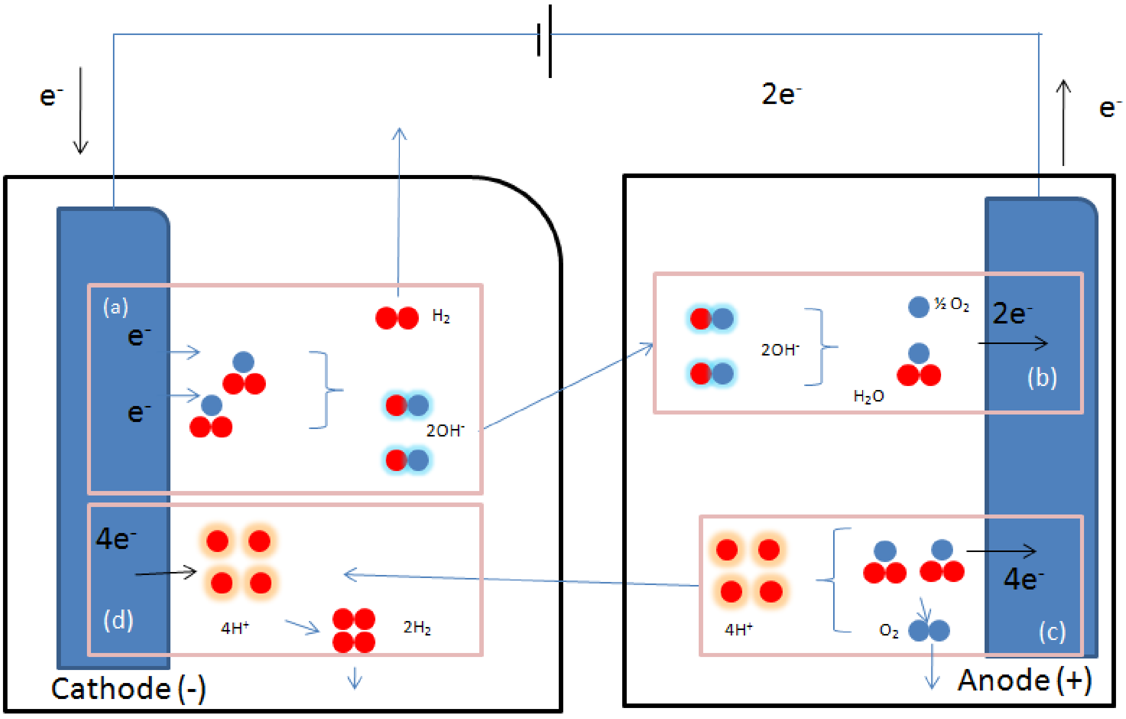

(a) $2H_2O\ (l) + 2e^- \rightarrow H_2\ (g) + 2OH^-\ (aq)$
(b) $2H_2O\ (l) \rightarrow O_2\ (g) + 4H^+\ (aq) + 4e^-$
(c) $4H^+ + 4e^- \rightarrow 2H_2\ (g)$
(d) $2OH^- \rightarrow \frac{1}{2}\ O_2\ (g) + H_2O\ (l) + 2e^-$
Total gas produced = 3 H_2 & 1.5 O_2 **[2:1 ratio]**

Figure B.1: Electrolysis chemical reaction pathway

In general, looking at figure B.1 as a visual guide, the first reaction involves the creation of gaseous H_2 species and two hydroxyl OH^- radicals from the injection of two electrons from the cathode (figure B.1, part (a), equation B.1). These radicals migrate to the positively charged anode, through the water, due to their net negative charge. Upon arrival at the anode they lose their negative charge in the form of two electrons, which are injected into the anode, causing the formation of a stable water molecule and an unstable oxygen atom (figure B.1, part (b), equation B.2) which would subsequently form a stable O_2 gaseous species with another unstable oxygen atom: this is a continuous process. Also at the anode, two water molecules would lose a total of four electrons creating a stable gaseous oxygen molecule as well as four positively charged hydrogen ions H^+ (figure B.1, part (c), equation B.3). Due to their net positive charge these ions will migrate to the negatively charged cathode terminal where they will then form two gaseous hydrogen molecules (H_2) due to the injection of four counter electrons (figure B.1, part (d), equation B.4). By counting up all the gaseous species produced a total of three H_2 and 1.5 O_2 molecules are produced – which is a ratio of 2:1, the same ratio of hydrogen to oxygen atoms in a single water molecule. The primary way in which the RF apparatus differs from this standard electrolysis reaction pathway is the *source of electrons* – as the buffer solutions are situated in mid-air between the RF field there is no constant external source of electrons as in the case of the cathode/anode setup. Another proposed mechanism and chemical pathway must be given.

As the manufacturers of the Ag/Au NPs do not specify exactly what the constitutional elements of their buffers are (for proprietary reasons) it was not possible to re-synthesise these buffers. However, RF heating experiments could be performed on aqueous NaCl solutions of NaCl concentrations 0.5, 5, and 50 mg/l which were equal to the Ag/Au NPs concentrations. As will be seen, these NaCl solutions liberate large amounts of heat energy – more so in fact than the Ag/Au NPs. Finally, it is suggested by this author that the electric field strength is high enough to ionise chlorine atoms in aqueous solutions causing chlorine oxidation which in turn starts a new chemical pathway – the free electrons are able to reduce the sodium which subsequently reacts with water to produce sodium hydroxide (NaOH) and hydrogen gas by-products. Chlorine gas would also be liberated in this proposed chemical pathway. Possible evidence is now presented.

B.2: Experimental Conditions

Aqueous NaCl solutions of concentrations 0.5, 5, and 50 mg/L were created with high purity HPLC water and stored in polypropylene centrifuge tubes. Approximately 1.3 ml of each solution was then subjected to a 600 W RF capacitively-coupled electric field (identical to the previous setup in chapter 6) and exposed until the samples reached 70°C or after 120 s. If the salt water was being electrolysed (chloralkali process) then the separated by-products would be hydrogen and chlorine gas as well as sodium hydroxide (NaOH) or if mixed, sodium hypochlorite or sodium chlorate would be produced. These could be indicated via an increase in pH due to their strong base properties. Starch-iodide paper (coated with starch and potassium iodine) was also created to help detect any oxidative chlorine gas species – which would turn the paper blue if present – as free chlorine gas would oxidize potassium iodide to form elemental iodine which reacts with the starch. The pH of the sample before and after RF exposure was also tested using a digital pH meter (Oakton, ion 510 series). Figure B.2 depicts the heating rate results for the concentrations used whilst figure B.3 depicts the pH results.

As can be seen from figure B.2 the heating rates of the NaCl solutions are directly proportional to the NaCl concentrations, exhibiting heating rates of approximately 0.02, 0.1, and 1.7 °C/s for concentrations of 0.5, 5, and 50 mg/l, respectively. Although the heating rates are comparable to Ag and Au NPs for 0.5 mg/l, the larger concentrations are almost 1 to 2 orders of magnitude greater than their NP equivalent concentrations.

Figure B.3 depicts the pH readings of the NaCl solutions before and after exposure to the RF field. Generally, the pH reading has decreased after RF exposure for all the NaCl samples by approximately 0.4 to 0.5. Although this is a relatively small value it is

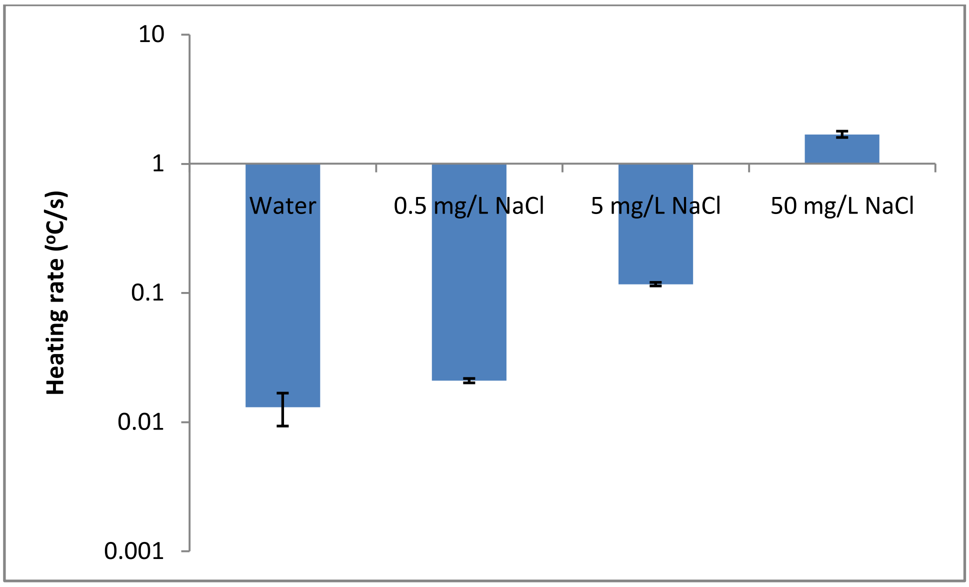

Figure B.2: Heating rates for 0.5, 5, and 50 mg/l NaCl solutions. The y-axis is on a logarithmic scale. As can be seen the heating rate is proportional to NaCl concentration.

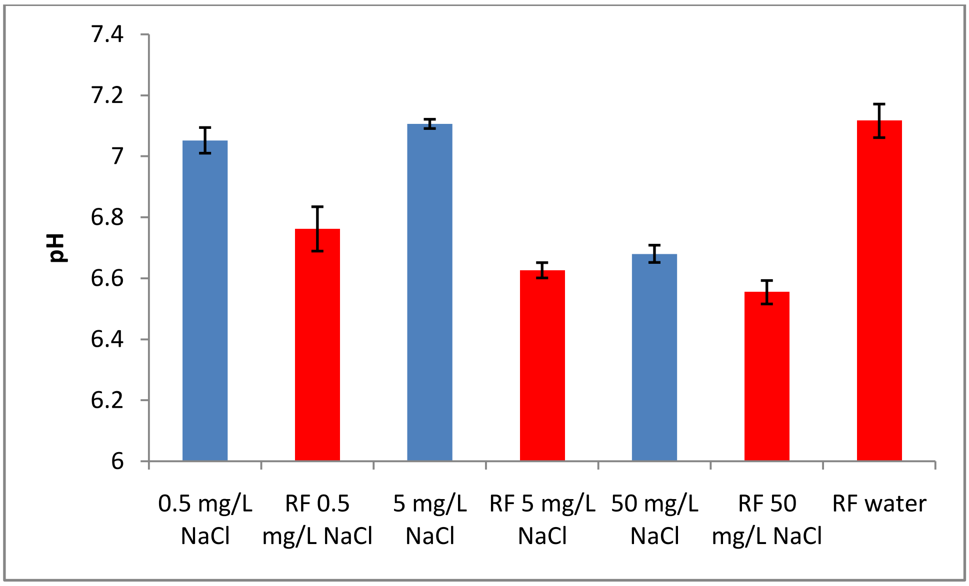

Figure B.3: pH of NaCl solutions before (blue) and after (red) exposure to RF field. For all NaCl solutions a reduction in pH is present.

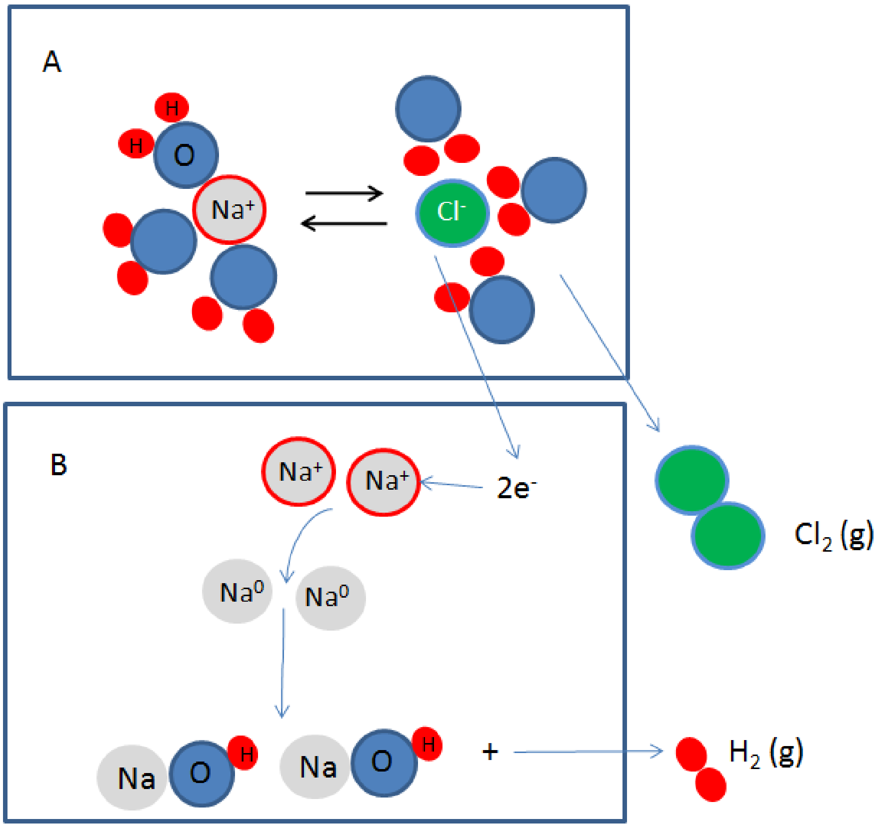

Figure B.4: Proposed chemical reaction pathway for H_2 dissociation from water.

surprising as any sodium by-products such as sodium hydroxide, etc. would increase the value of pH: that is if the proposed mechanism is correct. The proposed mechanism is shown in figure B.4.

The main idea behind such a mechanism is that the chlorine atoms are able to ionise under the influence of an RF field. In figure B.4, part A, the NaCl salts are able to fully dissolve in an aqueous solution. The Na^+ ion will be attracted to the negative dipole terminal of adjacent water molecules whilst the Cl^- ion will be attracted to the positive dipole terminals. In part B, if the two chlorine atoms can lose one of their outer electrons via RF ionisation (as in plasma mechanics) then these two electrons are free to react with the Na^+ ions to reduce them to Na^0 which subsequently reacts with water molecules creating H_2 gas and sodium hydroxide. The chlorine atoms would

Figure B.5: Starch iodide paper after RF exposure. RF field effectively dries out the moist paper and ignites it after approximately 6 seconds (indicated by black burn line).

subsequently combine to become chlorine gas. The full proposed chemical pathway equation is given in equation B.1.

$$2e^- + 2Na + 2H_2O \text{ -> } H_2 + 2NaHO + Cl_2 \qquad \text{(B.1)}$$

It has already been shown that salt water combusts under ignition for as long as the RF field is present [1] but there has been no evidence yet of chlorine gas production. Although the use of starch-iodide paper seemed a good preliminary indicator of Cl_2 gaseous species, in reality it was very hard to use as the RF field would actually dry out the moist starch-iodide paper (which had to be lightly soaked with water before use) and then ignite it, all within approximately 6 seconds of RF exposure. This can be seen in figure B.5. It should be noted that the cuvette containing the NaCl solution was located approximately 0.42 cm from the transmitting RF head whilst the starch-iodide paper was directly stuck to this transmitting head due to its aqueous nature.

Figure B.6: Possible evidence of Cl_2 by-products. The blue ink-like colour was from the starch-iodide solutions which had stuck to the bottom of the transmitting head surface, located directly above the NaCl solutions. When wiped off with a paper towel the solution turned the paper blue.

However, these experiments were repeated several times and at one point, after removal of one of the starch-iodide papers from the transmitting head, several small droplets were remained stuck to the bottom of the transmitting head. After another experiment was performed it was noticed these droplets turned blue and were wiped off with a paper towel (figure B.6). As can be seen in figure B.6 there is a definite blue colour observed on the paper towel which could be possible evidence of Cl_2 gas production.

All these results are *strictly preliminary* and do by no way validate any proposal made throughout this appendix. Rather, they give a small insight into the possible mechanism behind heat production from NaCl solutions which could then be applied to buffer solutions and finally to new, advanced NP design. That is, once the mechanism is known, steps could be taken to unleash the full potential of their heat production.

References:

[1] R. Roy, M.L. Rao, J. Kanzius, *Mater. Res. Innov*. **2008**, 12, 1.

[2] S. Z. Baykara, *Int. J. Hydrogen Energy* **2004**, 29, 1459.

[3] E. A. Fletcher, R. L. Moen, *Science* **1977**, 197, 1050.

[4] A. Kudo, H. Kato, I. Tsuji, *Chem. Lett*. **2004**, 33, 1534.

[5] E. Chibowski, L. Holysz, *Coll. Surf. A*. **1995**, 101A, 99.

[6] K. W. Whitten, R. E. Davis, M. Larry Peck, G. C. Stanley, 'Chemistry', 9th Edition, Brooks/Cole Cengage Learning, **2010**.